Numerical Modelling of Groundwater - Surface Water Interactions with the Double-Averaged Navier-Stokes Equations

---

A thesis submitted in partial fulfilment of the requirements for the Degree of

Doctor of Philosophy in Civil Engineering

in the University of Canterbury

by

A. L. Dark

2017

This thesis is dedicated to my family: Catherine, Sophie and Hamish. Hamish was born in the midst of it, Sophie has grown up with it, and Catherine has been exceptionally patient with it.

Acknowledgements

I would like to acknowledge the help and support of the following people and organisations:

My thesis supervisors, Professor Roger Nokes and Dr John Bright.

The technical staff in the Fluid Mechanics Laboratory: Ian Sheppard and Kevin Wines.

My colleagues at Aqualinc Research Ltd, and Dr David Painter.

The funders of this research, the Ministry of Business, Innovation and Employment, under the "Waterscape" research programme.

Last, but by no means least, my family.

Abstract

The ability to model groundwater and surface water flows as two interacting components of a single resource is highly important for robust catchment management.

Existing methods for spatially-distributed numerical modelling of flow in connected river-aquifer systems treat rivers and aquifers as separate sub-domains, with different governing equations for the flow in each. Mass-fluxes exchanged between the sub-domains are modelled using one of several coupling methods, which do not accurately represent the physics of the flow across the interface between the surface and subsurface flows. This can be problematic for model stability and mass conservation.

This thesis investigates the feasibility of modelling interacting surface water and groundwater flows in a single domain, using a single system of equations.

It is shown that the governing equations in existing numerical models for river and aquifer flow can be derived from the Navier-Stokes Equations. A time- and space-averaged form of Navier-Stokes Equations, the Double-Averaged Navier-Stokes (DANS) Equations, can be used to model both groundwater and surface water flows. The volume-averaging process allows the porous medium to be represented as a continuum.

A novel two-dimensional numerical model is developed from the DANS Equations to simulate flows in connected groundwater and surface water systems. The DANS equations are solved using the finite-volume method. The model simulates two-dimensional flow in a vertical slice.

This allows the horizontal and vertical velocity components and pressure to be modelled over the depth of a stream and the underlying aquifer or hyporheic zone. The model does not require the location of the interface between surface and subsurface flows to be specified explicitly: this is determined by the spatial distribution of hydraulic properties (permeability and porosity).

The numerical model handles the transition between laminar and turbulent flows using an adaptive damping approach to modify the terms in a single-equation turbulence model, based on a locally-defined porous Reynolds number, Re_p. This approach removes the need to specify *a priori* whether flows in any part of the domain are laminar or turbulent. Turbulent porous media flows can be simulated.

The model is verified for porous-media and clear-fluid flows separately, before being used to simulate coupled groundwater - surface water flow scenarios.

For porous-media flows with low Re_p the numerical model results agree exactly with Darcy's Law. The value of Re_p at which the model results begin to deviate from Darcy's Law is consistent with published values.

For turbulent clear-fluid flows the time-averaged velocity and turbulent kinetic energy (TKE) results from the numerical model are verified against a RANS model and published data. A good match is achieved for both velocity and TKE.

Energy grade-line slopes for free-surface flows simulated in the numerical model are a reasonably good match to equivalent results to the one-dimensional hydraulic model HEC-RAS.

Idealised river-aquifer interaction experiments are conducted in a laboratory flume to provide verification data for the numerical model. An innovative combination of optical flow measurement and refractive-index-matched transparent soil is used to measure two-dimensional velocities and turbulent statistics in laboratory flow scenarios that

simulate flow in both losing and gaining streams, and the underlying connected porous layer.

The "gaining stream" laboratory scenario is replicated using the numerical model. The model simulates the key features of the mean flow well. Turbulent statistics deviate substantially from the laboratory results where vertical velocities across the surface-subsurface interface are high, but are a better match elsewhere.

The "losing stream" laboratory results are unable to be reproduced with the numerical model. Results for a similar scenario with lower outflow velocities are presented. These results are qualitatively consistent with the laboratory results.

The numerical model is expected to perform better in simulations of field-like conditions that involve less extreme gradients than the laboratory scenarios.

Contents

List of Figures

List of Tables

Nomenclature

Roman Symbols

F	Forchheimer coefficient
f_p	Porous damping function
g	Gravitational constant $[M^{-1}L^3T^{-2}]$
h	Piezometric head $[L]$
K	Saturated hydraulic conductivity $[LT^{-1}]$
k	Turbulent kinetic energy $[ML^2T^{-2}]$
k_i	Intrinsic permeability $[L^2]$
ℓ	Turbulence mixing length $[L]$
$\dot{m}$	Mass flux $[MT^{-1}]$
p	Pressure $[M/LT^2]$
$\boldsymbol{q}$	Specific flux vector $[L^2T^{-1}]$
S	Storage coefficient
S_s	Specific storage of a confined aquifer $[L^{-1}]$
S_y	Specific yield
t	Time $[T]$

$\mathbf{u}$ Velocity vector $[LT^{-1}]$

U Time-mean horizontal velocity $[LT^{-1}]$

u' Temporally-fluctuating component of velocity $[LT^{-1}]$

$\overline{u}$ Reynolds-averaged velocity $[LT^{-1}]$

$\langle u \rangle$ Spatially-averaged velocity $[L^2T^{-1}]$

$\langle U \rangle$ Double-averaged velocity $[L^2T^{-1}]$

u^+ Normalised wall velocity

u_τ Wall shear stress velocity $[LT^{-1}]$

V Time-mean vertical velocity $[LT^{-1}]$

y^+ Normalised distance from wall boundary

z Elevation above datum $[L]$

Greek Symbols

ϵ Turbulence dissipation rate $[T^2T^{-3}]$

κ von Kármán constant

μ Dynamic viscosity $[ML^{-1}T^{-1}]$

μ_t Turbulent viscosity $[ML^{-1}T^{-1}]$

ν Kinematic viscosity $[L^2T^{-1}]$

ϕ Porosity

ψ Pressure head $[L]$

ρ Density $[ML^{-3}]$

τ_w Wall shear stress $[ML^{-1}T^{-2}]$

θ Water content

ζ Free-surface correction term

Acronyms and Abbreviations

CDS Central differencing scheme

CFD Computational Fluid Dynamics

Da Darcy number

DANS Double-Averaged Navier-Stokes Equations

NSE Navier-Stokes Equations

PTV Particle tracking velocimetry

RANS Reynolds-Averaged Navier-Stokes Equations

Re Reynolds number

Re_p Porous flow Reynolds number

RMS Root-mean-squared

SIMPLE Semi-implicit method for pressure-linked equations

SVE Saint-Venant Equations

SWE Shallow Water Equations

UDS Upwind differencing scheme

Chapter 1

Introduction

1.1 Water Resources Context

Groundwater makes up 30.1% of Earth's total freshwater, or 96% of non-frozen freshwater (Babkin and Vuglinsky, 2003). Globally, groundwater supplies 25 - 40% of drinking water (Vrba and van der Gun, 2004) and contributes to the production of 50% of all irrigated crops (IGRAC, 2013). Despite the high level of use, groundwater is referred to as "the hidden resource" due to the limited amount of data available on the sustainable yield and quality of available supplies (IGRAC, 2014).

Rivers and streams, which are a much more visible component of the total freshwater resource, make up only 0.006% of the earth's total freshwater, or 0.02% of non-frozen freshwater (Babkin and Vuglinsky, 2003).

To sustainably manage water resources, limits must be placed on their use. Setting abstractive use limits in ways that optimise the potential economic and societal benefits of the resource, while ensuring that effects on the environment stay within acceptable limits, requires robust information about water quantity and flow-paths. Limit-setting processes for water quality also require this information, as water quality and water quantity are inextricably linked.

Until relatively recently groundwater and surface water resources have been managed as separate entities, rather than as two components of a single resource. A major change to this approach was the introduction of the European Water

Framework Directive (European Commission, 2000), which required EU countries to prepare River Basin Management Plans and to ensure that groundwater and surface water bodies meet certain objectives. Under the Water Framework Directive, groundwater and surface water bodies must be managed in an integrated manner. If the objectives for a surface water body are not met, then the objectives for any groundwater body with which it interacts are also deemed not to have been met, and *vice versa*. In order to implement this approach, it is necessary to identify and quantify groundwater - surface water interactions.

1.2 New Zealand Context

Access to reliable and sustainable water supply is crucial in New Zealand. While water resources underpin New Zealand's economic growth and development in the agriculture and energy sectors, these same resources are highly valued from cultural, recreational and environmental perspectives (Land and Water Forum, 2010). Therefore robust management of New Zealand's water resources is of the utmost importance to the country's future success.

In 2010 there were approximately 20,500 consented freshwater takes in New Zealand (Aqualinc, 2010). Of the consented takes, 68% were from groundwater, 29% were run-of-river surface water takes, and the remaining 3% were takes from storage. The majority of the takes (75%) were for irrigation. If consented takes for hydro generation (which are generally non-consumptive) are excluded, irrigation makes up 78% of the consented volume (on a weekly average basis). Surface water takes make up 62% of the total consumptive use volume, with groundwater at 34% and storage at 4%.

The Resource Management Act encourages integrated management of natural resources, but how this is done is left up to Regional or District Councils. In the Canterbury Region, the Canterbury Water Management Strategy (Canterbury Mayoral Forum, 2009) has been set up to manage Canterbury's water resources in an integrated manner. The sub-regional planning processes that were put in place under the Strategy must consider a range of targets, many of which recognise that groundwater and surface water resources are highly connected. For example, the abstraction of groundwater on the Canterbury Plains has an effect on lowland

streamflows.

Moreau and Bekele (2015) identified New Zealand's aquifers on a national scale. Their data are shown in Figure 1.1. The areas shown as aquifers in Figure 1.1 approximately correspond to the areas of flat and undulating land ($0-7°$ slope) that represent the most intensively-used agricultural land in New Zealand. This is 37% of New Zealand's total land area (Landcare Research NZ Ltd, 2010).

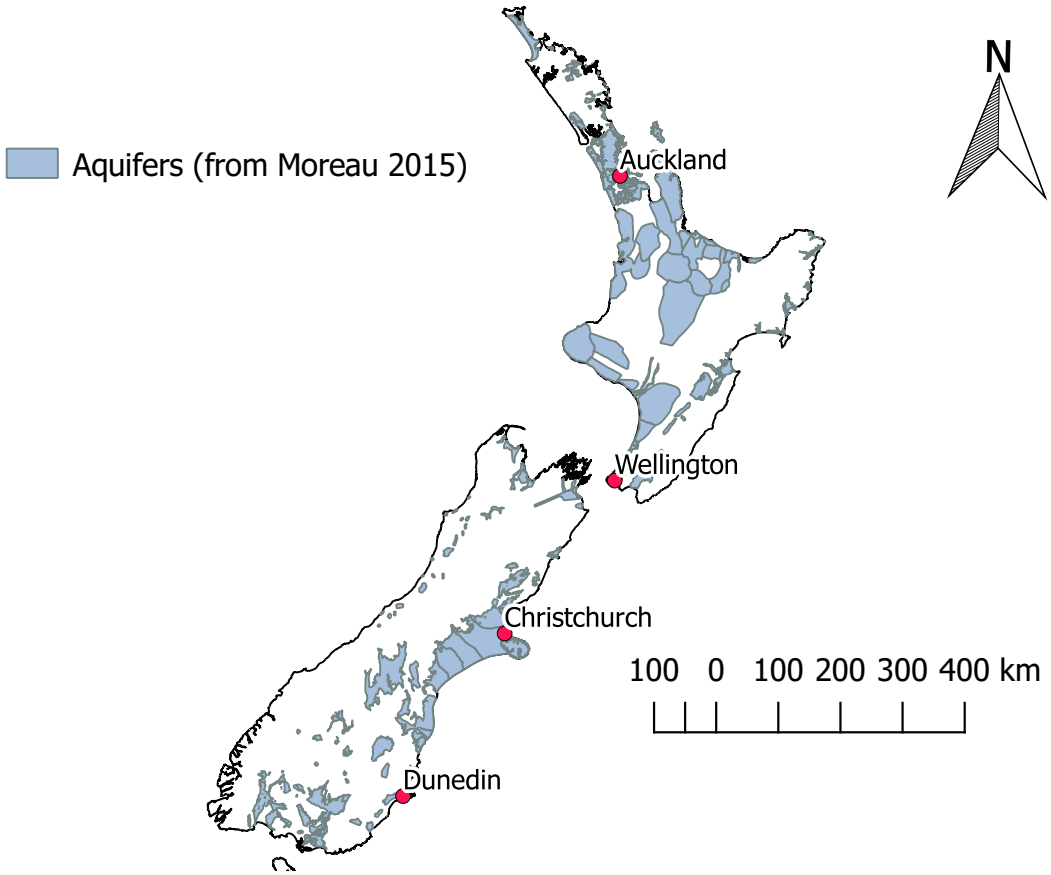

Figure 1.1: New Zealand aquifers (data from Moreau and Bekele (2015))

Because areas of intensive agricultural production in New Zealand tend to coincide with the major aquifers shown in Figure 1.1, abstraction irrigation water sourced from surface water bodies in these areas may have an effect on groundwa-

ter resources and *vice versa*. Smaller surface water bodies that flow through areas of intensive agricultural activity, while not necessarily being directly accessed as sources of water, may be sensitive to the effects of those activities.

An example of a New Zealand river catchment that is highly coupled to an aquifer system is the Selwyn River in central Canterbury. Figure 1.2 (from Larned et al. (2008)) shows how the reaches of the Selwyn River interact with groundwater, and how these reaches correspond with geomorphic regions. The majority of the Selwyn River catchment is within an area identified in Figure 1.1 as an aquifer. The two groundwater allocation zones covered by the surface catchment area are both currently considered to be more than 30% over-allocated (Environment Canterbury, 2013). The fact that the river has both gaining and losing reaches highlights the need for groundwater - surface water interactions to be carefully considered when calculating the total catchment water balance in order to set water allocation limits. Terminology relating to groundwater-surface water interactions and aquifer types is introduced in Chapter 2.

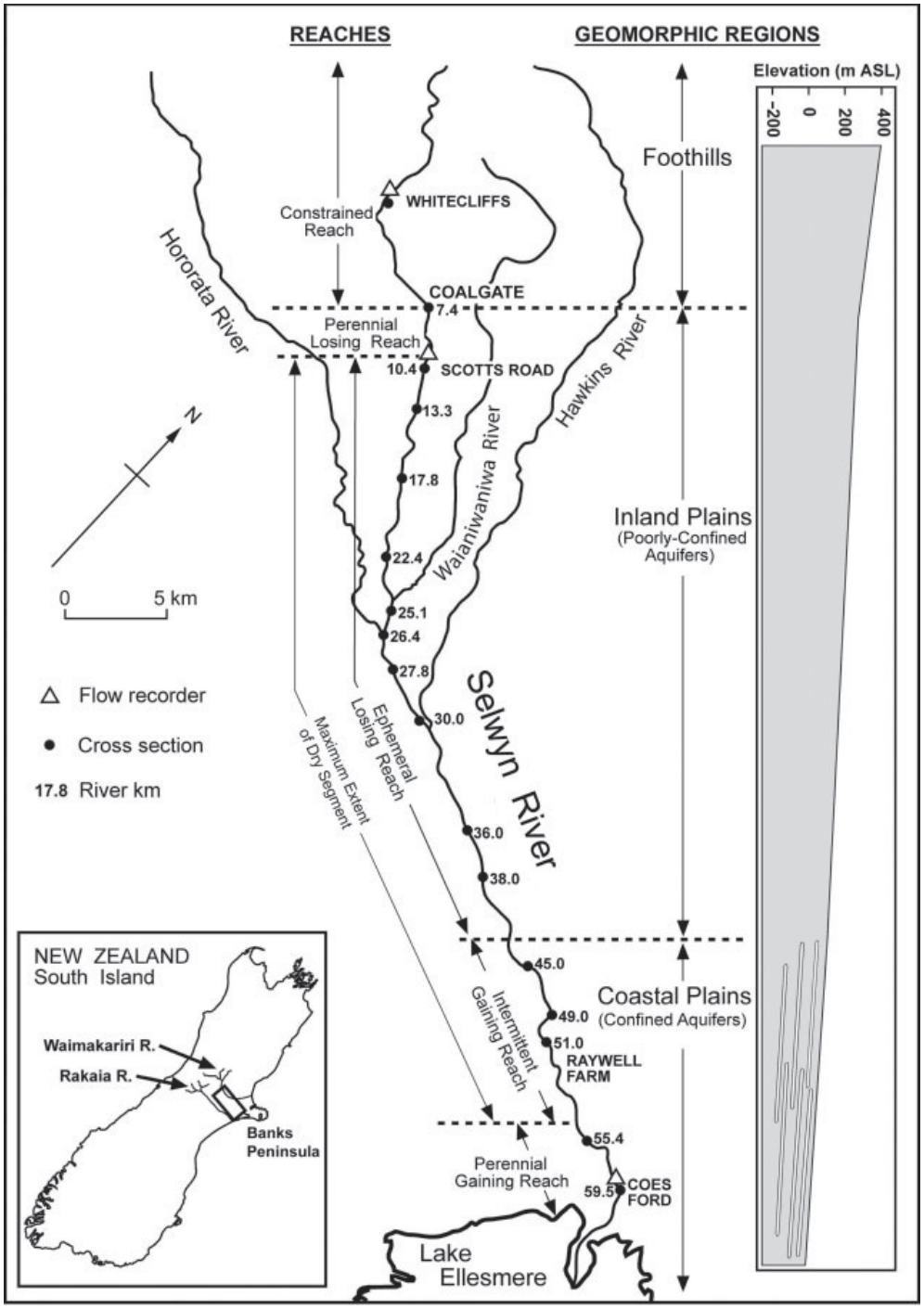

Figure 1.2: Reaches of the Selwyn River with corresponding geomorphic regions (from Larned et al. (2008))

1.3 The Need for Numerical Modelling

Due to the high cost and difficulty of major field investigations, and the fact that they are typically limited to point measurements, numerical modelling is often relied on as an important tool for informing water management decisions. A further advantage of numerical modelling is that it allows historical hydrological records to be incorporated and future scenarios to be tested, whereas field investigations are limited to providing a snapshot of the status quo. Despite this, in 2000 it was estimated that only about 20% of the allocated groundwater in New Zealand is from an aquifer for which there is a calibrated numerical groundwater model (Fenemor and Robb, 2001).

Results from numerical models of coupled groundwater / surface water systems are potentially useful for a number of aspects of water resource management, including :

- Determining the long-term sustainable yield from groundwater systems that are recharged by, or discharge to, surface water bodies.
- Assessing the potential for groundwater pumping to deplete streamflows.
- Assessing the potential effect of surface water abstraction on groundwater systems and groundwater-dependent ecosystems.
- Predicting the effects of large-scale land-use changes, such as the development of irrigation schemes, on both groundwater and surface water resources.

1.4 The Need for a Unified Approach

Although it is now widely acknowledged that groundwater and surface water are two components of a single resource, and need to be managed together, the range of modelling tools available still reflects the fact that groundwater and surface water flow modelling have evolved separately as two distinct sub-branches of water science / engineering. Researchers and practising engineers have tended to specialise in one or the other.

Existing methods for modelling flow in connected river-aquifer systems model rivers and aquifers separately and incorporate mass fluxes between them using one of several numerical coupling methods. These methods do not accurately represent the physics of flow exchange processes. This is problematic for model stability and mass conservation.

Treating groundwater and surface water flows as separate physical processes that are represented by different governing equations and then coupled numerically potentially results in deficiencies with how the physics at the surface - subsurface interface is represented. For example, conservation of momentum is typically ignored at the interface, and subsurface flow is assumed to be Darcian everywhere.

Therefore an approach that treats coupled groundwater and surface-water flows as a continuum, rather than two separate domains, will potentially result in a better representation of the physical processes at and around the interface, with a consequent improvement in the model's ability to simulate fluxes of mass and momentum.

A starting point for formulating an alternative modelling approach is to consider a vertical cross-section from impermeable bedrock level to the top of the atmosphere. This is shown schematically in Figure 1.3. In the form shown, the cross-section contains a two-phase (air / water) flow system. If atmospheric flows are ignored (and it is assumed that their effect on the type of surface water flows under consideration is negligible), and gas dynamics in the variably-saturated zone are ignored, then the system shown in Figure 1.3 is reduced to a single fluid phase. The hydraulic properties of the system are continuously-defined but highly spatially-variable.

Fluid flows in all parts of the global flow system shown in Figure 1.3 obey the same physical laws: conservation of mass and momentum. They can therefore be described, theoretically at least, by the Navier-Stokes Equations. To model this system with the Navier-Stokes Equations however, fluid motion in the porous medium would need to be resolved at pore-scale, and details of the surface flow (such as the bed topography) would also need to be highly resolved.

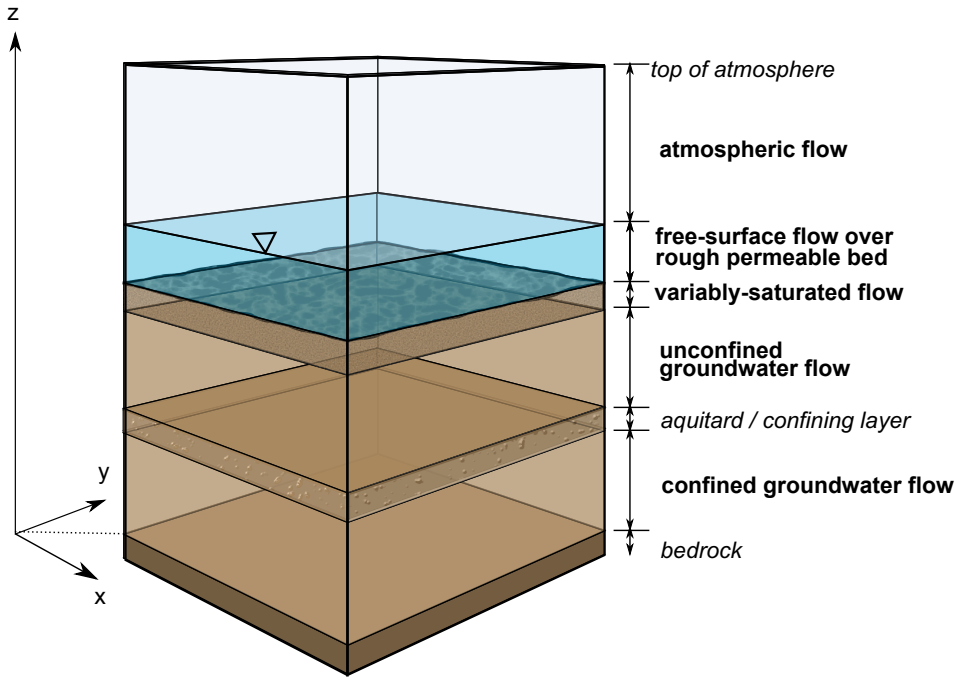

Figure 1.3: Global flow system schematic.

1.5 Study Objectives and Scope

This thesis aims to answer the question: can we eliminate the need for model coupling by developing a unified theory for 2D river-aquifer flow modelling?

It does not set out to evaluate the performance of existing coupled modelling approaches or individual modelling packages, or to benchmark the performance of the proposed unified approach against existing coupled modelling approaches.

The key objective of this thesis is to show the technical feasibility of using a single system of equations in a single computational domain for numerical modelling of coupled groundwater and surface-water flows. A sub-objective is to physically model and measure velocity fields in coupled surface - subsurface flows in the laboratory by extending the use of existing optical flow measurement and visualisation methods to transparent porous media.

The numerical model developed in this thesis deals with a sub-system of the global flow system shown in Figure 1.3. It simulates flow in a surface layer underlain by a fully-saturated, unconfined porous layer. Confined flow and unsaturated

flow are not simulated.

This thesis is intended to be useful to water resources professionals who do not necessarily have a strong background in fluid mechanics. Some details are therefore included that would have been assumed to be common knowledge if the target reader's background was in fluid mechanics or hydrodynamics.

1.6 Thesis Overview

Chapter 2 sets out to provide the basis of the governing equations that are used in existing numerical modelling approaches for both groundwater and surface water, and how these can all be derived from the Navier-Stokes Equations. Numerical methods for solving the governing equations are introduced. This in turn provides the theoretical foundations for the model that is developed later in the thesis.

In Chapter 3 a range of literature from topics relevant to modelling groundwater - surface water interactions is reviewed. The topics addressed include the physical mechanisms, both natural and anthropogenic, that control groundwater - surface water interactions, and a summary of the existing methods used for numerical modelling of coupled groundwater - surface water systems. A range of literature on the general subject of flow over permeable beds is reviewed: a high proportion of this is from outside of the water resources field. The double-averaging methodology that is the basis of the numerical model is introduced in this chapter.

Chapter 4 describes the steps that were taken to firstly develop a Reynolds-Averaged Navier-Stokes (RANS) numerical model using the finite volume method, and to then convert this model to solve the double-averaged Navier-Stokes (DANS) equations, along with adaptations that were made to allow the model to handle the transition between turbulent clear-fluid flow and laminar porous medium flow.

Chapters 5 and 6 describe the methodology and results respectively of the experimental programme that was completed in parallel with the numerical modelling to provide a data-set for verifying the numerical model. The results chapter (Chapter 6) considers the velocity field and turbulence data from the experimental programme in its own right, without reference to the numerical model.

In Chapter 7 the results of the numerical model are verified for simple clear-

fluid and porous media flows using published data, analytical solutions and an existing numerical model. Numerical model results are then presented for interacting surface-subsurface flows in the same configurations as the flows modelled, and these results are compared to the laboratory data.

Finally, in Chapter 8, the conclusions of the study are summarised, and recommendations for further work are made.

Chapter 2

Theoretical Foundations

2.1 Overview

This chapter contains an introduction to the Navier-Stokes Equations (NSE), which are the governing equations for flow of a viscous fluid, and the Reynolds-Averaged Navier-Stokes (RANS) equations, which are the governing equations for the mean turbulent flow of a viscous fluid.

In practice, both groundwater and surface water resources are typically modelled with other equations: the Shallow Water or Saint-Venant Equations for surface flows, and Darcy's Law or the Richards' Equation for saturated and unsaturated subsurface flows, respectively. These equations, and their relationship to the Navier-Stokes Equations, are introduced in this chapter.

Apart from limited exceptions involving idealised, simplified flows, it is not practical to solve the governing equations of fluid flow (both the NSE and other equations specific to particular flows) analytically, and it is therefore frequently necessary to use numerical solution methods. In this chapter the range of numerical methods commonly used for solving the governing equations are introduced, and the reasons for selecting the finite volume method for this work are discussed. The mathematical background of the finite volume method is developed for a general partial differential equation (PDE); the specific application to the NSE is discussed in Chapter 4.

2.2 The Navier-Stokes Equations

The Navier-Stokes Equations are non-linear partial differential equations that are, in their most general form, the governing equations for all viscous fluid flows. The equations result from applying Newton's second law and conservation of mass to an arbitrary volume of fluid.

For all environmental water flows it is reasonable to make the simplifying assumption of incompressibility. In an incompressible flow the density of an arbitrary small volume of fluid does not change as it moves in the flow field.

Solving the NSE yields a velocity and pressure field for the flow. Solution of the equations is difficult, however, due to their non-linearity. Except for highly simplified, idealised flows, analytical solutions for the NSE are not known to exist. It is therefore generally necessary to resort to numerical approximations, which are discussed in Section 2.5, and further in Chapter 4.

2.2.1 Equations and description of terms

In vector form, the incompressible Navier-Stokes Equations are:

$$\overbrace{\rho\Big(\underbrace{\frac{\partial \mathbf{u}}{\partial t}}_{\substack{\text{local}\\ \text{acceleration}}} + \underbrace{(\mathbf{u}\cdot\nabla)\mathbf{u}}_{\substack{\text{advective}\\ \text{acceleration}}}\Big)}^{\text{inertial terms}} = \overbrace{\underbrace{-\nabla p}_{\substack{\text{pressure}\\ \text{gradient}}} + \underbrace{\mu\nabla^2\mathbf{u}}_{\substack{\text{viscous}\\ \text{term}}}}^{\text{divergence of stress}} + \underbrace{\mathbf{f}}_{\substack{\text{sum of}\\ \text{external forces}}} \tag{2.1}$$

$$\nabla\cdot\mathbf{u} = 0 \tag{2.2}$$

where $\mathbf{u}$ $[LT^{-1}]$ is the velocity vector, p $[ML^{-1}T^{-2}]$ is pressure, μ $[ML^{-1}T^{-1}]$ is the dynamic viscosity of the fluid and $\mathbf{f}$ is the sum of any external forces (for example gravity in the case of a free-surface flow, or wind shear acting on the surface of a water body).

Equation 2.1 is the momentum conservation equation (there is one equation for each spatial dimension being considered) and Equation 2.2 is the continuity (or conservation of mass) equation.

The left-hand side of Equation 2.1 contains the inertial terms. The first term

is the local acceleration and the second term is the advective acceleration. The first two terms on the right-hand side of Equation 2.1 are the divergence of stress, comprised of the pressure gradient and viscous stress terms. The viscous term represents diffusion of the flow's momentum by the fluid's viscosity.

The model developed in this thesis is limited to 2-dimensional flows. In component form, for a 2-dimensional flow in Cartesian co-ordinates (and ignoring external forces other than gravity), the NSE can be written as:

$$\rho\frac{\partial u}{\partial t} + \rho u\frac{\partial u}{\partial x} + \rho v\frac{\partial u}{\partial y} = -\frac{\partial p}{\partial x} + \mu\left(\frac{\partial^2 u}{\partial x^2} + \frac{\partial^2 u}{\partial y^2}\right) \tag{2.3a}$$

$$\rho\frac{\partial v}{\partial t} + \rho u\frac{\partial v}{\partial x} + \rho v\frac{\partial v}{\partial y} = -\frac{\partial p}{\partial y} + \mu\left(\frac{\partial^2 v}{\partial x^2} + \frac{\partial^2 v}{\partial y^2}\right) - \rho g \tag{2.3b}$$

$$\frac{\partial u}{\partial x} + \frac{\partial v}{\partial y} = 0 \tag{2.4}$$

where Equations 2.3a and 2.3b are the horizontal and vertical momentum equations, respectively, and Equation 2.4 is the continuity equation.

2.2.2 Turbulence

Turbulence occurs in many environmental flows. The turbulent characteristics of a high-velocity open-channel flow can be easily observed: random fluctuations in time and space, superimposed on a mean flow (which may itself be varying in time over a much longer time-scale than the turbulent fluctuations). Even slower-velocity streams are likely to be influenced by turbulent motions. Although groundwater flows are typically laminar (non-turbulent), turbulence may occur around well-screens during pumping, or in more open porous media, for example layers of coarse gravel in a stream-bed.

Turbulence occurs in flows with high Reynolds number. The Reynolds number

is generally defined as:

$$Re = \frac{inertial forces}{viscous forces} = \frac{\rho U L}{\mu} = \frac{U L}{\nu} \tag{2.5}$$

where U and L are representative velocity and length scales in the flow, respectively. For $Re \gg 1$ the inertial terms are dominant over viscous effects. Small instabilities, which may be caused by roughness at the boundaries or obstacles in the flow, are magnified by the non-linear terms in the Navier-Stokes Equations. The relatively small contribution of the viscous terms at high Re means that viscosity is unable to suppress these instabilities, and the flow becomes increasingly "disorganised" as Re increases.

There is no fixed value of Re that divides laminar (non-turbulent) and turbulent flows, although flows with $Re << 10^3$ are generally laminar. The transition from laminar to fully turbulent flow may occur over several orders of magnitude of Re (Pope, 2000).

Hinze (1959) defines turbulence as follows:

> *"Turbulent fluid motion is an irregular condition of the flow in which the various quantities show a random variation with time and space coordinates, so that statistically distinct average values can be discerned."*

A turbulent flow is made up of eddies with a range of length scales. The upper bound of the range of length scales is determined by the characteristic length scale of the flow, L, for example the diameter of a pipe or the depth of a free-surface flow. The lower bound of the range of length scales is determined by the fluid's viscosity. This lower bound, at which turbulent kinetic energy is dissipated by viscosity, is known as the Kolmogorov microscale, η (Tennekes and Lumley, 1972). The Kolmogorov length scale can be defined in terms of the turbulent kinetic energy dissipation rate, ϵ and the viscosity, as follows:

$$\eta = \left(\frac{\nu^3}{\epsilon}\right)^{\frac{1}{4}} \tag{2.6}$$

The dissipation rate can be estimated in terms of the large eddy length and velocity scales. The turbulent kinetic energy can be assumed to be proportional

to u^2, where u is the large eddy velocity scale. A time scale associated with the large-scale eddies, known as the "large eddy turnover time", can be defined from the large eddy length and velocity scales:

$$t_\ell = \frac{\ell}{u} \tag{2.7}$$

The Kolmogorov length scale (Equation 2.6) can then be re-written in terms of the viscosity and large eddy scales:

$$\eta = \left(\frac{\nu^3 \ell}{u^3}\right)^{\frac{1}{4}} \tag{2.8}$$

A time scale for the small eddies can be defined as:

$$t_\eta = \left(\frac{\nu}{\eta}\right)^{\frac{1}{2}} = \frac{\nu \ell}{u^3} \tag{2.9}$$

In a turbulent flow the majority of the kinetic energy is contained in large-scale eddies. As these eddies are stretched by the flow they break up, transferring their energy to smaller eddies, which then in turn undergo the same process. This process of transferring energy to progressively smaller and smaller eddies is known as the "energy cascade" (Pope, 2000). The transfer of energy from large eddies to small eddies is what makes turbulent flows highly dissipative. This is somewhat counter-intuitive, as in the absence of turbulence viscous effects would be assumed to be negligible for a high-Re flow.

The Kolmogorov length scale (Equation 2.8) and the large eddy length scale can be combined to give a ratio of the large and small length scales in a turbulent flow, expressed in terms of the Reynolds number:

$$\frac{\ell}{\eta} \sim \left(\frac{u\ell}{\nu}\right)^{\frac{3}{4}} = Re^{\frac{3}{4}} \tag{2.10}$$

The ratio of the time-scales associated with the large and small eddies can be expressed similarly:

$$\frac{t_\ell}{t_\eta} \sim \left(\frac{u\ell}{\nu}\right)^{\frac{1}{2}} = Re^{\frac{1}{2}} \tag{2.11}$$

A range of approaches exist for numerical modelling of turbulent flows. The random, irregular nature of the flow means that it is generally not practical to solve turbulent flow problems deterministically. Modelling approaches are categorised in terms of how the spatial and temporal scales of the turbulent eddies are resolved in the model.

A direct numerical simulation (DNS) attempts to resolve all turbulent scales in the flow. For a relatively simple channel flow with a large eddy length scale of 1 m and a large eddy velocity scale of 1 m/s, the Reynolds number is around 10^6. Using Equations 2.10 and 2.11 to estimate the ratios of the large and small length and time-scales shows that a DNS simulation of this flows would need a spatial resolution of approximately 10^{-5} m and a time-step of approximately 10^{-3} s. Even for a short length of channel the number of grid points and time-steps required would make a DNS simulation computationally expensive. Although the use of DNS as a research tool for small-scale flows with moderate Reynolds numbers is becoming more common, it is not yet seen as a practical approach for modelling larger scale environmental flows.

An alternative, less computationally-demanding approach is to time-average the NSE and solve for the time-averaged values referred to in Hinze's definition of turbulence. Turbulence effects are then taken into account using a suitable statistical model. The time-averaging process, which splits the flow variables into mean and fluctuating components, is called Reynolds averaging, and the resulting equations are known as the Reynolds-averaged Navier-Stokes Equations (RANS). This is the most commonly-used approach in computational fluid dynamics.

An intermediate approach between the DNS and RANS approaches is large eddy simulation (LES), where large scale turbulent eddies are resolved in the numerical model grid and sub-grid scale turbulence is represented with a model.

2.2.3 Reynolds-averaged Navier-Stokes Equations

The averaging rules required to derive the RANS equations are given in Appendix A.

The Reynolds-averaged continuity and momentum equations are as follows:

$$\overline{\frac{\partial u_i}{\partial x_i}} = \frac{\partial}{\partial x_i}\overline{u_i} = \frac{\partial U_i}{\partial x_i} = 0 \tag{2.12}$$

$$\rho\frac{\partial U_i}{\partial t} + \rho U_j\frac{\partial U_i}{\partial x_j} = -\frac{\partial P}{\partial x_i} + \frac{\partial}{\partial x_j}\left(\mu\frac{\partial U_i}{\partial x_j} - \rho\overline{u_i' u_j'}\right) + \rho g_i \tag{2.13}$$

The RANS momentum equation (Equation 2.13) contains additional terms, arising from the correlation between temporally-fluctuating velocity components. These terms have the form $-\overline{u_i' u_j'}$ and are known as the Reynolds stresses. The presence of these terms generates a closure problem, i.e. there are more unknowns than equations. A closure scheme for the Reynolds stress terms is therefore required to solve the RANS equations. Closure schemes of varying complexity, known as turbulence models, are available.

2.2.3.1 Turbulence models

At the highest level, turbulence models can be split into those which use the concept of an eddy viscosity to approximate the Reynolds stresses, and those which attempt to determine the Reynolds stress directly from a transport equation (Rodi, 1980). The eddy viscosity concept is more commonly used.

The basis of the eddy viscosity, or turbulent viscosity, approach is Boussinesq's 1877 definition of the Reynold's stresses:

$$\rho\overline{u_i' u_j'} = -\mu_t\left(\frac{\partial U_i}{\partial x_j} + \frac{\partial U_j}{\partial x_i}\right) + \frac{2}{3}\rho\delta_{ij}k \tag{2.14}$$

where μ_t is the turbulent viscosity, k is the turbulent kinetic energy and δ_{ij} is the Kronecker delta (i.e. $\delta_{ij} = 0$ if $i \neq j$ and $\delta_{ij} = 1$ if $i = j$).

The turbulent kinetic energy (TKE), which is the kinetic energy associated

with turbulent eddies, is defined as:

$$k = \frac{1}{2}\overline{u_i' u_i'} \tag{2.15}$$

Unlike the dynamic viscosity, μ, which is a property of the fluid itself and only varies with temperature for a Newtonian fluid, the turbulent viscosity is a property of the flow.

The definition of μ_t (Equation 2.14) is not a turbulence model itself. The function of a turbulence model is to determine the spatial and temporal distribution of μ_t. Eddy viscosity models can be further categorised according to how this distribution is determined, using transport equations or otherwise.

Zero-equation models either use a constant eddy viscosity (determined experimentally or empirically) or use an algebraic expression based on an estimate of the turbulence length scale in the flow. An example of this is Prandtl's mixing-length theory, in which the eddy viscosity is related to mean flow properties. In one-equation and two-equation models the eddy viscosity is determined using turbulence properties such as TKE, and transport equations for these quantities.

In a one-equation model the most meaningful scale to represent turbulent fluctuations is $\sqrt{k}$, and a transport equation for k is therefore used (Rodi, 1980). In order to calculate values of μ_t (which can be defined in terms of turbulent length and velocity scales as $\mu_t = \rho \ell u$) using a one-equation model an estimate of the turbulence length scale is still required.

The most well-known single-equation turbulence model is the Kolmogorov-Prandtl model, which was developed independently by both Kolmogorov and Prandtl (Rodi, 1980). The turbulence model that was eventually used in the numerical model developed in this thesis is an adaptation of the Kolmogorov-Prandtl single-equation model. Further details of the Kolmogorov-Prandtl model are given in Section2.2.3.3.

Two-equation models attempt to do away with the need to estimate a length scale by introducing an additional transport equation for a property that is representative of a length scale. The most popular choice of variable for the second equation is the turbulent kinetic energy dissipation rate, ϵ, which represents the rate at which turbulent kinetic energy is converted into thermal energy, and is

defined as follows:

$$\epsilon = \frac{\mu}{\rho}\overline{\frac{\partial u_i'}{\partial x_j}\frac{\partial u_i'}{\partial x_j}} \tag{2.16}$$

An alternative choice of variable for the second transport equation in a two-equation turbulence model is the specific dissipation rate, ω, which is defined as:

$$\omega = \frac{\epsilon}{\beta k} \tag{2.17}$$

where β is a constant.

The $k-\epsilon$ model (Launder and Spalding, 1974) is one of the most widely-used turbulence models. It has been used as a baseline case for comparison to the numerical model developed in this thesis. The details of the $k-\epsilon$ model are discussed in more detail below.

2.2.3.2 The $k-\epsilon$ model

In the $k-\epsilon$ model it is assumed that μ_t can be written as a function of the TKE and the dissipation rate, ϵ, as follows:

$$\mu_t = C_\mu \rho \frac{k^2}{\epsilon} \tag{2.18}$$

where C_μ is an empirical constant.

To calculate values for μ_t from Equation 2.18 transport equations for k and ϵ are required. These each take the form of a scalar advection-diffusion equation, with only the source terms and diffusion coefficients being specific (Schäfer, 2006):

$$\frac{\partial \rho k}{\partial t} + \frac{\partial}{\partial x_j}\left[\rho\overline{u_j}k - \left(\mu + \frac{\mu_t}{\sigma_k}\right)\frac{\partial k}{\partial x_j}\right] = G - \rho\epsilon \tag{2.19}$$

$$\frac{\partial \rho \epsilon}{\partial t} + \frac{\partial}{\partial x_j}\left[\rho\overline{u_j}\epsilon - \left(\mu + \frac{\mu_t}{\sigma_\epsilon}\right)\frac{\partial \epsilon}{\partial x_j}\right] = C_{\epsilon 1} G \frac{\epsilon}{k} - C_{\epsilon 2}\rho\frac{\epsilon^2}{k} \tag{2.20}$$

In Equations 2.19 and 2.20, G is the rate of production of TKE. This is defined

as:

$$G = \mu_t \left(\frac{\partial U_i}{\partial x_j} + \frac{\partial U_j}{\partial x_i} \right) \frac{\partial U_i}{\partial x_j} \tag{2.21}$$

For two-dimensional flows the TKE production rate can be re-written as:

$$G = \mu_t \left[2 \left(\left(\frac{\partial U}{\partial x} \right)^2 + \left(\frac{\partial V}{\partial y} \right)^2 \right) + \left(\frac{\partial U}{\partial y} + \frac{\partial V}{\partial x} \right)^2 \right] \tag{2.22}$$

The k and ϵ transport equations (Equations 2.19 and 2.20) contain a number of empirically-determined constants. Typical values for these (Schäfer, 2006) are given in table 2.1.

Table 2.1: $k - \epsilon$ model constants (Schäfer, 2006)

$C\mu$	0.09
σ_k	1.0
σ_ϵ	1.33
$C_{\epsilon 1}$	1.44
$C_{\epsilon 2}$	1.92

The $k - \epsilon$ model requires special treatment at solid boundaries; defining a boundary condition for ϵ is problematic. Implementation of boundary conditions is discussed in Chapter 4.

2.2.3.3 Kolmogorov-Prandtl single-equation model

The key assumption of the Kolmogorov-Prandtl single-equation turbulence model is that the turbulent viscosity can be represented as:

$$\mu_t = C_\mu \rho k^{\frac{1}{2}} \ell \tag{2.23}$$

where ℓ is an estimate of the turbulence mixing length, and $C_\mu \approx 0.08$ Wilcox (1993).

Defining the turbulent viscosity in this way avoids the need to model ϵ with a transport equation, and the complications that this presents at boundaries.

In the single-equation model a transport equation for k is still required. The form of this equation is the same as for the $k-\epsilon$ model (Equation 2.19). Because the transport equation for k (Equation 2.19) contains the turbulence dissipation rate, an expression for ϵ is required. This is defined as:

$$\epsilon = C_d \frac{k^{\frac{3}{2}}}{l} \tag{2.24}$$

where $C_d = C_\mu \approx 0.08$.

Methodology for estimating the turbulent length scale, ℓ, and for handling boundary conditions for the k equation are discussed in Chapter 4.

2.3 Governing Equations for Groundwater Flow

Groundwater is any flowing or stagnant water beneath the ground surface. Although in some cases groundwater may occupy large underground drainage systems, such as caves or solution channels in limestone, this thesis is concerned with groundwater flow through porous media. In the context of groundwater flow, a porous medium is a geological formation or stratum with sufficiently interconnected void spaces to allow water to flow through it (Bear, 1972).

Water flow in a porous medium can be fully saturated, where all of the voids are filled with water, or unsaturated, where the voids are only partially filled with water and the remaining space is taken up with air. Unsaturated flow is also referred to as partially-saturated flow. If the porous medium varies temporally between full and partial saturation, the flow can be described as variably-saturated. Although the numerical and experimental work discussed in this thesis deal exclusively with fully-saturated flow, unsaturated flow is introduced in this chapter as it is important for understanding the applicability of the numerical model and the implications for potentially extending it to handle unsaturated flow.

Groundwater flow is sometimes referred to as subsurface flow. In the context of integrated hydrological systems, as discussed in this thesis, the term subsurface refers to the land surface, as opposed to more general fluid-mechanics applications where it may be used to refer to a point in the water column beneath the free-surface.

2.3.1 Saturated subsurface flow

In groundwater hydraulics (and other fields that deal with flow in a porous medium)flow of a homogeneous incompressible fluid through a porous medium is typically described by Darcy's Law. (Bear, 1972):

$$\boldsymbol{q} = -K\nabla h \tag{2.25}$$

where $\mathbf{q}$ is the specific flux vector $[LT^{-1}]$, K is the saturated hydraulic conduc-

tivity $[LT^{-1}]$ and h is the piezometric head $[L]$, which is defined as

$$h = z + \psi \tag{2.26}$$

where z is the elevation above a datum and ψ is the pressure head. The definition of the piezometric head is illustrated in Figure 2.1. With respect to a piezometer installed in an aquifer, z is the elevation of the base of the piezometer and ψ is the elevation of the piezometric surface (which can be above or below ground level), measured from the base of the piezometer.

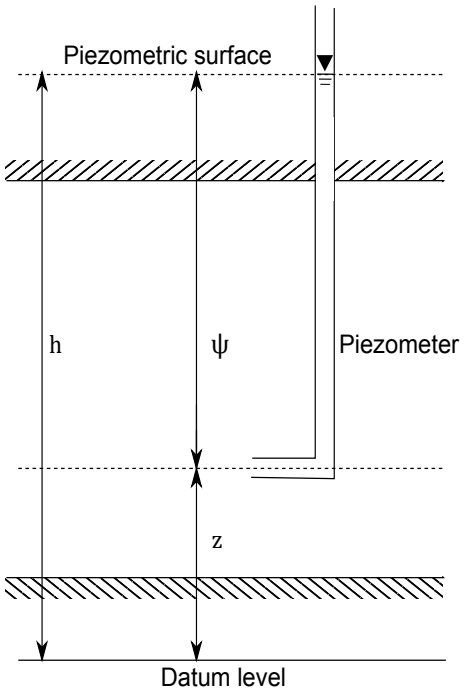

Figure 2.1: Definition of piezometric head

Darcy's Law (Equation 2.25) was phenomenologically derived by Henry Darcy in 1856 as part of his investigations into flow-rates through sand filters for the municipal water supply in Dijon, France. Darcy theorised an analogy between porous media flow and Poiseuille flow (low-velocity laminar flow in pipes), recognising that a porous matrix provided resistance to flow (Brown, 2002). He applied continuum concepts to consider flow per unit area through a column packed with sand, and conducted experiments to confirm his theory. A diagram of Darcy's experimental apparatus (which bears a close resemblance to the apparatus to a

hydraulic conductivity test cell, as described in Chapter 5) is shown in Figure 2.2.

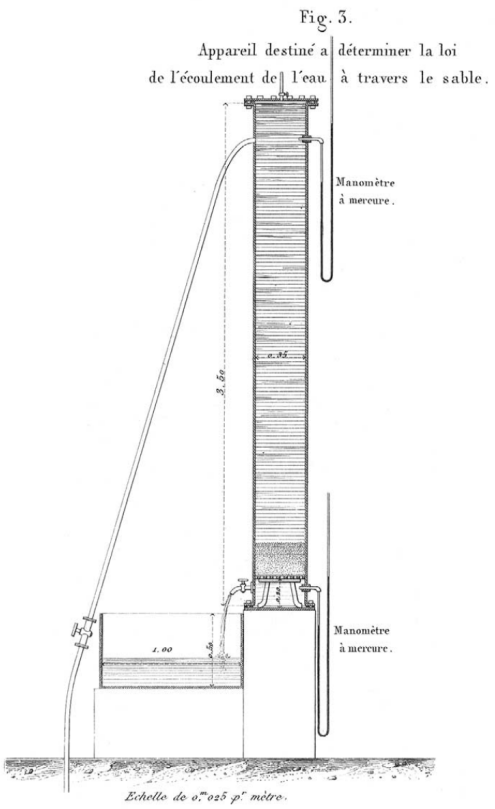

Figure 2.2: Darcy's sand column apparatus (Darcy, 1856)

By substituting Darcy's Law into a conservation of mass equation for a representative elementary volume (i.e. a cubic element large enough for the bulk hydraulic properties to apply, but small enough for the change in head within the volume to be relatively small) the governing equation for saturated groundwater flow in 3 dimensions is obtained:

$$S\frac{\partial h}{\partial t} - \nabla \cdot (K \nabla h) = q \tag{2.27}$$

where S is a dimensionless storage coefficient and q $[LT^{-1}]$ is a generalised mass sink / source term (i.e. due to pumping or injection)(Bear and Bachmat, 1990).

2.3.1.1 Saturated hydraulic properties

The hydraulic conductivity, K, (as introduced in Equation 2.25) is a measure of a porous medium's ability to convey fluid under hydraulic gradients. It is a combined property of both the porous medium itself and the fluid flowing through it. The hydraulic conductivity can be expressed as follows:

$$K = \frac{\rho g k}{\mu} \tag{2.28}$$

where k $[L^2]$ is the intrinsic permeability, which is solely a property of the porous matrix (Bear, 1972).

In groundwater hydraulics, where the flow can often be assumed to be primarily horizontal, the hydraulic conductivity is often multiplied by the aquifer's saturated thickness to give a measure of the aquifer's ability to transmit water over its full depth:

$$T = Kb \tag{2.29}$$

where T is the aquifer's transmissivity $[L^2/T]$ and b is the saturated thickness.

For the unconsolidated sedimentary materials that typically make up alluvial aquifers, values of the hydraulic conductivity K range from $1 \times 10^{-11} m/s$ for clay to $3 \times 10^{-2} m/s$ for gravel (Domenico and Schwartz, 1990).

The storage coefficient, S, (introduced in Equation 2.27) indicates the relationship between changes of head in an aquifer and the corresponding change in the amount of water stored in the aquifer. This is defined as the volume of water that is released from a unit area of the porous matrix under a unit reduction in head, and is dominated by different mechanisms for confined and unconfined aquifers[1].

Figure 2.3 shows a schematic cross-section of a shallow unconfined aquifer underlain by a confined aquifer, and the water levels in each. A confined aquifer is overlain by a layer of low-permeability material, such as clay. Water level

[1] An aquifer is often defined as a porous medium from which an economically feasible quantity of water can be extracted via a well. That definition is too restrictive however when considering groundwater systems that are hydraulically connected to surface water bodies, as there may be fluxes of water between surface water and a porous layer that is not capable of producing an economic volume of water. Therefore in this thesis an aquifer is defined more broadly as a saturated porous medium.

elevations in piezometers installed in a confined aquifer are above the top of the aquifer. Interpolating water levels from two or more piezometers in a confined aquifer gives a piezometric surface. The upper boundary of an unconfined aquifer is the water table. This is the interface between the saturated and unsaturated zones. It is possible for the piezometric surface in a confined aquifer to be above the water table in the overlying unconfined aquifer. Fully confined and unconfined aquifers are two ends of a spectrum; in between the two are semi-confined aquifers, which are overlain by a more permeable aquitard layer that allows some degree of vertical flow.

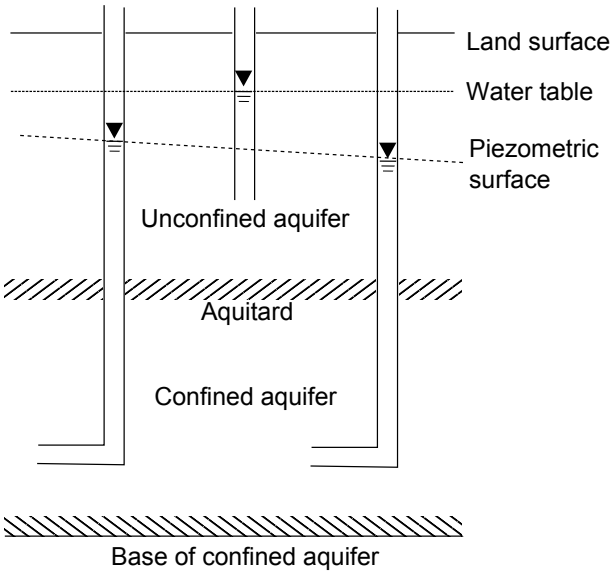

Figure 2.3: Confined and unconfined aquifers

The storage coefficient can be generally defined as:

$$S = \frac{dV_w}{dh}\frac{1}{A} = S_s b + S_y \tag{2.30}$$

where V_w is the volume of water released, b is the confined aquifer thickness, S_s is the specific storage and S_y is the specific yield (also known as the drainable porosity).

The specific storage, S_s $[L^{-1}]$ dominates the storage coefficient in a confined aquifer. Two physical properties contribute to the specific storage: the compressibility of the porous matrix, α, and the compressibility of water, β (Freeze and

Cherry, 1979). The specific storage can be expressed as:

$$S_s = \rho g(\alpha + \phi\beta) \tag{2.31}$$

where ϕ is the porosity of the porous medium. The porosity is defined as:

$$\phi = \frac{V_v}{V_t} \tag{2.32}$$

where V_v is the volume of voids (i.e. the volume able to be filled with water, air or another fluid) in a representative total volume, V_t, of the porous medium.

The storage coefficient for a confined aquifer, $S_s b$, is often referred to as a storativity, and typically ranges from 5×10^{-3} to 5×10^{-5} (Freeze and Cherry, 1979).

In an unconfined aquifer the value of the storage coefficient is dominated by the specific yield S_y, which typically has a value in the range 0.01 - 0.3. These values are substantially higher than the typical range for the storativity because the release of water from storage in an unconfined aquifer involves de-watering of pore spaces at the water table. Therefore the specific yield can be expected to be of the same order as the porosity, although S_y is always less than ϕ as some pore fluid will not drain under gravity due to surface tension, and "dead-end" pore spaces.

2.3.1.2 Aquifer response to pumping

When water is pumped from a well, water in the surrounding aquifer flows radially towards the well from the surrounding aquifer (assuming that the aquifer material is homogeneous and isotropic). This flow induces horizontal hydraulic gradients towards the well, resulting in a lowered water table in the area surrounding the well. The modified piezometric surface around the well is known as a drawdown cone, or cone of depression.

Figure 2.4 shows a cross-section through the cone of depression due to pumping from a well in an unconfined aquifer. The radius of influence (r_i) is the radial distance from the well at which the drawdown is effectively zero.

An aquifer's response to pumping is relevant to groundwater - surface water

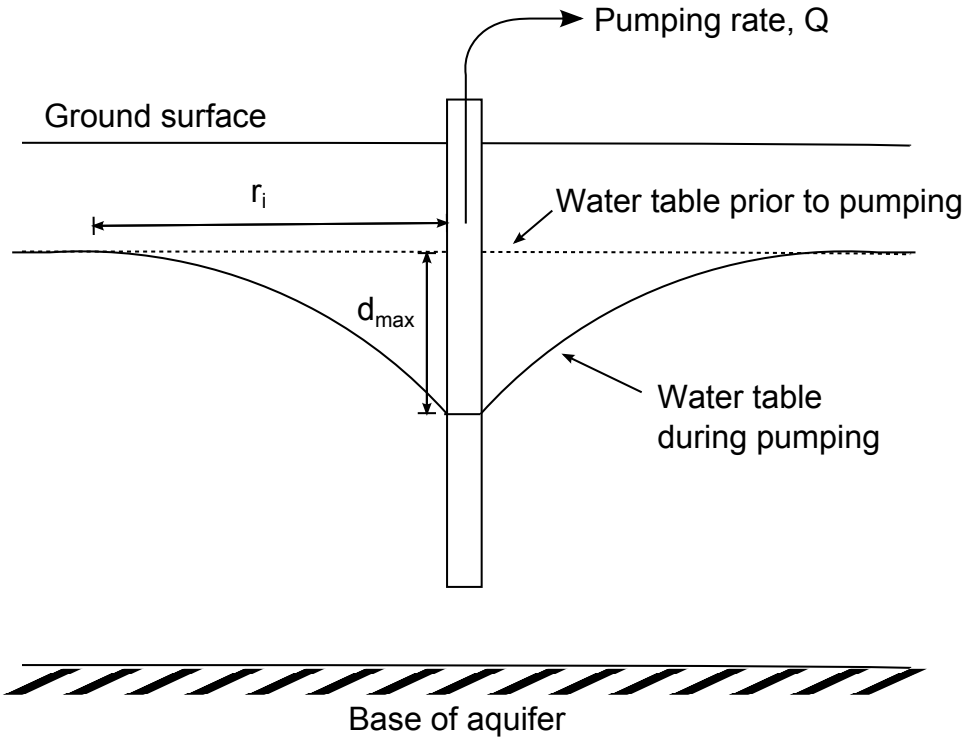

Figure 2.4: Aquifer drawdown due to pumping

interactions as drawing down the water level in the aquifer can result in stream depletion. This is discussed further in Chapter 3.

Under certain assumptions, such as the aquifer being homogeneous and of infinite lateral extent,the groundwater flow equation (Equation 2.27) can be solved analytically in radial co-ordinates to predict transient drawdown at time t and at a radius r from a pumped well.

Theis (1935) used an analogy with heat-flow theory to develop an analytical equation for transient drawdown in a confined aquifer:

$$h_0 - h(r,t) = \frac{Q}{4\pi T} \int_u^\infty \frac{e^{-u}}{u} du \tag{2.33}$$

where h is the height of the piezometric surface above a datum, h_0 is the initial head before the start of pumping, Q is the pumping rate, T is the transmissivity

(defined as $T = Kb$) and u is defined as:

$$u = \frac{r^2 S}{4Tt} \tag{2.34}$$

The integral in Equation 2.33 is known as the well function, $W(u)$. Values of the well function are typically found graphically from a log-log plot of $W(u)$ versus $\frac{1}{u}$.

An analytical function for drawdown in an unconfined aquifer was developed by Neuman (1972) (and subsequent papers). The solution, which requires similar assumptions to the Theis solution, is in two parts, accounting for water that is released initially by the aquifer's elastic response immediately after pumping begins, and then later by de-watering at the water table. The Neumann solution is given as:

$$h_0 - h(r,t) = \frac{Q}{4\pi T} W(u_A, u_B, \eta) \tag{2.35}$$

where u_A applies to the early part of the solution:

$$u_A = \frac{r^2 S_s b}{4Tt} \tag{2.36}$$

and u_B applies to the later part of the solution:

$$u_B = \frac{r^2 S_y}{4Tt} \tag{2.37}$$

The other parameter in the well function, η, accounts for the anisotropy of the aquifer, and is defined as:

$$\eta = \frac{r^2 K_v}{b^2 K_h} \tag{2.38}$$

where K_h and K_v are the horizontal and vertical hydraulic conductivities, respectively.

Like the Theis solution, Equation 2.35 is typically solved using a graphical method. Curves for u_A and u_B are joined by a set of curves for different values of η.

A range of other analytical solutions exist, including those that handle leaky

confined aquifers, multiple-layer aquifer systems and aquifers of finite width.

Scenarios that more closely resemble "real world" conditions, for example multiple wells, time-varying pumping rates, impermeable boundaries, and recharge sources, can be handled analytically using the principle of superposition of solutions. Despite this, due to restrictive assumptions such as aquifer homogeneity, and the need to resort to graphical methods in order to evaluate complicated integral terms, numerical methods (as discussed later in this chapter) are frequently used in practice, instead of analytical solutions.

2.3.1.3 Applicability of Darcy's Law

If the specific discharge is increased sufficiently in a porous media flow, the relationship between $\mathbf{q}$ and $\nabla\phi$ eventually becomes non-linear. At this point Darcy's Law is no longer a valid description of the flow. A Reynolds number, analogous to that used for clear-fluid flows, can be used to define a range of applicability for Darcy's Law. The Reynolds number for flow in porous media is defined as follows:

$$Re_p = \frac{\boldsymbol{q}d}{\nu} \tag{2.39}$$

where ν is the kinematic viscosity of the fluid and d is a length scale representing the pore space. As direct measurement of the pore space geometry is not usually practical, some measure of grain size, or another measurable property of the porous matrix, is typically used. This may be the mean or median grain size, or another point from the particle size distribution such as d_{10}, the 10th percentile grain diameter (by weight).

Other options for approximating the pore length scale include combinations of the intrinsic permeability and porosity. Ward (1964) gives a definition of the length scale for Re_p as:

$$d \approx \left(\frac{k}{\phi}\right)^{\frac{1}{2}} \tag{2.40}$$

This definition makes more sense as a proxy for a pore-space length scale than an estimate based on the particle size distribution, as the porosity describes the proportion of void space in the porous matrix, and the permeability relates to

how fluid is able to flow through those voids.

The validity of Darcy's Law can be tested by plotting the relationship between Re_p and a friction factor, analogous to those used to account for head-losses in pipe or open-channel flow. Figure 2.5 from Bear (1972) shows this relationship using a Fanning friction factor (using a representative length scale for the porous matrix rather than a pipe diameter).

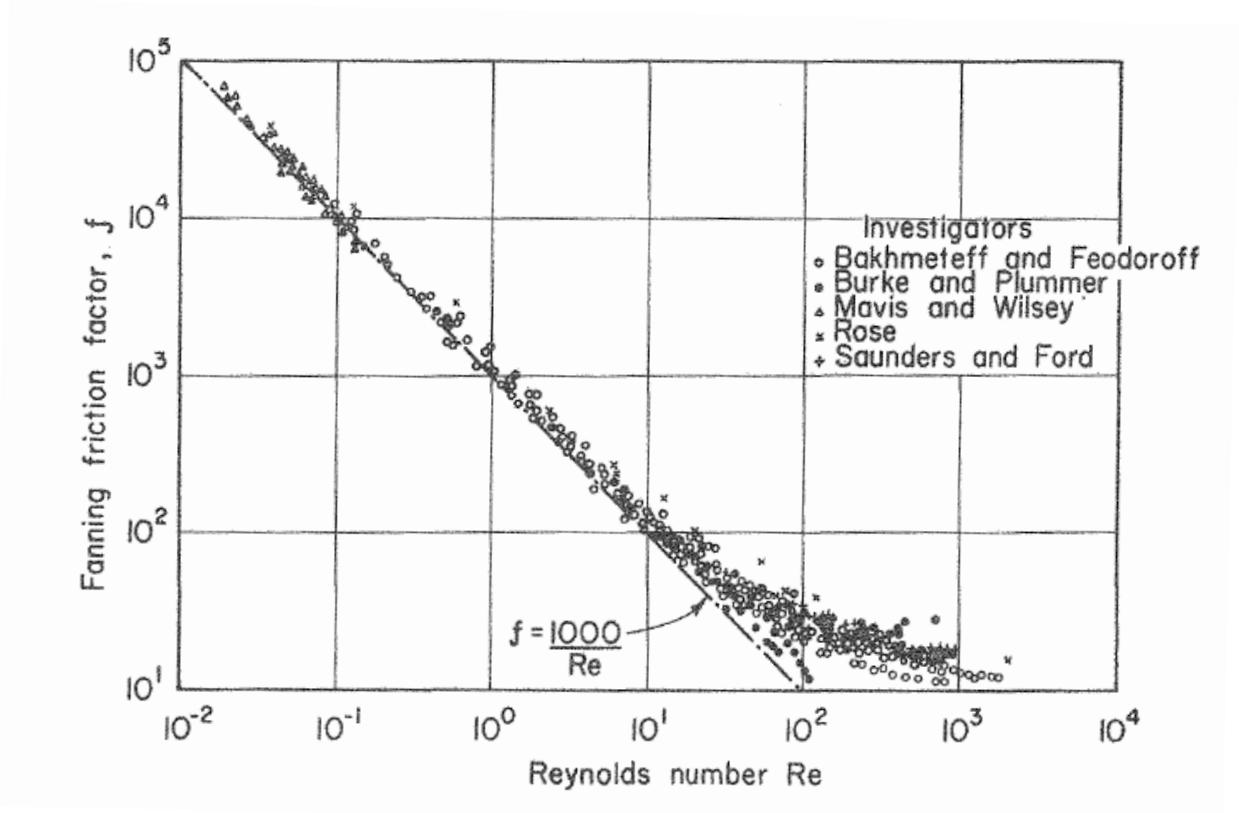

Figure 2.5: Relationship between Fanning friction factor and Reynolds number for porous flow (Bear, 1972)

It can be seen in Figure 2.5 that there is a linear relationship between the friction factor and Re_p for values for Re_p less than approximately 10. Bear (1972) states that Darcy's Law is valid in practically all cases if Re_p (based on the mean grain diameter) is less than some value between 1 and 10.

For Re_p in the range of approximately 10 to 100 the flow is in a non-linear laminar regime where inertial forces become predominant over viscous forces.

Underflow in gravel-bed rivers is typically in the non-linear regime (Sriboonlue, 1985). Flow with Re_p greater than 100 are likely to be turbulent. It should be noted that a non-Darcian flow is not necessarily turbulent: flows in the non-linear post-Darcian regime (i.e. Re_p approximately in the range $10 - 100$)are still laminar. Turbulence in porous media is discussed further in Chapter 3.

Darcy's Law is also invalid for very low values of Re_p in some fine-grained soils as there is a threshold hydraulic gradient required to instigate flow (Bear, 1972).

2.3.1.4 Governing equations for non-Darcian flow

There are two less widely-used governing equations for flow in porous media where Darcy's Law does not apply: the Brinkman and Forchheimer equations. In a groundwater flow context, these equations attempt to provide a better representation of the subsurface flow processes near the interface between subsurface and surface flows where the combination of higher velocities and larger mean particle diameters potentially result in values of Re_p that are higher than the range of applicability for Darcy's Law

Although there are a number of examples in the literature of applications of these equations, using artificial / man-made porous media in some cases, there does not appear to be general agreement about the conditions for their applicability, their exact form and the definition of their variables.

In the Brinkman equation a macroscopic viscous shear stress term is added to the familiar form of Darcy's Law (Vafai and Kim, 1995). The form of the equation is:

$$\mu_{eff}\nabla^2\boldsymbol{q} + \boldsymbol{q} = -K\nabla h \tag{2.41}$$

where μ_{eff} is an effective viscosity term, which tends towards the viscosity for the clear fluid, μ, as the porosity of the porous medium tends towards 1.

Although the Brinkman equation is sometimes referred to as "Brinkman's extension to Darcy's Law", this is misleading, as Brinkman obtained a relationship between the conductivity, K, and the porosity, ϕ, rather than simply adding a term to the existing linear form of Darcy's Law (Nield and Bejan, 2013).

The procedure used by Brinkman is only valid for $\phi > 0.6$, which does not often occur in naturally-occurring porous media (Nield, 1991).

Forchheimer (1901) added a non-linear term to Darcy's Law, giving the following general form of equation:

$$\frac{1}{K}\boldsymbol{q} + F\boldsymbol{q}^2 = -\nabla h \tag{2.42}$$

where F is the Forchheimer coefficient (Bear, 1972).

The transition from Darcy flow to Forchheimer flow begins when Re_p is in the range $1 - 10$ and the flow is fully in the Forchheimer regime when Re_p is in the order of 10^2 (Nield and Bejan, 2013). Some researchers have explained Forchheimer's non-linear term as accounting for the appearance of turbulence in the porous medium as the Reynolds number increases, with the quadratic term being analogous to the head-loss term for turbulent flow in hydraulically rough pipes. Bear (1972) concludes that this is unlikely for several reasons, including that the deviation from the standard Darcy's Law occurs much more gradually than the transition between the laminar and turbulent regimes in pipe flow, and that it occurs at a much lower Reynolds number, citing several studies that observed the onset of turbulence in porous media at $Re_p = 60 - 150$. A more plausible explanation is that the non-linear term accounts for inertial forces, which gradually become predominant relative to viscous forces (Bear, 1972). Whitaker (1996) showed that the Forchheimer equation can be derived using volumetric averaging of the Navier-Stokes Equations.

In practice the Forchheimer equation can be used in cases where velocities (and therefore Re_p) are too high for Darcy's Law to apply (COMSOL Multiphysics, 2011), and has been used by Wen et al. (2011) to model flow to a well in a leaky confined aquifer. Sriboonlue (1985) used a modified Forchheimer equation to model underflow in gravel bed rivers, where the flow regime is post-linear due to the mean diameter of the riverbed sediments being significantly larger than typical aquifer material.

The Brinkman and Forchheimer terms can be combined into a single equation with Darcy's Law, known as the Brinkman-Forchheimer-extended Darcy equation, representing a generalisation of Darcy's Law for flow in a saturated porous

medium near an interface with a free-surface flow (Tan and Pillai, 2009). For low Reynolds numbers ($Re_p < 1$) the Forchheimer term becomes negligible, and away from the surface / subsurface interface the Brinkman term becomes negligible. Vafai and Kim (1990, 1995) note that the Brinkman-Forchheimer-extended Darcy's Law enables a single-domain approach for composite porous - free fluid regions. However, this is only applicable for laminar flows, and the porosity of the porous medium must be close to 1 (Nield, 1991).

2.3.2 Unsaturated subsurface flow

In the near-surface area, where interactions between groundwater and surface flows occur, the porous medium can be less than fully saturated. On the upper Canterbury Plains (see Figure 1.2) the unsaturated layer can be several tens of metres thick (Larned et al., 2008, 2015). Variably-saturated groundwater flow is of particular importance for rivers that are "perched" over aquifer systems.

The general form of Darcy's Law ($\boldsymbol{q} = -K\nabla h$) is valid for both fully-saturated and variably-saturated flows in porous media, however in the unsaturated case K cannot be assumed to be constant.

2.3.2.1 Richards' Equation

Flow in unsaturated or variably-saturated porous media is described by Richards' Equation, which is an extension of the groundwater flow equation obtained by substituting Darcy's Law into a conservation of mass equation (i.e. Equation 2.27).

The continuity equation can be re-written as:

$$\frac{\partial \theta}{\partial t} = -\nabla \boldsymbol{q} \tag{2.43}$$

where θ is the water content, defined as:

$$\theta = \frac{V_w}{V} \tag{2.44}$$

and V_w is the volume of water contained in a representative volume V of the porous matrix. If the porous medium is fully saturated then $\theta = \phi$.

When a porous medium is less than fully saturated the pore space is partly filled with air, making some of the pore volume unavailable for water flow. The hydraulic conductivity, K, is therefore lower than for saturated flow, and is a function of the water content, θ (Ritzema, 1994).

Expressing K as a function of θ and substituting Darcy's Law into Equation 2.43 gives:

$$\frac{\partial \theta}{\partial t} = \frac{\partial}{\partial x}\left(K(\theta)\frac{\partial h}{\partial x}\right) + \frac{\partial}{\partial y}\left(K(\theta)\frac{\partial h}{\partial y}\right) + \frac{\partial}{\partial z}\left(K(\theta)\frac{\partial h}{\partial z}\right) \tag{2.45}$$

Substituting the definition of the piezometric head, $h = z + \psi$, into Equation 2.45 gives:

$$\frac{\partial \theta}{\partial t} = \frac{\partial}{\partial x}\left(K(\theta)\frac{\partial \psi}{\partial x}\right) + \frac{\partial}{\partial y}\left(K(\theta)\frac{\partial \psi}{\partial y}\right) + \frac{\partial}{\partial z}\left(K(\theta)\frac{\partial \psi}{\partial z}\right) + \frac{\partial K(\theta)}{\partial z} \tag{2.46}$$

Equation 2.46 is known as the "mixed form" of Richards' Equation, as it is expressed in terms of both the water content θ and the pressure head ψ (Celia et al., 1990).

Because the water content is related to the pressure head, $K(\theta)$ can also be expressed as $K(\psi.)$ Richards' Equation can then be expressed solely in terms of ψ, as follows:

$$C(\psi)\frac{\partial \psi}{\partial t} - \nabla \cdot K(\psi)\nabla\psi - \frac{\partial K}{\partial z} = 0 \tag{2.47}$$

where $C(\psi)$ is the specific water capacity, which is the unsaturated equivalent of the storage coefficient in the saturated groundwater flow equation (Equation 2.27). The relationship between the temporal derivative terms in the mixed and head-based forms of Richards' Equation is as follows:

$$\frac{\partial \theta}{\partial t} = \frac{d\theta}{dh}\frac{\partial \psi}{\partial t} = C(\psi)\frac{\partial \psi}{\partial t} \tag{2.48}$$

Richards' Equation can also be written solely in terms of moisture content

(θ):

$$\frac{\partial \theta}{\partial t} - \nabla \cdot D(\theta) \nabla \theta - \frac{\partial K}{\partial z} = 0 \tag{2.49}$$

where $D(\theta)$ is the unsaturated diffusivity, defined as:

$$D(\theta) = \frac{K(\theta)}{C(\theta)} \tag{2.50}$$

Numerical solutions of the ψ-based form of Richards' Equation can produce unacceptably large mass-balance errors (Celia et al., 1990). However, the θ-based form is not suitable for variably-saturated flow (i.e. flow that may be saturated or unsaturated) and can be problematic for soil profiles containing multiple layers (Shahraiyni and Ataie-Ashtiani, 2012). Therefore most numerical models of unsaturated flow use the mixed form.

2.3.2.2 Unsaturated hydraulic properties

For numerical modelling purposes, $C(\psi)$ and $K(\psi)$ or $K(\theta)$ can be defined using either interpolation from look-up tables, or parametric models. The latter causes fewer numerical problems (Kosugi et al., 2002). The most widely-used parametric model for characterising unsaturated soils is the van Genuchten-Mualem model (van Genuchten, 1980). This defines the shape of the soil water retention curve (i.e. the relationship between water content and pressure head), as follows:

$$\theta(\psi) = \begin{cases} \theta_r + \frac{\theta_s - \theta_r}{(1+|\alpha\psi|^n)^m} & \psi < 0 \\ \theta_s & \psi \geqslant 0 \end{cases} \tag{2.51}$$

where θ_s is the saturated water content, θ_r is a soil-specific residual (or minimum) water content and α, m and n are model parameters. Values for the van Genuchten model parameters can be obtained from published tables for different soil types, determined from laboratory or field experiment data, or treated as calibration parameters.

2.3.3 Derivation of the groundwater flow equations from the Navier-Stokes Equations

Although Darcy's Law was originally derived phenomenologically (i.e. an interpretation of experimental results that is consistent, but not directly derived from, fundamental theory), a number of authors (e.g. Neuman (1977), Gray and Oneill (1976), Whitaker (1986), Whitaker (1996)) have shown that it can be derived theoretically from the Navier-Stokes Equations or a similar conservation of momentum expression. These derivations rely on the method of volume averaging (Whitaker, 1998).

Theoretically, the Navier-Stokes Equations can be applied directly to describe water flows through the pore space in a porous medium. However, except for highly idealised cases it is not practical to describe the geometry of the pore space. Therefore it is necessary to replace the actual porous medium with a fictitious continuum, in which the parameters and variables in the equations of motion can be re-defined as average values over a representative elementary volume.

In the volume-averaging derivations the saturated porous medium is conceptualised as a two-phase system, where σ is the solid phase (i.e. the porous matrix) and β is the fluid phase. The σ-phase is assumed to be rigid and immobile, and the β-phase is assumed to be a single-phase, Newtonian, incompressible fluid.

The *superficial average* (also known as the phase average)for an arbitrary function f_β, defined in the β phase is (Whitaker, 1996):

$$\langle f_\beta \rangle = \frac{1}{V} \int_{V_\beta} f_\beta \, dV \tag{2.52}$$

where V_β is the volume of the β-phase contained in the total averaging volume V. The angle brackets denote a spatial average.

The *intrinsic average* (or intrinsic phase average), is defined as:

$$\langle f_\beta \rangle^\beta = \frac{1}{V_\beta} \int_{V_\beta} f_\beta \, dV \tag{2.53}$$

The two averages can be related using the porosity of the porous medium,

which is defined as:

$$\phi = \frac{V_\beta}{V} \tag{2.54}$$

Therefore:

$$\langle f_\beta \rangle = \phi \langle f_\beta \rangle^\beta \tag{2.55}$$

Several averaging theorems are required to relate the averages of derivatives to derivatives of averages. The first of these is the transport theorem for temporal derivatives (Whitaker, 1973):

$$\langle \frac{\partial f_\beta}{\partial t} \rangle = \frac{\partial}{\partial t} \langle f_\beta \rangle - \frac{1}{V} \int\limits_{A_{\sigma\beta}} f_\beta \mathbf{v}_\beta \cdot \mathbf{n}_\beta \, dS \tag{2.56}$$

The Reynolds Transport Theorem, which is frequently used in fluid mechanics, is a special case of Equation 2.56 (Nikora et al., 2007a).

Whitaker (1967) gives an averaging theorem for spatial derivatives:

$$\langle \nabla f_\beta \rangle = \nabla \langle f_\beta \rangle + \frac{1}{V} \int\limits_{A_{\sigma\beta}} \mathbf{n}_\beta f_\beta \, dS \tag{2.57}$$

where $\mathbf{v}_\beta$ is the velocity in the β-phase, $A_{\sigma\beta}$ is the area of the interface between the β and σ phases, and $\mathbf{n}_\beta$ is a unit normal vector on the interface of the phases, pointing outwards from the β phase.

Gray (1975) modified the averaging theorem so that it is terms of the intrinsic average rather then the superficial average:

$$\langle \nabla f_\beta \rangle = \phi \nabla \langle f_\beta \rangle^\alpha + \frac{1}{V} \int\limits_{A_{\sigma\beta}} \mathbf{n}_\beta \hat{f}_\beta \, dS \tag{2.58}$$

where $\hat{f}_\beta$ is the deviation of f_β from its intrinsic average, i.e. $\hat{f}_\beta = f_\beta - \langle f_\beta \rangle^\beta$

To derive the governing equation for Darcy groundwater flow (or non-Darcian flow), the above averaging theorems are applied to the Navier-Stokes Equations with appropriate boundary conditions: a no-slip condition at the interface between the β- and σ-phases, and the β-phase velocity field specified as a function

of position and time at the entrances and exits to the averaging volume.

In order to apply Equation 2.58 the velocity and pressure fields must be decomposed into spatially-averaged and spatially-fluctuating components. This is analogous to the Reynolds decomposition that is required to average the Navier-Stokes Equations in time, and it creates a similar closure problem.

The closure problem can be split into two parts: the Darcy permeability and the Forchheimer correction (Whitaker, 1996). The Forchheimer correction is a second-order term that accounts for inertial effects in higher-velocity flows. A further term that arises is the Brinkman correction, which is in the form of an effective viscosity, and is usually negligible (Gray and Oneill, 1976). The solution of the closure problem results in the definition of the hydraulic conductivity and the less widely-used Forchheimer coefficient.

If a flow is expected to remain Darcian throughout, the Brinkman and Forchheimer terms can be neglected.

2.4 Governing Equations for Surface Water Flow

2.4.1 The Shallow Water Equations

In practice, free-surface flows in rivers, flood-plains and other natural and engineered channels are modelled almost exclusively using the Shallow Water Equations (SWE), or a simplified form thereof. A flow is deemed to be "shallow" (and therefore able to be described by the SWE) if its horizontal length scales are significantly greater than its vertical length scale. Under this condition conservation of mass implies that the vertical velocity components are significantly smaller than the horizontal ones (Vreugdenhil, 1994).

In their two-dimensional form the SWE consist of two depth-averaged momentum equations (for two horizontal velocity components) and a continuity (mass-conservation) equation. The SWE can be expressed in a number of ways. In conservative form (i.e. a balance of mass and momentum fluxes)the two-dimensional SWE can be written as a single vector equation:

$$\frac{\partial \mathbf{v}}{\partial t} + \frac{\partial \mathbf{f}_1}{\partial x} + \frac{\partial \mathbf{f}_2}{\partial y} = -\mathbf{s} \tag{2.59}$$

The flux terms on the left-hand side of the equation can be defined as:

$$\mathbf{v} = \begin{bmatrix} au \\ av \\ a \end{bmatrix} \quad \mathbf{f}_1 = \begin{bmatrix} au^2 + \frac{1}{2}ga^2 \\ auv \\ au \end{bmatrix} \quad \mathbf{f}_2 = \begin{bmatrix} auv \\ av^2 + \frac{1}{2}ga^2 \\ av \end{bmatrix} \tag{2.60}$$

where u and v are the two horizontal velocity components, a is the water depth, and g is gravitational acceleration.

The first two components of each of the vectors in Equation 2.60 are the terms of the momentum equations and the third component of each is the continuity equation.

The $\mathbf{s}$ term on the right-hand side of Equation 2.59 is a momentum source / sink term representing bed roughness and topography. These terms are discussed further below.

Alternatively the individual equations of the two-dimensional form of the SWE

can be expressed as follows:

$$\frac{\partial a}{\partial t} + \frac{\partial ua}{\partial x} + \frac{\partial va}{\partial y} = 0 \tag{2.61}$$

$$\frac{\partial ua}{\partial t} + \frac{\partial u^2 a}{\partial x} + \frac{\partial uva}{\partial y} + ga\frac{\partial a}{\partial x} = ga(S_0 x - S_f x) \tag{2.62}$$

$$\frac{\partial va}{\partial t} + \frac{\partial v^2 a}{\partial y} + \frac{\partial uva}{\partial x} + ga\frac{\partial a}{\partial y} = ga(S_0 y - S_f y) \tag{2.63}$$

where Equation 2.61 is the continuity equation, and Equations 2.62 and 2.63 are the momentum equations in the x and y directions, respectively. The x and y-components of the velocity (u and v respectively) and the flow depth a are defined at points in the x-y plane.

The terms on the right-hand sides of the momentum equations (Equations 2.62 and 2.63) are momentum sources / sinks due to bed topography and roughness. S_{0x} and S_{0y} are the slopes of the channel bottom in the x and y directions respectively. Defining the bed slope in two components means that complex bed topography can be represented in the model. S_{fx} and S_{fy} are the friction slope (i.e. the slope of the energy grade line) and the x and y directions respectively. The friction slope is typically estimated using an empirical method such as the Manning or Chézy equation. Representations of bed roughness are discussed further below in Section 2.4.2.

Other momentum source / sink terms such as Coriolis and wind shear can be added for specific applications.

2.4.1.1 The Saint-Venant Equations

In modelling flow in a natural or engineered open channel it is often acceptable to ignore the spatial variability in velocities across the channel and over the flow depth (Chow et al., 1988). In this case the one-dimensional form of the SWE, known as the Saint-Venant Equations, can be used to model the flow.

The Saint-Venant Equations are comprised of a conservation of mass equation and one momentum equation, as follows:

$$\frac{\partial Q}{\partial x} + \frac{\partial A}{\partial t} = 0 \tag{2.64}$$

$$\frac{\partial Q}{\partial t} + \frac{\partial Q^2 A}{\partial x} + gA\frac{\partial a}{\partial x} = gA(S_0 - S_f) \tag{2.65}$$

where Q is the volumetric flow rate and A is the wetted cross-sectional area at a given flow depth, a. Variables in the Saint-Venant Equations are cross-section averages: the channel cross-section and plan form are not represented explicitly in the equations.

The Saint-Venant Equations can also be expressed in non-conservation form, using the cross-section average velocity, V as a dependent variable rather than Q.

Figure 2.6 defines the bed slope, S_0, and the friction slope, S_f for the one-dimensional case.

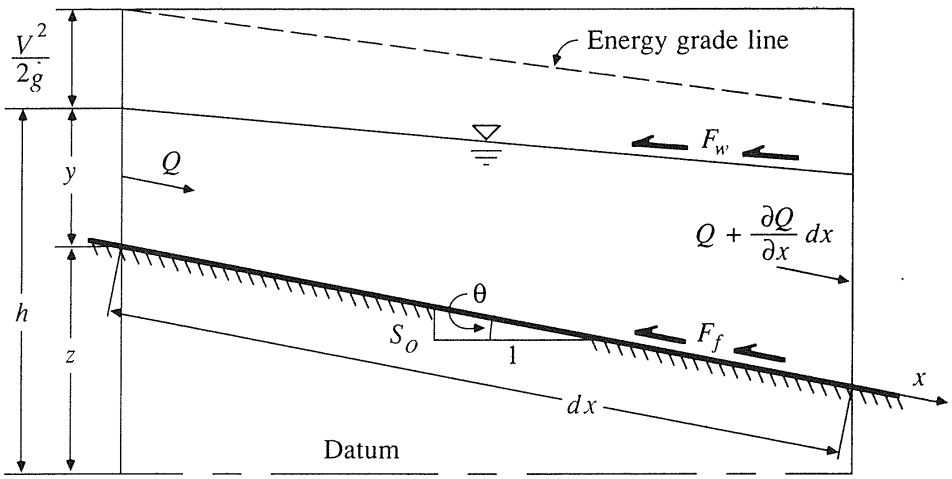

Figure 2.6: Definition sketch for the Saint-Venant Equations (from Chow et al. (1988))

The relationship between the frictional force at the bed (as shown in Figure 2.6)and the friction slope is:

$$F_f = -\rho g A S_f dx \tag{2.66}$$

where dx is the length of a control volume oriented with the flow.

2.4.1.2 Simplified forms of the SWE

For some applications such as catchment-scale flood-flow routing, and overland flow the SWE and Saint Venant Equations can be simplified.

Eliminating the inertial terms (i.e. the local and convective acceleration)results in a diffusive wave model. In one dimension, the momentum equation then reduces to:

$$gA\frac{\partial a}{\partial x} = gA(S_0 - S_f) \tag{2.67}$$

A diffusive wave model is appropriate if the flow is expected to remain subcritical. Retaining the pressure gradient term allows non-uniform flow to be considered (Chow et al., 1988).

Eliminating the inertial terms and the pressure gradient results in a kinematic wave model. The remaining terms in the momentum represent a balance between gravity and friction forces, i.e.:

$$S_0 = S_f \tag{2.68}$$

The key assumptions of a kinematic wave model are that the flow is steady and uniform (within a differential length), and that the friction slope is equal to the channel slope (i.e. the energy grade line is parallel to the channel bed). These assumptions are valid when changes in depth and velocity are negligible relative to the bed slope. In practice, these assumptions are often appropriate for modelling overland flow on relatively steep slopes. An advantage of kinematic wave models is that they can solved analytically. An implication of assuming that the bed and the energy grade line are parallel is that kinematic wave models cannot handle adverse bed slopes, which limits the resolution at which channel features such as riffles and pools can be modelled.

Figure 2.7 illustrates the differences between a dynamic wave (i.e. the full SWE or Saint Venant Equations) and a kinematic wave from the perspective of an observer on the channel bank. For the kinematic wave the water surface and energy grade line remain parallel to the channel bed over time as the flow

increases. For the dynamic wave this is not the case, even within a differential element dx.

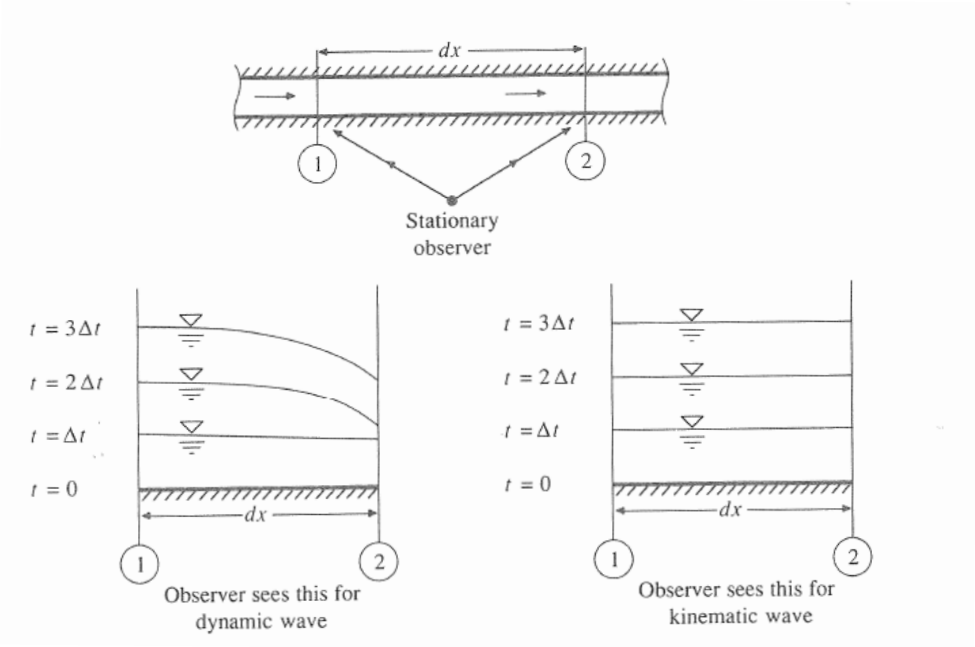

Figure 2.7: Comparison of kinematic and dynamic waves (from Chow et al. (1988))

2.4.2 Representation of bed roughness

The two equations that are typically used to represent bed roughness in the SWE or Saint Venant Equations are the Chézy Equation and the Manning Equation.

From dimensional analysis, the shear stress at the bed can be expressed in the following form:

$$\tau_0 = \alpha \rho V^2 \tag{2.69}$$

where α is dimensionless but not necessarily constant and may depend on the boundary roughness, the Reynolds number of the flow and the cross-section geometry (Henderson, 1966).

Combining Equations 2.69 and 2.66 and solving for V gives:

$$V = \sqrt{\frac{g}{\alpha} R S_f} \tag{2.70}$$

where R is the hydraulic radius, which is defined as $R = \frac{A}{P}$. P is the wetted perimeter of the cross-section.

If $\sqrt{\frac{g}{\alpha}}$ is re-rewritten as a single coefficient, C, Equation 2.70 becomes:

$$V = C\sqrt{RS} \tag{2.71}$$

which is the Chézy Equation.

The Chézy Equation is similar in form to the Darcy-Weisbach Equation, which is commonly used to estimate head losses due to boundary friction in pipe flow (Henderson, 1966). Because of this, the Moody Diagram, which is used to graphically estimate values of the Darcy-Weisbach friction factor, f, for pipe flow can also be used to estimate values of the Chézy coefficient, C, using the following relationship:

$$C = \sqrt{\frac{8g}{f}} \tag{2.72}$$

If C in the Chézy Equation is set to:

$$C = \frac{R^{\frac{1}{6}}}{n} \tag{2.73}$$

then the Chézy Equation becomes the Manning Equation[1]:

$$V = \frac{R^{\frac{2}{3}} S^{\frac{1}{2}}}{n} \tag{2.74}$$

where n is the Manning roughness coefficient, or "Manning's n". In Europe the Manning equation is sometimes referred to as the Strickler equation.

Values of Manning's n can also be estimated from the Moody diagram using

[1]Henderson (1966) explains that the equation was incorrectly attributed to Manning, when in fact the conclusion that C varies as the sixth root of R was actually reached independently by Gauckler in 1869 and Hagen in 1881.

the relationship:

$$n = \sqrt{\frac{f}{8g}} R^{\frac{1}{6}} \tag{2.75}$$

provided that the flow is fully turbulent (i.e. independent of Re). This implies that the Manning Equation itself is also only valid for fully turbulent flow. Henderson (1966) gives the following criterion for determining whether a flow is fully turbulent:

$$n^6 \sqrt{RS_f} \leq 1.1 \times 10^{-13} \tag{2.76}$$

Values of n can also be estimated using tables that give typical values for various channel materials and floodplain covers, for example $n = 0.012$ for a concrete-lined channel and $n = 0.1$ for a floodplain covered with dense trees (Chow et al., 1988). Although Mannings n itself is dimensionless, there is an implied dimensional constant of 1.0 $m^{\frac{1}{3}} s^{-1}$ in Equation 2.74 (where the equation is expressed in SI units of metres and seconds). For imperial units (feet and seconds) the value of the constant is 1.49.

Hicks and Mason (1991) present calculated n and C values for 78 New Zealand river and canal reaches, based on flow gaugings and measured water surface slope and cross-sections. Photos of the river reaches are provided so that a visual comparison approach can be used to estimate roughness coefficients for similar rivers. For each surveyed reach the roughness coefficients are calculated for a range of discharges, highlighting the fact that roughness varies under different flow conditions. This is a limitation of using tabulated values.

Roughness coefficients are often used as a calibration parameter in open channel flow models, with estimates from tables or visual references used as a starting point.

2.4.3 Derivation of the surface water flow equations from the Navier-Stokes Equations

The SWE and the Saint-Venant Equations are derived by vertically integrating the Navier-Stokes Equations and applying appropriate boundary conditions at the water surface and channel bottom.

It is assumed that the velocity only varies in the $x - y$ plane for the SWE. For the Saint Venant Equations it is assumed that depth and velocity vary only in the longitudinal direction, i.e. the water surface is horizontal and the velocity is constant across any cross-section perpendicular to the channel's longitudinal axis (Chow et al., 1988).

The pressure is assumed to be hydrostatic. This allows the flow depth to be used as a variable in the equations, rather than pressure.

2.4.3.1 Boundary conditions

The derivation of the SWE from the Navier-Stokes Equations requires kinematic and dynamic boundary conditions to be imposed both at the channel bottom and at the free surface (Vreugdenhil, 1994).

The kinematic boundary condition requires that no water particles cross either boundary. In other words there is no velocity component normal to the bed and the free surface. In the case of the channel bottom the kinematic boundary condition implies an impermeable bed. In the case of the free surface boundary, the free surface itself may be moving, so the boundary condition refers to normal velocity relative to that of the surface.

The dynamic boundary condition at the channel bottom results in the "no-slip" condition (i.e. zero velocity tangential to the bed). At the free surface continuity of stresses is required. For water resources applications typically the only relevant stress is atmospheric pressure (i.e. $p = p_a$ at the free surface). Shear stress from wind can be included in applications where this is important, such as ocean models.

At the channel bottom both the kinematic and dynamic boundary conditions are inappropriate if the bed is permeable. This is discussed further in Chapter 3 in the context of models that attempt to account for interactions between

groundwater and surface water flows.

2.4.3.2 Integration over depth

Integration of the two horizontal momentum equations and the continuity equation over the flow depth, $a = h - z_b$ (where h is the free surface elevation and z_b is the bed elevation above an arbitrary datum) results in the system of depth-averaged equations.

The depth-integration of the momentum equations results in "differential advection" terms that represent a deviation from the depth-averaged values. This is analogous to the Reynolds stresses that arise from time-averaging the Navier-Stokes Equations, but the additional terms are nothing to do with turbulence in this case. These terms are lumped in with the other lateral momentum exchange terms (viscous and turbulent stresses) and are typically neglected in the "standard" form of the SWE as they cannot be accurately modelled (Vreugdenhil, 1994).

In a full three-dimensional simulation with a no-slip boundary condition the stress at the bed can be calculated by the model. However in order to close the system of depth-averaged equations the bottom stress must be parameterised in terms of the other depth-averaged variables (Vreugdenhil, 1994). This is the origin of the bed-roughness terms in the SWE and Saint-Venant Equations. The formulation of the bed roughness terms and methods for estimating roughness coefficients are discussed in Section 2.4.2.

2.5 Numerical Methods

Under sufficient levels of simplification and idealisation the Navier-Stokes Equations and the classical equations of groundwater and surface water hydraulics (as discussed in this chapter) can be solved analytically. In many cases, however, the level of simplification required rules out the use of analytical solutions for modelling "real world" flows. In order to represent spatially-distributed physical properties, complicated geometry, temporally varying boundary conditions, and any other situations in which the assumptions in analytical solutions cannot be justified, it is necessary to use numerical solutions.

Numerical solutions are a discretised approximation of the continuous solution to whatever mathematical model is being used to represent a physical process. The discretisation process involves two main tasks (Schäfer, 2006):

- discretisation of the overall problem domain into a finite number of sub-domains.
- discretisation of the relevant governing equations.

It is generally assumed that the error introduced in the discretisation process is less than the error associated with the assumptions that would be required if an analytical solution was to be used.

A properly constructed and calibrated numerical model can potentially offer more insights than field or experimental investigations due to the ability to generate spatially-distributed results, and to test the consequences of scenarios.

In this section a range of commonly-used numerical methods is introduced, with an emphasis on the finite volume method, which was the method selected for the development of the numerical model described in this thesis (Chapter 4).

2.5.1 Range of available methods

In both surface and subsurface computational hydraulics the most commonly-used methods are the finite difference and finite element methods. The finite volume method is the preferred numerical method for computational fluid dynamics (CFD) but until recently has been seldom used in computational hydraulics.

Other available methods are the integrated finite difference method, boundary element method (also known as the boundary integral method) and the analytical element method. These three methods are seldom used in practice, however (Anderson and Woessner, 1992).

Within each general form of numerical method there are a wide range of options for how the spatial and temporal discretisations are handled.

2.5.1.1 Finite difference

The finite difference method (FDM) was initially developed in 1910 by Richardson: it is the oldest of the commonly-used numerical methods.

The FDM is implemented by discretising the solution domain into a series of grid points. A structured orthogonal grid is required (i.e. the grid points can be organised into rows and columns for a 2D case, and there is a direct relationship between the physical location of points in the grid and the data structures used by the numerical method).

The governing equations are discretised in differential form at the grid points. A truncated Taylor series expansion is used to approximate derivatives in the equations. The resulting system of algebraic equations is then solved either iteratively or simultaneously, dependent on the form of temporal discretisation chosen.

The main advantage of the FDM is that it is relatively simple to implement. This simplicity can also be a limitation, however, as the requirement for a structured orthogonal grid may lead to errors where the boundaries of the physical domain are irregular and don't align with the model grid. Conservation of mass, momentum and energy is not guaranteed on a coarse grid.

2.5.1.2 Finite element

The finite element method (FEM) was first developed by Courant in 1943, and was significantly refined in the 1960s and 1970s, predominantly for use in structural mechanics problems.

Like the FDM, the governing equations are discretised in differential form for a FEM model. The main advantage of FEM models over the FDM is that

the size and shape of the elements in a FEM mesh can be varied, enabling the model to accurately handle much more complex geometry. Triangular elements are frequently used.

A fundamental difference between the finite difference and finite element methods is that finite differences make no assumption about the variation of values between nodes, whereas finite elements define the variation of values over an element by means of an interpolation function. It can be shown, however, that the finite difference method is a special case of the finite element method (Wang and Anderson, 1982).

In addition to increased geometrical flexibility, an advantage of FEM models is that they are more accurate than FDM models on a coarse grid. Although they are potentially more stable than finite volume models, FEM models must be carefully formulated to ensure a conservative solution, and they can be more computationally demanding than other methods (Huebner et al., 1995).

FEM models are popular for groundwater flow modelling. They are not well suited to turbulent flows, however (Bakker, 2006).

2.5.1.3 Finite volume

In the finite volume method (FVM) the domain is divided up into a mesh of control volumes. The meshing process for the FVM offers similar flexibility to the FEM. It is possible to use cells of different shape, and it is not necessary for the grid to be structured (i.e. the cells can be arranged in such a way that it is not possible to assign row and column numbers), although a model with an unstructured grid is considerably more complicated to set up.

The governing equations are discretised in integral form and fluxes of mass and momentum at the cell faces are calculated. Assumptions need to be made about how values vary over the cell faces. The discretisation process results in an algebraic equation for each control volume in the mesh. As for the other methods, these can be solved iteratively or simultaneously.

A key advantage of the FVM is that mass, momentum and energy conservation at the cell faces is guaranteed, even with a coarse mesh. The FVM is also computationally efficient compared to other methods.

A disadvantage of the FVM is that "false diffusion" can occur if overly simple differencing schemes are used (Bakker, 2006).

The justification for selecting the FVM for the numerical model developed in this thesis is discussed in Chapter 4.

2.5.2 The finite volume method

The FVM can be used to solve any partial differential equation (PDE), or system of PDEs, that can be written in the following form:

$$\frac{\partial \mathbf{U}}{\partial t} + \nabla \cdot \mathbf{H} = \mathbf{S} \tag{2.77}$$

where $\mathbf{U}$ is the conserved vector variable, $\mathbf{H} = \mathbf{H}(\mathbf{U})$ is the flux density and $\mathbf{S}$ is a vector of source terms.

For simplicity, and because the numerical model developed later in this thesis is two-dimensional, the following description of the finite volume method is limited to two spatial dimensions.

For a two-dimensional domain, (assuming for simplicity that $\mathbf{S} = 0$, although the numerical model development in Chapter 4 includes source terms) Equation 2.77 can be integrated over an arbitrary region, R,representing a finite-volume cell in the x-y plane:

$$\iint_R \left(\frac{\partial \mathbf{U}}{\partial t} + \nabla \cdot \mathbf{H} \right) \mathrm{d}R = \iint_R 0 \tag{2.78}$$

which simplifies to:

$$\iint_R \frac{\partial \mathbf{U}}{\partial t} \, \mathrm{d}R + \iint_R \nabla \cdot \mathbf{H} \, \mathrm{d}\mathbf{R} = \mathbf{0} \tag{2.79}$$

Green's theorem allows the second integral term in Equation 2.79 to be replaced with a line integral around the perimeter, P, of the region, R:

$$\iint_R \frac{\partial \mathbf{U}}{\partial t} \, \mathrm{d}R + \oint_P \mathbf{H} \cdot \mathbf{n} \, \mathrm{d}\mathbf{P} = \mathbf{0} \tag{2.80}$$

where $\mathbf{n}$ is a unit normal vector pointing outwards from any point on the perime-

ter, P. If the conserved vector variable is re-defined as an average value, $\overline{\mathbf{U}}$, over the area A of region R, (rather than a point value) the integral in the first term of Equation 2.80 can be re-written as follows:

$$A\frac{\partial \overline{\mathbf{U}}}{\partial t} + \oint_P \mathbf{H} \cdot \mathbf{n}\, \mathrm{d}\mathbf{P} = \mathbf{0} \tag{2.81}$$

Re-arranging Equation 2.81 gives the semi-integral form of Equation 2.77:

$$\frac{\partial \overline{\mathbf{U}}}{\partial t} = -\frac{1}{A}\oint_P \mathbf{H} \cdot \mathbf{n}\, \mathrm{d}\mathbf{P} \tag{2.82}$$

Equation 2.82 is valid for any region in the $x-y$ plane for which Equation 2.77 holds (Causon et al., 2011).

Implementation of a FVM scheme requires spatial and temporal discretisation of Equation 2.82. The spatial discretisation is achieved by dividing the computational domain into a mesh of polygonal cells. Equation 2.82 is approximated over each cell.

For any cell in the finite volume mesh, the line integral in Equation 2.82 is the net flux out of the cell, and is approximated as:

$$\oint_P \mathbf{H} \cdot \mathbf{n}\, \mathrm{d}\mathbf{P} = \sum_{\mathbf{sides}} \mathbf{H} \cdot \mathbf{s} \tag{2.83}$$

where $\mathbf{s}$ is the outward normal vector for each side of the computational cell, with a magnitude equal to the cell length.

Discretisation of the temporal term in Equation 2.82 can be handled in a number of ways, the simplest of which is a forward difference (or explicit) scheme, in which updated variable values are calculated using values from previous time-steps. Implementing a forward-differencing scheme results in Equation 2.82 being re-written as:

$$\frac{u_{i,j}^{n+1} - u_{i,j}^{n}}{\Delta t} = -\frac{1}{A_{i,j}} \sum_{sides} \mathbf{H^n} \cdot \mathbf{s} \tag{2.84}$$

where u is the approximation of the average value $\overline{\mathbf{U}}$, i, j is the cell identifier,

n is the current time-step and $n+1$ is the future time-step for which values are to be determined. Temporal discretisation is discussed further in Section 2.5.2.5. Re-arranging Equation 2.84 gives the final form of a generalised finite volume scheme:

$$u_{i,j}^{n+1} = u_{i,j}^{n} - \frac{\Delta t}{A_{i,j}} \sum_{sides} \mathbf{H^n} \cdot \mathbf{s} \tag{2.85}$$

Equation 2.85 is illustrated in Figure 2.8 for a arbitrary region of a finite-volume mesh at time-step n.

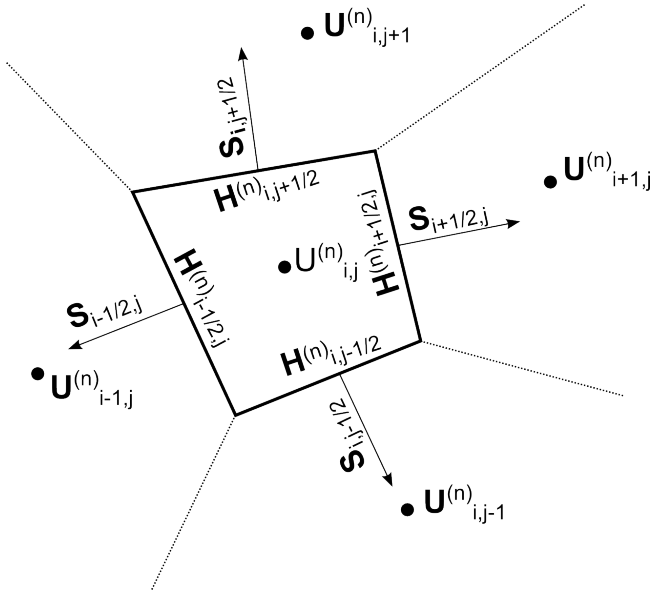

Figure 2.8: Finite volume cells, showing cell-centre values and cell-face fluxes

Finite volume schemes can be more specifically classified by the difference schemes used to estimate fluxes at the cell boundaries and the method of temporal discretisation.

2.5.2.1 Spatial difference schemes

In the FVM the values being solved for are specified at the centre of the mesh cells. In order to calculate fluxes at the cell faces, however, it is necessary to interpolate values of this variable at the faces. A number of options are available for this.

2.5.2.2 Upwind schemes

In upwind differencing schemes an upstream value is used to determine the value of the variable at the cell face. It is necessary to know the flow direction in advance (either from a previous time-step's results or from known / estimated initial conditions) in order to know which direction is "upwind". A first-order upwind scheme for a three-cell computational molecule is shown in Figure 2.9. In this scheme the cell-face values are assumed to be identical to the upstream cell-centre value.

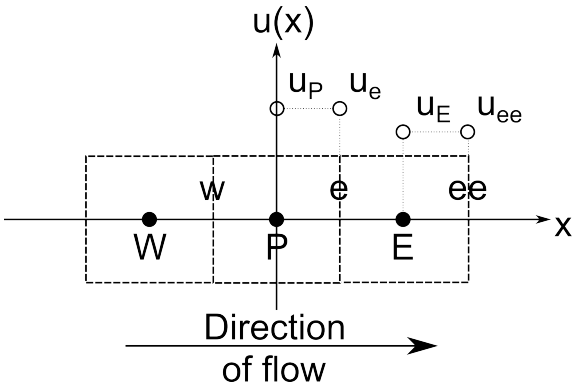

Figure 2.9: First-order upwind interpolation of cell-face values

In figure 2.9 the central cell is labelled P, and the outer cells are labelled according to their compass directions (E and W) with respect to cell P. Capital letters refer to cell centres and lower-case letters refer to cell-faces. Because the cell-face references are also with respect to cell P, the eastern face of cell E is labelled ee (and the western face of cell W would be ww). With a first-order upwind scheme $U_e = U_P$ and $U_{ee} = U_E$.

First order upwind schemes are very stable, but can result in gradients being "smeared out" (Causon et al., 2011).

Greater accuracy can be achieved by using a second-order upwind scheme, in which the cell-face value is linearly extrapolated from two upwind values. If strong gradients exist in the flow, however, a second-order method can result in "overshoot" at the cell faces. It may be necessary to build in a limiter to keep the cell-face values within the expected range.

2.5.2.3 Central difference schemes

In a central difference scheme the cell-face values are determined by linear interpolation between neighbouring cell-centres. It is not necessary to know the flow direction in advance for this method. A central differencing scheme is shown in Figure 2.10.

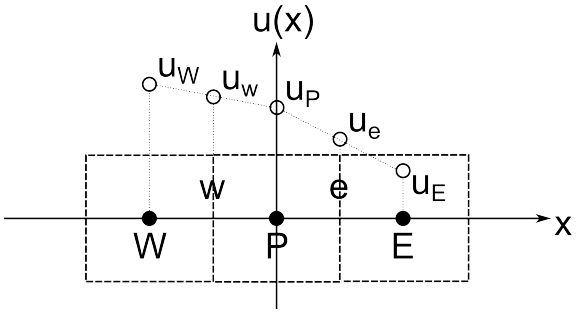

Figure 2.10: Central differencing interpolation of cell-face values

Central differencing is more accurate than a first-order upwind scheme, but may result in oscillatory behaviour if the local Peclet number (the ratio of convective and diffusive transport) is greater than 2 (Bakker, 2006).

2.5.2.4 Other difference schemes

A range of alternatives to upwind and central differencing exist, including using a power-law rather than a linear interpolation, and QUICK (quadratic upwind interpolation for convective kinematics), in which a quadratic curve is fitted through two upwind cell values and one downwind value.

It is also possible to switch between differencing schemes during a model run to ensure that the most appropriate scheme is being used, based on local Peclet number values for example. This is referred to as a hybrid scheme.

A weighted average of estimates from two (or more) difference schemes is referred to as a blended scheme.

2.5.2.5 Temporal discretisation

For unsteady flows a method must also be selected for discretising the unsteady terms in the governing equations. At the highest level these can be categorised

as explicit or implicit.

Explicit (or backwards-time) methods calculate solutions at a future time-step based on the current solution (and also perhaps previous known values), whereas implicit (or forwards-time) methods also incorporate the future unknown values into the equation to be solved.

2.5.2.6 Explicit methods

Explicit time-stepping methods can be expressed as:

$$\frac{\partial u}{\partial t} \approx \frac{u^{n+1} - u^n}{\Delta t} = F\left(u^n, u^{n-1}, ...\right) \tag{2.86}$$

where u_n is the value of u at the current time-step, and u_{n+1} is the value at $t+\Delta t$. F is an operator that summarises the temporal discretisation of the PDE.

Numerical schemes with temporal discretisations based on Equation 2.86 are typically relatively easy to implement and solve. Explicit methods can, however, be unstable at larger time-steps. The stability of an explicit method is determined by the CourantFriedrichsLewy (CFL) condition, which can be expressed as follows:

$$C = \frac{u\Delta t}{\Delta x} \leq C_{max} \tag{2.87}$$

where u is a representative velocity for the problem being solved, Δx is the grid spacing and Δt is the time-step. C is the Courant number, and C_{max} is typically 1.0. An explicit method with $C > C_{max}$ will typically be unstable. This requirement can result in impractically small time-steps in some cases.

2.5.2.7 Implicit methods

Implicit methods can be expressed as follows:

$$\frac{\partial u}{\partial t} \approx \frac{u^{n+1} - u^n}{\Delta t} = F\left(u^{n+1}, u^n, u^{n-1}, ...\right) \tag{2.88}$$

Equation 2.88 must be solved for u_{n+1} using matrix or iterative methods. This typically makes implicit methods more difficult to implement. Fully implicit methods are not subject to the CFL condition, meaning that larger time-steps

can be used. Despite the greater difficulty of implementation, this potentially results in greater computational efficiency.

Weighted averages of the fully-explicit (Equation 2.86) and fully-implicit (Equation 2.88) methods are also possible:

$$\frac{u^{n+1} - u^n}{\Delta t} = \theta F\left(u^{n+1}\right) + (\theta - 1)F\left(u^n\right) \tag{2.89}$$

where θ is a weighting parameter. If $\theta = 0$ the scheme is fully explicit and if $\theta = 1$ it is fully implicit. One popular example of a mixed temporal discretisation scheme is the Crank-Nicholson method, which results if $\theta = 0.5$.

Within the general categorisation of explicit and implicit schemes, there is a wide range of options for how the value of u^{n+1} is calculated. The simplest of these are Euler schemes, which assume that value being solved for can be approximated using the slope of the tangent at point n. Other schemes incorporate estimates of the slope at points between n and $n + 1$.

2.6 Chapter Summary

In this chapter the Navier-Stokes and Reynolds-averaged Navier-Stokes Equations have been described. Turbulence, and the need for turbulence modelling, have been introduced. The $k - \epsilon$ and Kolmogorov-Prandtl single-equation turbulence models have been described.

The traditionally-used governing equations for groundwater and surface water flows have been introduced. In both cases the methodology and assumptions required to derive the governing equations from the Navier-Stokes Equations have been described.

For fully-saturated groundwater flow the governing equation is typically derived from Darcy's Law and a mass-conservation expression. This can also be derived directly from the Navier-Stokes Equations using volume-averaging. The governing equation for unsaturated groundwater flow is Richards' Equation, which can also be derived from Darcy's Law, with the conservation of mass expression modified to account for varying water content in the porous matrix. Although analytical solutions exist for some groundwater flow scenarios, such as

an aquifer's response to pumping, these require significant simplifying assumptions.

The governing equations for surface water flow, the Shallow Water Equations (or the St Venant Equations for the one-dimensional case) can be derived from the Navier-Stokes Equations by averaging in time and over the depth of flow. Stresses at the bed are parameterised with a bed roughness equation such as the Chézy Equation or the Manning Equation.

There are a range of numerical methods that can be used to solve the governing equations, given that analytical solutions are generally only available for highly idealised and simplified cases. The basis of the finite volume method, which was used for the numerical model developed in this thesis, was introduced. Further details of the numerical methods used in this thesis are given in Chapter 4.

Chapter 3

Literature Review

3.1 Overview

This chapter builds on the theoretical foundations of Chapter 2 by reviewing literature from several diverse areas that are relevant to numerical modelling of groundwater-surface water interactions.

Background literature on the physical controls on groundwater - surface-water interactions is reviewed. In its most general sense the term "surface water" encompasses all forms of water body on the earth's surface, including lakes, wetlands and oceans, and also includes snow and ice (Winter et al., 1998). In this review, however, the definition of surface water is generally restricted to rivers and streams.

The existing approaches that are used in both practice and research for numerical modelling of coupled groundwater - surface water systems are identified and discussed. Potential problems with these approaches are considered.

Other numerical and experimental studies of flow over and within permeable beds are reviewed. Among these are studies that consider turbulent flows in porous media, and the application of a single-domain approach to coupled clear-fluid / porous media flows. This area of research is not limited to environmental flows; in fact the most relevant literature comes from industrial applications.

The double-averaging approach and previous applications of the double-averaged Navier-Stokes (DANS) Equations, which are the basis of the methodology used

in this thesis, are introduced and discussed.

3.2 Physical Controls on Groundwater - Surface Water Interactions

Groundwater - surface water interactions are typically described from the stream's point of view. The ways in which surface water and groundwater flows interact are summarised by Winter et al. (1998):

> *Streams interact with ground water in three basic ways: streams gain water from inflow of ground water through the streambed (gaining stream), they lose water to ground water by outflow through the streambed (losing stream), or they do both, gaining in some reaches and losing in other reaches*

3.2.1 Gaining and losing streams

Whether a stream gains or loses water from an aquifer is determined by the head difference between the two (Brunner et al., 2009).

For a stream to gain water from groundwater the free-surface of the stream must be lower than the water table in the surrounding aquifer. The aquifer may be part of a larger groundwater system, or it may be limited to the adjacent bed and banks of the stream.

Conversely, for a stream to lose water to the surrounding aquifer, the level of the stream's free-surface must be higher than the water table in the aquifer. A losing stream may be fully connected to the groundwater system, or it can be disconnected, in which case there is an unsaturated layer between the stream bed and the water table.

Figure 3.1 shows schematic diagrams of gaining and losing (both connected and disconnected) streams.

"Disconnected" is a potentially misleading term. It does not mean that there is no exchange between the river and the groundwater system. In fact, the infiltration rate through the stream bed in a disconnected system is greater than

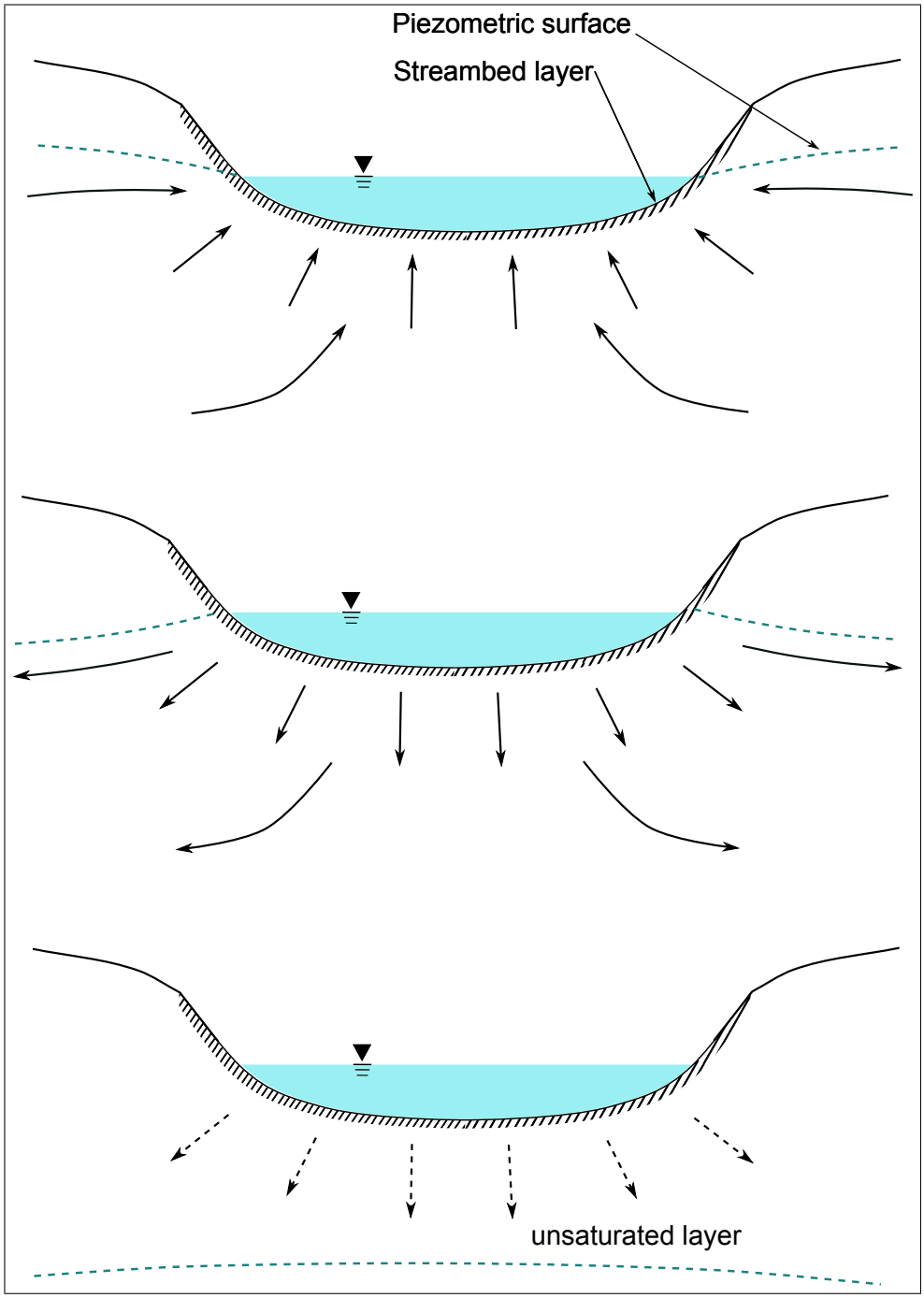

Figure 3.1: Gaining, connected losing and disconnected streams

if it was connected (with all other factors held constant). This scenario can also be described as an unsaturated connection or a perched river / stream. The term disconnected only refers to the fact that changes in the groundwater system will not affect the rate of infiltration (Brunner et al., 2009). However, changes in the surface flow depth will result in a change of infiltration rate through the streambed (Brownbill et al., 2011).

If the longitudinal slope of a stream's free surface (which at a catchment scale can be approximated by the slope of the land surface) is different to the hydraulic gradient in the underlying aquifer then the stream may lose water to groundwater in some reaches and gain water from groundwater in others. This spatial variability in groundwater - surface water interactions can control which sections of a stream flow perennially and which are ephemeral (i.e. where flow only occurs for brief periods following rainfall or snowmelt), particularly if the losing reach is perched.

Figure 3.2 shows a schematic of a long-section down the invert of a stream channel underlain by a shallow unconfined aquifer, with the water table shown at two different levels in diagrams A and B. Downstream of the point where the water table intersects the channel invert there is perennial flow in the stream due to groundwater discharge. Upstream of this point the streamflow is ephemeral. Raising the water table from the level shown in diagram A of the figure to that shown in diagram B results in increased streamflow in the perennial reach. The perennial reach also extends further upstream. Seasonal changes in the regional water table, due to groundwater pumping or climate, can determine where the transition from losing to gaining occurs.

Temporal variability in groundwater - surface water interactions can also occur due to changes in streamflow. For example water that infiltrates into the stream banks during high-flow events is stored in the banks and discharged back to the stream when the water level decreases. This process, known as bank storage, occurs over a timeframe of days or weeks. However if a flood event overtops the normal river channel and inundates surrounding land the discharge back to the stream may take place over months or even years due to the longer flowpaths in the groundwater system (Winter et al., 1998). Bank storage can reduce the magnitude of flood-peaks, delay the arrival of flood waves and lengthen the tail

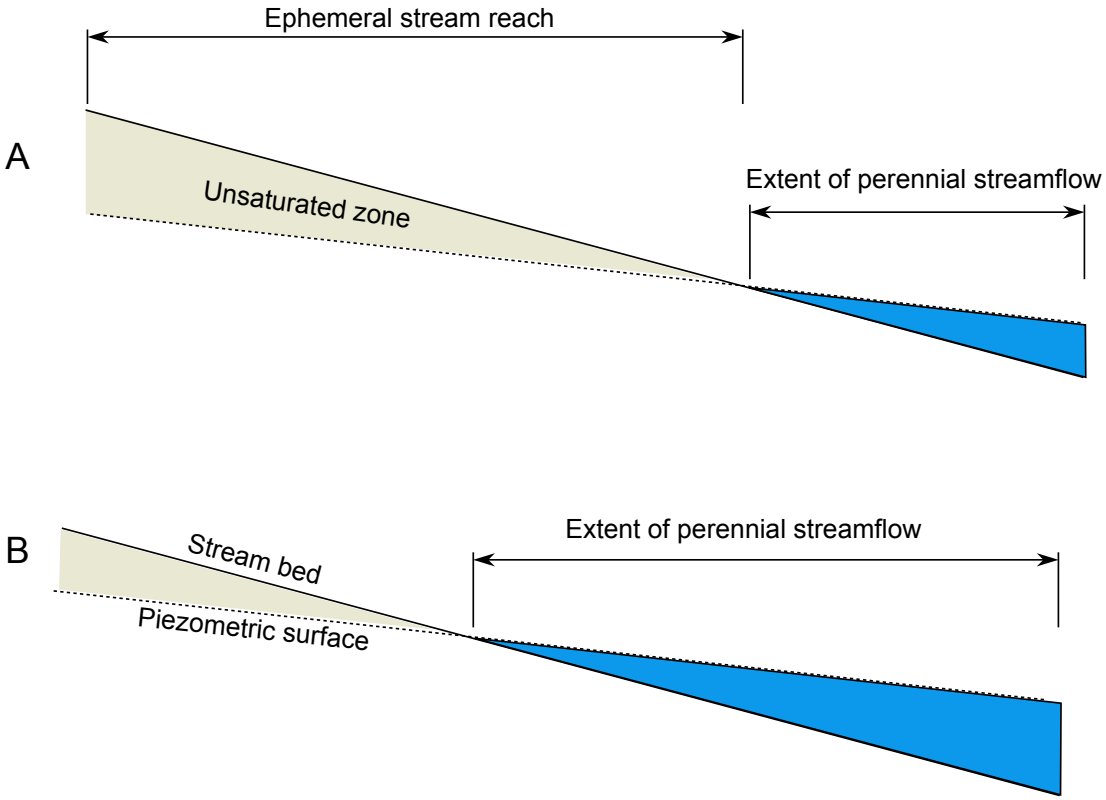

Figure 3.2: Long section of a stream, showing effect of raising water table

of flood recessions. Analytical solutions exist for estimating the effect of bank storage on a streamflow hydrograph, for example Hunt (1990).

3.2.1.1 Transition from connected to disconnected

Between the connected and disconnected losing stream cases there is a transition state, in which an unsaturated zone starts to develop beneath the stream bed but the infiltration rate is still somewhat dependent on the water table level (Brunner et al., 2009).

Figure 3.3 shows the transition from a connected losing stream, where the infiltration flux increases linearly with water-table depth, to a disconnected stream where the infiltration flux is independent of the water table. In the transition state the infiltration rate increases asymptotically to the constant value that occurs in the fully disconnected case.

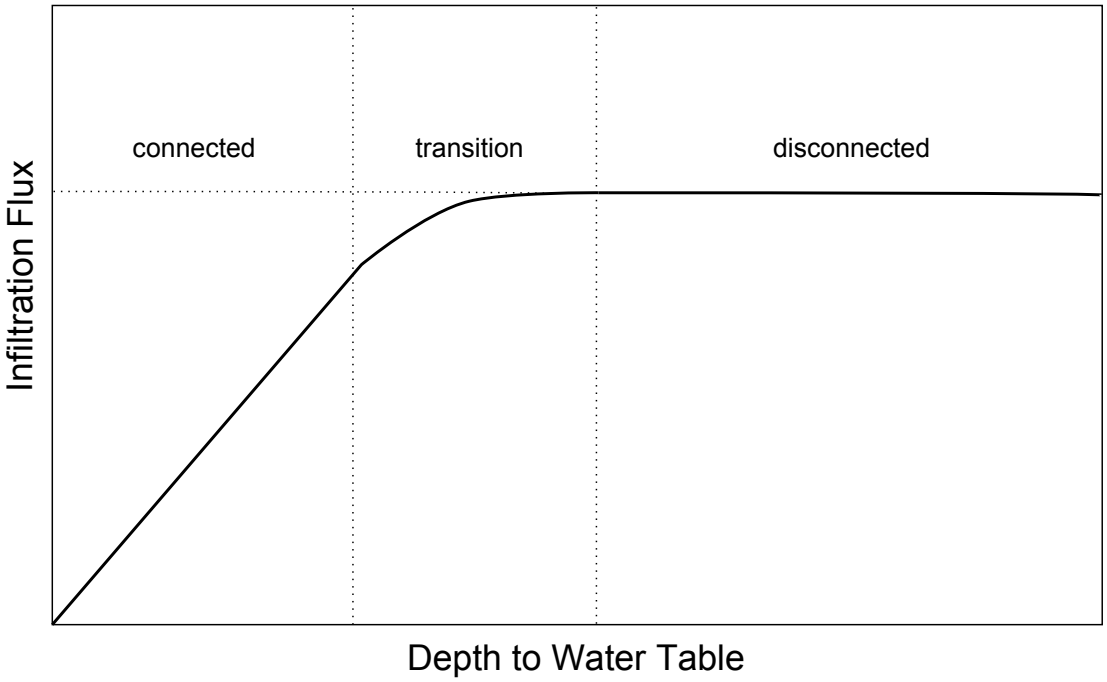

Figure 3.3: Transition from connected to disconnected infiltration

Using a 1D analysis of a two-layer soil column overlain by a depth of ponded water, Brunner et al. (2009) derived a criteria for determining whether discon-

nection can potentially occur beneath a stream:

$$\frac{K_c}{K_a} \leq \frac{h_c}{d + h_c} \tag{3.1}$$

where K_c is the hydraulic conductivity of the streamed "clogging layer", K_a is the conductivity of the underlying aquifer, d is the water depth on the surface and h_c is the thickness of the clogging layer.

This relationship shows that a clogging layer (i.e. a layer of material beneath the streambed that is less conductive than the underlying aquifer) is a necessary, but not sufficient, condition for disconnection to occur.

3.2.1.2 Stream depletion due to groundwater pumping

As discussed in Chapter 2, pumping a well results in a local drawdown of the water table. Pumping a well in an aquifer that is hydraulically connected to a stream will reduce the flow in the stream, either by intercepting water that would have otherwise contributed to streamflow, or by directly inducing losses from the stream. Figure 3.4 (from Winter et al. (1998))shows the effect of groundwater pumping on a gaining stream. With no pumping (diagram A in Figure 3.4) the height of the water table is above the water level in the stream and the groundwater flow direction is towards the stream. As the water level is drawn down due to pumping a flow divide forms in the aquifer and the well intercepts a proportion of the flow that would have otherwise been discharged to the stream (diagram B). In this case, the stream still gains water from the aquifer but the rate of gain is reduced.

If the pumping rate from the well is increased so that the cone of depression reaches the stream (diagram C in Figure 3.4) the hydraulic gradient between the well and the stream is reversed, causing the stream to lose water into the aquifer.

If the stream shown in Figure 3.4 had been losing water to the aquifer prior to the well being pumped (i.e. the piezometric surface sloped away from the stream rather than towards it), pumping the well would steepen the hydraulic gradient between the well and the stream. This would result in an increased loss of water from the stream to the aquifer.

A number of analytical solutions are available to predict stream depletion.

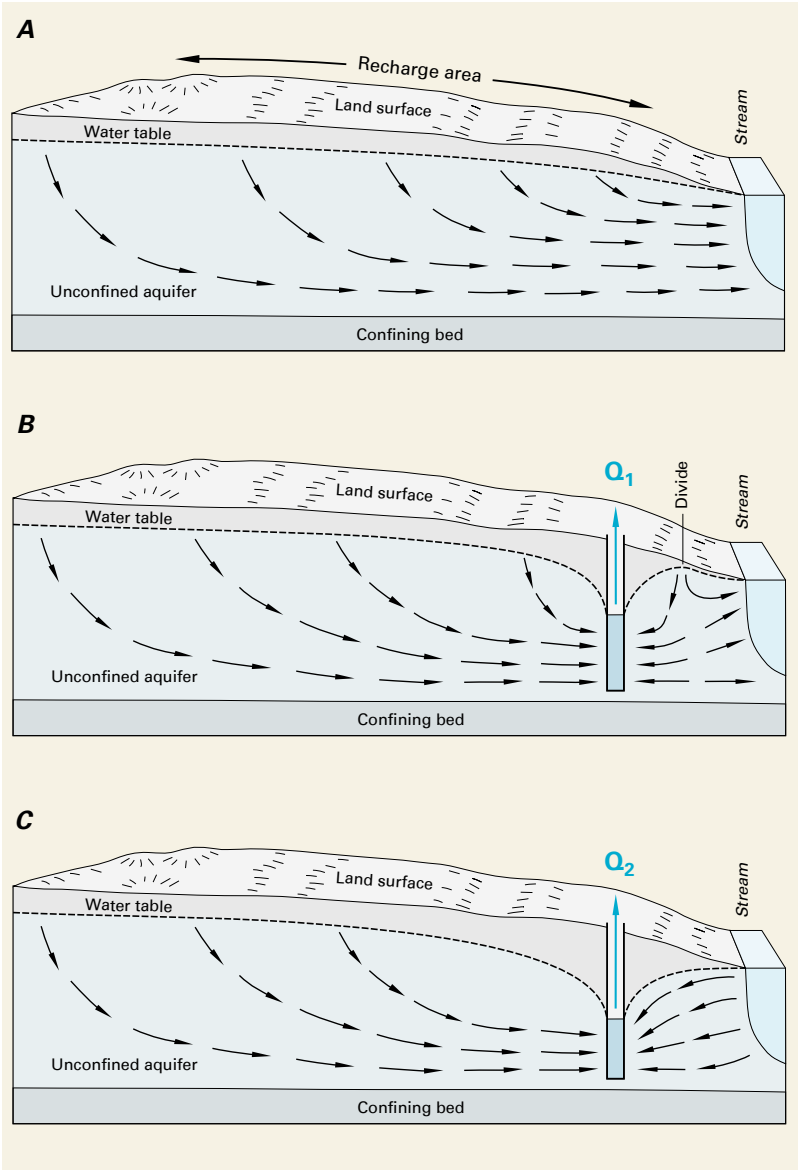

Figure 3.4: Stream recharge interception and stream depletion (from Winter et al. (1998))

Hunt (2014) provides a review of these, and the assumptions and simplifications that they contain. The earliest analytical stream depletion solution, Theis (1941), assumes a very simplified hydrogeological setting, with a river fully penetrating a homogeneous aquifer of semi-infinite extent. More recent solutions provide more realistic representations of the hydrogeology. For example, Hunt (2003) considers a situation where a stream partially penetrates the aquifer and there is an overlying aquitard present.

In situations where the simplifications inherent in analytical solutions cannot be justified, numerical modelling may be necessary to assess the effects of groundwater pumping on streamflows.

3.2.1.3 Effects of water distribution and use on groundwater - surface water interactions

Additional discharge to streams can occur if irrigation or other artificial recharge causes groundwater mounding, either due to infiltration through the soil profile beneath the irrigated area, or leakage from the distribution network. If the water source for an irrigation scheme is a river that is hydraulically connected to the aquifer underlying the irrigated area, then an elevated groundwater table may result in gains to the river that partially re-balance the abstraction at the scheme's intake.

Depending on the spatial extent of the irrigated area, the additional recharge from an irrigation scheme may result in increased groundwater levels in the catchments of streams other than the scheme's water source. This occurs on the mid-Canterbury plains, where irrigation schemes are supplied with water from the major alpine rivers. Groundwater mounding beneath the irrigated areas has resulted in enhanced flows in lowland streams. Dark et al. (2009) used an integrated numerical groundwater - surface water model to investigate the potential effects of changing water management policies and irrigation practices on groundwater levels, and consequently lowland stream flows. It was found that if border-dyke irrigation systems with open-race distribution networks were converted to more efficient spray irrigation with piped distribution, lowland stream flows would reduce to a flow regime closer to the natural pre-development state due to a reduction

in groundwater mounding.

Taking groundwater for irrigation from a deep confined aquifer near a stream may result in gains to the stream, rather than stream depletion.

3.2.2 Hyporheic flow

Hyporheic flow is short-term exchange flow between a stream and its bed sediments, where water leaves a stream and re-enters further downstream. The flow paths for hyporheic flow can be lateral or vertical.

As shown in Figure 3.5, hyporheic flow can be caused by changes in bed gradient (diagram *A*) or meanders (diagram *B*). Longitudinal features such as ripples, dunes and pools drive relatively short hyporheic flow paths, whereas meanders result in longer flow paths (Sawyer and Cardenas, 2009). Hyporheic flows can also be generated by heterogeneity in streambed sediments, which may deflect flow from the bed material upwards into the channel (Sawyer and Cardenas, 2009), or by the pressure gradients created by debris such as logs on the streambed (Sawyer et al., 2011).

The hyporheic zone (i.e. the zone in which hyporheic flow occurs) is of interest to researchers from a number of fields, including freshwater ecology, hydrology and hydrogeology. As a result, there are variations across research disciplines in the conceptual models, terminology and definitions used to describe the hyporheic zone, particularly when it comes to the distinction between hyporheic flow and the groundwater / surface-water interface. This potentially leads to confusion if authors do not clearly state the definition that they are using. The groundwater - surface water interface is defined by Environment Agency (UK) (2009) as:

> *...the fluvial riverbed sediments through which there is an exchange of water (over any time period) between a stream and geologic media.*

and the hyporheic zone is defined as:

> *...that portion of the fluvial sediments in which there is exchange of water from the stream into the riverbed sediments and then returning to the stream, within time-scales of days to months.*

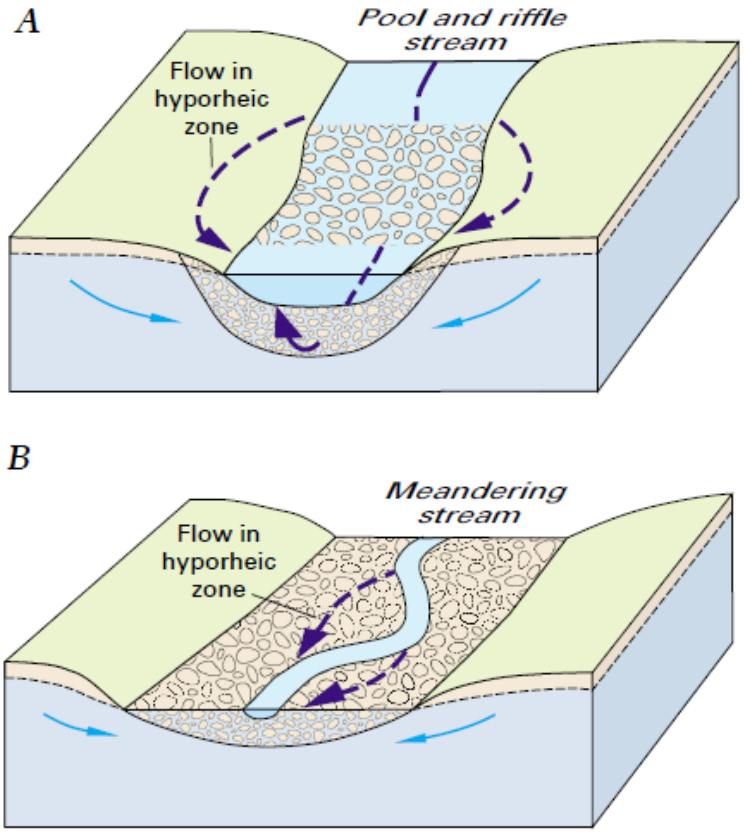

Figure 3.5: Exchange flows in the hyporheic zone (from Winter et al. (1998))

Hyporheic exchange flows can occur over a wide range of spatial scales, from sub-metre up to scales approaching that of regional aquifer systems. Within this range of scales hyporheic exchanges can be "nested", i.e. small-scale interactions can take place within the spatial scale of larger-scale interaction. Poole et al. (2008) proposed the term "hydrologic spiralling" to describe the multiple interacting flow paths with different scales and directions.

3.2.2.1 Ecological importance

Understanding the fluxes of water (and the potential flux of contaminants) through the hyporheic zone is important, as the zone provides a number of ecological services (Environment Agency (UK), 2009). It is the root zone for aquatic plants, and a spawning ground for fish. Some organisms spend their entire life-cycle in the hyporheic zone, while others spend their larval stages in the zone and emerge into the surface water as adults (Smith, 2005).

Hyporheic flow exchanges between groundwater and surface water (and larger-scale groundwater - surface water interactions) can have a regulating effect on surface water temperature. The hyporheic zone provides for attenuation of some contaminant loads by mixing, sorption and biodegradation (Hannah et al., 2009)

3.2.2.2 Numerical modelling studies of hyporheic flow

Some detailed studies of small-scale hyporheic flow have employed CFD-type models. Although these may be capable of modelling more detailed flow structures in the free-surface flow (as they are not depth-averaged like the SWE), some of the coupling methodologies and assumptions employed are questionable.

Cardenas and Wilson (2006) investigated the effect of ambient groundwater discharge (i.e. streamflow gains from the regional groundwater system) on hyporheic flows. A Navier-Stokes model was solved for the surface flow, and a Darcy's Law model was used for the hyporheic zone. The two sub-domains were coupled using sequential coupling, i.e. the flow in one sub-domain was solved first, with the solution from the boundary of that sub-domain being used as a boundary condition for the other sub-domain. This approach allows no feedback between the two sub-domains. In this case the pressure-distribution from

the NSE model was used as a boundary condition at the top of the Darcy model. The bottom boundary of the NSE model was a no-slip, no-flow condition, and the flow was assumed to be laminar throughout the entire domain. The free-surface was treated as a rigid no-flow boundary with a slip condition (i.e. a symmetry boundary).

Cardenas and Wilson (2007) modelled hyporheic exchange between a turbulent streamflow and a sandy porous bed with immobile dunes at the surface - subsurface interface. The surface flow was modelled using a RANS model with a $k-\omega$ turbulence model. In all other respects the model was similar to Cardenas and Wilson (2006). The use of a impermeable no-slip boundary at the surface - subsurface interface was justified on the basis that the permeability of the bed material was low.

Sawyer et al. (2011) modelled the effect of logs on the streambed on hyporheic exchanges, using a similar modelling approach to Cardenas and Wilson (2007). In this case the free-surface was modelled as a deforming surface due to the effect that channel-spanning logs have on the surface flow depth.

3.3 Existing Numerical Modelling Approaches for Groundwater - Surface Water Interactions

Although analytical solutions exist for some cases of groundwater - surface water interactions (for example stream depletion due to groundwater pumping) the applicability of these is typically limited by their simplifying assumptions. Therefore it is often necessary to use models that employ the numerical methods introduced in Chapter 2.

A relatively wide range of numerical modelling approaches exists for modelling coupled groundwater - surface water systems. The models vary in terms of what numerical methods are used, the robustness with which the various physical processes are handled, and how the surface and groundwater components are coupled.

All models that are used in practice, even those that are referred to as "integrated models", rely on numerically coupling two or more systems of equations to represent the different components of the coupled groundwater - surface water system.

3.3.1 Range of modelling approaches

Existing surface water models tend to represent groundwater interactions as a lumped loss / gain term per river reach (if at all) with no consideration of hydraulic effects caused by momentum transfer across the bed.

In existing groundwater models that do not incorporate any of the approaches discussed below, surface water bodies are typically treated as boundary conditions, for example as a constant specified-head boundary. If surface water flows are considered at all by the model, they are often over-simplified, and used mainly to generate modified boundary conditions to the groundwater model rather than to make robust predictions of groundwater - surface-water interactions.

Several approaches exist for numerical modelling of surface water - groundwater interactions. The approaches can be broadly categorised as one of the following:

- add-ons to existing models
- linkages between exiting models
- integrated models

These three categories of model vary in complexity and in the accuracy with which they are able to model coupled flow systems. All of the models referred to are spatially distributed and physics-based to at least some extent (i.e. they attempt to solve the governing partial differential equations for at least some of the physical processes involved, as opposed to spatially lumped, conceptual-level hydrological models).

3.3.1.1 Add-ons to existing models

The most simplistic approach to incorporating surface water-groundwater interactions into a numerical water flow model is with an add-on package that provides modified boundary conditions for the main model.

HEC-RAS[1] (Brunner, 2002) allows the hydraulic properties of the streambed and the level of the water table in the aquifer to be specified. The vertical hydraulic gradient is calculated from the modelled free-surface water level and the flow of water into or out of the reach is calculated using Darcy's Law. The water table level is assumed to be independent of any interactions with the stream, and flow in the aquifer is not actually modelled.

Numerical groundwater models frequently have add-on packages, for example there are various streams packages for MODFLOW[2] (Harbaugh et al., 2000) that incorporate surface water - groundwater interactions into a groundwater simulation, often at a relatively simplistic level, providing time-varying boundary conditions for the main model. Data from the main model can be passed back to the add-on package to provide streamflow results, but the accuracy and resolution of these results will be limited by the level of sophistication of the add-on package.

[1] HEC-RAS is a 1D open-channel hydraulics model developed by the Hydrologic Engineering Centre (HEC) of the U.S. Army Corps of Engineers. RAS stands for "river analysis system". It is in the public domain and is considered by many to be standard for comparing other models.

[2] MODFLOW is the U.S. Geological Survey's modular groundwater flow model. The source-code is in the public domain, and is one of the preferred options for groundwater modelling.

The opposite case, where a groundwater flow package is added to a surface water model, is rarely seen.

At their most simplistic level, streams packages do not solve the SWE. Instead, a river channel is discretised into a number of reaches, and specified or calculated free surface water levels are used to calculate exchange fluxes.

In the RIV package for MODFLOW rivers are treated as head-dependent flux boundaries. The user specifies the stream stage, bed invert level and bed conductance (Harbaugh et al., 2000). In terms of level of sophistication this is similar to the groundwater loss calculations in HEC-RAS.

An add-on package is used to represent rivers and streams in the Canterbury groundwater model (Aqualinc, 2007), in which a custom-written "streams package" has been added to FEMWATER. Similar packages, with varying levels of sophistication, are available for MODFLOW, for example SFR1 (Prudic et al., 2004) and SFR2 (Niswonger and Prudic, 2010). It is noted by Niswonger and Prudic (2010) that numerical oscillations can occur in both the SFR1 and SFR2 streams packages. The channel flow component (CHF) of MODHMS (Panday and Huyakorn, 2004) is conceptually similar to these packages, although MODHMS as a whole is considered to be an integrated model (see Section 3.3.1.3).

The Aqualinc streams package and the MODFLOW SFR packages do not solve the Saint Venant equations for river flow. Each river is discretised into a number of reaches. At the upstream reach a time-series of inflow is specified. At each time-step of the model a water balance is calculated sequentially for each river reach, starting at the upstream end. Exchange flows between the stream and groundwater are calculated based on the hydraulic gradient at the streambed, which is determined using Mannings equation to estimate the stream stage, and groundwater head results from the groundwater model.

Potential problems with the add-on approach in groundwater models are lack of detail in the surface water calculations (e.g. rectangular or v-shaped cross-sectional geometry) and poor spatial resolution. The stability of the groundwater model can also be sensitive to parameters used in the add-on package (Weir, *pers. comm.*, 2011). Add-on packages that use a kinematic wave approximation (e.g. Niswonger and Prudic (2010)) cannot handle adverse bed slopes as this would result in the square-root of a negative number being used in Manning's equation.

This means that riffle and pool structures in a river channel cannot be adequately modelled.

In MODFLOW a stream is considered to be hydraulically connected to the underlying aquifer if the water table is above the elevation of the channel invert, otherwise it is considered to be disconnected (Brunner et al., 2010). This does not account for the transition state described in Brunner et al. (2009). In the connected case the volumetric exchange flux is calculated as:

$$Q = \frac{K_c L w}{h_c}(h_{riv} - h) \tag{3.2}$$

where K_c is the hydraulic conductivity of the streambed clogging layer, L is the length of the river within a computational cell, w is the width of the river, h_c is the thickness of the clogging layer, h_{riv} is the hydraulic head of the river, and h is the head in the aquifer (Brunner et al., 2010). If the stream is disconnected the exchange flux calculation is modified to:

$$Q = \frac{K_c L w}{h_c}(h_{riv} - z_a) \tag{3.3}$$

where z_a is the elevation of the streambed invert.

In addition to the inability to model a transition state between connected and fully disconnected, Brunner et al. (2010) identified a number of other concerns about modelling groundwater - surface water interactions with MODFLOW and its streamflow packages. These included the inability to model negative pressures beneath the streambed, and the fact that a river can only be linked to one grid cell, potentially creating a mismatch between the actual river width and the width of the underlying computational cell. Although there is an unsaturated zone flow (UZF) package for MODFLOW (Niswonger et al., 2006), this does not couple with the SFR packages. The SFR2 package uses a 1D kinematic wave approximation of Richards' equation to route flow through the unsaturated layer beneath a disconnected stream, without considering the negative pressures (Brunner et al., 2010). If both the SFR and UZF packages are used in a MODFLOW model, flow from the SFR package bypasses the UZF package completely (Niswonger, *pers. comm.*, 2016)

3.3.1.2 Linkages between models

Existing models can be linked together using proprietary or custom-built external modules. For example, DHI-WASY Software provide an interface manager, IfmMIKE11, for coupling FEFLOW (a finite element groundwater model) and MIKE-11 (DHI Software's 1-dimensional open-channel model) (Monnikhoff, 2011).

This approach takes advantage of the significant effort that has gone into development of the two component models. The key feature in the linkage approach is the way the two component models are linked i.e. how data is passed between them and how time-steps and iterations are managed. The linkage is conceptually similar to add-on packages, in that the model results are passed from one component to the other, providing modified boundary conditions. The difference is that both components include robust calculations, in contrast to the add-on packages that generally impose significant simplifications.

Anecdotally, the FEFLOW-MIKE11 linkage is difficult to set up (Weir, *pers. comm.*, 2011).

The coupling in IfmMIKE11 is not iterative. At the beginning of each FEFLOW time-step the water levels from the previous MIKE11 time-step are passed to the FEFLOW boundary nodes. After the time-step has been run, groundwater exchange flows are passed from FEFLOW to MIKE11 as lateral inflow / outflow. As discussed below in Section 3.3.2, this time-lagged weakly-coupled approach is not favoured.

3.3.1.3 Integrated models

There are a relatively small number of more complex models that attempt, on some level, to model groundwater - surface water interaction processes in a more robust manner by coupling the governing equations for groundwater and surface water flow in a single model framework. This category of models includes MIKE-SHE (Graham and Butts, 2005), WASH123d (Yeh et al., 2005), MODHMS (Panday and Huyakorn, 2004) and HydroGeoSphere (Brunner and Simmons, 2012). This is not an exhaustive list, and it is not within the scope of this work to fully review or test each model. Methods for physics-based coupling of surface and

subsurface flows has been a topic of active research in recent years (Huang and Yeh, 2009). Recent research has also focused on coupling integrated hydrological models to land-surface, ecological, dynamic vegetation, solute transport and atmospheric models (Maxwell et al., 2014).

A blueprint for a fully integrated model of surface water and groundwater flow was proposed more than 40 years ago by Freeze and Harlan (1969). Progress beyond the "blueprint" stage was not made at the time of publication, however, due to limitations in computational power. Although the computational resource issue has now been largely resolved, truly coupled models, fitting the Freeze and Harlan blueprint have only appeared in the literature in the last 10 years or so (Maxwell, 2009). It should be noted, however, that even the most sophisticated coupled models are unable to properly replicate the hydraulics of the interface between surface and subsurface flow. Continuity of momentum at the interface is typically neglected (Maxwell et al., 2014). The derivation of the shallow-water equations requires a no-flow, no-slip bottom boundary condition to be imposed. This assumption is violated if interactions with an underlying porous layer are being considered. Furman (2008) notes that while ignoring momentum transfer may be acceptable in a large-scale watershed model, it will result in inaccuracies in smaller-scale, more detailed applications.

In the absence of other approaches, integrated models currently present the greatest opportunity to accurately represent the physics of the interface between surface and groundwater as they (typically) provide physics-based solutions for all processes represented in the model. It can be argued, however, that in some circumstances it is appropriate to use simpler, less computationally-demanding processes to represent "less important" processes. For example, in MIKE-SHE there are options to represent the unsaturated zone as a two-layer water balance and groundwater system as a lumped reservoir, rather than using the Richards and Darcy equations (Graham and Butts, 2005). The potential danger of this approach is that the modeller must determine in advance what processes are important.

Channel flow in MIKE-SHE is calculated using MIKE-11, and the coupling mechanism is believed to be similar to that described in Section 3.3.1.2 above for IfmMIKE11. Likewise, the coupling between overland flow and the unsat-

urated zone is relatively weak, with data being exchanged once at the start of the time-step. The most detailed option for modelling the unsaturated zone is a 1-D Richards equation, which rules out the ability to model horizontal flows in variably-saturated layers beneath river beds.

WASH123d (Yeh et al., 2005) models 1-dimensional channel flow, 2-dimensional overland flow and 3-dimensional variably saturated groundwater flow. With sufficient discretisation it could potentially be used for detailed simulations of stream-aquifer interactions, although as discussed below in Section 3.3.3 this may not be realistic with a 1-dimensional channel model.

In a benchmarking study that compares the performance of seven integrated models Maxwell et al. (2014) give a brief description of each model. All of the models considered in the benchmarking study solve Richards' equation for subsurface flows and the SWE (or a simplification such as diffusive or kinematic wave in some cases) for surface flows. The greatest variations between the models are in terms of dimensionality and coupling methodology. Some of the models solve the 3-D Richards' equation throughout the subsurface sub-domain, while others combine a 1-D Richards equation with a 3-D saturated groundwater flow equation, which adds another coupling procedure into the model. In the surface sub-domain some models solve for 2-D flows throughout, for both overland and channel flow, while one model, CATHY (Camporese et al., 2010) represents overland flow as 1-D "rivulets". Coupling methods are discussed further below.

Because analytical solutions do not exist for anything other than very simplified groundwater surface water interactions it is not possible to validate integrated models in the normal sense, and therefore it is necessary to resort to comparing similar numerical models (Maxwell et al., 2014). This approach does not provide any information on whether the models are correct, it only highlights differences between models. Maxwell et al. (2014) concluded from their benchmarking study that in general all of the models considered performed similarly. For simple test cases the model results were quantitatively similar. When more complex scenarios were run, more significant differences were apparent (for example a 50% difference in the time taken to reach steady-state) and the model results tended to be grouped by dimensionality and solution technique.

3.3.2 Solution techniques for coupled models

Yeh and Huang (2007) and Huang and Yeh (2009) present a comparison of approaches for handling coupling between the surface water and groundwater subdomains of integrated numerical models. Options for dealing with the surface - subsurface interface, and numerical coupling approaches are discussed in terms of modelling both overland flow interacting with a shallow subsurface layer, and stream - aquifer interactions.

Three numerical solution techniques are discussed by Huang and Yeh (2009):

- time-lagged, decoupled / weakly-coupled
- iterative implicit coupling
- fully implicit coupling.

In the time-lagged approach the fluxes between the surface and subsurface domains are calculated using results from the previous time-step. The iterative implicit coupling approach uses coupling iterations within a time-step to update the solution in both sub-domains until convergence is reached at the surface-subsurface interface. In the fully implicit approach all equations (surface, subsurface and interface conditions) are solved simultaneously in a global matrix.

In a more general review of hydrological models Kampf and Burges (2007) also discuss sequential non-iterative coupling. In this technique the equations for one sub-domain are solved and the solution is used as a boundary condition for the other sub-domain, without any iteration. Sequential non-iterative or time-lagged coupling is only suitable when the physical processes at the interfaces can be represented as one-way links between the sub-domains.

The time-lagged approach is not favoured by Huang and Yeh (2009) as it potentially introduces numerical errors, and conservation of mass across the interface cannot be ensured. The fully implicit approach is preferred, however it requires the time-step for the surface and subsurface domains to be identical. The iterative implicit coupling approach is still robust, and can handle different time-steps in the surface and subsurface domains.

In order to properly categorise and evaluate the coupling methods used in integrated models, it is necessary to fully understand the methodology that they

use, which cannot always be achieved from reading papers or software documentation published about a particular model. For example,Kampf and Burges (2007) incorrectly categorised WASH123d as using sequential coupling, when in fact it uses a more rigorous method (Yeh, pers. comm., 2011).

Huang and Yeh (2009) note that if weakly coupled or decoupled methods are used to reduce the computational burden without consideration of whether the assumptions and simplifications made are appropriate, the simulation results may not be fit-for-purpose.

3.3.3 Surface-subsurface coupling strategies

Two options are presented in (Yeh and Huang, 2007) and Huang and Yeh (2009) for representing the physics of the interface between the surface and subsurface domains: continuous and discontinuous approaches. The continuous approach includes all sediment layers in the model domain. This approach is also referred to as a pressure-continuity approach by Kollet and Maxwell (2006) and Maxwell et al. (2014).

The discontinuous approach, which dominates current literature, removes the sediment layer at the interface from the model domain, and replaces it with a leakage / linkage term (also called an exchange-flux term in Huang and Yeh (2009)). This approach is also referred to as first-order coupling (Kampf and Burges, 2007) and first-order exchange (Maxwell et al., 2014). This approach is frequently taken for reasons of computational efficiency, but can only be justified if there is a continuous layer of less permeable material at the interface. If this is not the case, the discontinuous approach introduces non-physical parameters into the model. Using a linkage term also assumes that the storage in the interface layer is negligible. The exchange-flux term is often used solely as a model fitting parameter due to a lack of field data on the properties of the interface(Kollet and Maxwell, 2006).

Models that represent surface flow using 1-D equations almost exclusively use the discontinuous approach. This is because, in order to avoid excessive discretisation of the subsurface domain, each cross-section in the channel model is normally connected to only one subsurface node. Yeh and Huang (2007) recom-

mend simulating the channel flow as two-dimensional overland flow if finer spatial resolution is required.

A third approach, known as boundary-condition switching, is used in the CATHY model (Camporese et al., 2010). This approach determines at each time-step whether a computational cell at the surface-subsurface interface is ponded, saturated, unsaturated or dry and enforces pressure and mass-flux continuity. Although Maxwell et al. (2014) categorise this as a separate approach, it appears to be a sub-set of the continuous approach, as no new parameters are introduced to represent fluxes or interface properties.

Some models, for example HydroGeoSphere (Brunner and Simmons, 2012), give the modeller the option to employ either the continuous or discontinuous approaches (Maxwell et al., 2014).

Each of the solution techniques discussed above in Section 3.3.2 can be applied to both the continuous and discontinuous interface options.

3.3.4 Summary of deficiencies in existing approaches

In summary, the deficiencies in the existing approaches available for numerical modelling of groundwater - surface water interactions are as follows:

- In all existing approaches the governing equations are based on assumptions that include no flow between the surface and subsurface flow domains.
- In the case of linkages between existing models, the two models were not originally developed to consider groundwater surface water interactions. This is also the case for add-on packages, in which the main model (typically a groundwater model) in its original state does not consider interactions.
- "Add-on" packages for groundwater models typically over-simplify the surface flow component.
- It is common practice to not explicitly include the stream-bed layer in the model domain, and to represent the flux across the interface with a non-physical parameter.

- If decoupled or weakly-coupled (i.e. time-lagged) methods are used it is not possible to guarantee conservation of mass across the interface and simulation results may not be fit for purpose.
- It is often difficult to know the details of coupling schemes. This is especially the case with commercial software, the documentation for which tends to focus on operation of the model rather than technical background.
- Due to the lack of suitable analytical solutions, proper verification of integrated numerical models is generally not possible, and it is necessary to rely on comparisons between similar models.

3.4 Modelling Flow Over and Within Permeable Beds

A number of numerical studies have considered both laminar and turbulent flows over and within permeable beds, considering both the clear-fluid flow (with either a free-surface or a rigid boundary) and flow in a shallow porous layer. These studies are distinct from the modelling approaches described in Section 3.3 as they are more focussed on representing or attempting to understand the physics of the flow in a coupled domain, rather than coupling together models based on traditional hydraulics equations. Some recent studies use a double-averaging approach, analogous to the volume-averaging approach required to derive the governing equations for porous media flow from the Navier-Stokes equations.

Many of the examples in the literature are focused on mechanical or chemical process applications, for example oil filters, heat exchangers, and fluidised bed reactors. Channels or ducts with a porous layer against one boundary are referred to in some literature as "hybrid domains" or "composite ducts / channels". A common feature of numerical studies of flow in this type of domain is that the flow in the porous layer is generated by shear at the interface between the clear fluid and porous sub-domains, or by a horizontal pressure gradient in the composite channel (i.e. there is nothing driving vertical flows across the interface). Some studies have investigated flow in hybrid domains as a means to understand the effect of the porous medium on heat transfer.

Beavers and Joseph (1967) experimentally investigated Poiseuille flow (laminar pressure-gradient driven flow in a pipe / duct) over a permeable block. They showed that the traditional "no-slip" boundary condition was not valid at the porous boundary, and that at the interface between the clear fluid and the porous medium there is a "slip-velocity" that is greater than the expected Darcy's Law velocity within the porous medium. An empirically-based correlation was developed for the velocity gradient at the interface, in terms of the velocities in both the fluid layer and the porous medium.

Stevenson (1963) derived a modified logarithmic wall law for a turbulent boundary layer over a porous surface that includes an injection / seepage velocity. While this approach acknowledges that an exchange of mass between a

clear fluid flow and a porous medium has an effect on the flow's velocity profile, it does not consider the flow in the porous medium, and treats the edge of the porous region as a rigid boundary rather than a continuum.

Kuznetsov and Becker (2004) modelled flows in a composite duct, assuming that the flow in the clear fluid region was turbulent, and that the flow in the porous region remained laminar. A simple algebraic turbulence model was used in the clear fluid region, and the Brinkman-Forchheimer-extended Darcy equation was used in the porous region. The solutions for the turbulent and laminar flows were matched at the clear-fluid / porous interface. A $k - \epsilon$ model was added in Kuznetsov (2004)

In a paper primarily focused on coupled surface - subsurface models (as discussed in Section 3.3) Furman (2008) provides a summary of conceptual models for representing the physics of the interface between surface and subsurface flows in a way that attempts to conserve mass and momentum. These are categorised as follows:

- continuity of velocity and velocity gradient.
- continuity of velocity, and continuity of viscosity-weighted velocity gradients, with an "effective viscosity" defined in the porous region.
- continuity of velocity, and a "jump" condition in the gradient.
- defining an interface velocity in terms of the clear-fluid velocity and gradient (this is the Beavers and Joseph approach).

Furman (2008) notes that the range of approaches has arisen due to different governing equations being used in the two sub-domains, and the difficulty of defining the interface. Models that use continuity of velocity or velocity gradient tend to be academic in nature, while those used in practice tend to use boundary conditions that maintain continuity of mass flux and head (as a proxy for energy).

Lane and Hardy (2002) discuss the concept of "porous rivers" and highlight some of the deficiencies in traditional hydraulic modelling practice that result from the assumption of an impermeable bed. In the Saint-Venant equations the only physically-based parameter available for representing the river channel's

geometric variability is the discretisation in the downstream direction, dx. This presents practical limitations in terms of how many cross-sections can realistically be included in a model, and theoretical limitations in terms of what is actually being represented by the model's roughness parameter. Although the roughness parameter is primarily thought of as representing friction losses at the bed, it is also implicitly accounting for variability in the channel geometry that is unable to be represented by the model discretisation, and the effects of lateral and vertical mass and momentum fluxes that are assumed by the governing equations to be negligible.

In a 2D shallow-water equation model, or a 3D RANS-based surface water model the model geometry is typically a surface fitted to discrete points in the bed. Part (a) of Figure 3.6 shows that this can lead to parts of the channel that contain flow being excluded from the model domain, and *vice versa*, resulting in mass and momentum conservation errors. The roughness parameter must then be used to represent the spatial scales in the bed topography that are not represented by the modelled bed surface. In 3D models a roughness height rather than a Manning's n-type parameter is typically used. This approach has more physical basis, but still requires adjustment to account for spatial scales not captured in the model mesh. Lane and Hardy (2002) argue that the bed should be treated as a porous medium in order to overcome the deficiencies in how current modelling practices allow bed geometry to be defined. Parts(b) and (c) of Figure 3.6 illustrate a porosity-based approach for defining bed geometry using high-resolution topographic data (e.g. a DEM generated from low-level aerial photography) and discrete samples of the bed elevation, respectively. The dark-shaded cells contain solid material ($\phi = 0$) and the unshaded cells are entirely water($\phi = 1$). Cells with $\phi < 1$ are used to define the bed surface. Lane and Hardy (2002) draw analogies with methods used for modelling atmospheric flows (this field of research is also the origin of the double-averaging methodology, discussed below in Section 3.4.1).

It should be noted that although the methodology suggested by Lane and Hardy (2002) uses the concept of a porous riverbed, it does not actually consider flow in the porous region, i.e. the normal assumptions of a no-flow, no-slip boundary at the bed surface still apply.

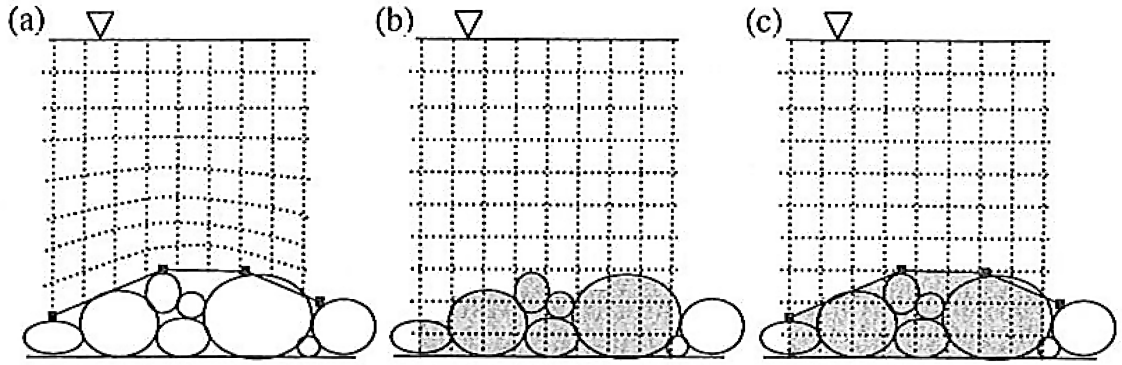

Figure 3.6: The basis for treating a riverbed as a porous medium (from Lane and Hardy (2002))

There are a number of examples in the literature of hybrid domains being modelled using a single system of equations, rather than different governing equations for the surface and subsurface sub-domains. Some of these studies use methodologies that are only valid under certain conditions, or impose rigid assumptions on the nature of the flow, for example assuming that the flow must be fully turbulent throughout or laminar throughout.

Vafai and Kim (1990) developed what they described as an "exact solution" for the flow at the interface between a porous region and a clear fluid flow (i.e. the same configuration considered by Beavers and Joseph (1967)), and also investigated the influence of non-dimensional parameters that govern the flow at the interface. The velocity distribution was shown to be affected by the Darcy number:

$$Da = \frac{k}{H^2} \tag{3.4}$$

where k is the intrinsic permeability and H is the depth of the clear fluid layer, and also by the product of the Reynolds number and an inertia parameter:

$$A = Re_H \Lambda_H \tag{3.5}$$

where Re_H is a Reynolds number based on the clear-fluid flow velocity and length-

scale. The inertia parameter, Λ_H, is defined as:

$$\Lambda_H = \frac{F\phi H}{\sqrt{k}} \tag{3.6}$$

where F is the Forchheimer drag coefficient (Nield and Bejan, 2013), and ϕ is the porosity. It was found by Vafai and Kim that increasing the A parameter (the product of the Reynolds number and inertia parameter) resulted in a greater proportion of the volumetric flow rate passing through the clear fluid region due to increased flow resistance in the porous region. Increasing Da, which corresponds to an increase in k if the depth is held constant, resulted in a higher proportion of the flow passing through the porous region.

Nield (1991) notes that the approach used by Vafai and Kim (1990) is a form of Brinkman-Forchheimer equation, and that the use of the Brinkman term cannot be justified if $\phi \leq 6$, which is not valid for most natural porous media. Further, Nield argues that the use of the Brinkman term will result in an over-estimate of the extent to which motion in the clear-fluid flow penetrates into the porous region. Vafai and Kim's counter-argument was that although the Brinkman-Forchheimer was not perfect, it enabled treatment of composite clear fluid / porous regions as a single domain, even if porosity was smaller than the recommended value (Vafai and Kim, 1995).

The Brinkman equation is sometimes used in problems that include an interface between a porous medium and a free-surface flow, with the justification that the porosity becomes sufficiently large at the interface. Shavit et al. (2002) developed a set of modified Brinkman equations to model flows at the interface between a free-surface flow and an idealised porous media. These equations, the form of which changes depending on the vertical location in the domain, appear to be specific to the idealised configuration that was investigated.

Choi and Waller (1997) used a semi-empirically derived generalised flow model, based on a Brinkman-Forchheimer extended Darcy flow model, to simulate laminar flow over a layer of porous medium. They investigated the thickness of the transition region between the surface and subsurface flows, and found that the penetration depth (i.e. the thickness of the transition layer) was only dependent on the Darcy Number, which was defined in the same way as Vafai and Kim

(1995) (i.e. Equation 3.4), except that H was the thickness of the total domain (surface and subsurface layers).

Breugem et al. (2006) used volume-averaged Navier-Stokes Equations as a framework for describing the results of direct numerical simulations (DNS) of turbulent flow in a closed channel with one permeable wall. This is different to the double-averaging concept discussed below in Section 3.4.1, as it did not involve time-averaging. It was found that a key parameter was the permeability Reynolds number, which is defined as:

$$Re_k = \frac{\sqrt{k}u_\tau}{\nu} \tag{3.7}$$

where k is the intrinsic permeability of the porous wall, u_τ is the wall friction velocity and ν is the kinematic viscosity. Breugem et al. (2006) interpret Re_k as "the ratio of the effective pore diameter to the characteristic length scale of the viscous sublayers over the individual wall elements." For $Re_k \ll 1$ a wall is effectively impermeable and viscous effects are dominant near the wall. For $Re_k \gg 1$ viscous effects are of minor importance near the wall, and the wall can be classified as highly permeable (although "wall" is perhaps a misnomer in this case). In the highly permeable case turbulent transport of mean kinetic energy (MKE) in the region just above the interface is balanced by Reynolds shear stress. Below the interface, in the porous region, the Forchheimer drag force contributes to dissipation (Breugem et al., 2006).

3.4.1 The double-averaged Navier-Stokes Equations

Some recent studies apply the concept of double-averaging to flows over and within permeable beds.

In the double-averaging methodology (also known as macroscopic averaging), flow variables are averaged in both time and space. This methodology stems from aerodynamics, in particular modelling of airflows over forest canopies. The double-averaging process is described by de Lemos (2005) (who referred to it as "double-decomposition") and Nikora et al. (2007a). The double-averaged equations can be obtained either by averaging the Navier-Stokes Equations in time and then in space, or in space and then in time. The time-space option is equiv-

alent to applying a spatial average to the RANS equations. Nikora et al. (2007a) note that this option is more physically transparent and is more in keeping with the traditions of turbulence research than the space-time option.

The double-averaged Navier-Stokes (DANS) equations are stated and the additional terms that arise out of the averaging process are described in Chapter 4. The details of the averaging process are given in Appendix B.

The spatial averaging process is very similar to the volume-averaging process used in porous media hydrodynamics (as discussed in Section 2.3.3), which suggests that the approach is equally applicable to both surface and subsurface flows. This is alluded to by Nikora et al. (2007a), but to date applications of the DANS equations appear to have been limited to surface and near-bed flows. The double-averaged equations contain a parameter, ϕ, which is referred to by Nikora et al. (2001) as a "roughness geometry function", but is in fact equivalent to a porosity (as defined in Equation 2.54). Double-averaging is justified in the case of surface flows because most applications deal with spatially averaged roughness parameters, rather than point values. Nikora et al. (2007a) also give a double-averaged transport equation for a passive scalar. This provides the general basis of the transport equations required for a implementing a double-averaged turbulence model. De Lemos (2005) gives double-averaged equations for the turbulent kinetic energy and dissipation, including an additional term accounting for TKE produced by the presence of the porous matrix.

In a second paper focused on applications of double-averaging for rough-bed open-channel flows, Nikora et al. (2007b) identified flow layers and flow types, depending on relative submergence (flow depth divided by roughness height). In terms of surface flows, the bottom layer is the interfacial sub-layer between roughness crests and troughs. Skin friction and form drag contribute to the momentum balance in this layer, which is the least-studied part of the roughness layer. If the bed is permeable there is an additional subsurface layer beneath the interfacial sub-layer, beginning at the point where the roughness geometry function becomes independent of depth.

Manes et al. (2009) conducted a comparative study of the turbulence structure of open channel flows over permeable and impermeable rough beds, using the double-averaging approach as a framework for analysing experimental results.

They stated that it is not clear how the permeability of the bed influences the turbulence properties of the surface flow, and how the surface flow interacts with the subsurface flow in the transition layer (the portion of the subsurface flow that is influenced by the turbulent motion of the surface flow). (Manes et al., 2009) found that friction factors for permeable beds increase with the Reynolds number, above the Reynolds number for which hydraulically rough (i.e. Re-independent) flows would normally be expected, and are higher than friction factors for impermeable beds with identical roughness texture. This has implications for the methods normally used to estimate flow resistance (e.g. grain size analysis or visual assessment with no consideration of permeability). The increased flow resistance is attributed to more efficient energy dissipation caused by exchange of momentum between the surface and subsurface flows. For large values of Re_k (Equation 3.7), turbulent eddies are able to penetrate into the permeable layer. It is therefore possible for two types of turbulence to occur within the porous bed: that generated in the bed at the pore scale, and that generated in the surface flow and then imposed on the bed.

The experiments conducted by Manes et al. (2009) produced counter-intuitive results in the sub-surface layer, with the mean velocity increasing with depth. It should be noted that their experimental set-up did not actually generate a subsurface flow; it was a surface flow over a saturated porous medium.

Dey et al. (2011) investigated turbulence characteristics of rough-bed open-channel flows with seepage (i.e. vertical flow across the surface - subsurface interface), using the double-averaging approach to analyse the results of an experimental study. Both upwards and downwards seepage were considered, with a seepage velocity of around 1% of the mean stream velocity. It was found that seepage normal to the bed modifies the streamwise time-averaged velocity profile. This is consistent with earlier studies. In the surface flow, turbulence intensities were increased by injection (upwards seepage) and decreased by suction (downwards seepage), while Reynolds stresses and shear velocities near the bed were decreased by injection and increased by suction. Flows with suction have higher frictional resistance than the no-seepage case, while those with injection have lower resistance. Like the findings of Manes et al. (2009), this has implications for bed roughness estimation methods.

There appear to be relatively few examples of the DANS equations being used for numerical modelling. Walters and Plew (2008) investigated rough-bed channel flows and vegetated flood-plain flows using a finite-difference model with various closure schemes. Rameshwaran et al. (2011) used a finite-volume DANS model to simulate flows in gravel-bed rivers. The model was created by adding the additional DANS terms to an existing RANS model in the general-purpose CFD package Phoenics (Rameshwaran, pers. comm., 2013). A double-averaged $k-\epsilon$ turbulence model was used, with the standard wall-function boundary condition. The double-averaging approach helped to overcome the impracticality of reproducing the bed topography in sufficient detail to use a RANS-based model.

De Lemos and Silva (2006) modelled turbulent flows in a composite channel (i.e. a channel partly filled with a porous medium) using "macroscopic time-mean Navier-Stokes" equations to investigate the conditions at the interface between the clear fluid and porous regions. Although the authors do not identify their methodology as the DANS equations, their macroscopic approach appears to be identical to the DANS approach. The flow was assumed to be fully turbulent throughout both the clear-fluid and porous layers. A double-averaged $k-\epsilon$ turbulence model was used. Because the flow was assumed to be turbulent throughout the porous layer, it was possible to use the standard wall-function boundary condition at the bottom of the porous layer. At the clear-fluid / porous interface a "stress-jump" condition was used. The physical basis for using this condition is unclear, except perhaps for allowing a less detailed representation of the interface. The "jump" condition contains an empirical constant, which becomes a calibration parameter. The shapes of the modelled velocity and TKE profiles in the interface region were found to be relatively sensitive to the value of this constant de Lemos and Silva (2006).

Chan et al. (2007) used the DANS equations in a numerical model of turbulent free-surface flow over a porous layer (i.e. the flow in the porous layer was generated by shear at the interface). Although the authors state different equations for the two layers, a single-domain approach was used: additional terms that are present in the equations for the porous region vanish when appropriate values of porosity and permeability for the free-surface flow are used. The Launder-Sharma "low-Reynolds-number" $k-\epsilon$ turbulence model (Launder and Sharma,

1974) was used to transition between turbulent flow in the free-surface layer and laminar flow in the porous layer. It appears however that not all of the terms in the Launder-Sharma model were implemented in the model, and given that the Launder-Sharma model was developed for flow over an impermeable boundary, it is unclear whether there is a physical basis for this using this approach for a permeable interface region. Chan et al. (2007) found that propagation of the turbulent flow across the interface created an "interface boundary layer" in the upper part of the porous region. Increasing the Darcy number and the porosity increased the extent to which turbulence penetrated into the porous layer.

3.5 Chapter Summary

Literature relevant to numerical modelling of groundwater - surface water interactions is spread over a range of diverse areas, from hydrology to industrial processes.

The physical mechanisms that control groundwater - surface-water interactions at a river reach or catchment scale are well-researched and well-understood. A number of widely-used analytical solutions exist for predicting the effect of groundwater abstraction on streamflows at a reach scale, using simplifying assumptions.

Relatively recently there has been interest in understanding the finer-scale physical processes that control flow exchanges between river flows and the hyporheic zone (the sediments immediately beneath the streambed). Although detailed modelling studies have been attempted in this area, the numerical coupling between the surface and porous flows is not believed to be robust.

A range of methods exists for incorporating groundwater - surface-water interactions into numerical models. The complexity of these methods varies widely, from simple modifications to boundary conditions to "integrated models" that solve the governing equations for both surface and groundwater flows in a single model framework. Coupled models can be further categorised according to the solution techniques used to handle the numerical coupling. A common feature of all existing methods that are used in practice is that they solve two (or more) separate systems of governing equations in order to handle the different components

of the coupled groundwater - surface water system.

The governing equations used in existing coupled models were not originally developed to handle groundwater - surface water interactions, and include assumptions (such as the no-slip boundary condition in the Shallow Water Equations) that are based on no flow occurring between the surface and subsurface flow domains. This, along with over-simplification of the physical processes and weak numerical coupling methods can lead to mass conservation errors and model stability problems.

Flows over permeable beds have been studied extensively. Many of the examples in the literature relate to mechanical or chemical process applications. Modelling studies in this area of research typically employ a greater level of robustness in the representation of the physics at the surface - subsurface interface, compared to coupled hydrological or hydraulic models.

The double-averaged Navier-Stokes (DANS) Equations can be obtained by averaging the Navier-Stokes Equations in time and space, or by averaging the RANS equations over a representative volume. These equations are applicable to flows in both clear fluids and porous media. Although the DANS equations have been applied in a number of studies as a framework for interpreting experimental results, there are relatively few examples of them being used for numerical modelling. The examples that exist tend to impose restrictive assumptions, such as the flow being turbulent throughout the entire domain.

Chapter 4

Numerical Model Development

4.1 Overview

The double-averaging methodology, which was introduced in Chapter 3, was selected as being a suitable basis for developing a unified modelling approach for groundwater and surface-water flows. This chapter describes the steps taken to develop a numerical model to solve the DANS equations, and the modifications that were necessary to apply this model in situations where there is a transition between laminar porous media flow and turbulent clear-fluid flow. Justification for the choice of the double-averaging approach is discussed in Section 4.8.

Firstly, the methods used to discretise the Reynolds-Averaged Navier-Stokes (RANS) equations for the finite volume method (FVM) are introduced, followed by a description of the solution algorithm used to solve the RANS equations and the turbulence model. This is the foundation of the methodology required to eventually formulate and solve the double-averaged Navier-Stokes (DANS) model, which is discussed later in the chapter.

The numerical model was developed first for the RANS equations. This is a relatively standard exercise in the field of CFD modelling, and the results from this stage of the model development could be verified against published data for turbulent clear-fluid flows (as discussed in Chapter 7).

Following on from the RANS model, the double-averaging methodology was applied to the continuity and momentum equations. This resulted in a volume-

averaged model that could be applied to modelling laminar flows in both the porous media and clear fluid cases.

Finally, the double-averaging methodology was applied to the turbulence model so that turbulent flows in domains containing both porous media and clear-fluid flows could be modelled. Methodology for handling the free-surface boundary was selected and implemented. The turbulence model was then adapted to allow the transition between turbulent flow in the surface layer and laminar flow in the porous layer to be handled. The modified turbulence model is structured in a way that does not require *a priori* specification of the surface - subsurface interface location, or whether the flow regime in either the porous or clear-fluid parts of the domain is laminar or turbulent.

The numerical model has been formulated to represent a two-dimensional vertical cross-section through a surface-water body and the underlying shallow unconfined aquifer. It should be noted that this is a different orientation to two-dimensional SWE models that are used for modelling river and floodplain flows; these are two-dimensional in plan view. The model is currently limited to fully-connected surface-subsurface systems, as it does not handle unsaturated flow.

4.2 Choice of Numerical Method

A number of factors make the FVM the most appropriate method for implementing the DANS equations. Although the FVM is currently more popular in CFD modelling than it is in traditional hydraulic modelling, the recently-released MODFLOW-USG (Panday et al., 2013) uses the finite volume method on an unstructured grid: this may indicate the start of a trend towards the use of the FVM in hydraulics. The DANS methodology used in this thesis has more in common with CFD than with traditional computational hydraulics. There are useful parallels between the governing equations being averaged in space over a representative volume, and the numerical method being volume-based (or area-based in terms of both the governing equations and numerical method, for 2D). Given that one of the shortcomings that has been identified with current coupling methods for integrated groundwater - surface water models is lack of mass conser-

vation at the interface between surface and subsurface flows, a numerical method that guarantees mass conservation at cell faces is likely to be advantageous. The FVM has therefore been used for this work.

The model has been developed for a structured Cartesian mesh, although the numerical methods used generally do not preclude future conversion to a non-Cartesian mesh.

4.3 Mesh Generation

A 2D Cartesian mesh was generated in MATLAB by specifying the overall dimensions of the domain and the default values for Δx and Δy. The mesh was able to be refined in both the x and y directions by specifying the location and number of cells to be refined, and the degree of refinement required. The ability to refine the mesh was considered to be important for modelling flows with an interface between porous and clear-fluid conditions, where there are sharp vertical gradients in hydraulic properties. An example of a model mesh with refinement in both directions is shown in Figure 4.1.

To assist with implementation of boundary conditions "ghost cells" were included outside of the model domain. These cells are included in the mesh shown in Figure 4.1: this is why the mesh extends below $x = 0$ and $y = 0$.

The mesh-generation code calculated the mesh properties required for implementing the finite volume method, including cell areas, cell-face lengths, components of cell-face normal vectors, and the co-ordinates of cell centres, vertices and cell-face centres.

For the DANS model the spatial distributions of hydraulic properties (porosity and permeability) throughout the domain were specified, and interpolation was used to assign values of these properties to each cell in the mesh. It was assumed that the hydraulic properties did not change during a simulation (i.e. sediment transport was not considered), and therefore they could be assigned to cells at the mesh-generation step.

Fluid properties (viscosity and density) were assumed to remain constant throughout the domain, and they were therefore specified as global variables rather than being assigned to mesh cells.

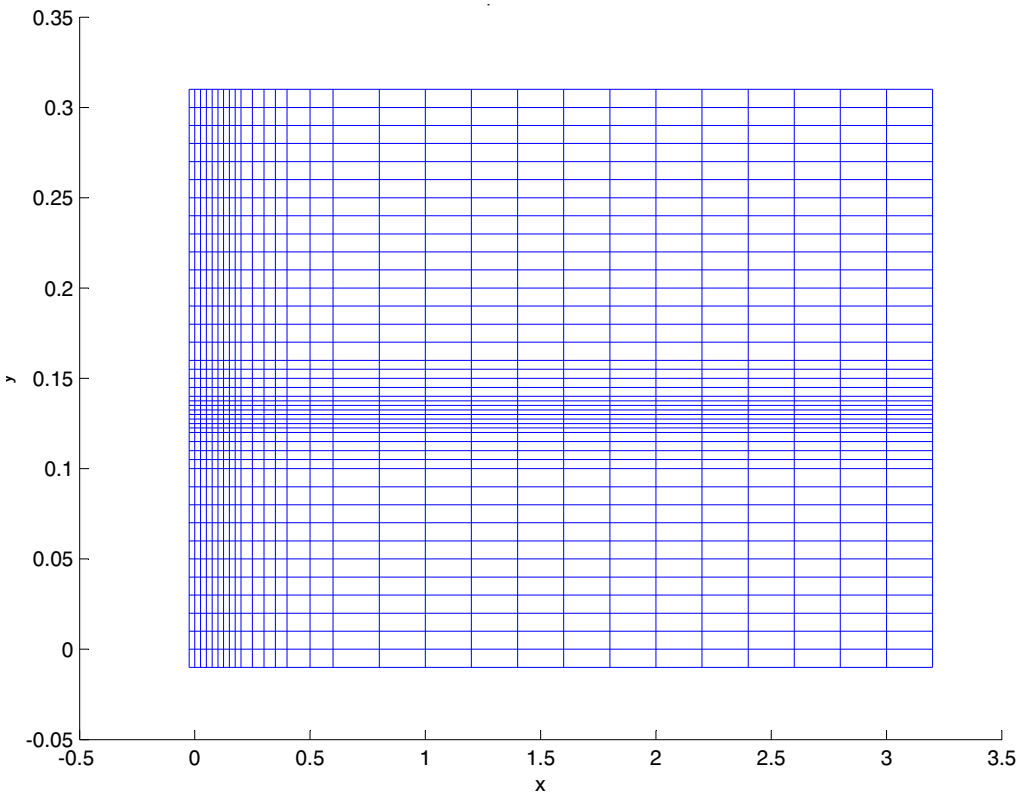

Figure 4.1: Example of Cartesian finite volume mesh with x and y refinement

Some implementations of the FVM use a "staggered mesh" where pressures are solved for at the cell-centres and velocities are solved for at the cell faces: this is effectively the same as using two separate meshes, offset from each other by half a cell in each direction. The key advantage of a staggered mesh is that it removes the need to interpolate cell-face velocity values (as discussed below in Section 4.4). However, staggered meshes can become particularly complicated if complex geometry and / or 3D flows are being considered. To be useful in practice it is likely that the numerical model will need to be extended to 3D, and therefore a non-staggered (or co-located) mesh has been used, where both the pressures and velocities are calculated at cell centres.

An unstructured mesh was not considered necessary for testing the feasibility of the DANS approach for modelling groundwater - surface water interactions

due to the regular geometry of the scenarios that were modelled. For future modelling of natural systems with complex geometry, conversion of the model to an unstructured mesh (such as a Voronoi mesh) could be advantageous.

4.4 Discretisation of the RANS Equations

For the finite volume method the RANS equations are written in terms of the fluxes of mass and momentum. In discrete form, these fluxes are then calculated at cell faces.

In this section examples of the discrete forms of the equation terms are generally given for a single velocity component at a single cell face. Expressions for the other cell faces typically follow by analogy.

4.4.1 Continuity equation

Using the methodology introduced in Section 2.5.2, the finite volume discretisation of the 2D continuity equation (Equation 2.4) starts by integrating the equation over an arbitrary region R:

$$\iint_R \left(\frac{\partial U}{\partial x} + \frac{\partial V}{\partial y} \right) \mathrm{d}R = \iint_R 0 \tag{4.1}$$

where U and V are the horizontal and vertical mean (time-averaged) velocity components, respectively.

Applying Green's theorem allows the double integral in Equation 4.1 to be re-written as a line integral around the perimeter P_R of region R:

$$\oint_{P_R} \mathbf{U} \cdot \mathbf{n} dP_R = 0 \tag{4.2}$$

where $\mathbf{n}$ is an outward-pointing unit vector, and $\mathbf{U}$ is the velocity vector. Equation 4.2 is the net flux of mass (per unit density) out of region R. Replacing the arbitrary region R with a polygonal finite volume cell of area A and sides of length S_c (where the subscript c refers to any one of the cell faces), Equation 4.2 can be

approximated as the sum of the flux through each side of the cell, as follows:

$$\sum_{c} \mathbf{U} \cdot \mathbf{s} \approx \mathbf{0} \tag{4.3}$$

where $\mathbf{s}$ is an outward-pointing vector normal to each cell face, with a magnitude equal to the length of the cell face.

Equation 4.3 can be re-written in terms of mass fluxes per unit density at cell faces, as follows:

$$\frac{\dot{m}_e}{\rho_e} + \frac{\dot{m}_w}{\rho_w} + \frac{\dot{m}_n}{\rho_n} + \frac{\dot{m}_s}{\rho_s} = 0 \tag{4.4}$$

where $\dot{m}$ is the mass flux, and the subscripts refer to the faces of the finite volume cell (east, west, north and south, respectively).

For the flows under consideration it can be assumed that the density is constant throughout the domain (i.e. $\rho_e = \rho_w = \rho_n = \rho_s = \rho$), and therefore the cell-face density values can be replaced with a single value, ρ.

A further assumption is required to relate values integrated over a cell-face to values calculated at the cell-centre. Using the midpoint rule (i.e. the value at the mid-point of the cell-face is assumed to be a good approximation for the value over the entire face) the mass fluxes (per unit density) in Equation 4.4 can expressed in terms of cell-face velocities as follows:

$$\begin{aligned}
\frac{\dot{m}_e}{\rho} &\approx U_e(y_{ne} - y_{se}) - V_e(x_{ne} - x_{se}) \\
\frac{\dot{m}_w}{\rho} &\approx U_w(y_{sw} - y_{nw}) - V_w(x_{sw} - x_{nw}) \\
\frac{\dot{m}_n}{\rho} &\approx V_n(x_{ne} - x_{nw}) - U_n(y_{ne} - y_{nw}) \\
\frac{\dot{m}_s}{\rho} &\approx V_s(x_{sw} - y_{se}) - U_s(y_{sw} - y_{se})
\end{aligned} \tag{4.5}$$

where U_e (for example) is the velocity at the centre of the east cell-face, which is assumed to be representative of the velocity over that entire face. It should be noted that as the discretisations presented in this chapter are for the 2D continuity and momentum equations, the mass-flux ($\dot{m}$) in Equations 4.4 and 4.5

are 2D fluxes $[L^2T^{-1}]$. Therefore Equation 4.5 is dimensionally correct.

4.4.1.1 Simplification with Cartesian mesh

The discretised mass flux expressions simplify considerably if the model mesh is Cartesian i.e. the cell faces can be described in terms of Δx and Δy, rather than the co-ordinates of the cell vertices. For example, the mass-flux for the east cell-face can be re-written as:

$$\begin{aligned} \frac{\dot{m}_e}{\rho} &\approx U_e(y_{ne} - y_{se}) - V_e\cancelto{0}{(x_{ne} - x_{se})} \\ &\approx U_e \Delta y \end{aligned} \tag{4.6}$$

The horizontal and vertical mesh spacing, Δx and Δy, are not necessarily constant throughout the model domain: they can be varied to allow local mesh refinement.

Because the model solves for cell-centre values it is necessary to interpolate to estimate cell-face values. Using linear interpolation between adjacent cell centres to estimate a value for u_e, the horizontal velocity component at the eastern cell-face allows the mass-flux at that face to be re-written in terms of cell centre velocities:

$$\frac{\dot{m}_e}{\rho} \approx \frac{U_E + U_P}{2}(\Delta y) \tag{4.7}$$

where U_P is the cell-centre velocity for central cell in the computational molecules, and U_E is the cell-centre velocity in the cell immediately adjacent to the east.

Writing all the cell-face mass fluxes terms in terms of cell-centre velocities, as in Equation 4.7, allows the continuity equation to be re-written as:

$$\frac{U_E + U_P}{2}(\Delta y) + \frac{U_W + U_P}{2}(-\Delta y) + \frac{V_N + V_P}{2}(\Delta x) + \frac{V_S + V_P}{2}(-\Delta x) = 0 \tag{4.8}$$

which further simplifies to:

$$(U_E - U_W)\Delta y + (V_N - V_S)\Delta x = 0 \tag{4.9}$$

The convention used in Equation 4.9 is that fluxes out of a finite volume cell are positive.

4.4.2 Momentum equations

The finite volume discretisation of the RANS momentum equations (Equation 2.13) starts by integrating the equations over an arbitrary region R, as follows:

$$\iint_R \left(\rho\frac{\partial U_i}{\partial t} + \rho U_j\frac{\partial U_i}{\partial x_j}\right) dR = \iint_R \left(-\frac{\partial P}{\partial x_i} + \frac{\partial}{\partial x_j}\left(\mu\frac{\partial U_i}{\partial x_j} - \rho\overline{u_i' u_i'}\right) + \rho g_i\right) dR \tag{4.10}$$

As with the continuity equation, Green's theorem can then be used, where appropriate, to convert the double integrals to line integrals around the perimeter P_R of region R:

$$\iint_R \rho\frac{\partial U_i}{\partial t} dR + \oint_{P_R} \rho U_j U_i n_j dP_R = -\oint_{P_R} P n_i dP_R + \oint_{P_R}\left(\mu\frac{\partial U_i}{\partial x_j} - \rho\overline{u_i' u_i'}\right) n_j dP_R + \rho g_i R \tag{4.11}$$

Replacing the arbitrary region R with a polygonal finite volume cell of area A and side length S_c, the line integral terms in Equation 4.11 can be approximated as the sum of cell-face fluxes:

$$\overbrace{\rho\frac{\partial U_i}{\partial t}A}^{\substack{\text{unsteady}\\ \text{term}}} + \overbrace{\sum_c \left(\rho U_j U_i n_j S\right)_c}^{\text{convective flux, } F_c^C} = \underbrace{\sum_c \left(P n_i S\right)_c}_{\substack{\text{pressure}\\ \text{gradient}}} + \underbrace{\sum_c \left[\left(\mu\frac{\partial U_i}{\partial x_j} - \rho\overline{u_i' u_i'}\right) niS\right]_c}_{\text{diffusive flux, } F_c^D} + \underbrace{\rho g_i A}_{\substack{\text{gravity}\\ \text{term}}} \tag{4.12}$$

The treatment of each term in Equation 4.12 is addressed below for a quadrilateral finite-volume cell on a Cartesian mesh.

4.4.2.1 Convective terms

The convective flux at the cell faces, using the east cell-face as an example, can be approximated as follows:

$$F_e^C = \int_{S_e} \rho(Un_1 + Vn_2)UdS_e \approx \dot{m}_e U_e \tag{4.13}$$

where n_1 and n_2 are the x and y components respectively of the unit vector normal to the cell-face, S_e is the length of the eastern cell-face and $\dot{m}_e$ is the mass flux for the east face, as defined previously in Section 4.4.1. Writing the convective flux in terms of the mass flux through the cell-face, and assuming that the mass flux is already known from a previous calculation step, linearises the convective term.

A "flux-blending" technique, as recommended by Schäfer (2006), was used for the convective flux terms. This technique combines upwind and central-difference estimates for the cell-face velocities. A blending parameter, β, controls the weighting of the two methods that are used. Applying this technique, the linearised convective flux term becomes:

$$\dot{m}_e U_e \approx \dot{m}_e U_e^{UDS} + \beta(\dot{m}_e U_e^{CDS} - \dot{m}_e U_e^{UDS}) \tag{4.14}$$

where the superscripts ^{UDS} and ^{CDS} refer to upwind and central differencing schemes, respectively. If $\beta = 1$ the convective flux terms are approximated with

a purely upwind difference, and if $\beta = 0$ a purely central difference approximation is used.

The bracketed terms on the right-hand side of Equation 4.14 were treated explicitly - i.e. they become a convective flux source term that is combined with the other source terms on the right-hand-side of the system of equations:

$$b_\beta^u, e = \beta(\dot{m}_e U_e^{CDS} - \dot{m}_e U_e^{UDS}) \tag{4.15}$$

where b_β^u, e is the convective flux contribution to the source terms in the u-momentum equation from the eastern cell-face.

Using upwind differencing, the convective flux (still using the east cell-face as an example) was calculated as follows:

$$\dot{m}_e U_e^{UDS} = \begin{cases} \dot{m}_e U_P & \text{if } \dot{m}_e \geq 0 \\ \dot{m}_e U_E & \text{if } \dot{m}_e < 0 \end{cases} \tag{4.16}$$

In Equation 4.16 a positive value of mass flux means that there is an outflow through the east cell-face, and therefore that the cell-centre value for cell P is the "upwind" value, and *vice versa*.

Using central differencing the convective flux was calculated using linear interpolation of the two cell-centre values adjacent to the cell-face, as was done in the mass flux calculations:

$$\dot{m}_e U_e^{CDS} = \dot{m}_e \left(\frac{U_P + U_E}{2} \right) \tag{4.17}$$

4.4.2.2 Diffusive terms

For an arbitrary cell-face, c, the diffusive flux term can be written as:

$$F_c^D = -\int_{S_c} \mu[2\frac{\partial U}{\partial x} n_1 + (\frac{\partial U}{\partial y} + \frac{\partial V}{\partial x} n_2)] dS_c \tag{4.18}$$

The Reynolds stress terms ($\rho\overline{u_i' u_i'}$) are excluded at this stage from Equation 4.18. These are approximated with the Boussinesq equation (Equation 2.14). Implementation of the Boussinesq equation in the numerical model is discussed

in Section 4.7.

If the dynamic viscosity μ is constant, which is a reasonable assumption for groundwater and surface water flows, then the following result applies from the continuity equation:

$$-\int_{S_c} \mu(\frac{\partial U}{\partial x}n_1 + \frac{\partial V}{\partial x}n_2)dS_c = 0 \tag{4.19}$$

and therefore Equation 4.18 simplifies to:

$$F_c^D = -\int_{S_c} \mu\ (\frac{\partial U}{\partial x}n_1 + \frac{\partial U}{\partial y}n_2)dS_c \tag{4.20}$$

Following the methodology in Schäfer (2006) the diffusive flux at the east cell-face was discretised as follows:

$$F_e^D \approx D_e(U_E - U_P) + N_e(U_{ne} - U_{se}) \tag{4.21}$$

where U_{ne} and U_{se} are the velocities at the north-east and south-east vertices of the finite volume cell, respectively, and D_e and N_e are defined as follows:

$$D_e = \frac{\mu[(y_{ne} - y_{se})^2 + (x_{ne} - x_{se})^2]}{(x_{ne} - x_{se})(y_E - y_P) - (y_{ne} - y_{se})(x_E - x_P)} \tag{4.22}$$

$$N_e = \frac{\mu[(y_{ne} - y_{se})(y_E - y_P) + (x_{ne} - x_{se})(y_E - y_P)]}{(y_{ne} - y_{se})(x_E - x_P) - (x_{ne} - x_{se})(y_E - y_P)} \tag{4.23}$$

The second part of Equation 4.21 is treated as a source term:

$$b_D^{u,e} = N_e(U_{ne} - U_{se}) \tag{4.24}$$

where $b_D^{u,e}$ is the is the diffusive flux contribution to the source terms in the u-momentum equation from the eastern cell-face.

Bi-linear interpolation is necessary if the cell vertex velocities U_{ne} and U_{se} need to be estimated. However, the N_e term (and therefore the source term b_D) vanishes for a Cartesian mesh. The diffusive coefficient D_e also simplifies considerably for a Cartesian mesh. Replacing the cell-centre and vertex co-ordinates in

Equation 4.22, with Δx and Δy gives:

$$D_e = -\mu \frac{\Delta x}{\Delta y} \tag{4.25}$$

4.4.2.3 Pressure terms

The pressure terms in the Navier-Stokes Equations can be expressed as either surface or volume integrals:

$$\int_V \frac{\partial P}{\partial x_i} dV = \int_S P n_i dS \tag{4.26}$$

However, if the mesh is non-Cartesian only the surface integral form is strictly conservative (Schäfer, 2006). To retain the option of future conversion to a non-Cartesian mesh the surface integral form was used. Applying the midpoint rule (i.e. the value at the midpoint of the cell-face is assumed to be representative of the entire face) results in the following discretisation for the surface-integral form of the pressure gradient term in the u-momentum equation:

$$\begin{aligned} \int_S P n_1 dS &\approx \sum_c (P n_1) S_c \\ &= P_e(y_{ne} - y_{se}) - P_w(y_{nw} - y_{sw}) + b_p^u \end{aligned} \tag{4.27}$$

where b_p^u is treated as a source term:

$$b_p^u = P_s(y_{se} - y_{sw}) - P_n(y_{ne} - y_{nw}) \tag{4.28}$$

The pressure gradient term for the v-momentum equation was discretised as follows:

$$P_n(x_{ne} - x_{nw}) - P_s(x_{se} - x_{sw}) + b_p^v \tag{4.29}$$

where the source term b_p^v is:

$$b_p^v = P_w(x_{nw} - x_{sw}) - P_e(x_{ne} - x_{se}) \tag{4.30}$$

In Equations 4.27 and 4.29, $\sum_c$ is the sum over all cell faces. Linear interpolation of the cell-centre pressures was used to estimate the cell-face pressure values, for example:

$$P_e = \frac{P_E + P_P}{2} \tag{4.31}$$

4.4.2.4 Local acceleration term

The local acceleration terms were discretised using the implicit Euler method, as follows:

$$\begin{aligned} \rho\frac{\partial(U_i)}{\partial t}A &\approx \frac{(\rho U_i)_P^{n+1} - (\rho U_i)_P^k}{\Delta t_n}A \\ &= a_t^{U_i}U_{iP}^{n+1} - b_t^{U_i} \end{aligned} \tag{4.32}$$

where A is the area of the finite-volume cell, $a_t^{U_i}$ is a coefficient defined as:

$$a_t^{U_i} = \frac{\rho A}{\Delta t_n} \tag{4.33}$$

and $b_t^{U_i}$ is the local acceleration's contribution to the source terms, defined as:

$$b_t^{U_i} = \frac{\rho A}{\Delta t_n}U_{iP}^n \tag{4.34}$$

The superscripts indicate the time-level: U_{iP}^{n+1} is the unknown "new" value to be calculated for the i^{th} velocity component at cell P, and U_{iP}^n is the known "old" value. The density, ρ, is assumed to be constant.

4.4.2.5 Gravity term

The pressure term in the RANS equations can be redefined as an effective pressure, i.e. the deviation from hydrostatic pressure, as follows:

$$P_e = P + \rho g_i z \tag{4.35}$$

where z is the vertical distance from a datum. Redefining the pressure in this way results in the gravity term not needing to be discretised. This approach is consistent with the definition of piezometric head that is used in groundwater hydraulics, i.e. the effective pressure is equivalent to the pressure head.

Strictly speaking, a modified dynamic boundary condition should be used at the free-surface when transforming the pressure in this way. However, the modified rigid-lid assumption that was used to handle the free-surface (as discussed in Section 4.6.2.2) makes this unnecessary.

To avoid confusion with the e subscript for the east cell-face, the subscript is dropped from the effective pressure P_e, and from here onwards all pressure terms can be assumed to be effective pressures.

4.4.3 System of equations

Replacing all terms of the u-momentum equation with their discretised form gives the following:

$$\begin{aligned} a_t^U U_P^{n+1} - b_t^U + \sum_c [\dot{m}_c U_c^{UDS} + b_\beta^{U,c}] - \sum_c [D_c(U_c - U_p) + b_D^{U,c}] \\ + [P_e(y_{ne} - y_{se}) - P_w(y_{nw} - y_{sw}) + b_p^U] = 0 \end{aligned} \tag{4.36}$$

Re-arranging Equation 4.36 and grouping all the b terms into a single source term, b^U, gives:

$$a_p^U U_P = \sum_c a_c^U U_c + b^U - P_e(y_{ne} - y_{se}) + P_w(y_{nw} - y_{sw}) \tag{4.37}$$

where the coefficients in the summation term are defined as:

$$\begin{aligned} a_E^U &= -D_e - min\{\dot{m}_e, 0\} \\ a_W^U &= -D_w - min\{\dot{m}_w, 0\} \\ a_N^U &= -D_n - min\{\dot{m}_n, 0\} \\ a_S^U &= -D_s - min\{\dot{m}_s, 0\} \end{aligned} \tag{4.38}$$

.
and the central coefficient a_P^U is defined as:

$$a_P^U = a_E^U + a_W^U + a_N^U + a_S^U + a_t^U + \dot{m}_e + \dot{m}_w + \dot{m}_n + \dot{m}_s \tag{4.39}$$

Upwind differencing (Equation 4.16) was implemented via the *min* operator in Equation 4.38. This ensures that the neighbouring cell-centre velocity only appears in the discretised convective flux if the mass-flux across the corresponding cell-face into cell P is negative, i.e. an inflow into cell P.

The source terms in Equation 4.37 are defined as:

$$b^U = b_D^U - b_\beta^U - b_p^U - b_t^U \tag{4.40}$$

On a Cartesian grid b_D^u and b_p^u are equal to zero, and the only remaining terms in b^U are b_β^U and b_t^U.

The discretised form of the v-momentum equation is:

$$a_p^V V_P = \sum_c a_c^V V_c + b^V - P_n(x_{ne} - x_{nw}) + P_s(x_{se} - y_{sw}) \tag{4.41}$$

The definitions of the coefficients and source terms in Equation 4.41 follow by analogy the definitions for the u-momentum equation (Equations 4.38 and 4.40)

The systems of linear equations expressed by Equations 4.37 and 4.41 can be represented as a matrix equation for each velocity component, as follows:

$$\mathbf{AU} = \mathbf{b} \tag{4.42}$$

where $\mathbf{A}$ is the coefficient matrix, $\mathbf{U}$ is a vector of cell-centre velocities, and $\mathbf{b}$

is a vector of source terms. The pressure gradient is incorporated into $\mathbf{b}$. For a computational domain of $N \times M$ cells, the coefficient matrix A is defined as:

$$\mathbf{A} = \begin{bmatrix}
a_P^{1,1} & -a_N^{1,1} & \cdots & 0 & \cdots & -a_E & \cdots & 0 & \cdots & \\
-a_S^{1,2} & \ddots & \ddots & & & & \ddots & & & \vdots \\
\vdots & \ddots & \ddots & \ddots & & & & \ddots & & 0 \\
0 & & \ddots & \ddots & \ddots & & & & \ddots & \vdots \\
\vdots & & & \ddots & \ddots & \ddots & & & & -a_E^{M-1,M} \\
-a_W^{2,1} & & & & \ddots & \ddots & \ddots & & & \vdots \\
\vdots & \ddots & & & & \ddots & \ddots & \ddots & & 0 \\
0 & & \ddots & & & & \ddots & \ddots & \ddots & \vdots \\
\vdots & & & \ddots & & & & \ddots & \ddots & -a_N^{N,M-1} \\
 & \cdots & 0 & \cdots & -a_W^{N,M} & \cdots & 0 & \cdots & -a_S^{N,M} & a_P^{N,M}
\end{bmatrix} \tag{4.43}$$

In Equation 4.43 the superscripts on the matrix entries are with respect to cell P, for example $a_S^{1,2}$ is the south coefficient for cell $[1, 2]$. The central coefficients all lie on the main diagonal and the north and south coefficients all lie on diagonals $+1$ and -1 respectively. The east and west coefficients are on diagonals offset by $+M$ and $-M$ respectively from the main diagonal. All other terms in the $\mathbf{A}$ matrix are zero, and it was therefore able to be treated as a sparse matrix in MATLAB, which improved the computational efficiency of the model.

4.5 Solution Methods

Solution of the incompressible Navier-Stokes Equations is complicated by the coupling between pressure and velocity. Pressure gradients appear in the momentum equations, but not in the continuity equation. For compressible flows it is possible to solve the continuity equation for the density, and hence the pressure via an equation of state. This option is not available for incompressible flows, however.

The methods available for dealing with pressure-velocity coupling in incompressible flows are *pressure-correction methods* and *artificial compressibility meth-*

ods. In artificial compressibility methods the incompressible flow equations are able to solved in a similar manner to the compressible flow equations by introducing a time derivative of pressure ($\frac{\partial p}{\partial t}$) and an artificial compressibility parameter into the continuity equation, thereby ensuring that pressure and velocity are present in both the continuity and momentum equations. The artificial compressibility parameter has no physical basis and therefore becomes a calibration parameter in the model.

Pressure correction methods use an iterative approach, in which preliminary velocity components are calculated from the linearised momentum equations, using an estimated pressure field. A pressure correction equation is then solved to give correction terms for the pressure and velocities, with the aim of satisfying the continuity equation. This procedure is iterated until convergence is achieved.

Schäfer (2006) notes that although systematic comparisons of pressure correction and artificial compressibility methods are missing in the literature, pressure correction is believed to be more computationally efficient. Artificial compressibility is not commonly used in practice (Meiburg, *pers. comm*). Therefore, a pressure correction method has been used in the development of the DANS model.

4.6 The SIMPLE Algorithm

The pressure-correction method used in this work is the SIMPLE algorithm (Patankar and Spalding, 1972), which stands for Semi-Implicit Method for Pressure-Linked Equations. Although this method was originally proposed for steady-state problems, it can be adapted for use with unsteady flows. The derivation shown here is for a Cartesian mesh.

The momentum and continuity equations are first re-written in terms of the current iteration, k, and the future iteration, $k+1$:

$$a_P^{U,k} U_P^{k+1} - \sum_c a_c^{U,k} U_c^{k+1} + \frac{\Delta y}{2}\left(P_E^{k+1} - P_W^{k+1}\right) = b^{U,k} \tag{4.44}$$

$$a_P^{V,k} V_P^{k+1} - \sum_c a_c^{V,k} V_c^{k+1} + \frac{\Delta x}{2}\left(P_E^{k+1} - P_W^{k+1}\right) = b^{V,k} \tag{4.45}$$

$$\left(U_E^{k+1} - U_W^{k+1}\right)\Delta y + \left(V_N^{k+1} - V_S^{k+1}\right)\Delta x = 0 \tag{4.46}$$

The coefficients and source terms are calculated using known values from iteration k. The values of U, V and P at iteration $k+1$ are to be solved for. At the beginning of each new iteration the coefficients and source terms are re-calculated with the updated values of U, V and P. Although the iterations k and $k+1$ are referred to as "current" and "future" iterations, they are not related to time-stepping. Iterations occur within a time-step.

Calculation of P^{k+1} is decoupled from the solution of the momentum equations by introducing a provisional pressure field, P^*. This is typically the pressure value from the end of the previous iteration, or a known / estimated value for the first iteration of a simulation. If $P^* = 0$ is used, the solution algorithm is known as a fractional-step or projection method (Schäfer, 2006). With provisional pressure values in place, the momentum equations are then solved for provisional velocity values U^* and V^*:

$$a_P^{U,k} U_P^* - \sum_c a_c^{U,k} U_c^* = b^{U,k} - \frac{\Delta y}{2}\left(P_E^* - P_W^*\right) \tag{4.47}$$

$$a_P^{V,k} V_P^* - \sum_c a_c^{V,k} V_c^* = b^{V,k} - \frac{\Delta x}{2}\left(P_N^* - P_S^*\right) \tag{4.48}$$

Because the provisional velocity values U^* and V^* are calculated based on provisional pressure values (P^*), the continuity equation (equation 4.46) is not necessarily satisfied by the solution of Equations 4.47 and 4.48. Re-writing equation 4.46 in terms of U^* and V^* therefore yields a mass-balance error term, b_m:

$$\left(U_E^* - U_W^*\right)\Delta y + \left(V_N^* - V_S^*\right)\Delta x = b_m \tag{4.49}$$

To move from the provisional values to the final ones, a set of velocity correction variables is introduced. These are the differences between the provisional values (U^*, etc.) and the final values for the iteration (U^{k+1}, etc.):

$$U' = U^{k+1} - U^* \tag{4.50}$$

$$V' = V^{k+1} - V^* \tag{4.51}$$

$$P' = P^{k+1} - P^* \tag{4.52}$$

Subtracting the equations written in terms of provisional velocities from their counterparts written in terms of the values at the end of the iteration (e.g. Equation 4.44 minus Equation 4.47 for the u-momentum equation) gives a new set of equations in terms of the velocity corrections:

$$a_P^{U,k} U'_P - \sum_c a_c^{U,k} U'_c = -\frac{\Delta y}{2} \left(P'_E - P'_W\right) \tag{4.53}$$

$$a_P^{V,k} V'_P - \sum_c a_c^{V,k} V'_c = -\frac{\Delta x}{2} \left(P'_N - P'_S\right) \tag{4.54}$$

$$\left(U'_E - U'_W\right) \Delta y + \left(V'_N - V'_S\right) \Delta x = b_m \tag{4.55}$$

The key assumption of the SIMPLE algorithm is to then neglect the velocity corrections from the cells adjacent to cell P in Equations 4.53 and 4.54, i.e.:

$$\sum_c a_c^{U,k} U'_c \approx 0 \tag{4.56}$$

$$\sum_c a_c^{V,k} V'_c \approx 0 \tag{4.57}$$

Having neglected the summation terms for the surrounding cells, Equations 4.53 and 4.54 can then be solved for the velocity corrections:

$$U'_P = -\frac{\Delta y}{2a_P^{U,k}}\left(P'_E - P'_W\right) \tag{4.58}$$

$$V'_P = -\frac{\Delta x}{2a_P^{V,k}}\left(P'_N - P'_S\right) \tag{4.59}$$

Substituting the velocity corrections in the above form into a mass-balance expression gives a continuity equation in terms of the pressure-correction variables:

$$\begin{aligned}\left[-\frac{\Delta y}{2a_{P,E}^{U,k}}\left(P'_{EE} - P'_P\right) + \frac{\Delta y}{2a_{P,W}^{U,k}}\left(P'_P - P'_{WW}\right)\right]\Delta y \\ + \left[-\frac{\Delta x}{2a_{P,N}^{V,k}}\left(P'_{NN} - P'_P\right) + \frac{\Delta x}{2a_{P,S}^{V,k}}\left(P'_P - P'_{SS}\right)\right]\Delta x = b_m\end{aligned} \tag{4.60}$$

where, for example, $a_{P,E}^{u,k}$ refers to the central coefficient for the control volume centred around cell E in the computational molecule for the u-momentum equation. The subscripts NN, SS, EE and WW refer to cells that are not immediately adjacent to cell P, for example cell EE is the cell to the east of cell E. Equation 4.60 can be re-arranged to give a system of linear equations for the pressure correction P', as follows:

$$a_P^{P,k}P'_P = a_{EE}^{P,k}P'_E E + a_{WW}^{P,k}P'_W W + a_{NN}^{P,k}P'_N N + a_{SS}^{P,k}P'_S S + b_m \tag{4.61}$$

where the coefficients are defined as:

$$a_{EE}^{P,k} = \frac{\Delta y^2}{2a_{P,E}^{U,k}} \quad , \quad a_{WW}^{P,k} = \frac{\Delta y^2}{2a_{P,W}^{U,k}} \quad , \quad a_{NN}^{P,k} = \frac{\Delta x^2}{2a_{P,N}^{V,k}} \quad , \quad a_{SS}^{P,k} = \frac{\Delta x^2}{2a_{P,S}^{V,k}} \tag{4.62}$$

and

$$a_P^{P,k} = a_{EE}^{P,k} + a_{WW}^{P,k} + a_{NN}^{P,k} + a_{SS}^{P,k} \tag{4.63}$$

In Equation 4.61 the size of the computational molecule has effectively dou-

bled compared to the discretised system of equations for the momentum equations, because it refers to cells EE, WW, NN and SS, which are $2\Delta x$ and $2\Delta y$ respectively from cell P (the centre of the computational molecule). This can result in stability problems or oscillatory solutions, and difficulties with defining coefficients near the boundaries of the domain. To avoid these problems a "selective interpolation" method, as developed by Rhie and Chow (1983), was implemented.

The basis of the selective interpolation method is to calculate velocity corrections at the cell faces rather than using cell-centre values. Solving a semi-discretised form of horizontal momentum equation (Equation 4.36, with the continuous form of the pressure gradient), for example, gives:

$$U_P = \frac{\sum_c a_c^U U_c + b^U}{a_p^U} - \frac{\Delta x \Delta y}{a_P^u} \left(\frac{\partial p}{\partial x} \right)_P \tag{4.64}$$

The cell-face velocity is then obtained by linearly interpolating all terms on the right-hand side of Equation 4.64 apart from the pressure gradient, which is discretised using a central difference. For the east cell-face of cell P, this is expressed as:

$$U_e = \overline{\left(\frac{\sum_c a_c^U U_c + b^U}{a_p^U} \right)}_e - \overline{\left(\frac{\Delta y}{a_P^u} \right)}_e (P_E - P_P) \tag{4.65}$$

where the overbar indicates linear interpolation between cell centres, which for uniform cell spacing is as follows:

$$\overline{\left(\frac{\Delta y}{a_P^{U,k}} \right)}_e = 0.5 \left(\frac{\Delta y}{a_P^U} \right)_E + 0.5 \left(\frac{\Delta y}{a_P^U} \right)_P \tag{4.66}$$

The mass-balance error term, b_m, is calculated by putting the provisional values of pressure and cell-centre velocity (i.e. P^* and U^* respectively) into Equation 4.65 and the equivalent equations for the other cell-faces, and constructing a conservation of mass expression from all of the cell-face velocities.

Following the same methodology as for the SIMPLE method without selective interpolation (i.e. splitting the velocity and pressure into provisional and

correction components, and neglecting the summed term in Equation 4.65), the horizontal velocity correction at the east cell-face becomes:

$$U'_e = -\overline{\left(\frac{\Delta y}{a_P^{U,k}}\right)}_e (P'_E - P'_P) \tag{4.67}$$

Substituting the interpolated cell-face velocity corrections into a mass-balance expression (as for Equation 4.60) results in a continuity equation that refers only to the immediate neighbour cells (E, W, N & S):

$$\left[-\overline{\left(\frac{\Delta y}{2a_{P,E}^{U,k}}\right)}_e (P'_E - P'_P) + \overline{\left(\frac{\Delta y}{2a_{P,W}^{U,k}}\right)}_w (P'_P - P'_W)\right]\Delta y$$
$$+\left[-\overline{\left(\frac{\Delta x}{2a_{P,N}^{V,k}}\right)}_n (P'_N - P'_P) + \overline{\left(\frac{\Delta x}{2a_{P,S}^{V,k}}\right)}_w (P'_P - P'_S)\right]\Delta x = b_m \tag{4.68}$$

Re-arranging Equation 4.68 into a system of equations for the pressure correction, P', gives:

$$a_P^{P,k} P'_P = a_E^{P,k} P'_E + a_W^{P,k} P'_W + a_N^{P,k} P'_N + a_S^{P,k} P'_S + b_m \tag{4.69}$$

where the coefficients are defined as:

$$a_E^{P,k} = \overline{\left(\frac{\Delta y^2}{a_P^{U,k}}\right)}_e \quad , \quad a_W^{P,k} = \overline{\left(\frac{\Delta y^2}{a_P^{U,k}}\right)}_w \quad , \quad a_N^{P,k} = \overline{\left(\frac{\Delta x^2}{a_P^{V,k}}\right)}_n \quad , \quad a_S^{p,k} = \overline{\left(\frac{\Delta x^2}{a_P^{V,k}}\right)}_s \tag{4.70}$$

and:

$$a_P^{p,k} = a_E^{p,k} + a_W^{p,k} + a_N^{p,k} + a_S^{p,k} \tag{4.71}$$

4.6.1 Under-relaxation

To improve the convergence behaviour and stability of the numerical model, under-relaxation (Patankar, 1980) was used. For each transport equation (U, V and turbulence statistics) the value at iteration $k+1$ is calculated as a linear

combination with the value from iteration k.

Using the u-momentum equation as an example, the under-relaxation method is implemented by adjusting the discretised system of equations (Equation 4.44) as follows:

$$U_P^{k+1} = \alpha_U \frac{\left(\sum_c a_c^{U,k} U_c^{k+1} - \frac{\Delta y}{2} \left(P_E^{k+1} - P_W^{k+1} \right) + b^{U,k} \right)}{a_P^{U,k}} + (1 - \alpha_U) U_P^k \quad (4.72)$$

where $0 < \alpha_U \leq 1$ is the under-relaxation parameter. Equation 4.72 is then re-arranged back into a the same form as Equation 4.44, with modified coefficients $a_P'^U$ and modified source terms (including the pressure gradient) $b_P'^U$:

$$\underbrace{\frac{a_P^{U,k}}{\alpha_U}}_{a_P'^{U,k}} U_P^{k+1} = \sum_c a_c^{U,k} U_c^{k+1} - \underbrace{\frac{\Delta y}{2} \left(P_E^{k+1} - P_W^{k+1} \right) + b^{U,k} + (1 - \alpha_U) \frac{a_P^{U,k}}{\alpha_U} U_P^k}_{b'^{U,k}} \quad (4.73)$$

Under-relaxation was also applied to the pressure-correction equation. In this case, rather than modifying the coefficients and source terms the under-relaxation parameter determines the proportion of the calculated pressure-correction P' that is actually applied to the provisional pressure value P^*, i.e.:

$$P^{k+1} = P^* + \alpha_P P' \quad (4.74)$$

where $0 < \alpha_P \leq 1$ is the under-relaxation parameter for pressure-correction.

The optimum values of α_U and α_U are mutually dependent, and generally $\alpha_P \approx 1 - \alpha_U$ (Schäfer, 2006). Some trial-and-error is required to select appropriate values for α_U and α_U. The values that are chosen do not effect the final model results, however selecting a value of α_U that is too high may result in the solution not converging. Selecting a value that is too low will cause the model to converge more slowly than it would do for the optimum value.

4.6.2 Boundary and initial conditions

4.6.2.1 Wall boundary

A channel with an impermeable bed has a no-slip, no-flow boundary condition at the bottom boundary. These conditions were implemented at the bottom boundary in the RANS numerical model. The mass flux through the south cell-face of the bottom row of cells (i.e. the bottom boundary) was set to zero, and the calculations of the convective and diffusive fluxes were adjusted at the boundary to ensure that the boundary condition was enforced.

The DANS model also contains a no-slip, no-flow boundary at the bottom of the domain. This allows it to revert to the RANS configuration if no porous layer is present. If a porous layer is present the no-flow boundary represents an impermeable bedrock surface at the base of the aquifer.

If the DANS model domain contains an interface between porous and clear-fluid regions, representing a permeable stream-bed, there will be a slip velocity at the interface, and there may be flow normal to the bed. In this case the interface does not act as a wall boundary, although if the porous layer's permeability is low it may behave somewhat like a wall. Flow at the stream-bed is controlled by the hydraulic properties of the porous layer and the flow regimes in both the clear-fluid and porous layers, rather than by specifying a boundary condition.

4.6.2.2 Free surface

Several different approaches exist for handling a free-surface boundary. For applications where highly accurate calculations of the free-surface geometry are important, there are methods that track the free-surface via an additional transport equation. As these methods identify the location of the free-surface by calculating the volume of fluid in a finite-volume cell, relative to the cell's total volume, they are referred to as volume-of-fluid (VOF) methods. These methods can be extended to include the airflow over the free-surface (Ingham and Ma, 2005). Some methods adjust the mesh during a simulation to match the calculated position of the free-surface.

Detailed computation of the free-surface geometry was not considered necessary for the current work, and therefore an approach based around the assumption

of a rigid lid was used. The simplest implementation of this approach uses a fixed mesh and assumes an impermeable rigid lid with a slip velocity (Leschziner and Rodi, 1979). A symmetry boundary condition is used at the lid. In a post-processing step after velocities and pressures have been calculated for each time-step (or at the end of the model run for a steady-state simulation) the pressure at the lid is used to calculate an adjustment to the height of the free-surface above or below the lid, as follows:

$$\Delta h = \frac{P_s - P_a}{\rho g} \tag{4.75}$$

where P_s is the modelled pressure in the surface cell and P_a is the atmospheric pressure (typically taken as zero). A negative value for Δh indicates that the actual location of the free-surface is below the rigid lid, and *vice versa*. The Leschziner and Rodi rigid-lid approach does not include any adjustment to velocities or mass-fluxes at the free-surface. This may result in unacceptably high errors if the adjustments to the free-surface elevation are large enough.

To improve the accuracy of the free-surface calculations without the need to use a VOF approach, a rigid-lid method with mass-flux corrections, based on Spalding (1985), was used in the current work. In this method a correction term is calculated based on the modelled pressure at the free surface:

$$\zeta = 1 + \frac{P_s}{\rho g h_c} \tag{4.76}$$

where ζ is the free-surface correction factor and h_c is the thickness of the finite volume cell at the surface.

A number of authors refer to the correction term ζ as a "porosity", as it represents the proportion of the cell's volume that is actually full of fluid for a given free-surface elevation (note that this proportion can be greater than 1.0 if the calculated free-surface is higher than the top of the cell). The use of the word "porosity" in this context has been avoided in this work, however, due to potential confusion with the physical property of the porous matrix.

The free-surface correction factor ζ was used to adjust side-lengths of the row of cells along the top of the model domain at the end of each iteration loop. The mass-fluxes were then re-calculated and the momentum equations were re-solved

before advancing to the next time-step.

4.6.2.3 Inflow and outflow boundaries

Appropriate velocity and pressure boundary conditions were set, depending on the scenario being modelled.

The specific boundary conditions that were used for modelling the experimental gaining and losing stream scenarios (as described in Chapter 6) are described in Chapter 7.

4.6.2.4 Initial conditions

Model runs were started with a uniform initial velocity throughout the domain.

The initial effective pressure was zero throughout the domain, i.e. there was initially no deviation from hydrostatic pressure.

4.7 Turbulence Models

Both the $k-\epsilon$ and Kolmogorov-Prandtl single-equation models (as introduced in Chapter 2) were built into the numerical model. The $k-\epsilon$ model was used as a benchmark case for clear-fluid flows as it is the most commonly-used turbulence model in commercial CFD packages and published results are available for verifying simple scenarios. The single-equation model, which was used in the DANS model, was compared against the $k-\epsilon$ model for the clear-fluid case.

The k and ϵ transport equations were introduced in Chapter 2. As the general form of these equations is similar to the RANS momentum equations, their finite volume discretisation is also similar. Using the east cell-face as an example, the linear system coefficients for the k and ϵ equations are defined as:

$$a_E^k = -D_e^k - min\{\dot{m}_e, 0\} \quad (4.77)$$

$$a_E^\epsilon = -D_e^\epsilon - min\{\dot{m}_e, 0\} \quad (4.78)$$

where the diffusive flux coefficients D_e^k and D_e^ϵ are defined as:

$$D_e^k = -\left(\mu + \frac{\mu_t}{\sigma_k}\right)\frac{\Delta x}{\Delta y} \tag{4.79}$$

$$D_e^\epsilon = -\left(\mu + \frac{\mu_t}{\sigma_\epsilon}\right)\frac{\Delta x}{\Delta y} \tag{4.80}$$

To implement the Boussinesq equation (Equation 2.14) for the Reynolds stresses, the viscosity μ in the momentum equations is replaced by $(\mu + \mu_t)$.

The Boussinesq equation also contains the term $\frac{2}{3}\rho\delta_{ij}k$. To avoid the derivative of the turbulent kinetic energy k appearing in the momentum equations, the effective pressure term in the momentum equation was further modified to:

$$\tilde{P} = P + \frac{2}{3}k \tag{4.81}$$

The effective pressure was calculated from Equation 4.81 at the end of each iteration after the transport equation for k had been solved.

Under-relaxation was applied to the turbulence transport equations. This was implemented in the same way as for the momentum equations (Equation 4.73).

The calculation of the turbulent viscosity was also under-relaxed, as follows:

$$\mu_t^{k+1} = \alpha_{\mu_t} C_\mu \frac{k^2}{\epsilon} + (1 - \alpha_{\mu_t})\mu_t^k \tag{4.82}$$

The under-relaxation coefficients α_k, α_ϵ (where applicable), and α_{μ_t} were set to the same value as α_u.

4.7.1 Discretisation of source terms

The source terms for the k equation and ϵ equation (where applicable) were split, so that there is a contribution to the main diagonal of the coefficient matrix for each equation, thereby increasing the diagonal dominance of the matrix. This approach is recommended by Schäfer (2006) to improve the convergence behaviour

of the model. The source terms were split as follows:

$$-\int_V (\rho\epsilon - G)\, dV \approx \underbrace{-\rho\delta V \frac{\epsilon_P^*}{k_P^*}}_{a_k} k_P + \underbrace{G_P \delta V}_{b_k} \tag{4.83}$$

$$-\int_V \left(C_{\epsilon 2}\rho\frac{\epsilon^2}{k} - C_{\epsilon 1} G \frac{\epsilon}{k}\right) dV \approx \underbrace{-C_{\epsilon 2}\rho\delta V \frac{\epsilon_P^*}{k_P^*}}_{a_\epsilon} \epsilon_P + \underbrace{C_{\epsilon 1} G_P \delta V \frac{\epsilon_P^*}{k_P^*}}_{b_\epsilon} \tag{4.84}$$

where a_k and a_ϵ are the contributions to the central coefficients a_P^k and a_P^ϵ in the respective system matrices, and b_k and b_ϵ are the contributions to the right-hand-side of the systems of equations. G_P is the rate of production of TKE at cell P.

In Equations 4.83 and 4.84 the values with a * superscript are treated explicitly, i.e. the "old" values from the previous iterations are used. In Equation 4.83 the dissipation term was multiplied and divided by k to allow it to be incorporated into the system matrix as a contribution to the central coefficient.

4.7.2 Solution of the turbulence transport equations

Similar to the momentum equations, the transport equations for k and ϵ were formulated as matrix equations:

$$\mathbf{A}_k k = \mathbf{b}_k \tag{4.85}$$

$$\mathbf{A}_\epsilon \epsilon = \mathbf{b}_\epsilon \tag{4.86}$$

where $\mathbf{A}_k$ and $\mathbf{b}_k$, and $\mathbf{A}_\epsilon$ and $\mathbf{b}_\epsilon$ are the coefficient matrices and source term vectors for the k and ϵ equations respectively.

The coefficient matrices $\mathbf{A}_k$ and $\mathbf{A}_\epsilon$ were assembled in the same way as the coefficient matrices for the momentum equations (Equation 4.43). The source term vectors $\mathbf{b}_k$ and $\mathbf{b}_\epsilon$ were made up of the source terms defined above in Equations 4.83 and 4.84, and contributions from the unsteady terms (analogous to

Equation 4.34).

In the $k-\epsilon$ model the two transport equations are coupled, as k is present in the source terms for the ϵ equation, and *vice versa*. However, as these values were treated explicitly the two equations could be solved independently without any modification (i.e. there was no need for an equivalent of the SIMPLE algorithm).

4.7.3 Impermeable-wall boundary conditions for the turbulence model

At solid boundaries where a no-slip, no-mass-flux boundary condition is implemented for the momentum equation, the assumptions of the turbulence model break down due to the high velocity gradients near the boundary and the presence of a viscous sub-layer. These issues can be resolved either by making the model grid sufficiently fine to resolve the viscous sub-layer, and adapting the turbulence model equations to handle lower Reynolds numbers, or by using a wall function to model the conditions at the wall in terms of the dependent variables outside of the viscous sub-layer. The former approach is computationally demanding, particularly for larger Reynolds numbers, as the thickness of the sub-layer is inversely proportional to the square root of the Reynolds number (Schäfer, 2006), which necessitates a very fine grid near the boundary if the layer is to resolved. For this reason the wall function approach is more commonly used.

For the coupled surface-subsurface flow case, where flow in the porous layer may or may not be turbulent and velocities at the bottom boundary of the computational domain may be negligible, the assumptions used in the standard wall function approach are unlikely to be valid. A modified damping-function approach was therefore developed and used in the DANS model. The modifications that were made are discussed in Section 4.8.4.

4.7.3.1 Wall function approach

The physical basis of the wall function typically used with a k-ϵ turbulence model is that outside of the viscous sub-layer there is a region in which the velocity increases logarithmically with distance from the wall. This can be stated as

follows:

$$u^+ = \frac{1}{\kappa} \ln y^+ + B \tag{4.87}$$

where u^+ is a normalised velocity tangential to the wall, y^+ is a normalised distance perpendicular to the wall, κ is the von Kármán constant ($\kappa = 0.41$) and B is a roughness parameter. For smooth walls $B = 5.0$, and for rough walls B can be adjusted using an equivalent sand-grain roughness, as used in the definition of roughness for pipe flow (Wilcox, 1993). The normalised velocity is defined as:

$$u^+ = \frac{U_t}{u_\tau} \tag{4.88}$$

where U_t is the mean velocity tangential to the wall and u_τ is the wall shear stress velocity, defined as:

$$u_\tau = \sqrt{\frac{\tau_w}{\rho}} \tag{4.89}$$

The normalised distance from the wall, y^+ is defined as:

$$y^+ = \frac{\rho u_\tau y}{\mu} \tag{4.90}$$

In Equation 4.89 τ_w is the shear stress at the solid boundary.

The logarithmic wall law is valid in the range $30 < y^+ < 100$ (Rodi, 1980), and it is necessary to ensure that the mesh is set up in such a way that this condition is valid in the cells closest to the boundary. Assuming that in this region the Reynolds stresses are constant and the production and dissipation of TKE are in equilibrium, the following expression for u_τ can be derived:

$$u_\tau = C_\mu^{\frac{1}{4}} \sqrt{k} \tag{4.91}$$

Substituting Equation 4.87 into an expression for the wall shear stress gives:

$$\tau_w = \frac{U_t \kappa \rho C_\mu^{\frac{1}{4}} \sqrt{k}}{\ln y^+ + \kappa B} \tag{4.92}$$

If Equation 4.92 is multiplied and divided by δ_P (the distance from the wall

boundary to the centre of cell adjacent to the boundary) it can be re-arranged to look like the general expression for wall shear stress (i.e. $\tau_w = \mu \frac{\partial U_t}{\partial x_i} n_i$), yielding a quantity μ_w that is analogous to a viscosity and can be used in place of μ_t in cells adjacent to solid boundaries:

$$\tau_w = \frac{U_t}{\delta_P} \underbrace{\frac{\kappa C_\mu^{\frac{1}{4}} \sqrt{k_P} \rho \delta_P}{\ln y_P^+ + \kappa B}}_{\mu_w} \tag{4.93}$$

In the boundary cells the TKE production term is replaced with:

$$G_P = \tau_w \frac{C_\mu^{\frac{1}{4}} \sqrt{k_P}}{\kappa \delta_P} \tag{4.94}$$

where τ_w is defined as in Equation 4.93.

In the wall function approach the transport equation for ϵ is not solved in the boundary cells. Instead, the following equation is used:

$$\epsilon_P = \frac{C_\mu^{\frac{3}{4}} k_P^{\frac{3}{2}}}{\kappa \delta_P} \tag{4.95}$$

4.7.3.2 Damping-function approach

Prandtl originally proposed that the turbulence mixing length to be used in the single-equation turbulence model could be defined as:

$$\ell = \kappa y \tag{4.96}$$

where y is the distance normal to a solid wall boundary and $\kappa = 0.41$ is the von Kármán constant. Prandtl noted, however, that this estimate is not expected to be valid in all parts of the boundary layer (Wilcox, 1993).

Van Driest (1956) introduced a damping function that allows the mixing length to be defined throughout the boundary layer in terms of the distance from a solid boundary, as follows:

$$\ell = \kappa y \left[1 - e^{\frac{-y^+}{A_0^+}} \right] \tag{4.97}$$

where $A_0^+ = 26$.

The van Driest damping-function approach (without modification) was implemented in the RANS numerical model with the single-equation turbulence model. Results were compared with the $k - \epsilon$ model (see Chapter 7).

Modifications to the van Driest approach that were used in the DANS model are discussed in Section 4.8.4.

4.8 Double-Averaging Methodology

As discussed in Chapter 3, applying the double-averaging methodology to the Navier-Stokes Equations (or alternatively, spatially-averaging the RANS Equations) results in a new set of equations known as the double-averaged Navier-Stokes Equations (DANS).

The traditional governing equations for both groundwater and surface water flow can be derived from the Navier-Stokes Equations. As discussed in Chapter 2, in the case of the groundwater flow equations this is done using a volume-averaging procedure. The depth-averaging of the RANS equations that results in the shallow-water equations requires assumptions about flow at bed-level that are unrealistic when the bed is treated as a permeable layer rather than an impermeable surface. Applying a volume-averaging procedure instead does not impose these assumptions. The DANS equations, which have been shown in previous work to be a suitable framework for describing flows over rough gravel beds, are also suitable for describing laminar flows in porous media. Doing so requires a suitable double-averaged turbulence model that can "switch off" if the flow is laminar, and handle the transition from laminar to turbulent flow that occurs near the surface - subsurface interface.

This section describes the double-averaging methodology, implementation of the DANS equations using the FVM, the double-averaged turbulence model, and modifications that were made to the turbulence model to handle the laminar - turbulent transition.

In the derivation of the RANS equations from the Navier-Stokes Equations (see Appendix A), Reynolds decomposition is used to split instantaneous variables into mean and time-fluctuating components:

$$a = A + a' \tag{4.98}$$

where A is the mean component of a and a' is the fluctuating component

In the double-averaging methodology a further decomposition is applied to split time-averaged variables into double-averaged and spatially-fluctuating val-

ues:

$$A = \langle A \rangle + \tilde{A} \tag{4.99}$$

where $\langle A \rangle$ is the spatial mean, and $\tilde{A}$ denotes the spatial fluctuation in the time-averaged variable.

A full derivation of the DANS equations, starting from the RANS equations, is included in Appendix B.

The double-averaged momentum and continuity equations, as given in Nikora et al. (2007a), are as follows:

$$\frac{\partial \langle U_i \rangle}{\partial t} + \langle U_j \rangle \frac{\partial \langle U_i \rangle}{\partial x_j} = g_i - \frac{1}{\rho\phi}\frac{\partial \phi \langle P \rangle}{\partial x_i} - \frac{1}{\phi}\frac{\partial \phi \langle \tilde{u}_i \tilde{u}_j \rangle}{\partial x_j} - \frac{1}{\phi}\frac{\partial \phi \langle \overline{u_i' u_j'} \rangle}{\partial x_j} + \frac{1}{\phi}\frac{\partial}{\partial x_j}\phi \langle \nu \frac{\partial U_i}{\partial x_j} \rangle + \frac{1}{\rho}\frac{1}{\langle \phi_t \rangle}\frac{1}{V_f}\overline{\iint_{S_{int}} p n_i dS}^{s} + \frac{1}{\langle \phi_t \rangle}\frac{1}{V_f}\overline{\iint_{S_{int}} \nu \frac{\partial u_i}{\partial x_j} n_j dS}^{s} \tag{4.100}$$

$$\langle \overline{\frac{\partial \rho}{\partial t} + \frac{\partial \rho u_i}{\partial x_i}}^{s} \rangle_s = \rho \frac{\partial \phi}{\partial t} + \rho \frac{\partial \phi \langle U_i \rangle}{\partial x_i} = 0 \tag{4.101}$$

Nikora et al. (2007a) also give the double-averaged form of the advection-diffusion equation for passive scalars:

$$\frac{\partial \langle C \rangle}{\partial t} + \langle \overline{u}_j \rangle \frac{\partial \langle C \rangle}{\partial x_j} = \frac{1}{\phi}\frac{\partial}{\partial x_j}\phi \langle \chi \overline{\frac{\partial C}{\partial x_j}} \rangle - \frac{1}{\phi}\frac{\partial \phi \langle \tilde{u}_j \tilde{C} \rangle}{\partial x_j} - \frac{1}{\phi}\frac{\partial \phi \langle \overline{u_j' c'} \rangle}{\partial x_j} - \frac{1}{\langle \phi_t \rangle}\frac{1}{V_f}\overline{\iint_{S_{int}} \chi \frac{\partial c}{\partial x_j} n_j dS}^{s} + \langle \overline{F} \rangle \tag{4.102}$$

where $\langle C \rangle$ is an arbitrary double-averaged scalar quantity, χ is its diffusivity and F is a source or sink of the quantity C.

Equation 4.102 is relevant as it is the basis for the equations used in turbulence modelling (e.g. k, epsilon).

In Equations 4.100 - 4.102 an overbar on a variable symbol represents a Reynolds-averaged variable and angle brackets represent a spatially-averaged vari-

able. The combination of the two (i.e. $\langle\overline{\theta}\rangle$) represents a double-averaged variable. As defined in Equation 4.98, capital letters denote the mean component of the Reynolds-averaged variable, and therefore $\langle U_i\rangle$, $\langle P\rangle$ and $\langle C\rangle$ represent the double-averaged velocity, pressure and arbitrary scalar quantity, respectively.

The DANS equations contain a "roughness geometry function", defined as:

$$\phi = \frac{V_f}{V_0} \tag{4.103}$$

which is analogous to the porosity of a porous medium (and is in fact exactly the same as the porosity for flows beneath stream-bed level).

The DANS equations are written in terms of intrinsic averages (as defined in Equation (2.53)). The intrinsic average form of the fluid velocity is equivalent to the pore velocity. Using the relationship between intrinsic and superficial averages, as defined in Equation 2.55, the relationship between the pore velocity and the superficial velocity (also known as the Darcy of flux velocity) can be defined as:

$$\langle U_i\rangle_s = \phi\langle U_i\rangle \tag{4.104}$$

where $\langle U_i\rangle_s$ is the superficial velocity.

A time-analogue of the roughness geometry function also appears in the surface integral terms in Equation 4.100:

$$\phi_t = \frac{T_f}{T_0} \tag{4.105}$$

where T_f is the sum of time periods in which a point under consideration is occupied by fluid during a total averaging time T_0. For an immobile bed $\phi_t = 1$. The ϕ_t term results from using versions of the volume-averaging theorem and general transport theorem that have been modified to handle roughness mobility (sediment transport or aquatic plants that move in the flow). As the numerical model developed in this thesis does not handle mobile beds, the derivation of the DANS equations presented in Appendix B has not used these modified averaging theorems.

The double-averaged momentum equation (Equation 4.100) contains addi-

tional terms that do not appear in the conventional Navier-Stokes or RANS equations. These terms arise out of the volume-averaging process, in a similar manner to the Reynolds stress terms that result from time-averaging the Navier-Stokes Equations. Nikora et al. (2007a) describe the additional terms as form-induced stresses:

$$\langle \tilde{u}_i \tilde{u}_j \rangle \tag{4.106}$$

form drag per unit fluid volume:

$$f_{pi} = -\frac{1}{\rho}\frac{1}{\langle \phi_t \rangle}\frac{1}{V_f}\overline{\iint_{S_{int}} p n_i dS}^{s} \tag{4.107}$$

and viscous drag per unit fluid volume:

$$f_{\nu i} = \frac{1}{\langle \phi_t \rangle}\frac{1}{V_f}\overline{\iint_{S_{int}} \nu \frac{\partial u_i}{\partial x_j} n_j dS}^{s} \tag{4.108}$$

respectively, where $\overline{\theta}^{s}$ indicates a superficial time average, which is analogous to the superficial spatial average defined in Equation 2.52.

In the double-averaged advection-diffusion equation (Equation 4.102)the additional terms that arise out of the volume averaging process are fluxes due to spatial variations in time-averaged fields:

$$\langle \tilde{u}_j \tilde{C} \rangle \tag{4.109}$$

and diffusive flux at bed level (i.e. at the interface between surface and subsurface flow):

$$J = -\frac{1}{\langle \phi_t \rangle}\frac{1}{V_f}\overline{\iint_{S_{int}} \chi \frac{\partial C}{\partial x_j} n_j dS}^{s} \tag{4.110}$$

4.8.1 Parameterisation of additional terms in the momentum equation

The double-averaging process (or equivalently the volume-averaging of the RANS equations) creates a closure problem, analogous to that which arises when the Navier-Stokes equations are time-averaged to give the RANS equations. In order to reduce the number of variables to the number of equations, it is necessary to parameterise the surface integral terms in Equation 4.100.

The parameterisation of the viscous drag (Equation 4.108) in the double-averaged equations is given by Nikora et al. (2007a) as:

$$\frac{1}{\langle \phi_t \rangle} \frac{1}{V_f} \overline{\iint_{S_{int}} \nu \frac{\partial u_i}{\partial x_j} n_j dS}^s = \frac{\nu}{k_i} \langle U_i \rangle_s \tag{4.111}$$

where k_i is the intrinsic permeability. Nikora et al. (2007a) refer to k_i as "an analogue of the permeability coefficient", which reflects the fact that their work was focussed on describing the near-bed regions of open-channel and overland flows, rather than subsurface and surface flows. The parametrisation in Equation 4.111 states that the viscous drag is linearly dependent on the mean superficial velocity. As discussed in Section 4.8.1.1, this results in the DANS momentum equation collapsing to Darcy's Law under suitable flow conditions, and therefore k_i has been treated as identical to the intrinsic permeability.[1]

Nikora et al. (2007a) give the following parameterisation for the form drag term:

$$-\frac{1}{\rho} \frac{1}{\langle \phi_t \rangle} \frac{1}{V_f} \overline{\iint_{S_{int}} p n_i dS}^s = 0.5 C_d a \left[\langle U_i \rangle_s \langle U_j \rangle_s \right]^{0.5} \langle U \rangle_s \tag{4.112}$$

where C_d is a drag coefficient, and $a(y)$ is a local roughness density, defined as the roughness frontal area per unit fluid volume. This parameterisation is in the

[1] In Nikora et al. (2007a) the velocity terms in the parameterisations for viscous drag and form drag are shown as the intrinsic velocity, $\langle U_i \rangle$. However, in order for the DANS momentum equation to collapse to Darcy's Law the superficial velocity $\langle U_i \rangle_s = \phi \langle U_i \rangle$ must be used. This is consistent with Pokrajac and Manes (2008) and de Lemos and Silva (2006). It is therefore assumed that the use of the intrinsic velocity in the parameterisations given in Nikora et al. (2007a) is an error, and the superficial velocity has been used in Equations 4.111and 4.112.

form of a general drag force equation.

Pokrajac and Manes (2008) and de Lemos and Silva (2006) give a parameterisation for the two volume-averaged drag-force terms combined:

$$f_j = \underbrace{\frac{\mu\phi}{k_i}\overline{\boldsymbol{u}}_D}_{\text{viscous drag}} + \underbrace{\frac{c_F\phi\rho}{\sqrt{k_i}}\overline{\boldsymbol{u}}_D|\overline{\boldsymbol{u}}_D|}_{\text{form drag}} \tag{4.113}$$

where c_F is a Forchheimer coefficient (as introduced in Section 2.3.1.4) and $\overline{\boldsymbol{u}}_D$ is the Darcy velocity, which is equivalent to $\langle U_i \rangle_s$.

With the exception of the general drag-force form of Equation 4.112 being replaced with the Forchheimer equation for the form drag term, the parametrisation in Equation 4.113 is essentially the same as the parametrisations for the viscous and form drag from Nikora et al. (2007a)(Equations 4.111 and 4.112) combined: although the coefficients are different there is still a dependence on $\langle U \rangle$ for the viscous drag and $\langle U \rangle^2$ for the form drag.

The roughness geometry function, or porosity ϕ appears in equation 4.113 as the form of the DANS momentum equation used in Pokrajac and Manes (2008) and de Lemos and Silva (2006) has been multiplied through by $\rho\phi$.

As the purpose of the numerical model developed in this thesis is to model both surface and subsurface flows, the parameterisations used in the DANS equations need to be appropriate for subsurface flows, rather than primarily for protruding roughness elements in an open-channel or overland flow. Therefore the form drag term in the numerical model was parameterised using the Forchheimer equation, as in Equation 4.113.

As discussed in Chapter 2, typical values of the intrinsic permeability k_i for different aquifer materials are available from text-books, or values can be determined from field or laboratory testing. Typical values of the Forchheimer coefficient c_F are less commonly available. A method given in Vafai (1984) was used to estimate c_F based on the porosity, as follows:

$$c_F = \frac{1.75}{\sqrt{150\phi^3}} \tag{4.114}$$

The form-induced stresses (Equation 4.106) are typically assumed to be neg-

ligible, and parameterisations have not been developed for these terms (Nikora et al., 2007a).

4.8.1.1 Expected behaviour of additional terms

The relative contributions of the viscous and form drag terms depends on the flow regime and hydraulic properties.

For Darcian porous media flows the contribution of the form drag term will be negligible and the viscous drag term will dominate the momentum equation, i.e. the DANS momentum equation approximates the groundwater flow equation (Equation 2.27). For a steady, horizontal uniform Darcian porous media flow the double-averaged pressure gradient balances the parameterised viscous drag term as follows:

$$\frac{\partial \phi \langle P \rangle}{\partial x_i} = \frac{\mu \phi}{k_i} \langle U_i \rangle_s \tag{4.115}$$

If the domain is homogeneous (i.e. $\frac{\partial \phi}{\partial x_i} = 0$)then both sides of Equation4.115 can be divided by ϕ, and the resulting equation is identical to Darcy's Law written in terms of pressure and the intrinsic permeability (Bear, 1972).

As discussed in Chapter 2, if the porous Reynolds number $Re_p > 1$ then the flow is likely to have entered a post-linear laminar regime, where the form drag term makes a greater contribution.

For a clear-fluid flow above any protruding roughness elements (i.e. where $\phi = 1$) a sufficiently large value of k_i was used to ensure that the form drag and viscous drag force terms were negligible. In this case the DANS momentum equation reverts to the RANS momentum equation.

4.8.2 Implementation of the DANS equations with the finite volume method

The modification of terms in the Navier-Stokes equations, and the introduction of new terms as a result of the double-averaging process, means that the discretisation of each term needs be revisited in order to solve the DANS equations with the finite volume method. Some terms need careful treatment to ensure that

cell-face fluxes are conserved.

Replacing the viscous drag and form drag surface integral terms with the parameterisations given in Equations 4.111 and 4.113 respectively, neglecting the form-induced stresses, and using the Boussinesq approximation to represent the Reynolds stresses, the DANS momentum equation (Equation 4.100) can be re-written as follows:

$$\frac{\partial\langle U_i\rangle}{\partial t} + \langle\, U_j\rangle\frac{\partial\langle U_i\rangle}{\partial x_j} = g_i - \frac{1}{\rho\phi}\frac{\partial\phi\langle\tilde{P}\rangle}{\partial x_i} + \frac{1}{\phi}\frac{\partial}{\partial x_j}\phi\langle\overline{(\nu+\nu_t)\frac{\partial u_i}{\partial x_j}}\rangle + \frac{c_F}{\sqrt{k_i}}\left[\langle U_i\rangle\langle U_j\rangle\right]^{0.5}\langle U\rangle + \frac{\nu}{k_i}\langle U_i\rangle \tag{4.116}$$

To avoid having the derivative of the turbulent kinetic energy k in the momentum equations, the pressure term in Equation 4.116 has been re-defined as $\langle\tilde{P}\rangle = \langle P\rangle + \frac{2\langle\bar{k}\rangle}{3}$. The pressure was then corrected after the momentum and k equations were solved. For clarity, the tilde on P is omitted in subsequent equations.

To put the DANS momentum equation into a similar format to that usually used in CFD modelling (i.e. for consistency with the RANS numerical model) Equation 4.116 was multiplied through by $\rho\phi$, and the diffusive term was brought onto the left-hand side as follows:

$$\frac{\partial\rho\phi\langle U_i\rangle}{\partial t} + \frac{\partial}{\partial x_j}\left[\rho\phi\langle\, U_i\rangle\langle U_j\rangle - \phi\langle\overline{(\mu+\mu_t)\frac{\partial u_i}{\partial x_j}}\rangle\right] = \rho\phi f \tag{4.117}$$

where f represents the gravitational, pressure gradient and drag force terms in Equation 4.116.

4.8.2.1 Mass fluxes

Following the same methodology as Section 4.4.1, the double-averaged continuity equation (Equation 4.101) can be written as the sum of mass-fluxes through each

side of a finite-volume cell, as follows:

$$\sum_{c} (\phi_c \mathbf{U}) \cdot \mathbf{s} = \mathbf{0} \tag{4.118}$$

where ϕ_c is the value of the roughness geometry function porosity at cell face c. It can be shown that the areal porosity (i.e. the area of void space in a plane passing through a porous medium) is the same as the volumetric porosity at a point on the plane (Bear, 1972). Following the same argument, the linear porosity is equivalent to the areal porosity. Therefore a spatially-averaged value of ϕ can also be used to represent ϕ on a cell-face.

As the DANS model solves for the intrinsic (or pore) velocity, mass conservation requires that a change in ϕ will result in a corresponding change in velocity (i.e. the Darcy velocity remains constant). Assuming that finite volume cell faces are aligned with a streambed or porous material layers, then where adjacent cells have different values of ϕ, a step-change in ϕ will occur at the shared cell-face. To ensure that a step-change in velocity occurs at the cell-face, and for mass to be conserved, the values of ϕ_c that are required for calculating cell-face fluxes cannot be obtained by linear interpolation of the neighbouring cell-centre values of ϕ. Instead, the cell-centre values of ϕ from either side of the cell-face must be used. This is illustrated in Figure 4.2. As the value of ϕ steps up at the cell face, there must be a corresponding step down in pore velocity. Rather than calculating the cell-face fluxes exactly at the cell-face where the step-change occurs, a infinitesimally smaller cell, with a boundary at a distance dx from the main cell face, can be considered. At the boundary of the smaller cell the porosity and pore velocity both have a single value, thus avoiding the complication of the step-change. Using the cell-centre values of ϕ means that unique values of the pore velocity can be calculated at the east cell-face of cell 1 and the west cell-face of cell 2, respectively.

4.8.2.2 Acceleration and diffusive terms

Using the same methodology as described in Section 4.4 for the RANS equation, the double-averaged convective and diffusive terms in Equation 4.117 were reformulated as fluxes through the boundary of an arbitrary control volume region

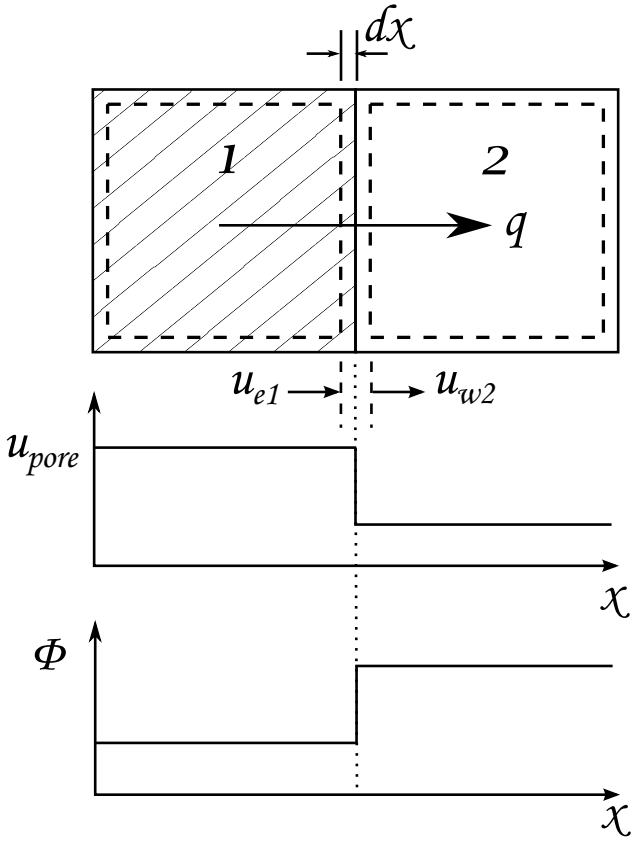

Figure 4.2: Double-averaged mass-flux

as follows:

$$F^C = \oint_{P_R} \left(\rho\phi\langle\overline{u}_i\rangle\langle\overline{u}_j\rangle\right) n_i dP_R \tag{4.119}$$

and

$$F^D = -\oint_{P_R} \left(\phi\langle\overline{(\mu+\mu_t)\frac{\partial u_i}{\partial x_j}}\rangle\right) n_i dP_R \tag{4.120}$$

where P_R is the perimeter of region R.

Replacing region R with a finite volume cell, and assuming that the surface integrals are evaluated at the middle of the cell face (the midpoint rule), the flux

terms for an arbitrary cell-face c become:

$$F_c^C = \sum_c \left(\rho\phi\langle\overline{u}_i\rangle\langle\overline{u}_j\rangle n_i S\right)_c \tag{4.121}$$

and

$$F_c^D = \sum_c \left[-\phi\langle\overline{(\mu+\mu_t)\frac{\partial u_i}{\partial x_j}}\rangle n_i S\right]_c \tag{4.122}$$

where S_c is the length of cell face c, S is the cell-face length and n_i is a unit vector normal to the face.

The convective flux term was then linearised using the mass-flux. For an arbitrary cell-face c, the linearised convective flux term is as follows:

$$F_c^C = \phi_c \dot{m}_c \langle U_c\rangle \tag{4.123}$$

Apart from the use of double-averaged flow variables, the convective and diffusive flux terms in the DANS equations differ from the RANS version (as discussed in Chapter 4) by a factor of ϕ. The contribution that these terms make to the system matrix coefficients will therefore also differ by a factor of ϕ. For example, the DANS version of the east coefficient for the momentum equation a_E^u is as follows:

$$a_E^U = -\phi_e D_e - min\{\phi_e \dot{m}_e, 0\} \tag{4.124}$$

where D_e is defined in the same way as it was for the RANS equations (Equation 4.22).

The unsteady term in Equation 4.117 was discretised using the implicit Euler method (the same method used for the RANS equations) as follows:

$$\int_V \frac{\partial \rho\phi\langle U_i\rangle}{\partial t} \approx \frac{(\rho\phi\langle\ U\rangle)_P^{n+1} - (\rho\phi\langle\ U\rangle)_P^n}{\Delta t_n}\delta V = a_t^U U_P^{n+1} - b_t^U \tag{4.125}$$

where a_t^U is the unsteady term's contribution to the coefficient matrix, defined

as:

$$a_t^U = \frac{\rho \phi_P A}{\Delta t_n} \tag{4.126}$$

and b_t^U is the contribution to the source terms:

$$b_u^t = \frac{\rho \phi_P A}{\Delta t_n} \langle U \rangle_P^n \tag{4.127}$$

where A is the area of cell P. In Equations 4.126 and 4.127 it was assumed that ρ is constant, and that ϕ only varies spatially.

4.8.2.3 Pressure gradient

The pressure gradient term was discretised by firstly applying the divergence theorem:

$$\int_V \frac{\partial \phi \langle P \rangle}{\partial x_i} dV = \int_S \phi \langle P \rangle n_i dS \tag{4.128}$$

Assuming that the mesh is Cartesian, the pressure term (using the u-momentum equation as an example) was approximated as:

$$\int_S \phi \langle P \rangle n_i dS \approx \Sigma_c \left(\phi \langle P \rangle n_i \right)_c \delta S_c = \phi_e \langle P \rangle_e - \phi_w \langle P \rangle_w \tag{4.129}$$

Following the same methodology as for the RANS equations, linear interpolation was used to estimate the values of ϕ and p at the cell faces (e.g. $P_e = 0.5P_E + 0.5P_P$). The double-averaged pressure gradient term can then be written in terms of cell-centre values as follows:

$$\frac{\Delta y}{2} \left(\phi_E p_E - \phi_W p_W \right) \tag{4.130}$$

It was found, however, that where there is a step-change in ϕ across a cell boundary the form of central difference shown in Equation 4.130 caused the double-averaged pressure gradient to reverse in some cases (i.e. $\phi_E p_E < \phi_W p_W$, even though $p_E > p_W$). A numerical scheme that would allow the sign of $\frac{\partial (\phi P)}{\partial x}$ to be difference to $\frac{\partial P}{\partial x}$ has no physical basis when considering a step-change in ϕ.

This problem becomes worse as the mesh is refined, which is counter-intuitive for numerical modelling. Therefore the discretised pressure gradient was modified to use only the cell-centre value of ϕ for the central cell, P, rather than the values from the adjacent cells, as follows:

$$\frac{\Delta y}{2}\left(\phi_P P_E - \phi_P P_W\right) \tag{4.131}$$

The justification for using the central value of ϕ in the double-averaged pressure gradient term is illustrated in Figure 4.3.

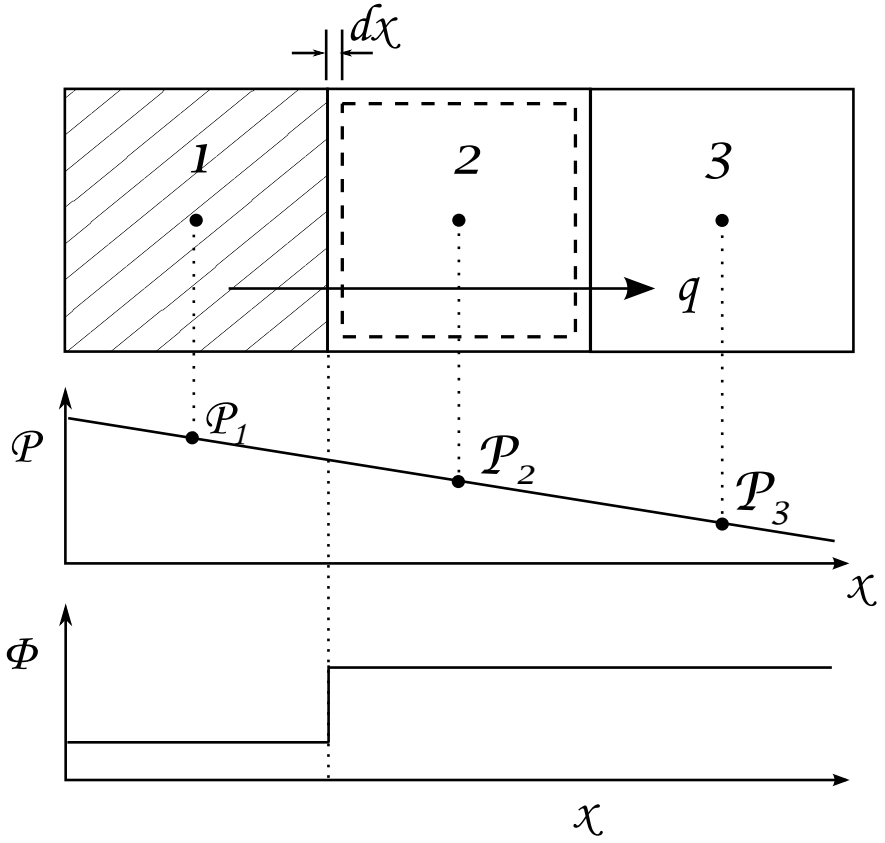

Figure 4.3: Double-averaged pressure gradient

Assuming that cell faces align with changes in material properties, ϕ is not a continuous function, and a step-change occurs at the cell face. Although the pressure values in the neighbouring cells are used to construct the central-difference estimate of the $\frac{\partial P}{\partial x}$, using the same approach with ϕ would not result in a valid estimate for $\frac{\partial(\phi P)}{\partial x}$. If a volume infinitesimally smaller than the central cell is

considered, with boundaries a distance dx from the cell face, then the pressure gradient estimated from the central difference is still applicable, but the only relevant value of ϕ is the central value (i.e. the cell-centre value for cell 2 in Figure 4.3). Additionally, the viscous drag (or Darcy) term contains the cell-centre value of ϕ. In order for the momentum equation to successfully collapse down to Darcy's Law for steady Darcian flows, the ϕ values used in both the pressure gradient and viscous drag terms must be consistent.

4.8.2.4 Drag terms

Both the form drag and viscous drag source terms are dependent on the double-averaged flow velocity. It is possible to treat them completely explicitly, using velocity values from the previous iteration, or incorporate them into the coefficient matrix, where they contribute to the terms on the main diagonal. The latter option was chosen as it should improve the convergence behaviour of the model by enhancing the diagonal dominance of the coefficient matrix.

For the form drag term, an explicit linearisation was used in the discretisation:

$$\int_V \left(\frac{c_F \phi \rho}{\sqrt{k_i}} \left[\langle U_i \rangle \langle U_j \rangle \right]^{0.5} \langle U \rangle \right) dV \approx \underbrace{\left(\frac{c_F \phi \rho}{\sqrt{k_i}} \left[\langle U_i \rangle^* \langle U_j \rangle^* \right]^{0.5} A_P \right)}_{a_f} \langle U_P \rangle \qquad (4.132)$$

where the bracketed component a_f is the form drag term's contribution to the coefficients on the main diagonal of the coefficient matrix. In a_f the velocity values, $\langle U_i \rangle^*$ and $\langle U_j \rangle^*$ are the values of $\langle U_i \rangle$ and $\langle U_j \rangle$ from the previous iteration, and A_P is the area of cell P.

The viscous drag term was discretised as follows:

$$\int_V \left(\frac{\mu \phi}{k_i} \langle U_i \rangle \right) dV \approx \underbrace{\left(\frac{\mu \phi}{k_i} A_P \right)}_{a_v} \langle U_P \rangle \qquad (4.133)$$

where a_v is the viscous drag term's contribution to the coefficients on the main diagonal of the system matrix.

4.8.2.5 Modifications to the SIMPLE algorithm

The SIMPLE algorithm with selective interpolation was implemented for the DANS equations using the same series of steps as for RANS version of the model (as described in Section 4.6). The coefficients and source terms for the mass-balance error term, the pressure correction equation and the velocity corrections are formed from the momentum equations' coefficients and source terms. Therefore the changes described above for the coefficients and source terms (including the additional drag-force source terms that are included in the DANS equations) carry through to the SIMPLE algorithm calculations.

To ensure that the mass-balance error is continuous across cell-faces, it was necessary to include the porosity in the calculation of the mass-balance error, b_m, and in the continuity equation written in terms of the pressure corrections, as follows:

$$\left[-\overline{\left(\frac{\Delta y}{2a_{P,E}^{U,k}}\right)}_e (P'_E - P'_P) + \overline{\left(\frac{\Delta y}{2a_{P,W}^{U,k}}\right)}_w (P'_P - P'_W)\right]\phi_P \Delta y$$
$$+\left[-\overline{\left(\frac{\Delta x}{2a_{P,N}^{V,k}}\right)}_n (P'_N - P'_P) + \overline{\left(\frac{\Delta x}{2a_{P,S}^{V,k}}\right)}_w (P'_P - P'_S)\right]\phi_P \Delta x = b_m \quad (4.134)$$

The coefficients for the double-averaged pressure-correction equation were modified to:

$$a_E^{P,k} = \overline{\left(\frac{\Delta y^2}{a_P^{U,k}}\right)}_e \phi_P \ , \ a_W^{P,k} = \overline{\left(\frac{\Delta y^2}{a_P^{U,k}}\right)}_w \phi_P \ , \ a_N^{P,k} = \overline{\left(\frac{\Delta x^2}{a_P^{V,k}}\right)}_n \phi_P \ , \ a_S^{p,k} = \overline{\left(\frac{\Delta x^2}{a_P^{V,k}}\right)}_s \phi_P \quad (4.135)$$

The double-averaged velocity correction equation is as follows:

$$U'_e = -\overline{\left(\frac{\Delta y}{a_P^{U,k}}\right)}_e \phi_P \, (P'_E - P'_P) \quad (4.136)$$

4.8.3 Double-averaged turbulence model

A "macroscopic", or volume-averaged, form of the Boussinesq approximation for the Reynolds stress is given in de Lemos and Silva (2006), as follows:

$$-\rho\phi\langle\overline{u_i'u_j'}\rangle = \mu_t\left(\frac{\partial\phi\langle U_i\rangle}{\partial x_j}+\frac{\partial\phi\langle U_j\rangle}{\partial x_i}\right)-\frac{2}{3}\phi\rho\langle\overline{k}\rangle\delta_{ij} \tag{4.137}$$

To implement the volume-averaged Boussinesq approximation in the DANS equations, double-averaged transport equations are required for turbulence properties in order to calculate μ_t. As the single-equation turbulence model was used for the DANS model, the only additional transport equation required was for the turbulent kinetic energy, k.

Assuming that form-induced fluxes ($\langle\tilde{u}_j\tilde{C}\rangle$ in Equation 4.102) are negligible (Nikora et al., 2007a) and that the turbulent flux term ($\langle\overline{u_j'C'}\rangle$) is dealt with through the Boussinesq approximation, the general double-averaged advection-diffusion equation(Equation 4.102) can be multiplied by $\rho\phi$ and re-arranged to give:

$$\frac{\partial\rho\phi\langle C\rangle}{\partial t}+\frac{\partial}{\partial x_j}\left[\rho\phi\langle U_i\rangle\langle C\rangle-\phi\langle\overline{(\chi+\chi_t)\frac{\partial C}{\partial x_j}}\rangle\right]=\rho\phi f \tag{4.138}$$

where $\rho\phi f$ represents the combined double-averaged surface integral and source / sink terms.

As for the DANS momentum equation, a parameterisation is required for the surface integral term that arises from the volume averaging process. Nikora et al. (2007b) refer to a parameterisation for the case of mass transfer of a substance between an open channel flow and a stream bed with a periphyton canopy. This parameterisation is unlikely to be appropriate for transport of turbulence properties, however.

A transport equation for $\langle\overline{k}\rangle$ is given by de Lemos and Silva (2006), as follows:

$$\frac{\partial\rho\phi\langle\overline{k}\rangle}{\partial t}+\frac{\partial}{\partial x_j}\left[\rho\phi\langle U_i\rangle\langle\overline{k}\rangle-\phi\langle\overline{(\mu+\frac{\mu_t}{\sigma_k})\frac{\partial k}{\partial x_j}}\rangle\right]=G+G_m-\rho\sigma\langle\overline{\epsilon}\rangle \tag{4.139}$$

where G is the production rate of TKE due to gradients in $\langle U\rangle$ (i.e. analogous

to the production term in the standard $k-\epsilon$ equations) and G_m is the production rate of TKE due to flow in the porous matrix, defined as:

$$G_m = c_k \rho \frac{\phi \langle \overline{k} \rangle |\langle \overline{u} \rangle|}{\sqrt{k_i}} \tag{4.140}$$

where $c_k = 0.28$ (de Lemos, 2005) is a constant and k_i is the intrinsic permeability of the porous medium.

Apart from G_m, the remaining source terms in Equation 4.139 are very similar to those in the transport equation for k in the standard $k-\epsilon$ and single-equation models. It is possible that the new production term, G_m, is effectively a parameterisation for the surface integral in Equation 4.102.

4.8.4 Modifications to the turbulence model

For the DANS numerical model to handle both laminar and turbulent flows in a hybrid porous / clear-fluid domain, it was necessary to build "adaptive damping" into the turbulence model. The approach described in this section allows the model to determine for itself where the flow is laminar and where it is turbulent: this does not need to be specified *a priori*, as is normally the case in CFD models.

If a porous layer is present in the domain there are two "book-end" cases:

- The porous medium is sufficiently permeable for the flow to be turbulent throughout, if the velocities are sufficiently high. The bottom boundary of the domain acts as an impermeable no-slip boundary. The solid fraction of the porous matrix acts more like obstacles in the flow. In this case a standard wall boundary treatment (wall function or damping function) could be used at the bottom boundary.

- The porous medium is relatively impermeable. Flow in the porous layer is laminar throughout, with velocities that are negligible compared to those in the surface layer. The interface behaves similarly to a no-slip boundary, and a standard wall boundary treatment could be used at the interface.

In between the two limiting cases the porous layer interface may act only somewhat like a wall boundary, and the flow may be turbulent for at least part

of the depth of the porous layer. In this case the standard wall treatments for turbulence models are not valid either at the bottom of the domain, or at the porous / clear-fluid interface. At some depth below the interface the surface flow will cease to influence the flow in the porous layer. This depth can be conceptualised as a wall boundary, and estimating the location of this "boundary" provides a start-point for a modified wall treatment in the turbulence model that will allow a transition between laminar and turbulent flow. This location is referred to as the effective bed level. The effective surface flow depth was defined as the depth of flow above the point where the porous medium acts like a wall boundary.

As a means of defining the effective flow depth, and (as discussed below) damping out terms in the turbulence model where the flow transitions between laminar and turbulent, a "porous damping function" was defined as follows:

$$f_p = 0.5 + 0.5 \tanh\left(\frac{Re_p - a}{b}\right) \tag{4.141}$$

where Re_p is the porous Reynolds number (as defined in Equation 2.39) calculated at each cell-centre, a defines the midpoint of the transition from $f_p \approx 0$ to $f_p \approx 1$, and b is a steepness parameter that determines the shape of the transition. Providing that $b > 1$, f_p does not actually reach zero for low values of Re_p, thus avoiding any divide-by-zero errors when the mixing length is used in Equation 2.24 to calculate epsilon. Figure 4.4 shows the porous damping function, plotted for a range of Re_p values, with $a = 50$ and $b = 20$, which provides a smooth transition from $f_p \approx 0$ to $f_p \approx 1$ over the range of Re_p given by Bear (1972) for the transition from non-linear laminar flow to fully turbulent flow in a porous medium (where the length scale in Re_p is based on the average particle diameter).

Re_p was used in the porous damping function as previous studies have found this parameter to have a strong influence on how surface flows interact with an underlying porous bed, and Bear (1972) gives a criteria for the transition from laminar to turbulent porous media flow in terms of Re_p.

Some studies refer to a permeability Reynolds number, Re_k. However, if the length-scale in Re_p is estimated using the permeability (or a combination of permeability and porosity), then Re_p and Re_k are either identical or close to

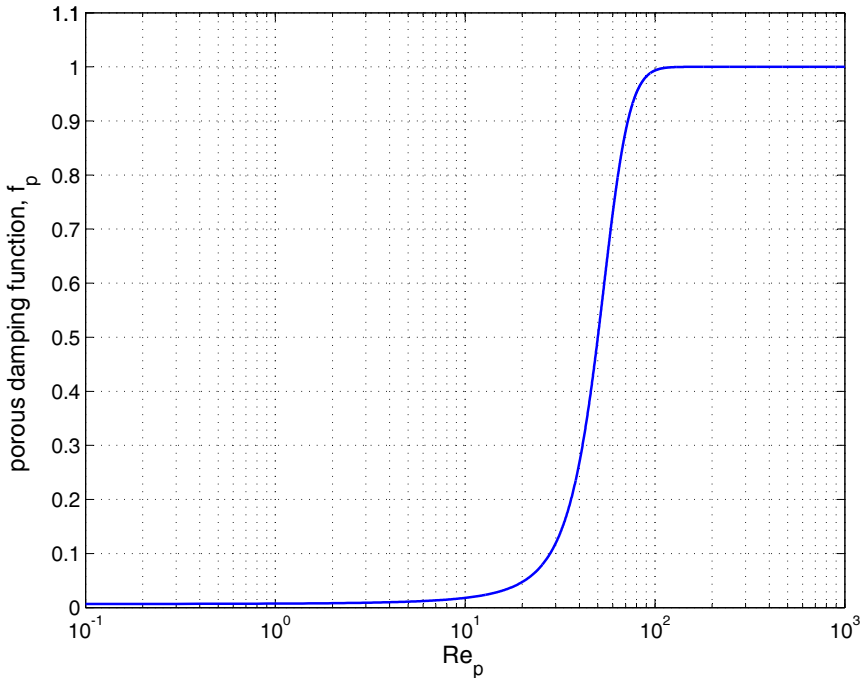

Figure 4.4: Porous damping function, f_p

equivalent.

To estimate the effective flow depth a porous Reynolds number using only the horizontal component of the Darcy velocity (Re_{p_h}) was calculated. This removed the potential influence of vertical flow on the location of the effective wall boundary. The effective flow depth at each vertical cross-section was defined as the point at which the porous damping function, $f_p > 0.5$. With no porous layer present in the model and the hydraulic properties set to appropriate values for clear-fluid flow, the effective flow depth will always be the depth of flow above the bottom boundary of the domain. Using Re_{p_h} to define the effective bed level means that the location of this level depends both on the hydraulic properties and on the flow: increasing the surface flow velocity with the porous layer's hydraulic properties held constant could increase the influence of the surface flow on flow in the porous region, and therefore lower the effective bed level.

If an interface between a porous layer and a clear-fluid region is included in the DANS model domain it is likely to be problematic to define τ_w, the wall

shear-stress, which is required to calculate the dimensionless distance y^+ that is normally used in the van Driest damping function (Equation 4.97). Wallin and Johansson (2000) proposed an alternative dimensionless length-scale, defined as:

$$y^T = C_{y1}\sqrt{Re_y} + C_{y2}Re_y^2 \tag{4.142}$$

where $C_{y1} = 2.4$, $C_{y2} = 0.003$ (Wallin and Johansson, 2000), and Re_y is a locally-defined Reynolds number based on the TKE and the distance from the wall boundary:

$$Re_y = \frac{\sqrt{k}y\rho}{\mu} \tag{4.143}$$

where y in this case is the distance from the effective bed level.

The van Driest damping function was therefore modified to:

$$\ell = \kappa y \left[1 - e^{\frac{-y^T}{A_0^+}}\right] \tag{4.144}$$

The value of the constant in Equation 4.144 was left unchanged at $A_0 = 26$.

A further modification was made to the van Driest damping function to ensure that the turbulence model was only active when the porous Reynolds number Re_p was greater than the threshold value given by Bear (1972). The porous damping function (Equation 4.141) was used to force the mixing length to approximately zero for local Re_p values below the lower end of the transition range, with a transition from zero to the unmodified value of Equation 4.144 for Re_p values that indicate a fully turbulent flow.

With the porous damping function incorporated, the mixing length equation becomes:

$$\ell = f_p \kappa y \left[1 - e^{\frac{-y^T}{A_0^+}}\right] \tag{4.145}$$

where f_p is the porous damping function defined in Equation 4.141. If $f_p \approx 0$ then the mixing length will also be approximately zero, and the turbulent viscosity μ_t (from Equation 2.23) will be negligible.

Although it is the local value of the turbulent viscosity that mainly affects

the momentum equations (absorbing the TKE term into the pressure as in Equation 4.81 has a relatively minor effect), "switching off" the turbulence model in this way does not necessarily prevent the model from generating TKE in the porous medium where the flow is predicted to be laminar. This TKE could then potentially be advected out of the laminar region, resulting in an elevated turbulent viscosity if it is not dissipated before it reaches a region where the flow is predicted to be turbulent.

The expression for the standard production term, G, in the TKE transport equation (Equation 2.21) contains the turbulent viscosity. Applying the porous damping function to the mixing length (and hence to the turbulent viscosity) should therefore also damp out the production term. However, the turbulent viscosity is calculated at the end of each iteration, and therefore if μ_t is changing rapidly between iterations then relying on damping μ_t to suppress the production term may not be reliable. Therefore the porous damping function was incorporated into both the standard TKE production term, and the additional porous TKE production term (Equation 4.8.3). The modified production terms are as follows:

$$G = f_p \mu_t \left(\frac{\partial u_i}{\partial x_j} + \frac{\partial u_j}{\partial x_i} \right) \frac{\partial u_i}{\partial x_j} \tag{4.146}$$

$$G_m = f_p c_k \rho \frac{\phi \langle \overline{k} \rangle |\langle \overline{u} \rangle|}{\sqrt{k_i}} \tag{4.147}$$

Wall boundary treatments in turbulence models are generally formulated on the basis that the wall is an impermeable boundary and therefore, at least in the near-wall region, the mean flow will be parallel to the boundary. Some previous studies (e.g. Andersen et al. (1975) and Wang and Papell (1983)) suggest that the mixing length may be modified near a wall boundary if there is flow perpendicular to the wall. This is supported by the laboratory results presented in Chapter 6. Mixing length estimates from the laboratory results are shown in Appendix E In the absence of any directly-applicable previous work, a simple modification based on the dimensionless vertical velocity was made to the mixing-length calculation. This modification was applied if it resulted in a greater mixing length

than the modified van Driest damping function. Below the effective bed level the mixing length was constrained to an estimate of the pore length scale (as used in the porous Reynolds number), multiplied by the porous damping function. The mixing length for all cases can be summarised as follows:

$$\ell = \begin{cases} \max\left(\min\left(c_v y \frac{V}{U_f}; \kappa y_{max}\right); f_p \kappa y \left[1 - e^{\frac{-y^T}{A_0^+}}\right]\right) & \textit{above effective bed level} \\ f_p \left(\frac{k_i}{\phi}\right)^{\frac{1}{2}} & \textit{below effective bed level} \end{cases} \tag{4.148}$$

where c_v is a constant, y is the vertical distance above the effective bed and y_{max} is the maximum surface flow depth. The mixing length with vertical flow modification is constrained to κy_{max}, which is the maximum value that can be reached with the van Driest mixing length function.

4.9 Solution Process

The sequence in which the various components of the numerical model are implemented is shown in Figure 4.5.

After initialising the mesh and assigning hydraulic properties to mesh cells, the initial conditions were set.

The overall model structure is two nested loops: an outer loop for time-stepping and in inner loop for the iterations required to implement the SIMPLE algorithm. The turbulence transport equations were solved at each iteration of the SIMPLE algorithm so that each iteration uses an updated value of the turbulent viscosity μ_t. As Figure 4.5 is the sequence for the DANS model it shows only the k transport equation being solved. If the $k - \epsilon$ is used in the RANS model then the ϵ is solved immediately after the k equation.

The linear systems for the momentum, pressure-correction and turbulence equations were solved with MATLAB's back-slash operator[1].

[1]The back-slash, or *mldivide* operator in MATLAB solves a system of linear equations $\mathbf{A}x = \mathbf{b}$ for x. MATLAB aims to minimise computation time by using an algorithm to select the most appropriate method for solving the system of equations, based on the form of $\mathbf{A}$. This includes checking whether $\mathbf{A}$ is a sparse matrix (MathWorks, 2016)

The free-surface correction was applied at the end of each time-step after the inner iteration loop had finished. After applying the free-surface correction the continuity and momentum equations were solved for a final time before either advancing to the next time-step or finishing the model run.

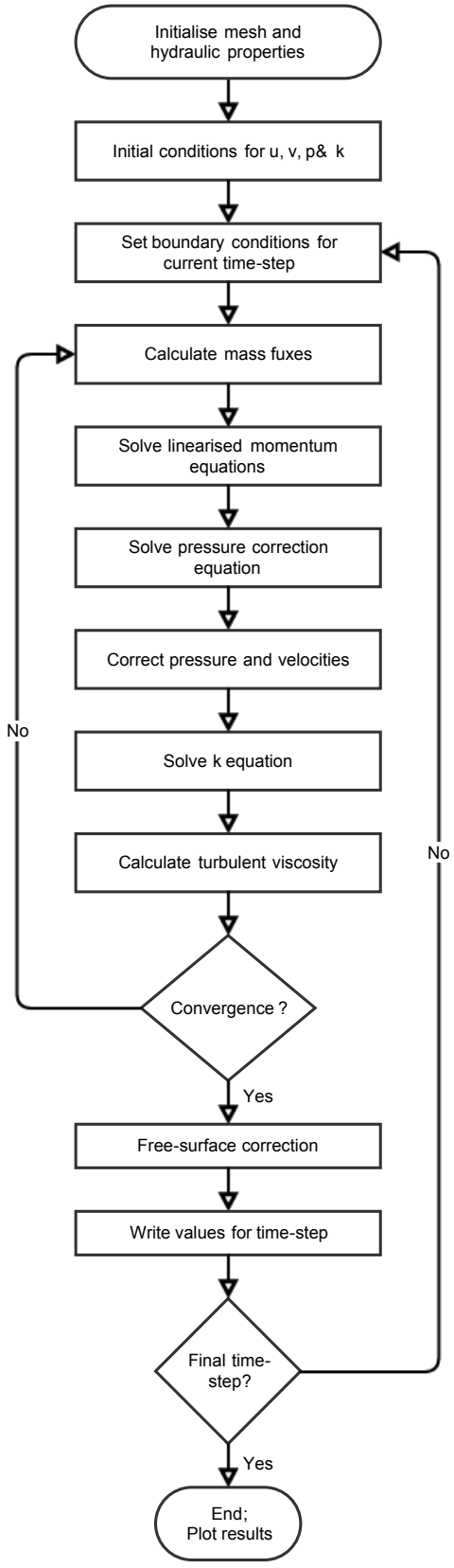

Figure 4.5: Flowchart showing solution process for the DANS model

4.10 Chapter Summary

As an intermediate step towards building a numerical model to solve the DANS equations for coupled surface - subsurface flows, the RANS equations were discretised for solution with the finite-volume method. The SIMPLE algorithm was used to handle pressure-velocity coupling.

Two turbulence models were implemented for the RANS numerical model: the $k-\epsilon$ model (as a baseline case) and the Kolmogorov-Prandtl single-equation model. Solid boundaries in the $k-\epsilon$ model were handled with the "standard" wall-function approach. In the single-equation model a damping-function was used to handle boundaries.

The RANS model and the single-equation turbulence model were then altered to handle the modifications and additional terms that arise from the double-averaging process. This resulted in a DANS model. An additional "porous damping function" was incorporated into the double-averaged version of the single-equation turbulence model to allow it to handle a flow regime that transitions from laminar to turbulent at or near the interface between porous and clear-fluid flow, without the need to specify the location of the transition *a priori*.

The end result of the model development described in this chapter is a 2D finite-volume numerical model, coded in MATLAB, for solving the DANS equations. By specifying an appropriate spatial distribution of hydraulic properties the model can simulate groundwater flow, surface water flow or in domains containing both groundwater and surface water flows.

Chapter 5

Physical Modelling Methodology

5.1 Introduction

The purpose of the experimental programme was to gather a data set suitable for verifying the DANS model. A key objective of the physical modelling work was to measure fluxes across the surface-subsurface interface. A technique was developed that allowed the two-dimensional velocity field in the subsurface flow to be measured.

Traditionally, measurements of porous media flow, both in the field and in the laboratory, have been limited to water level / pressure measurement at discrete points, and bulk measurements of discharge. Although point velocity probes are available (e.g. Devlin et al. (2012)) it is generally not possible to collect spatially-distributed velocity field information in a naturally-occurring porous medium.

The use of a refractive-index-matched transparent porous medium, combined with an optical flow visualisation and measurement technique, has enabled detailed measurements of the subsurface velocity field including vertical flows across the surface-subsurface interface.

The experiments were conducted in a glass-walled flume in the Fluid Mechanics Laboratory at the University of Canterbury. Two false-floor sections were inserted into the flume so that a free-surface flow could be established over a layer of transparent porous medium. Further details of the modified flume are given in Section 5.3.

This chapter contains an introduction to optical flow visualisation and measurement techniques, with an emphasis on particle tracking velocimetry (PTV), which was used in the experimental programme. This is followed by details of the experimental set-up and procedures, specifics of how the PTV analysis was applied, and quality assurance checks that were done to confirm that the methodology was robust and repeatable.

5.2 Optical Flow Measurement and Visualisation Techniques

Flow visualisation is a long-established method of gaining a qualitative understanding of fluid flows. Techniques used to visualise flows typically involve the use of a passive, dynamically unimportant tracer (i.e. the addition of the tracer does not substantially alter the fluid or flow properties), which is visible either under ambient lighting or using special lighting conditions. Van Dyke (1982) contains numerous examples of images of fluid flows visualised using long-exposure photographs and various tracers, including dye, metal filings and air bubbles. Although these images are highly valuable for understanding the flow qualitatively, they provide no quantitative information about scalar or vector properties of the flow.

As image capturing and processing capability has increased, flow visualisation has also become a flow measurement tool. By capturing and analysing sequences of images, flow and fluid properties such as velocity and solute concentration can be quantified. Quantitative flow visualisation can be divided into two categories: those that provide information about velocity fields, and those that allow the measurement of a scalar quantity, for example the concentration of a contaminant that has been added to the flow, or the density of the fluid (Nokes, 2013).

The two most common techniques used for velocity field measurement are particle image velocimetry (PIV) and particle tracking velocimetry (PTV). In both of these techniques a sequence of images is analysed to extract velocity field information. Particle displacements between sequential images, in conjunction with the frame rate (i.e the time-step between frames), are used to calculate local

velocities. The two techniques differ in how the displacements are calculated. PIV relies on correlating the intensity fields from two sequential image frames. To extract meaningful velocity information using this technique a dense seeding of particles is required.

The analysis required for PTV is more complicated than PIV. Particles must be individually identified in each frame, and then tracked from frame to frame. Further details of the PTV process are given in Section 5.2.1.

The most commonly-used scalar field techniques are laser-induced fluorescence (LIF), in which a laser light-source (or an LED light-source with the correct wavelength) is used to optically excite the molecules of a fluorescent dye tracer, and light-attenuation (LA), in which the flow field is back-lit and the width-integrated concentration of a dye is measured. Initial attempts at both of these techniques were made in the flume, however they were not progressed further as they did not have the potential to provide as much information as the PTV technique that was finally employed.

5.2.1 Particle tracking velocimetry

PTV was used for the experiments as state-of-the art software for PTV analysis, the Streams package (Nokes, 2013) has been developed at the University of Canterbury. Additionally, it would have been impractical to achieve sufficient particle seeding densities in the porous flow layer for PIV to be successful.

In PTV, the fluid flow is seeded with tracer particles that are dynamically unimportant, i.e. they have no significant influence on the flow. A cross-section of the flow is illuminated with a sheet of high-intensity light. With ambient light excluded from the experimental set-up, images of the illuminated particles are then recorded with a camera located perpendicular to the plane of the light-sheet. Although it is possible to extend PTV techniques to three spatial dimensions, this discussion is limited to the 2D case.

In general, the PTV process contains four steps (Nokes, 2013):

1. Image capture

2. Image processing and particle identification

3. Particle tracking

4. Velocity field generation

The implementation of these steps for the experimental programme is described in Sections 5.3 and 5.6.

Images are captured by a high-resolution video camera. The camera settings such as focus, aperture and shutter speed need to be manually adjustable. The frame rate must be sufficiently high to ensure that the particle displacement between frames is not too large to allow matching between frames. In selecting the shutter speed, a balance must be achieved between allowing enough light to enter the camera so that the particles can be readily identified in each frame, and ensuring that the images of the particles are not excessively blurred or streaked.

After assembling the captured images into a sequence, the next step is to identify the particles in each image frame. This is done using diameter and intensity thresholds. Correct identification of particles is crucial for the success of the particle tracking step.

Tracking of individual particles from frame to frame in the image sequence is done in Streams using an optimisation algorithm. Figure 5.1 illustrates the process of matching a particle between two sequential image frames.

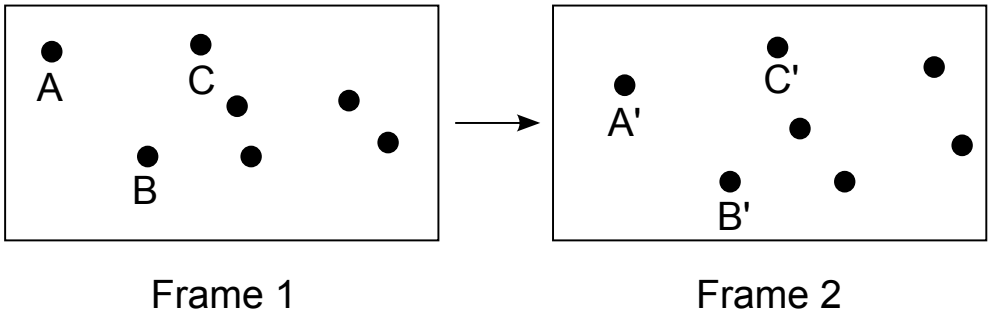

Figure 5.1: Schematic of particle matching process for two sequential image frames

In Figure 5.1 each particle in frame 1 has seven possible locations in frame 2. The algorithm determines the "cost" of matching each particle in frame 1 with each of the potential matches in frame 2. The optimal solution is the one with the lowest total matching cost, and is determined using an auction algorithm,

in which the particles in frame 1 are the bidders and the particles in frame 2 are the objects that are being bid for. In practice, to reduce the computational cost of the matching process, a search window is defined relative to each particle. Any particles outside of this window in the second frame are not considered as potential matches.

The optimisation process can be applied globally or locally. In a global optimisation the cost for the image frame as a whole is minimised. This can result in some particles being matched incorrectly. If local optimisation is used, two criteria must be met in order for a match to be made. Firstly, the cost of the potential match in frame 2 must be the smallest for the frame 1 particle, and secondly, from the perspective of the frame 2 particle, no frame 1 particle has a lower matching cost for this particle. This form of optimisation typically results in fewer matches than a global optimisation, but the matches that do occur are more likely to be correct.

In Streams there are 16 different strategies available for assigning costs to particle matches. These can be categorised as state-based costings and matching-based costings. State-based costings rely only on information about particles in a pair of image frames. Matching-based costings rely on a previous set of matches. The matching process must therefore begin with a state-based costing. Matching-based costings can be used to create new matches, or as a"clean-up" process to check the validity of a previous match and remove incorrect matches.

A more detailed discussion of both the auction algorithm and the costing strategies can be found in Nokes (2013).

Matching particles from frame to frame enables Lagrangian velocities to be calculated. A further step is required to interpolate velocities onto a grid, thus generating an Eulerian velocity field. If the flow is densely seeded with particles (and the matching process has been successful) the accuracy of the velocity field interpolation process is relatively insensitive to the grid dimensions and interpolation scheme that are used. However, if the flow is sparsely seeded then care must be taken to use appropriate interpolation settings.

Further details of the components of the PTV system that were used for the experiments are given in Section 5.3. The specifics of the analysis process used are described in Section 5.6.

5.3 Experimental Setup

5.3.1 Transparent porous medium

In order to use optical flow measurement and visualisation with a transparent porous medium, the optical properties of the saturated porous medium (i.e. the matrix and the pore fluid combined) must not vary spatially. Any distortion in the images recorded by the camera would affect the accuracy of the PTV analysis. Therefore the fluid filling the pore space must have the same, or very similar, optical properties to the porous medium. This ensures that no reflection or refraction occurs at the particle boundaries, and the particles making up the porous medium become close to indistinguishable from the pore fluid. It is only with the combination of a transparent porous matrix and a refractive-index-matched pore fluid that the pore fluid within the matrix can be viewed by the camera.

A number of combinations of transparent materials and refractive index matched pore fluids have been used in previous studies. Iskander and Tabe (2010) discuss the use of silica gel or amorphous silica powder to represent sand-sized material with either a blend of oils or a calcium bromide solution as the pore fluid. Specialised types of glass can also be used to represent larger particle sizes.

There are a number of disadvantages with transparent porous media that require an oil blend or an aqueous salt solution, particularly for an experimental set-up where free-surface flows are also being considered. There are practicality and safety considerations for handling these fluids in sufficient volumes to use in an experimental set-up. The blending or mixing must be done with sufficient accuracy to ensure that the refractive index is sufficiently close to the target value. If the pore fluid has a viscosity significantly greater than that of water it may be difficult to achieve high enough Reynolds numbers in the surface flow.

To allow water to be used as the pore fluid, Super-absorbent polymer (SAP) spheres were used as the transparent porous medium. SAP spheres are made of a Sodium polyacrylate-acrylamide cross-linked co-polymer, which absorbs large volumes of water and therefore has a refractive index very close to that of water in its hydrated form. In dry form they are opaque, clear to yellowish amorphous spheres, approximately 2 mm in diameter. When soaked in water for several hours

the SAP spheres increase in volume by approximately 100 times. In their hydrated form they are clear, transparent spheres approximately 10 mm in diameter, with a gelatinous texture.

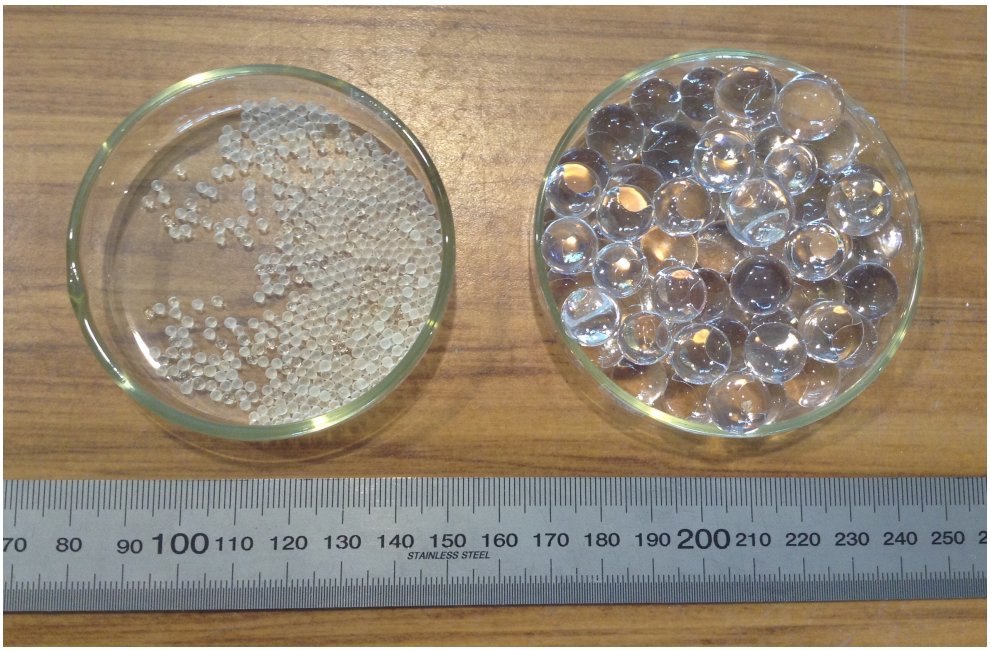

Figure 5.2: SAP spheres in dry (left) and hydrated (right) states

In industry, SAP products are used to stabilise waste sludge products, for ground improvement purposes (for example stabilising high water-content soil during excavation), and for improving the water-holding capacity of agricultural soils. For these applications the SAP is typically in powder form. SAP spheres, such as those used for the experiments, are typically used for novelty or decorative purposes.

Although in geotechnical terms the strength of SAP spheres is very poor (Iskander and Tabe, 2010), the hydrated spheres were sufficiently strong to maintain their shape when packed into a 200 mm deep layer in the flume.

Because most of the mass of the hydrated SAP spheres is the water that they have absorbed, the spheres are close to neutrally buoyant. This created challenges for holding the layer of SAP spheres in place beneath the free-surface flow. The methodology for overcoming this problem is discussed in Section 5.3.2.1.

5.3.2 Flume

A photograph of a 6 m long, 292 mm wide flume identical to the one that was modified for the experiments is shown in Figure 5.3.

Figure 5.3: Recirculating flume prior to modification

The flume's water supply was recirculating, with a reservoir underneath the glass-walled channel. Flows were delivered to the head tank by a Goulds GIS series 100x80-160 centrifugal pump with a 3 kW motor, connected to a Schneider Electric ATV61 variable-speed drive (VSD). The VSD controls were used to adjust the flow-rate being delivered to the head tank, which was measured with a Krohne Optiflux 1000 electromagnetic flow-meter (nominal diameter 80 mm), paired with a Krohne IFC100 signal converter.

To create space for a layer of porous material, two acrylic false-floor sections were installed, 200 mm above the base of the flume. This left space for a 200 mm layer of porous material, 2 m long, in the middle section of the flume between the steel support members. This location allowed an unobstructed view of the entire porous layer. A schematic of the modified recirculating flume is shown in Figure 5.4.

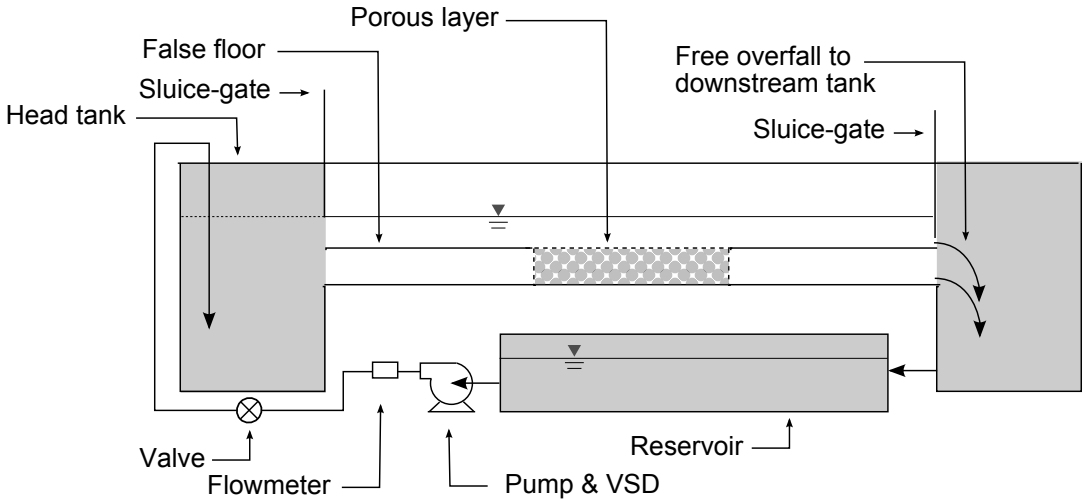

Figure 5.4: Schematic of flume

5.3.2.1 Boundary and interface conditions

At the upstream end of the flume the false floor section was open to the head tank. At the downstream end of the false floor section, where the flume discharged into the downstream tank, a solid plate with a series of removable bungs along its lower edge allowed the porous layer to be kept saturated if the bungs were in place and the valve on the upstream inflow pipe was closed. Removing the bungs allowed the porous layer to drain freely.

The depth of the surface flow was controlled with a sluice-gate at the downstream end of the flume, with a free overfall to the downstream tank.

At the upstream and downstream ends of the porous layer the transparent soil was contained by wire mesh screens. This allowed a horizontal inflow at the upstream end of the porous layer (i.e. an inflow that was independent of any interaction with the surface flow) to be delivered directly from the head tank. The downstream end of the porous layer was allowed to drain freely. Stainless steel plates and slotted polycarbonate plates (with varying open area) were used to alter the upstream and downstream boundary conditions for the porous layer, fully or partially restricting the flow.

By closing off the upstream end of the porous layer with a stainless steel plate and leaving the downstream end open, a "losing stream" configuration was

created, with downwards vertical flow across the surface - subsurface interface. The opposite configuration, analogous to a stream gaining flow from groundwater, was achieved by closing the downstream end of the porous layer and leaving the upstream end open.

For the "gaining stream" configuration the upstream sluice-gate was almost completely closed. This resulted in a drop in water level across the gate. As the downstream sluice-gate was also lowered, the upstream sluice gate was "drowned out" (i.e. the flow downstream of the gate remained sub-critical).

As the SAP spheres were close to neutrally buoyant, an unconfined layer of SAP spheres would be entrained and scoured away very easily by the surface flow. After unsuccessful attempts to use both plastic and steel mesh to hold the layer of SAP spheres in place, a "stream-bed layer" was manufactured out of 10 mm thick polycarbonate sheet. A regular pattern of slots, aligned with the flow direction, was cut through the polycarbonate with a CNC water-jet cutter. A number of transverse ribs were left to provide lateral stiffness, so that the sheet remained as flat as possible when placed on top of the SAP spheres. A CAD drawing of the polycarbonate layer is shown in Figure 5.5.

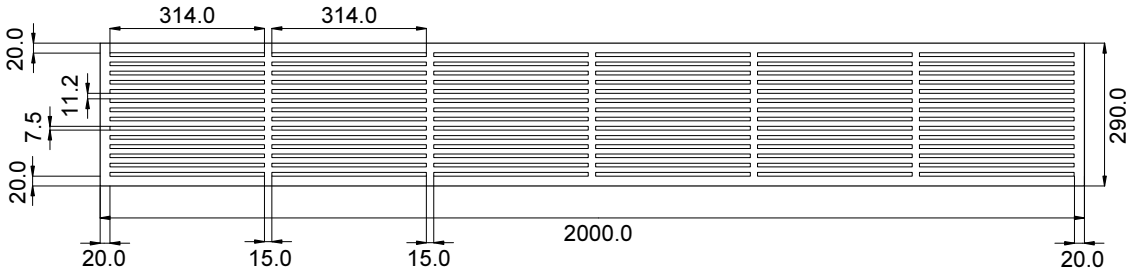

Figure 5.5: Polycarbonate "stream-bed layer". Dimensions are in mm.

The open slots in the polycarbonate stream-bed layer were made as wide as possible without allowing the SAP spheres to escape. Slots rather than circular holes were used because the spheres would tend to block the holes.

5.3.3 Lighting

The mid-section of the flume (containing the porous layer) was covered with a portable marquee and black polythene sheeting to provide blackout conditions for experiments.

The lighting for the PTV experiments was generated by a linear array of 66 white light-emitting diodes (LEDs) approximately 1.5 m long. The LEDs were mounted in an aluminium frame in 6 modules of 11. Each module had a heat-sink attached. The light from the LEDs was projected between parallel aluminium plates to form a continuous sheet of light approx 10 mm thick. A transparent acrylic stiffener was positioned between the aluminium plates to maintain the gap between them.

A plywood frame was attached to the light-sheet generator. This was supported on two plywood cross-members that rested on the flume's steel frame. This arrangement allowed the horizontal position of the light-sheet generator to be easily changed. As the flows in the flume did not take up the full depth the light-sheet generator was positioned within the flume so that the bottom edge of the parallel plates was close to the expected maximum water depth. This minimised spreading of the light-sheet. Figure 5.6 shows the light-sheet generator in position in the flume.

Initial tests with the SAP spheres showed that image quality started to degrade if the section illuminated by the light-sheet was viewed through more than 60 mm of porous medium. Therefore the light-sheet was positioned no more than 60 mm from the wall of the flume.

The thickness of the light-sheet was approximately the same as the diameter of the SAP spheres. If the packing of the SAP spheres is assumed to be approximately rhombohedral, which is consistent with the porosity measurements reported in Section 5.4.1, then the illuminated thickness will correspond to one pore space on average (Graton and Fraser, 1935). On a pore scale the flow through the porous media is three-dimensional and some motion will be out of the plane of the light-sheet. If the light-sheet is aligned with the mean flow, however, it is reasonable to assume that there is no net out-of-plane motion.

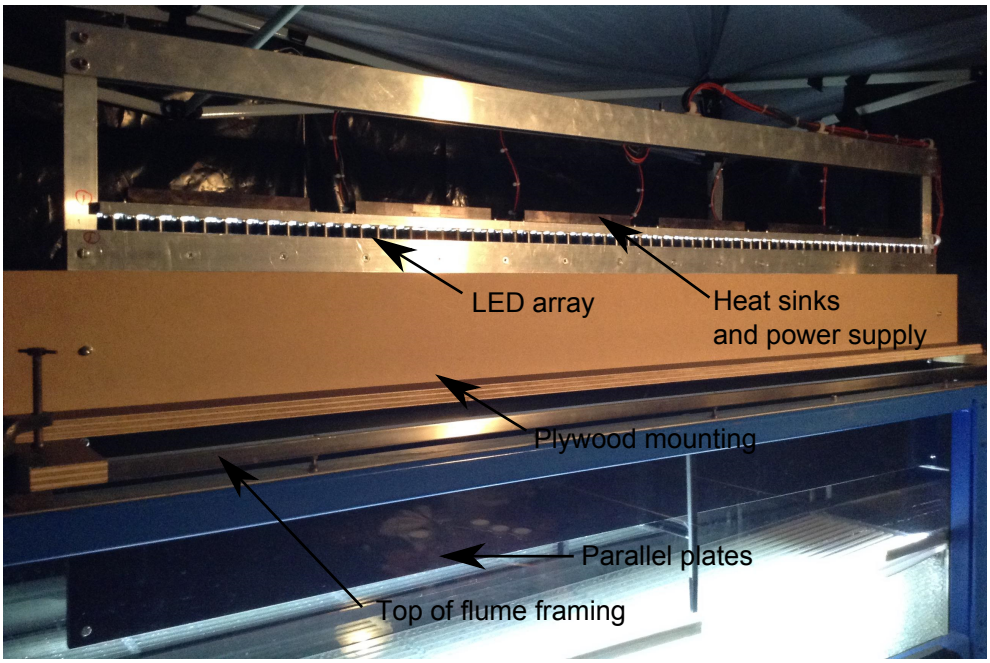

Figure 5.6: Light-sheet generator, positioned in flume

5.3.4 Particles

The particles that were added to the flow for PTV were Pliolite VTAC (Vinyl Toluene Acrylate) resin, ground to a particle size range of $180 - 250\mu m$. Pliolite is a polymer that is typically used as an ingredient of paints and coatings. The size range used ensured that the particles were dynamically unimportant in the flow.

The pliolite particles have a specific gravity of 1.03 (Omnova Solutions, 2012) and therefore settled over time in the flume and reservoir, particularly if water was not flowing. Because the flume's water supply was recirculating, once sufficient particles had been introduced to the system they were then present for multiple runs. However, it was necessary to stir the flume's reservoir with a paddle to re-suspend particles if the flow was stopped between runs. Over time some particles settled out in areas that could not be reached to re-suspend them, so it was occasionally necessary to add more particles to ensure that there were enough in the flow. This was done by eye rather than working to a specific concentration.

The settling velocity of the particles in a quiescent fluid was calculated using Stokes Law:

$$v_s = \frac{g\left(\rho_p - \rho_w\right) d_p^2}{18\mu} \tag{5.1}$$

where ρ_p is the particle density, ρ_w is the density of water, d_p is the particle diameter and μ is the dynamic viscosity of water. This equation is valid if the particle Reynolds number is less than 1. For the size range of pliolite particles used, the theoretical settling velocity was 0.53 - 1.02 mm/s, with particle Reynolds numbers ranging from 0.1 - 0.26. Observations of the particles in a quiescent fluid indicate that the actual settling velocity is significantly slower than the range calculated using Stokes Law. It is possible that this was due to the particle diameters being smaller than specified, minute air bubbles being trapped on the surface of the particles, or that some of the assumptions in Stokes Law, such as the particles being smooth spheres, are not met.

In the surface flow and in the subsurface flow near the interface, flow velocities were substantially higher than the theoretical settling velocity, and the effect of particle settling could therefore be ignored. In some areas of the porous layer, flow velocities were closer to the settling velocity. However the relatively uniform packing of the SAP spheres in the porous matrix ensured that there were no continuous vertical flow paths of more than a few millimetres, and a particle that was settling under gravity rather than moving with the flow field would soon make contact with one of the SAP spheres and stop moving. Particles that made contact with the SAP spheres tended to remain adhered to the sphere surface for the remainder of the experimental run. This is unlikely to have introduced significant error into the PTV analysis, as particles that settle out of the flow made contact with the surface of a SAP sphere within a timeframe that was significantly shorter than the length of the time-averaging period. Therefore the influence of the settling velocity on the calculated time-averaged velocities is likely to be limited.

5.3.5 Image capture system

Images were captured with a Jai AM-201GE monochrome camera with 1920 x 1080 pixels resolution, and a Goyo 50 mm fixed focal-length high-transmission lens. The camera was connected to a PC with an ethernet cable, and bitmap images were saved directly onto the computer's hard-drive at 38.3 frames per second. The focus and aperture were controlled manually with the lens. Other settings, such as shutter speed and the number of frames to be recorded in a run, were controlled via in-house image-capture software.

The camera was oriented perpendicular to the flume, approximately 2 m from the flume wall. A schematic of the camera and light-sheet orientation is shown in Figure 5.7.

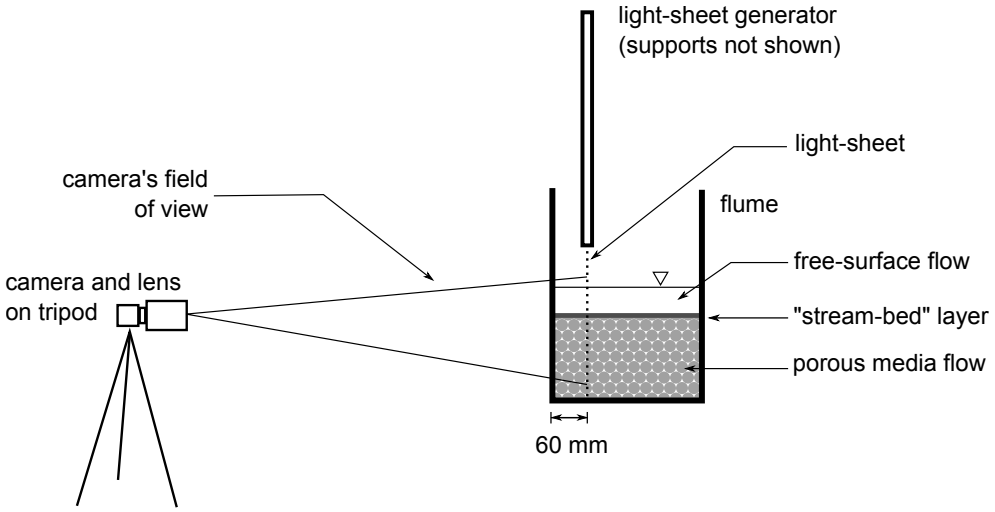

Figure 5.7: Cross-section showing orientation of camera and light-sheet

5.4 Measurement of Transparent Soil Hydraulic Properties

5.4.1 Porosity

The porosity of the SAP spheres was measured using the following procedure:

1. An acrylic cell of known volume was filled with hydrated SAP spheres, taken from a larger sample. This is shown in Figure 5.8a.

2. A cover was placed on the test cell to hold the spheres in place, and the cell was then filled to approximately 80% with a hose inserted through a hole in the cover (see Figure 5.8b).

3. A steel spatula was used to agitate air bubbles out of the pore space, ensuring that the void spaces were fully saturated.

4. The test cell was then completely filled, until water was overflowing between the top of the tank and the cover.

5. The contents of the test-cell were decanted out, with the SAP spheres caught in a sieve.

6. The pore-water volume was measured in a measuring cylinder.

The porosity was then calculated as follows:

$$\phi = \frac{V_v}{V_{total}} \tag{5.2}$$

where V_v, the volume of voids, is equal to the measured volume of pore water.

The porosity measurement was repeated four times. Between each test the SAP spheres from the test cell were re-combined with the larger sample to ensure that the particle size distribution at each repetition was representative of the larger sample. This, in turn, was assumed to be representative of the particle size distribution of the SAP spheres used in the flume.

The results of the porosity testing are shown in Table 5.1.

5.4.2 Hydraulic conductivity

A constant head permeability test was used to measure the hydraulic conductivity of the transparent soil. This is the test usually used for determining the permeability of coarse-grained soils in a geotechnical context (Craig, 1997). Iskander and Tabe (2010) give values of hydraulic conductivity for SAP spheres that

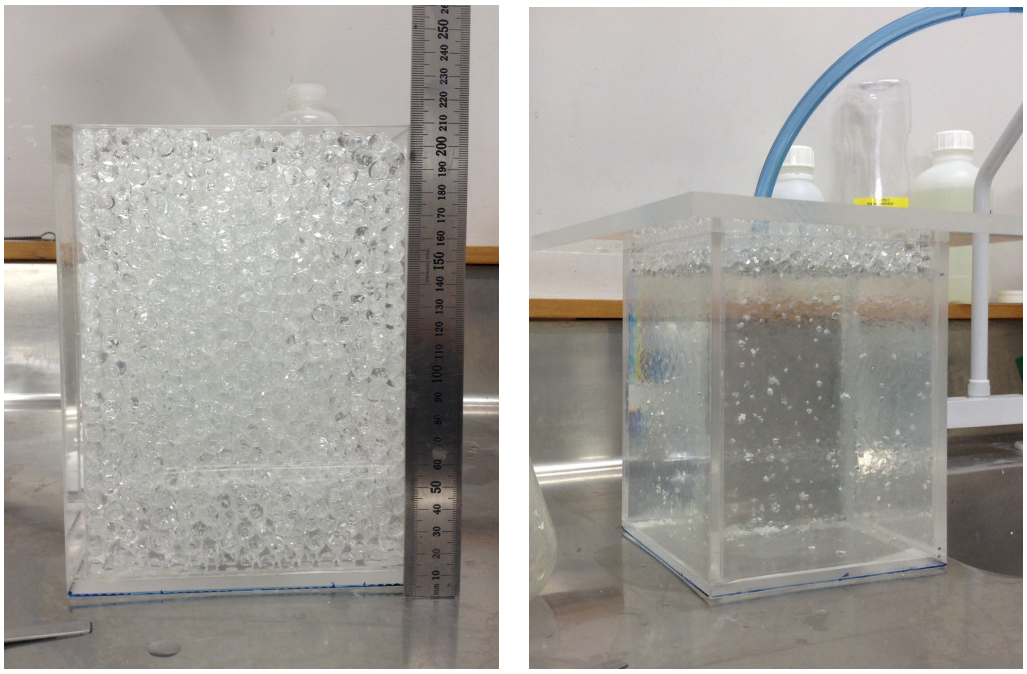

(a) unsaturated *(b) during filling*

Figure 5.8: Porosity measurement cell

Table 5.1: Porosity measurements

Measurement No.	Total volume (ℓ)	Pore-water volume (ℓ)	Porosity ϕ
1	4.41	1.04	0.236
2		1.03	0.234
3		1.01	0.229
4		1.02	0.231
		Mean:	0.233

are consistent with natural sands and gravels, therefore a constant-head test is considered to be appropriate.

It is noted that in geomechanics the terms permeability and hydraulic conductivity appear to be used interchangeably. In porous media flow, however, permeability normally refers to intrinsic permeability, which is a property of the porous matrix, whereas hydraulic conductivity is a flow property, incorporating aspects of the porous matrix and the fluid. The measurement provided by a constant head permeability test is the hydraulic conductivity.

In the constant head permeability test the soil sample is held in a cylinder of cross-sectional area A, with filters at each end. A steady flow of water is supplied from a constant-head tank and allowed to flow vertically through the soil sample. The hydraulic gradient ($\frac{dh}{dl}$) is measured from piezometers connected to pressure tappings on the test cylinder. Combined with a measurement of the volumetric flow rate, this allows the hydraulic conductivity to be calculated using Darcy's Law, as follows:

$$K = \frac{ql}{Ah} \tag{5.3}$$

where q is the volumetric flow-rate, l is the distance between pressure tappings, h is the difference in total head and A is the cross-sectional area of the soil sample, as illustrated in Figure 5.9.

The test apparatus used is shown in Figure 5.10.

The results of the conductivity tests are shown in Table 5.2. The values measured correspond to the upper end of the indicative range for clean sands and sand-gravel mixtures (Craig, 1997).

Figure 5.11 shows the results from all three conductivity test runs on a single chart, with a linear trendline applied to all the data. The error bars on the data points in the figure were based on the estimated precision of the hydraulic gradient and discharge measurements. The high R^2 value shows that the relationship between the discharge and the hydraulic conductivity is strongly linear, and that Darcy's Law is therefore applicable for determining the hydraulic conductivity.

To check the validity of the constant-head test for measuring the hydraulic conductivity of the SAP spheres, the pore Reynolds number,Re_p, was calculated

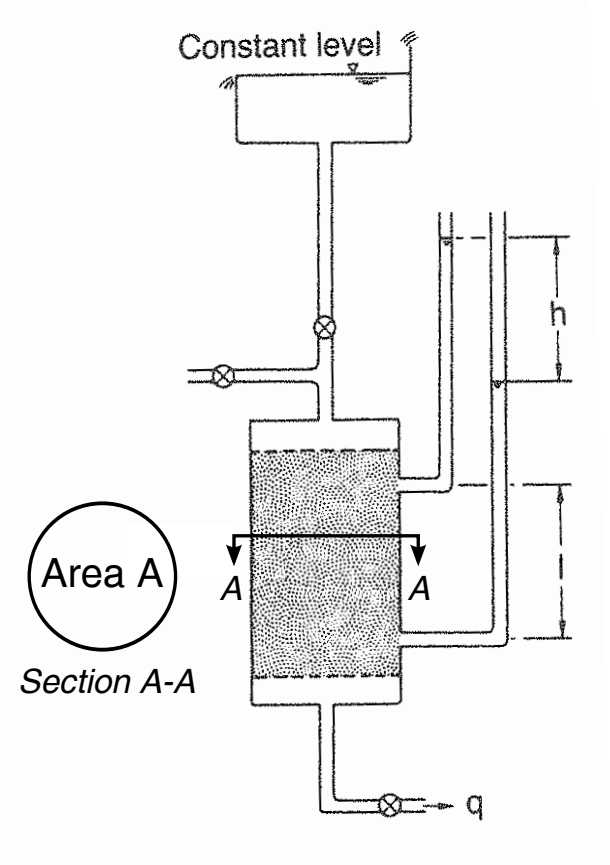

Figure 5.9: Schematic of constant-head permeability test, modified from Craig (1997)

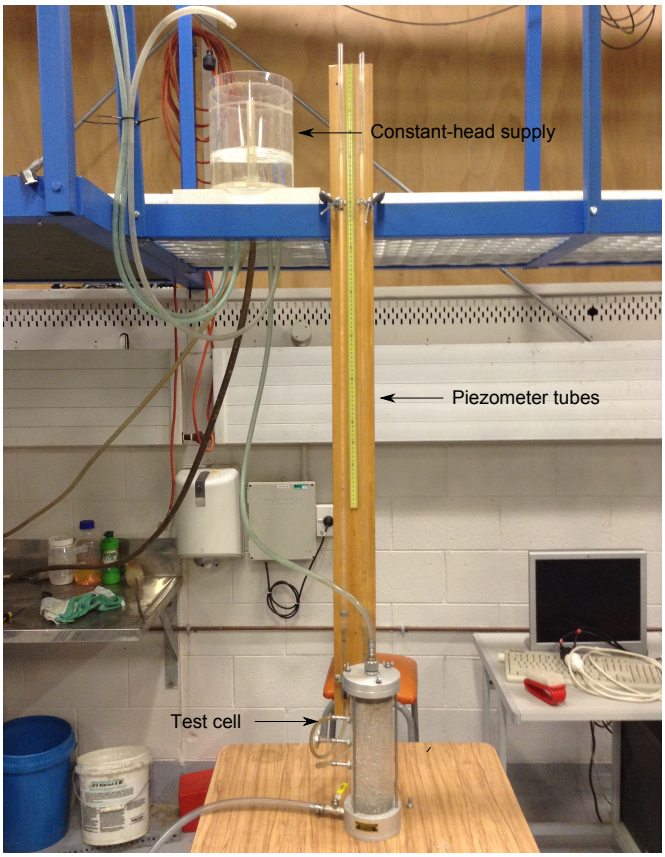

Figure 5.10: Constant-head permeability test rig

Table 5.2: Hydraulic conductivity measurements

Run	Discharge, q (l/s)	hydraulic gradient $\frac{dh}{dl}$	Conductivity, K (m/s)
1	1.74×10^{-3}	10	3.95×10^{-2}
	4.10×10^{-3}	20	4.64×10^{-2}
	6.52×10^{-3}	35	4.21×10^{-2}
	7.30×10^{-3}	40	4.13×10^{-2}
		mean:	4.23×10^{-2}
2	2.53×10^{-3}	15	3.82×10^{-2}
	4.90×10^{-3}	25	4.44×10^{-2}
	6.72×10^{-3}	35	4.35×10^{-2}
	7.31×10^{-3}	40	4.14×10^{-2}
		mean:	4.19×10^{-2}
3	1.92×10^{-3}	10	4.35×10^{-2}
	3.55×10^{-3}	20	4.01×10^{-2}
	6.76×10^{-3}	35	4.37×10^{-2}
	8.01×10^{-3}	45	4.03×10^{-2}
		mean:	4.19×10^{-2}
		overall mean:	4.20×10^{-2}

to determine if the flow through the test cell was Darcian. Using the definition of the pore length scale from Ward (1964) - $d \approx \left(\frac{k_i}{\phi}\right)^{\frac{1}{2}}$ (where k_i is the intrinsic permeability and ϕ is the porosity) - the values of Re_p range from 0.05 to 0.24. The upper limit for fully Darcian flow is a pore Reynolds number "somewhere between 1 and 10" (Bear, 1972). Therefore for the range of flows tested the flow was Darcian, and the constant-head test was a valid method.

During permeability testing it was found that the SAP spheres were not dimensionally stable when exposed to a high-velocity flow for a long period of time. The spheres in the permeability test cell became smaller and substantially less transparent when the test was run with the discharge valve fully open under a 2 m constant head for approximately one hour. The same occurred at lower flow rates, over a longer timeframe. This effect was not seen when the test cell was left under the same static head with no flow. It was highly desirable to prevent this happening to the SAP spheres in the flume, firstly because the geometry (and therefore the hydraulic properties) of the porous medium were changing

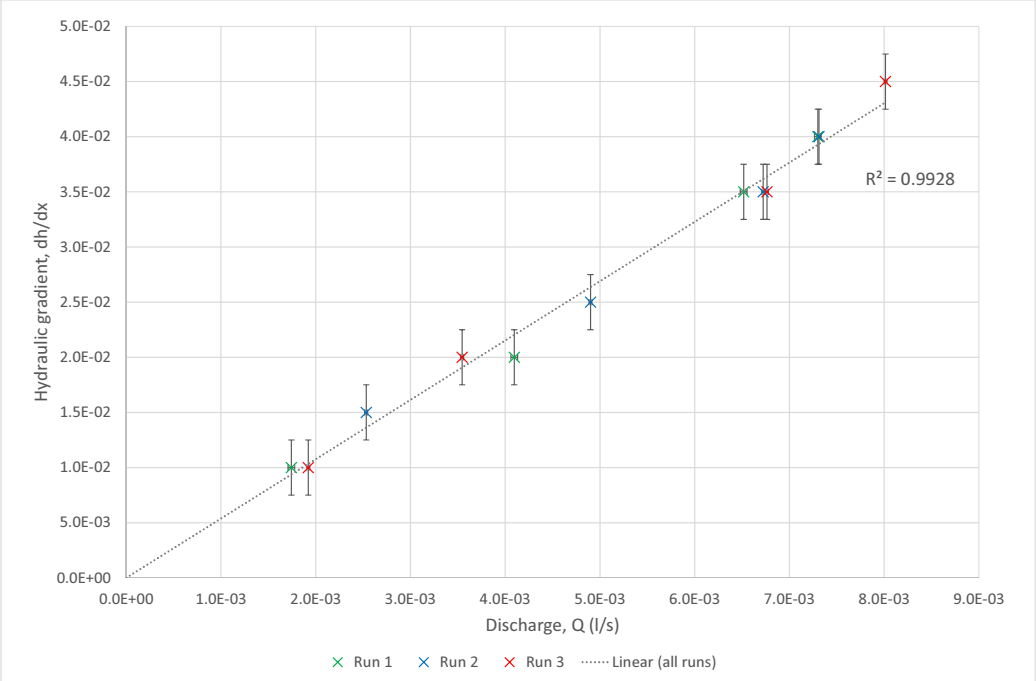

Figure 5.11: Hydraulic conductivity test results with linear trendline

over time, and secondly if the transparency of the porous medium reduced then the quality of the PTV data would be degraded. To reduce the risk of the SAP sphere dimensions and transparency changing in the flume the amount of time that water was flowing through the porous layer was minimised by closing the bungs at the downstream end of the false-floor section between experimental runs. Configurations that resulted in very high flow velocities in the porous layer were also avoided.

5.5 Experimental Procedure

The procedure that was followed for each experimental run is detailed below:

1. Ensure SAP spheres are fully hydrated and packed to the correct level in the flume.

2. Start pump and ensure that all air is purged from inlet pipework.

3. Fill flume up to false-floor level to saturate the porous layer. Stop pump and close flume inlet valve.
4. Remove air-bubbles from porous layer by manual agitation / stirring.
5. Replace polycarbonate "stream-bed" layer and secure in place.
6. Align light-sheet and camera. Check focus, aperture and exposure settings.
7. Record images of a ruler, to allow length scales to be set during processing.
8. Start pump and monitor flow depths and flow-meter output until steady-state is reached and subsurface region is well seeded with particles.
9. For "losing stream" configuration, remove downstream bungs and wait for new steady-state flow to be reached.
10. Start camera; monitor flow depth with a point gauge during run.
11. Check flow depth and flow-meter output at end of run.
12. Replace downstream bungs if necessary and stop flow.

Removing air-bubbles from the void spaces in the porous layer was necessary to ensure the success of the PTV analysis. Air bubbles affected the transparency of the SAP spheres, and any illuminated bubbles showed up as bright patches in the PTV images. It was also necessary to ensure that the porous layer remained fully saturated during and between runs so that no new air bubbles formed.

Because flow velocities in some areas of the porous layer were very low, it was necessary to allow sufficient run-up time for particles to reach these areas before data was collected. Neglecting to do this would affect the quality of the time-averaged results.

5.6 Experimental Data Analysis

The following sequence of processes was used in Streams to generate velocity fields:

1. Image files were assembled into an image sequence, with information about temporal (time-step between frames) and spatial scales (mm/pixel).
2. Sequential image frames were subtracted to remove non-mobile particles from the image sequence.
3. A particle identification algorithm was applied, with diameter and intensity thresholds specified, to create a particle record (i.e. a representation of the identified particles in the image sequence).
4. The particle matching process was undertaken (further details below) to match particles between frames.
5. Velocity fields were created, converting the Lagrangian path information from the particle tracks to Eulerian fields.

Figure 5.12 shows a raw image from the PTV process. The "stream bed" layer is clearly visible and faint outlines of the SAP spheres in the illuminated region can be seen. It should be noted, however, that the SAP spheres between the light sheet and the wall of the flume are not visible.

Figure 5.13 shows the same image after an image subtraction process has been applied. Subtracting sequential images removed stationary objects, leaving only the mobile particles visible.

Figure 5.14 shows examples of the results of the particle identification process. Figure 5.14a shows a single frame, while Figure 5.14b and Figure 5.14c show 10 and 200 sequential frames from the particle record, respectively. Displaying the particles for multiple frames gives an indication of the flow structure. In particular, Figure 5.14c gives an impression of the tortuous path that particles take through interconnected pore spaces. However, at this stage of the analysis there is no information about how particles are connected from frame to frame.

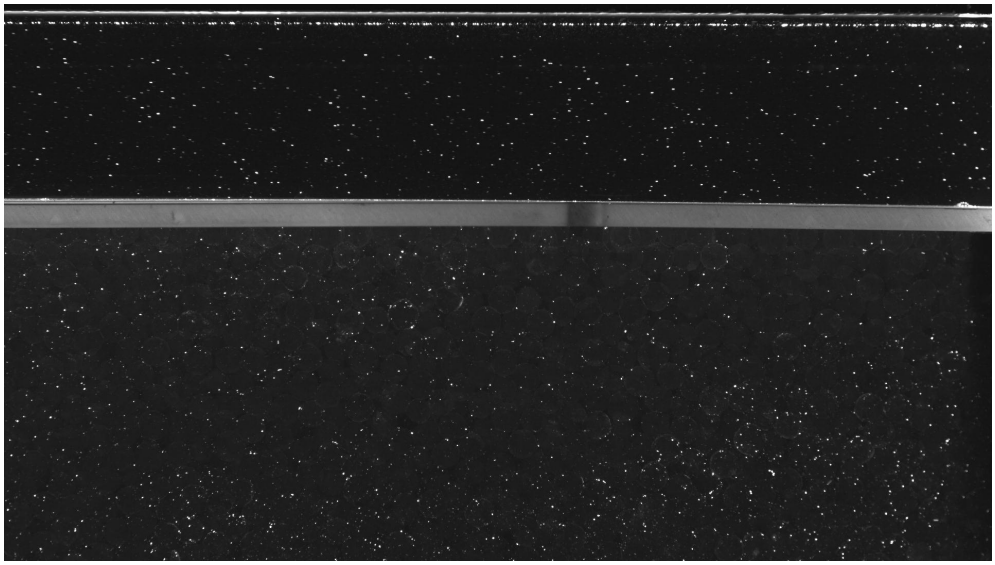

Figure 5.12: Raw PTV image frame

Figure 5.13: PTV image frame after subtraction of sequential frames

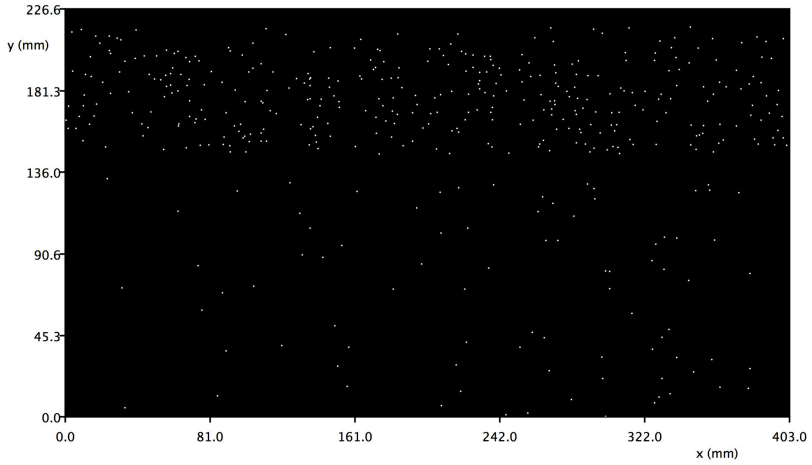

(a) One frame

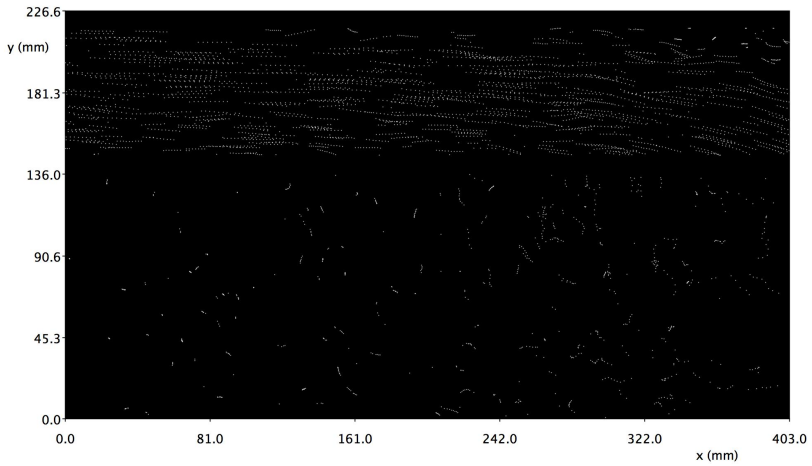

(b) Ten sequential frames

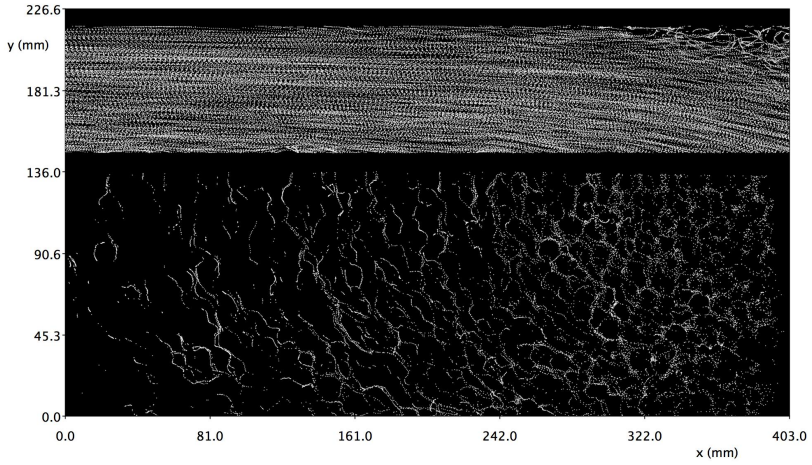

(c) 200 sequential frames

Figure 5.14: Particle identification

PTV analysis for the surface and subsurface flow regions was done separately, as different settings were used for the two flow regions. In the surface flow the density of particles was greater, and it was more likely that a particle could be matched from frame to frame. There were typically 250 - 350 particles per frame in the surface region, and 80 - 90% of these were able to be matched. In the subsurface region 60 - 80 particles per frame were typically detected, and 50 - 60% of these were able to be matched. The lower matching rate can most likely be attributed to some particles not being visible in sequential frames due to pore-scale motion out of the plane of the light-sheet.

For both the surface and subsurface flow regions a distance costing with local optimisation was used initially. In the most simple implementation of the distance costing, the cost of matching particles in sequential frames is proportional to the distance between the particles. In Streams an additional level of sophistication can be introduced to the distance costing by adding a user-defined velocity profile. The costing is then based on the distance between a particle in frame 2 and the position that would be reached by a particle from frame 1 travelling at the specified velocity. Using this method, if the velocity profile could be specified exactly, the predicted position of the particle from frame 1 would coincide exactly with its best match in frame 2. Although it is not generally possible to specify the velocity profile exactly, particularly for a turbulent flow, specifying an estimated profile improves the performance of the distance costing.

In the surface region the search window was defined slightly downstream of the position of the particle in the first frame, and a horizontal velocity was specified. In the subsurface region, where the flow direction was less predictable and velocities lower, the search window was smaller and centred on the first-frame particle. No estimate of the velocity was pre-defined in the subsurface region.

Following the distance-based optimisation a clean-up process was run in both layers. This process checked the validity of the particle matches created by the initial optimisation, and removed any matches where a threshold cost was exceeded. The costing used for the clean-up process was based on recent velocity. This costing strategy is based on the assumption that accelerations in the flow are small. Therefore if the velocity of a particle is known for a particular image frame then its position in the following frame can be estimated.

Figure 5.15 shows particle tracks for the two regions, which have been recombined after the PTV analysis was complete. Figure 5.15a shows 10 sequential frames and Figure 5.15b shows 200 frames. These are the same frames as Figures 5.14b and 5.14c.

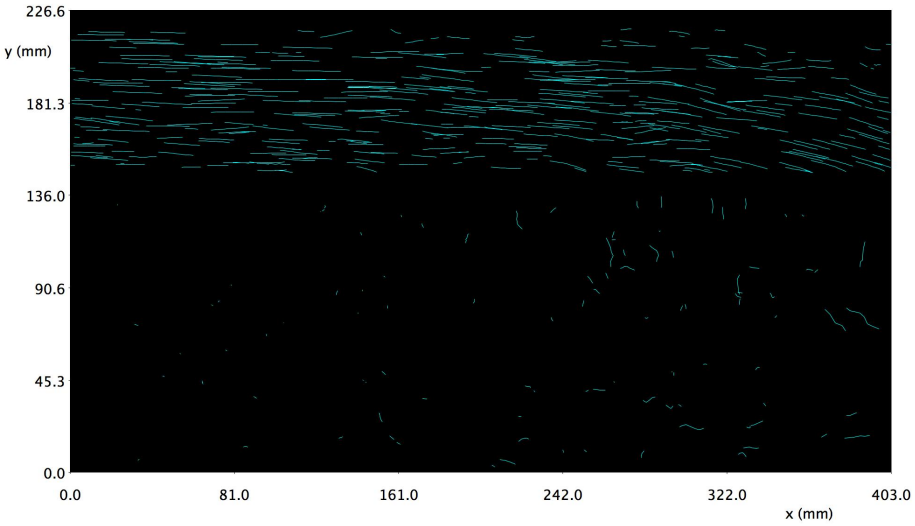

(a) Ten sequential frames

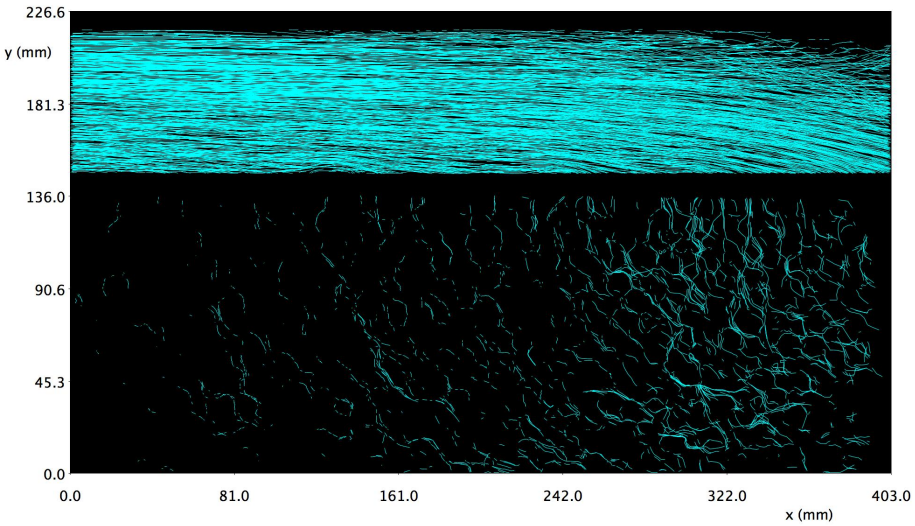

(b) 200 sequential frames

Figure 5.15: Particle tracks

The PTV analysis process in Streams does not include any information about the solid fraction of the porous matrix; there is nothing to differentiate it from the pore space, and the analysis treats the flow in the subsurface layer as a clear fluid flow. Therefore the subsurface velocity fields calculated in Streams are interpolated values of the local pore velocity, irrespective of whether that velocity could actually occur at any given point. The measured porosity (Table 5.1) can be used to transform the interpolated pore velocities to Darcy flux velocities. The velocity interpolation process is discussed further in Section 5.6.1.

5.6.1 Velocity field interpolation

A number of options are available in Streams for interpolating Eulerian velocity fields. The default option is triangulation-based, with no limitation on the size of the triangles. In a flow that is well-seeded with particles, this method tends to create triangles that are not long and thin, and therefore the velocity interpolations within the triangle will be based on three particles that are "close together" (Nokes, 2013). However, in a more sparsely-seeded flow, such as the sub-surface region, triangulation may result in interpolation between particles that are widely-spaced. This is illustrated in Figure 5.16.

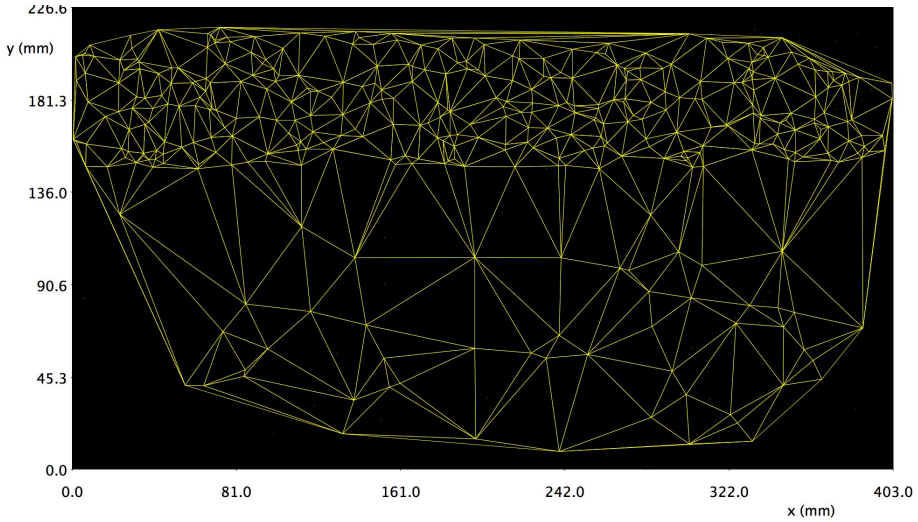

Figure 5.16: Example of triangulation

An alternative to triangulation is binned interpolation, where a rectangular region, or bin, is defined around each grid point. The velocities of the particles that fall within the bin are averaged to give a velocity at the grid point. If there are no particles within the bin area then the velocity is undefined.

For a flow such as the subsurface region, with relatively sparse particle seeding, successful velocity field creation requires finding a balance between the size of the interpolation region and getting sufficient coverage to provide meaningful time-averaged fields. Coverage is defined as zero if no velocity estimate exists at a grid point, and one if an estimate does exist. The time-averaged coverage field can be used as an indication of the success of an interpolation method, although this needs to be interpreted in the context of the size of the interpolation regions.

Four different interpolation methods were tested for the subsurface flows: triangulation with no size restriction (the default setting), triangulation with 40 mm size limit, 20 mm binned and 40 mm binned. Figure 5.17 shows the time-averaged coverage for each method. Although triangulation with no size limit (Figure 5.17a) gave high values of time-averaged coverage, this was due to large interpolation regions, which potentially reduce the accuracy of the velocity fields. Restricting the size of the triangles to 40 mm (Figure 5.17b) resulted in substantially lower coverage values. Similarly low coverage values were obtained using binned interpolation with the bin size set to 20 mm (Figure 5.17c). Increasing the bin size to 40 mm (figure 5.17d) provided a balance between coverage and interpolation region size, and this was the method that was used to produce the velocity fields. The suitability of this method was confirmed with flux balance checks (see Section 5.6.4). The binning method is closely aligned to the spatial-averaging approach that is used in the numerical model.

5.6.2 Flow stability

During the experimental runs the flow meter output and the depth of the free-surface flow were monitored to ensure that the flow in the flume was at steady-state.

As a further check, linear trendlines were fitted to the instantaneous velocity data at various points in the flow. A trendline with approximately zero slope was

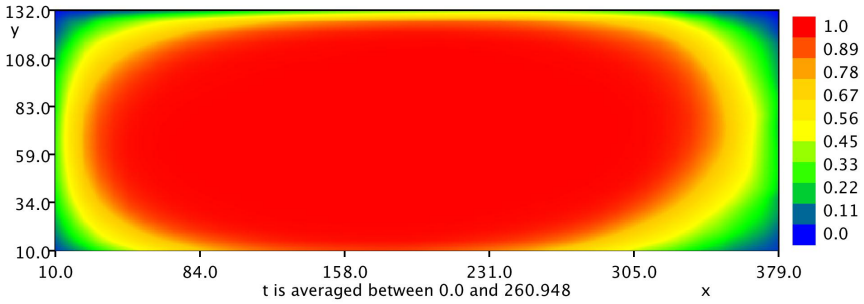

(a) Triangulation, size unlimited

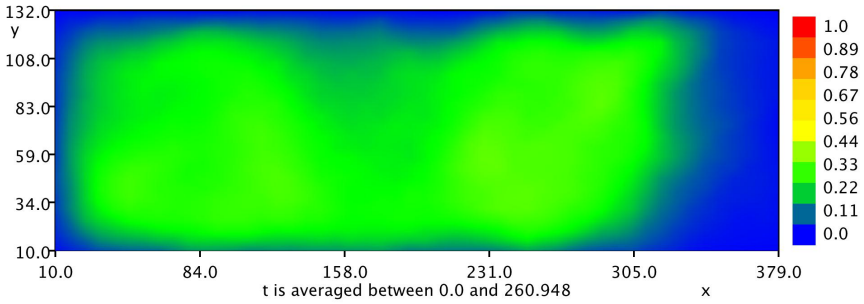

(b) Triangulation, 40 mm size limit

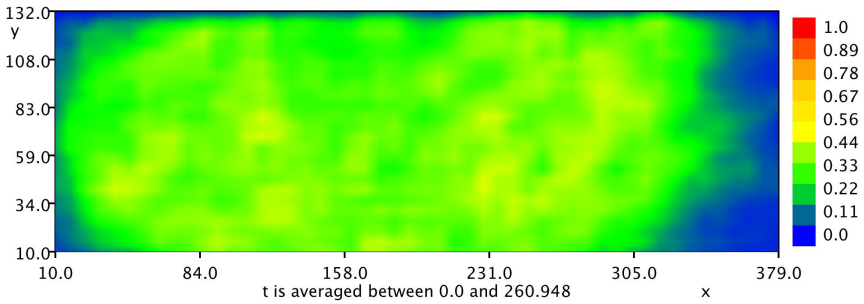

(c) Binning, 20 mm size limit

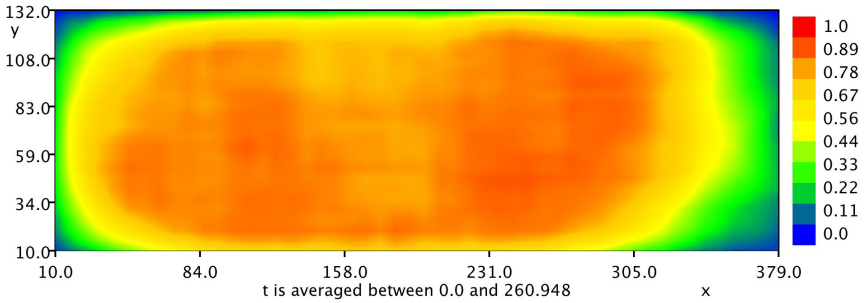

(d) Binning, 40 mm size limit

Figure 5.17: Time-averaged coverage for different interpolation schemes

considered to be confirmation that the flow was in steady-state. Figure 5.18 and Figure 5.19 show the instantaneous u-velocity at points in the surface layer and subsurface layer, respectively. In both figures the linear trendline is horizontal, showing that the time-averaged flow is steady over the length of the run (260 s).

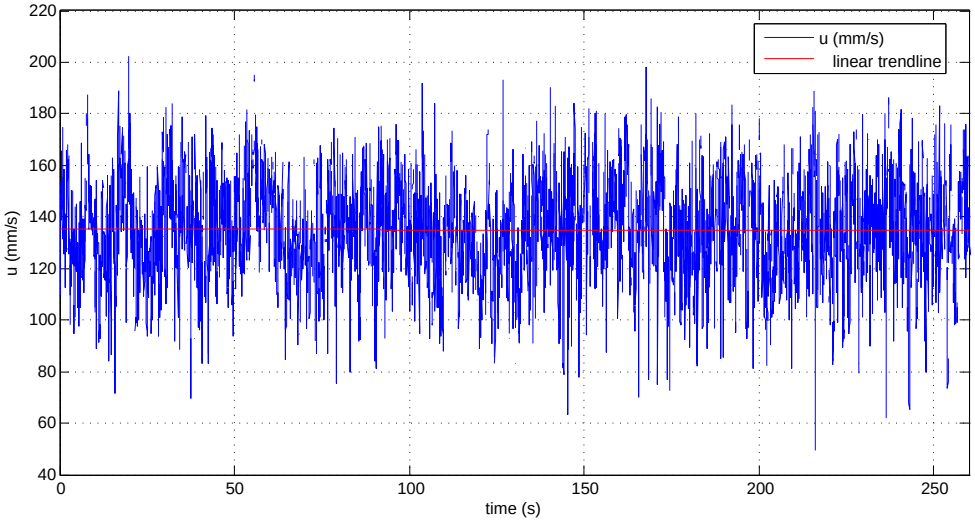

Figure 5.18: Instantaneous u-velocity; surface layer (x=270 mm, y=170 mm)

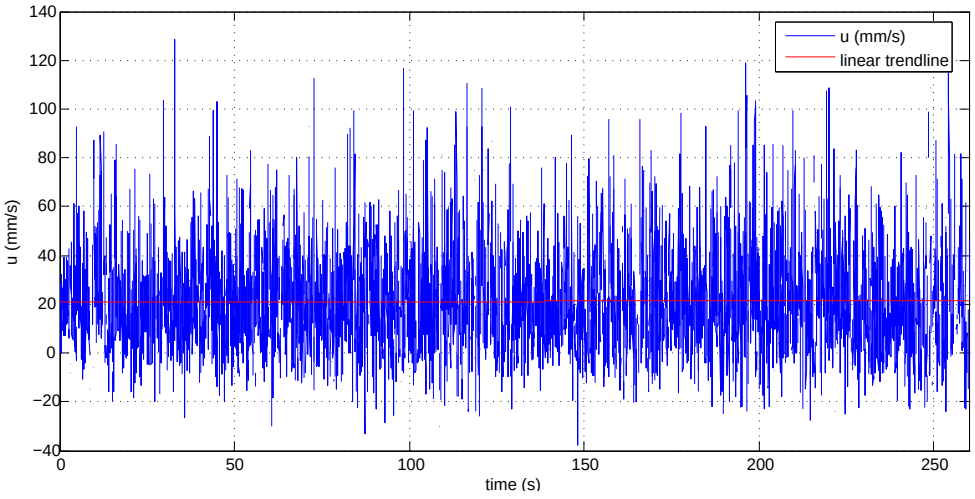

Figure 5.19: Instantaneous u-velocity; subsurface layer (x=55 mm, y=63 mm)

5.6.3 Repeatability

To check the repeatability of the methodology (both the experimental set-up and the data processing), a series of identical experiments was run for the "gaining stream" configuration. This was particularly important for the subsurface layer, as the image-capture system and the PTV analysis in Streams had not been applied to a porous media flow before.

Three runs were done with the light-sheet aligned with a slot in the polycarbonate layer, and three were done with the light sheet aligned with a bar. Each run was 10,000 image frames (263 seconds).

For each of these runs identical settings were used in all stages of the analysis process (particle identification, PTV and velocity field interpolation). The depth-averaged, time-averaged horizontal velocity in both layers, and the time-averaged vertical velocity along the stream-bed (i.e. the bottom of the analysis window for the surface flows and the top of the analysis window for subsurface flows), averaged in the x-direction were compared for the two sets of three runs. The locations used for the averaged velocities are shown in Figure 5.20.

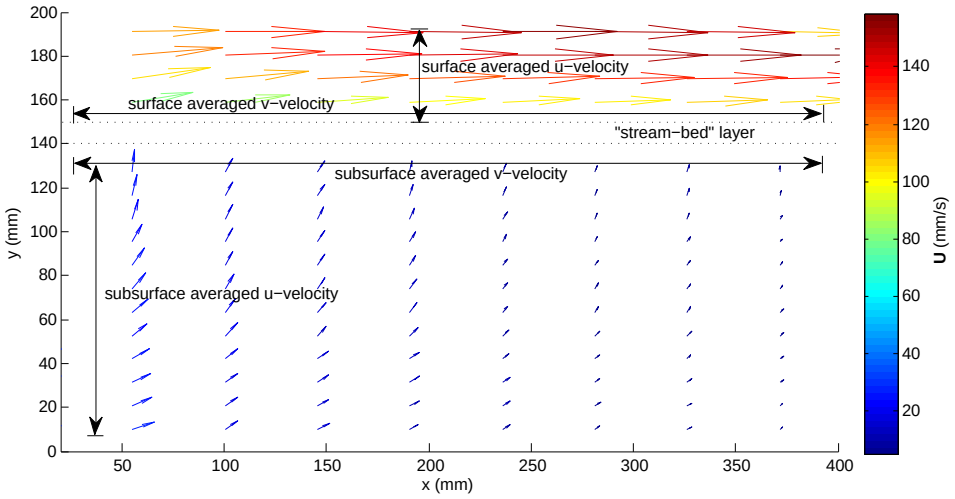

Figure 5.20: Location of averaged velocities for repeatability runs

The averaged surface flow velocities for the repeatability runs are shown in

Table 5.3. The horizontal (u) velocities are within ±2% of the mean value for both the runs aligned with the slot and those aligned with the bar. In absolute terms the variability in the vertical (v) velocities is similar to that of the u velocities, however as the v components are smaller the percentage error is higher. This is particularly the case for v velocities with the light-sheet aligned with one of the bars in the stream-bed layer. As expected, the velocities are substantially lower in this case as the bar is impermeable. The fact that non-zero v velocities are detected over the bar indicates that the light-sheet was also illuminating some particles in the cross-sections of the slots either side of the bar.

Table 5.3: Repeatability of averaged surface flow velocities

Run	u (mm/s)	% difference from mean	v (mm/s)	% difference from mean
Slot 1	126.7	1.6%	4.7	-2.8%
Slot 2	124.1	-0.5%	5.0	3.4%
Slot 3	123.4	-1.1%	4.8	-0.7%
mean:	*124.7*	*mean:*	*4.8*	
Bar 1	128.3	2.0%	1.15	26.4%
Bar 2	124.9	-0.7%	0.72	-20.9%
Bar 3	124.0	-1.4%	0.86	-5.5%
mean:	*125.7*	*mean:*	*0.91*	

Table 5.4 shows the averaged subsurface velocities for the repeatability runs. The u velocities were all within ±5% of the mean, and the v velocities were within ±2%.

Figures 5.21a and 5.21b show time-averaged horizontal and vertical velocity profiles, respectively, over the depth of the subsurface layer for the three runs with the light-sheet aligned with a slot. Figures 5.22a and 5.22b show the vertical velocity profiles for the three runs with the light-sheet aligned with a bar. In all cases the location of the velocity profiles is $x = 198\ mm$, approximately the mid-point of the view for this set of runs.

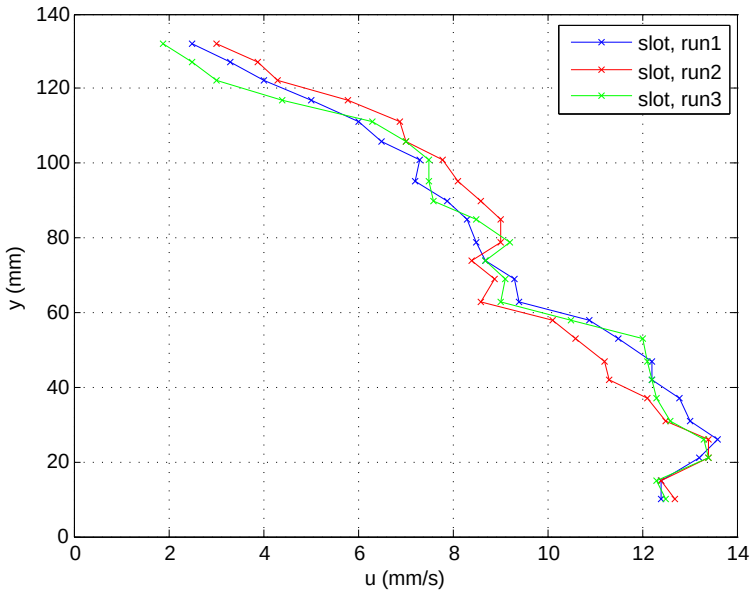

(a) U-velocity profile

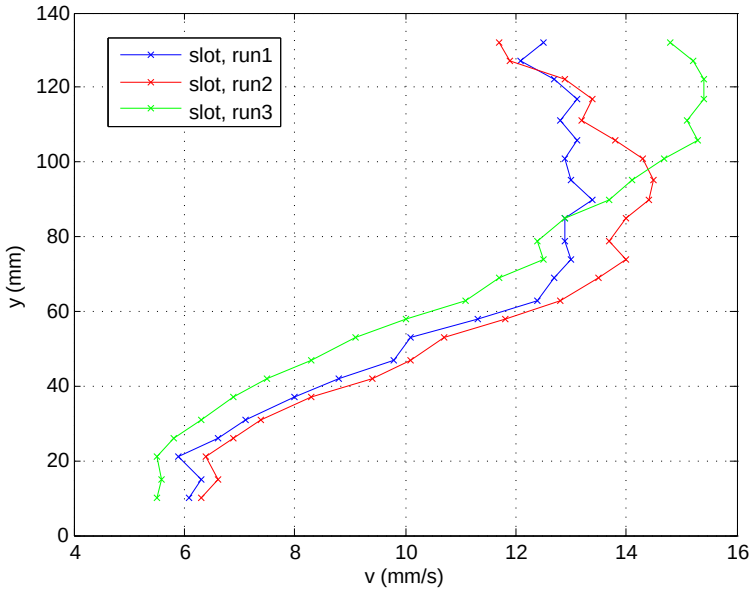

(b) V-velocity profile

Figure 5.21: Subsurface velocity profiles for repeatability runs aligned with slot

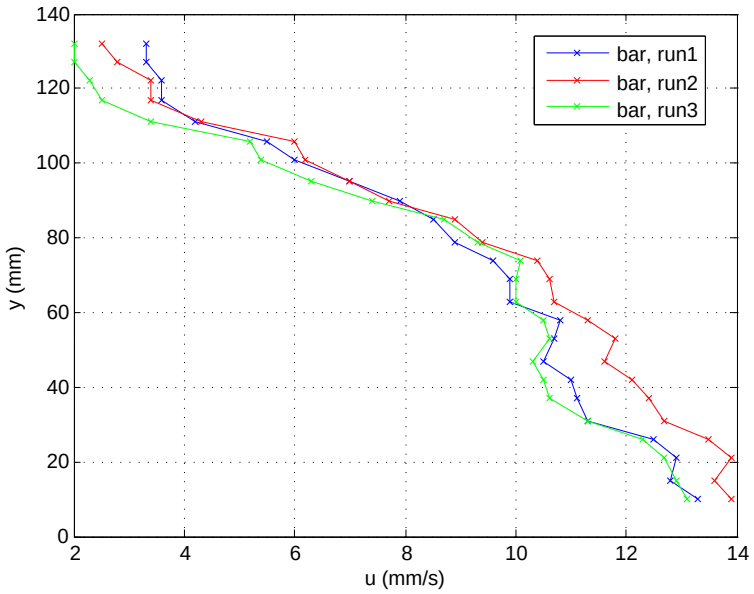

(a) U-velocity profile

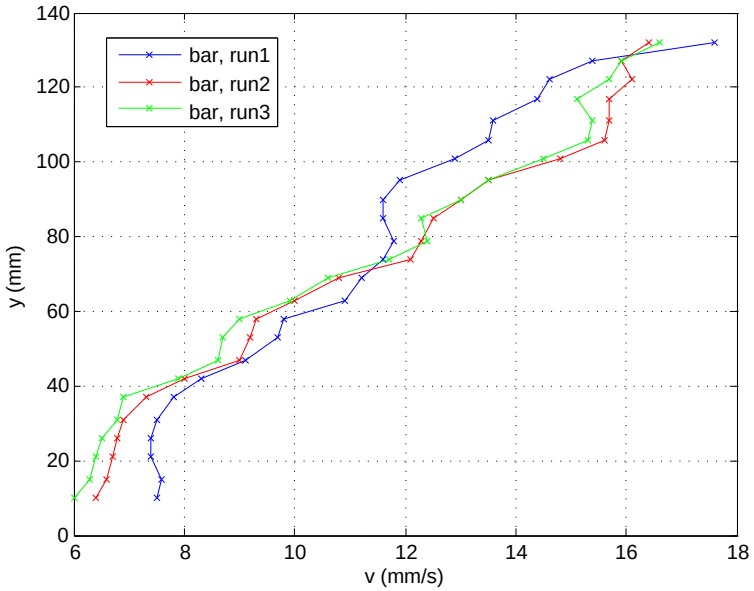

(b) V-velocity profile

Figure 5.22: Subsurface velocity profiles for repeatability runs aligned with bar

Table 5.4: Repeatability of averaged subsurface flow velocities

Run	u (mm/s)	% difference from mean	v (mm/s)	% difference from mean
Slot 1	25.4	-4.6%	14.6	-1.8%
Slot 2	27.2	2.1%	14.8	-0.4%
Slot 3	27.3	2.5%	15.2	2.2%
mean:	*26.6*	*mean:*	*14.9*	
Bar 1	26.0	1.4%	17.5	1.2%
Bar 2	26.2	2.2%	17.2	-0.6%
Bar 3	24.7	-3.6%	17.2	-0.6%
mean:	*25.6*	*mean:*	*17.3*	

5.6.4 Flux balance checks

Flux balances were checked for control volumes in both the surface and subsurface layers. The velocity components normal to the control volume boundaries were numerically integrated using Simpson's rule to give a 2D volume flux. The positions of the control volumes are shown in Figure 5.23

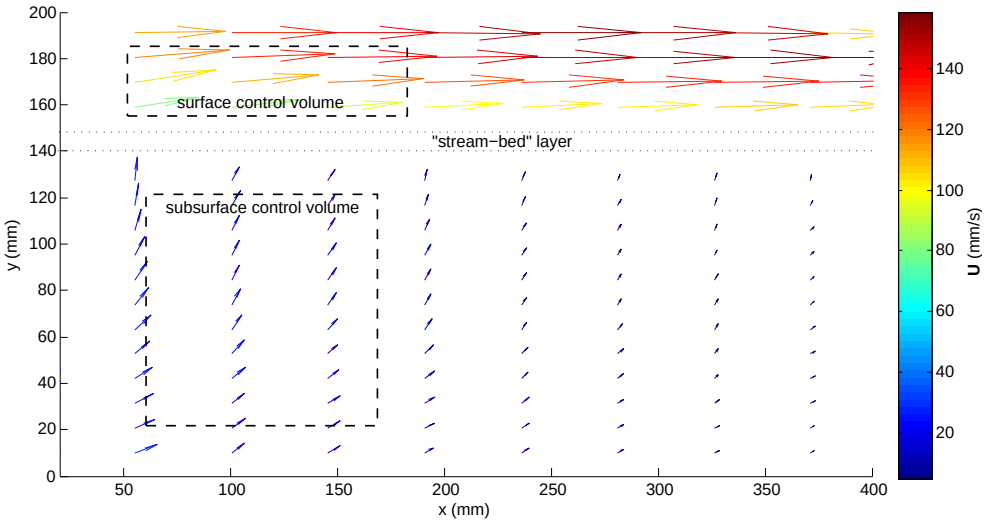

Figure 5.23: Positions of control volumes for flux balance checks

The results of the flux balance checks for the subsurface layer are shown in

Table 5.5. The results for the surface layer are shown in Table 5.6.

Table 5.5: Volume flux balances for subsurface layer

Run	Interpolation method	volume fluxes (mm^2/s) Q_{in}	Q_{out}	flux balance error
Slot 1	Binning, 40 mm	2627	2735	-3.9%
	Binning, 20 mm	2474	2642	-6.4%
	Triangulation, unlimited	2645	2909	-9.1%
	Triangulation, 40 mm	2586	2840	-8.9%
Slot 2	Binning, 40 mm	2703	2828	-4.4%
	Binning, 20 mm	2740	2755	-0.5%
	Triangulation, unlimited	2755	3038	-9.3%
	Triangulation, 40 mm	2654	2904	-8.6%
Slot 3	Binning, 40 mm	2792	2876	-2.9%
	Binning, 20 mm	2481	2776	-10.6%
	Triangulation, unlimited	2775	3206	-13.4%
	Triangulation, 40 mm	2698	3119	-13.5%
Bar 1	Binning, 40 mm	2952	2879	2.5%
	Binning, 20 mm	3035	2927	3.7%
	Triangulation, unlimited	2918	2943	-0.8%
	Triangulation, 40 mm	2939	2853	3.0%
Bar 2	Binning, 40 mm	3051	2973	2.6%
	Binning, 20 mm	3062	2876	6.5%
	Triangulation, unlimited	3053	3123	-2.3%
	Triangulation, 40 mm	3121	2992	4.3%
Bar 3	Binning, 40 mm	2987	3027	-1.3%
	Binning, 20 mm	2919	2800	4.2%
	Triangulation, unlimited	3019	2943	2.6%
	Triangulation, 40 mm	3078	2924	5.2%

In the subsurface layer the flux balance error for binning interpolation with a 40 mm size restriction was consistently within ±5%. Although for some of the individual runs the other interpolation methods had lower flux balance error values, their flux balance errors were larger overall. This, along with the time-averaged coverage (Figure 5.17) showed that binning with a 40 mm size restriction was the best choice for velocity field interpolation in the subsurface layer, and that the PTV methodology produces velocity fields that are within reasonable

Table 5.6: Volume flux balances for surface layer

	volume fluxes (mm^2/s)		
Run	Q_{in}	Q_{out}	flux balance error
Slot 1	4256	4281	-0.6%
Slot 2	4167	4135	0.8%
Slot 3	4300	4198	2.4%
Bar 1	4191	4353	-3.7%
Bar 2	3872	4014	-3.6%
Bar 3	3970	4190	-2.8%

error bounds for subsurface flows.

In the surface layer the flux balance errors were within ±4%.

In the subsurface layer the flux balance errors (shown in Table 5.5) tended to be negative (i.e. $Q_{in} < Q_{out}$) for the runs with the light-sheet aligned with a slot in the "stream-bed" layer. Conversely, for the runs aligned with a bar the error tended to be positive (i.e. $Q_{in} > Q_{out}$). This indicates that the geometry of the stream-bed layer was causing motion out of the plane of the light-sheet. For the "slot" runs there was a net unmeasured lateral inflow into the illuminated cross-section due to fluid being unable to pass vertically through the bars on either side. For the "bar" runs this was detected as a net unmeasured outflow.

In the surface layer the flux balances (Table 5.6) were negative for the all three "bar" runs and two out of three "slot" runs. Although this is the opposite to the subsurface runs, it is consistent with the concept of the stream-bed layer causing lateral motion. For the "bar" runs in the surface layer there is a net unmeasured lateral inflow from the neighbouring slots entering the illuminated cross-section.

Overall the "slot" runs are likely to be more representative of the mass and momentum fluxes between the layers as there is a more direct connection.

5.7 Chapter Summary

An experimental method was developed that allowed two-dimensional velocity fields to be measured in interacting surface and subsurface flows, using a combination of a refractive-index-matched transparent porous medium and optical

flow measurement. The primary purpose of the experimental programme was to gather a data set suitable for verifying the DANS numerical model, with an emphasis on measuring fluxes across the surface-subsurface interface.

In this chapter the principles of optical flow visualisation and measurement were introduced, in particular particle tracking velocimetry (PTV). The steps required to generate velocity fields in Streams using PTV were described.

The experimental set-up was described, including the flume, image-capture system, and the measurement of the hydraulic properties of the transparent porous medium.

A number of checks were done to ensure the stability of the flows and the repeatability of the analysis method. Flux balances were calculated to ensure that the PTV analysis produced reliable results in both the subsurface and surface layer. A number of options for velocity field interpolation were tested in order to achieve a balance between time-averaged data coverage and spatial resolution in the subsurface layer, where the PTV data was relatively sparse relative to the surface flow.

Chapter 6

Physical Modelling Results

This chapter contains the results of the experimental programme: mean flow fields, horizontal and vertical velocity profiles, and turbulent statistics. The results are discussed qualitatively. In Chapter 7 the results are quantitatively compared to numerical model outputs.

6.1 Summary of Experimental Programme

Runs were done for the following three configurations:

1. Impermeable bed. A thin sheet of acrylic was placed beneath the stream-bed layer to create an impermeable no-slip boundary.

2. "Gaining stream". A pressure gradient was created to drive flow vertically upwards through the stream-bed layer.

3. "Losing stream". The downstream end of the subsurface layer was allowed to drain freely into the cavity beneath the false floor.

For each of the three configurations data was collected both with the light-sheet aligned with a slot in the stream-bed layer, and aligned with a bar. There were subtle differences in the results from the two lateral positions as the bars in the stream-bed layer create a local impermeability and no-slip condition. The overall aim of the experimental programme, however, was to model the effect of a

permeable bed, and the alternating bar and slot structure was simply a means of retaining the porous medium. Therefore the data points from each set of "bar" and "slot" runs were averaged to give results that were representative of the flow structure integrated across the width of the flume.

Figure 6.1 shows the positions of the measurement windows for each configuration. For the impermeable and "gaining stream" configurations Position 1 was the upstream location and Position 2 was the downstream location. For the "losing stream" configuration the downstream location was labelled as Position 1, as this was where the majority of the interactions between the flows in the two layers occurred for this configuration. At each position the width (in the streamwise direction) captured by the camera was approximately 400 mm. The two positions for each configuration were overlapped by approximately 20 mm.

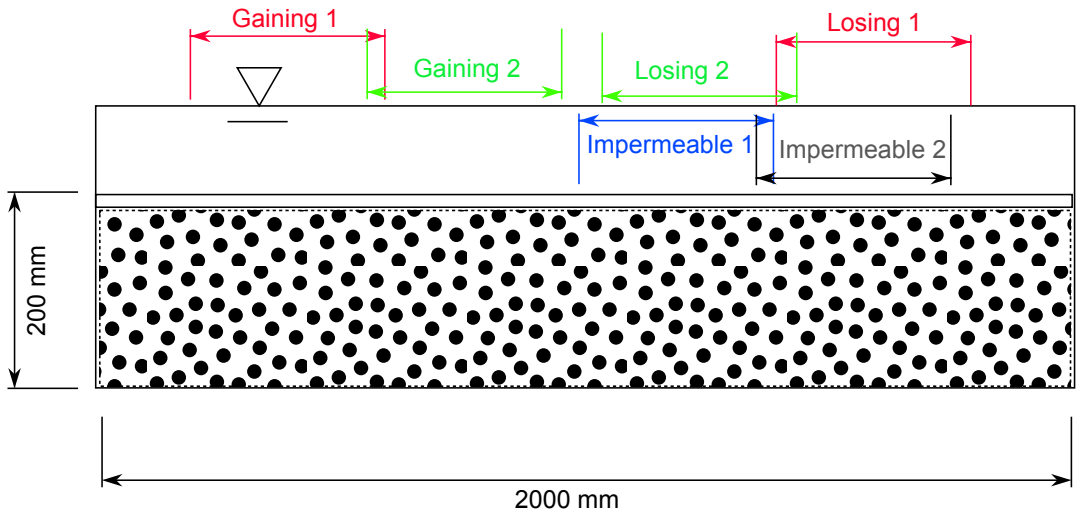

Figure 6.1: Location of measurement windows (not to scale)

Details of the flow-rates, depths and measurement window locations for the individual experimental runs are given in Appendix C.

Velocity fields were calculated in both the surface and subsurface layers for the losing and gaining configurations. The velocities reported in this chapter for the subsurface layer are pore velocities (i.e. the measured velocities of the particles through the pore space, with no adjustment for porosity).

Because the PTV process relies on advection of particles, it was more successful in the areas of the subsurface layer where velocities were highest (and therefore the coverage of particles was highest) for each configuration. For both configurations it was possible to calculate velocity fields for the full subsurface layer in position 1 (i.e. the upstream position for the gaining configuration, and the downstream position for the losing configuration). For position 2 in the gaining configuration there was sufficient coverage to calculate velocity fields for approximately $^2/_3$ of the subsurface layer. In the losing configuration there was negligible coverage of the subsurface layer for position 2. Figures showing the coverage for each run are included in Appendix D.

Turbulent statistics (turbulent kinetic energy and Reynolds stresses) were calculated in the surface layer for all three configurations. Although the flow in some areas of the subsurface layer may have been turbulent, the values of turbulent statistics calculated by Streams in this layer did not necessarily correspond to real turbulence. This is due to the velocity fields being interpolated over an area that contains a number of pore volumes, in order to get adequate coverage for calculating mean flow fields. Because Streams does not have any information about the structure of the porous matrix, it is unable to distinguish between temporal fluctuations in velocity and spatial fluctuations over the interpolation region. Therefore only mean flow fields have been reported for the subsurface layer.

At the downstream end of position 1 for the "losing stream" configuration, and (to a lesser extent) at the upstream end position 1 for the "gaining stream" configuration, it was noted that the u-velocities were suppressed near the free-surface. It is likely that this modification of the velocity profiles at the free-surface was caused by large-scale eddies or re-circulations developing in the free-surface flow outside of the region in which data was collected (i.e. where water was flowing over the false-floor, rather than over the porous matrix) due to the strength of interactions between the surface and subsurface layers.

6.1.1 Non-dimensionalisation

To allow comparisons to be made between the various experimental runs the results were non-dimensionalised.

The surface flow depth was used as the representative length scale for non-dimensionalising the spatial co-ordinates.

Velocity fields were non-dimensionalised by the flux velocity, U_f. This was calculated by dividing the measured flow rate (from the flume's flow meter) by the cross-sectional area of the surface flow at a point where the majority of the flow was in the surface layer.

For the "gaining stream" runs the depth was taken at a downstream point where subsurface motion was minimal, and *vice versa* for the "losing stream" runs. It should be noted, however, that the variation in the surface flow depth due to interactions appeared to be minimal. The non-dimensionalisation should therefore be insensitive to the point at which the flux velocity was calculated.

Turbulent statistics were non-dimensionalised by the flux velocity squared(U_f^2). It is more common to non-dimensionalise turbulent statistics by the shear velocity (U^*). However in cases where the stress profiles at the surface / subsurface interface were being influenced by vertical flows and varying with distance downstream, it was not always obvious what value of U^* would be appropriate to use. While the chosen non-dimensionalisation allows comparison of results for the scenarios presented in this thesis, it is not possible to make a direct comparison with results from other studies where U^* has been used to non-dimensionalise turbulent statistics.

6.2 Impermeable-bed Runs

6.2.1 Mean flows

Figure 6.2 shows velocity vectors (coloured according to magnitude) and streamlines for the impermeable bed runs in positions 1 and 2 respectively. The streamlines indicate that the mean flow was not entirely horizontal.

The u-velocity fields and vertical profiles for the impermeable configuration in positions 1 and 2 are shown in Figure 6.3, and the v-velocity fields and horizontal

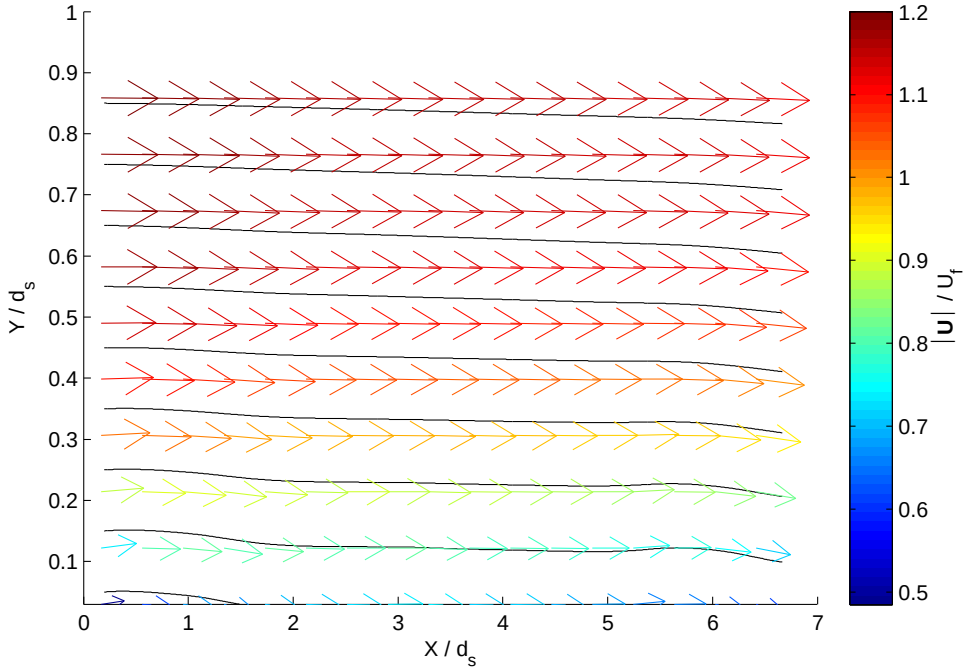

(a) Position 1

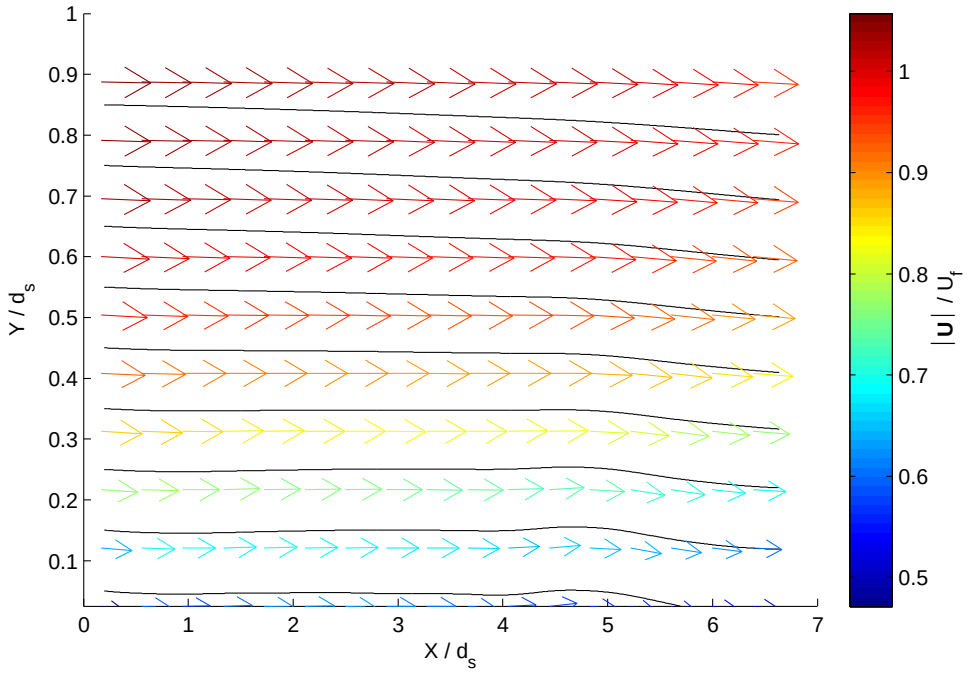

(b) Position 2

Figure 6.2: Vector and streamline plots for impermeable configuration

profiles for both positions are shown in Figure 6.4.

An unintended consequence of adding the impermeable layer beneath the stream-bed was that water was able to leak past the edges of the layer, due to it not being sealed to the flume walls. The u-velocity profiles for both positions show that mass was consistently being lost with increasing distance downstream. Although there was a downward trend in the vertical velocities, this was not sufficient to account for the change in mass flux, meaning that a secondary current (i.e. velocities out of the plane of the light sheet) must have been generated. Despite the decay in u-velocity, the shape of the velocity profiles remains consistent with that expected for an impermeable bed, providing a useful benchmark for the comparison with the gaining and losing configurations.

The lateral bars in the stream-bed layer (which were only included to increase the stiffness of the layer) act as obstacles on the bed. The flow structures over these can be seen clearly in the PTV data: the effects of two bars are seen in position 1 (at $x/d_s = 1$ and $x/d_s = 6$), and one bar in position 2 (at $x/d_s = 5$).

In the vector and streamline plots (Figure 6.2), curvature of the near-bed streamlines as a result of flow over the lateral bars can be seen immediately above the position of each bar. The same effect can be seen in more detail in the v-velocity profiles (Figure 6.4). Immediately upstream of the bar there is a region of positive (upwards) vertical velocity, followed immediately by a rapid transition to negative vertical velocities before returning to a near-zero velocity. The effect of the lateral bars becomes less significant with vertical distance upwards from the bed.

6.2.2 Turbulent statistics

Figure 6.5 shows colour plots and horizontal profiles of the turbulent kinetic energy (TKE) for the impermeable configuration in positions 1 and 2.

Vertical profiles of the TKE for both positions in the impermeable configuration are shown in Figure 6.6.

As expected for a free-surface flow, the maximum TKE occurs a short distance above the bed. Although TKE is expected to be zero at the impermeable bed (i.e. the bottom of the stream-bed layer), there is no PTV data below the top of

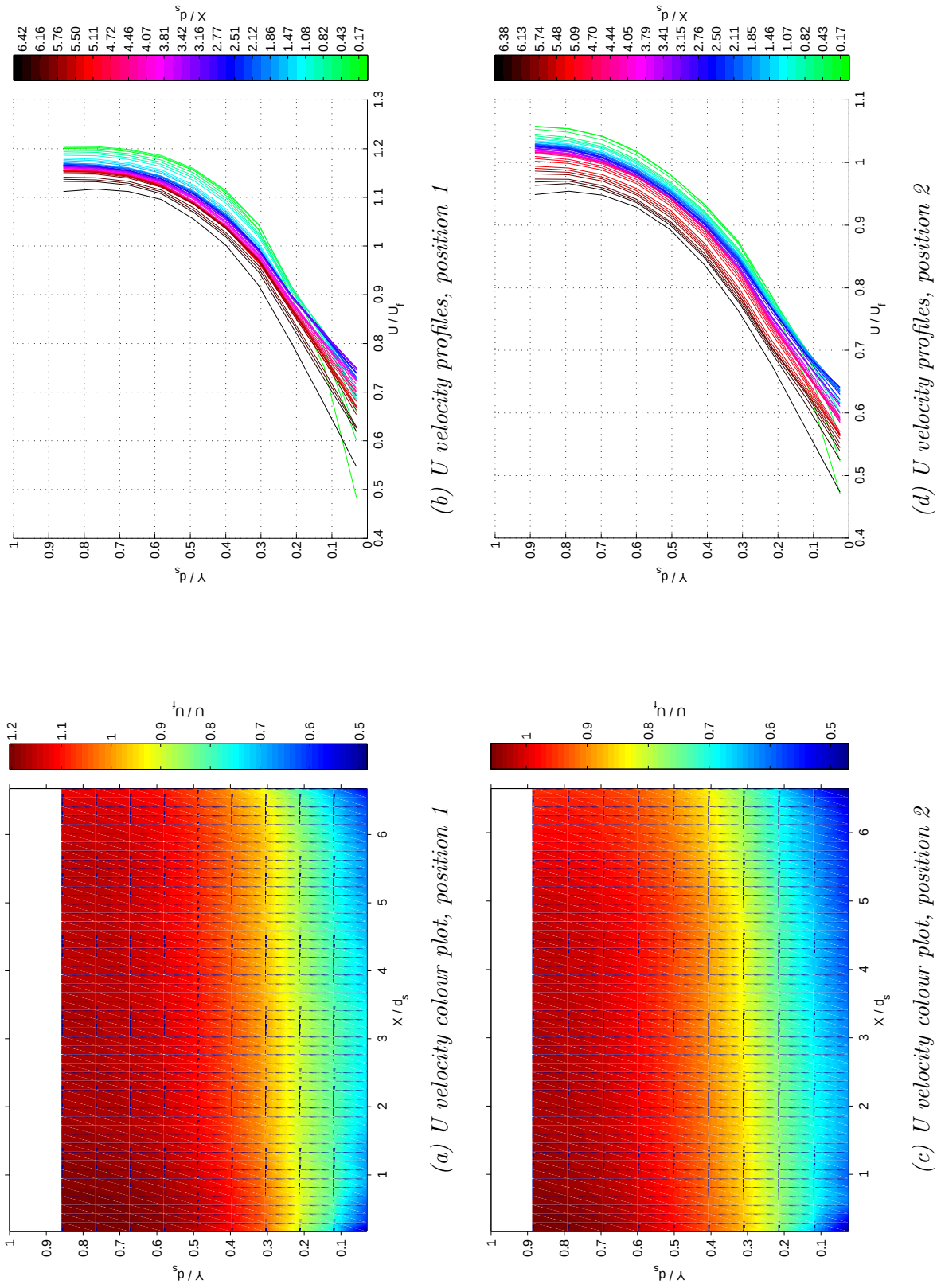

(a) U velocity colour plot, position 1

(b) U velocity profiles, position 1

(c) U velocity colour plot, position 2

(d) U velocity profiles, position 2

Figure 6.3: U velocities for impermeable configuration, positions 1 and 2

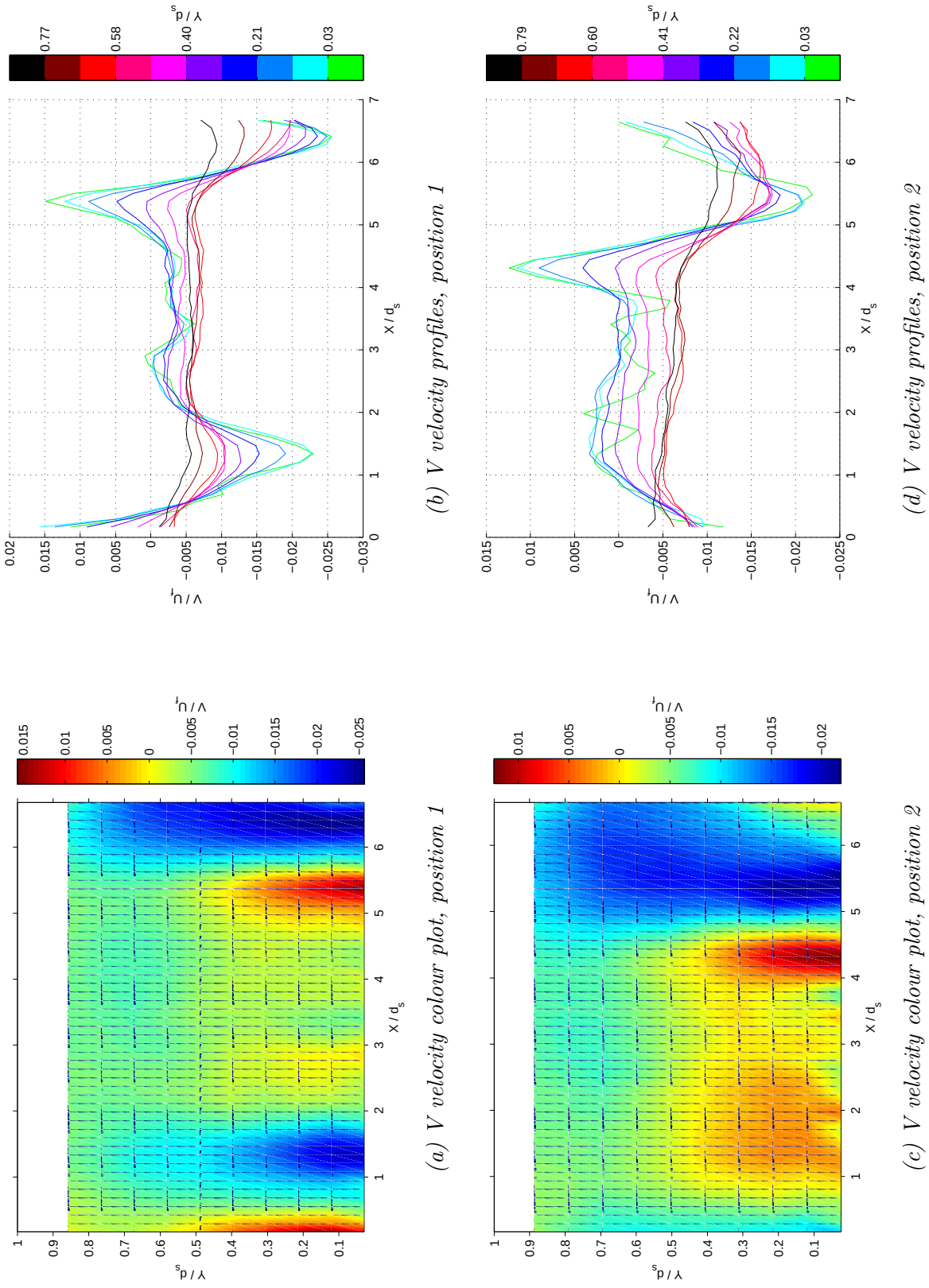

(a) V velocity colour plot, position 1

(b) V velocity profiles, position 1

(c) V velocity colour plot, position 2

(d) V velocity profiles, position 2

Figure 6.4: V velocities for impermeable configuration, positions 1 and 2

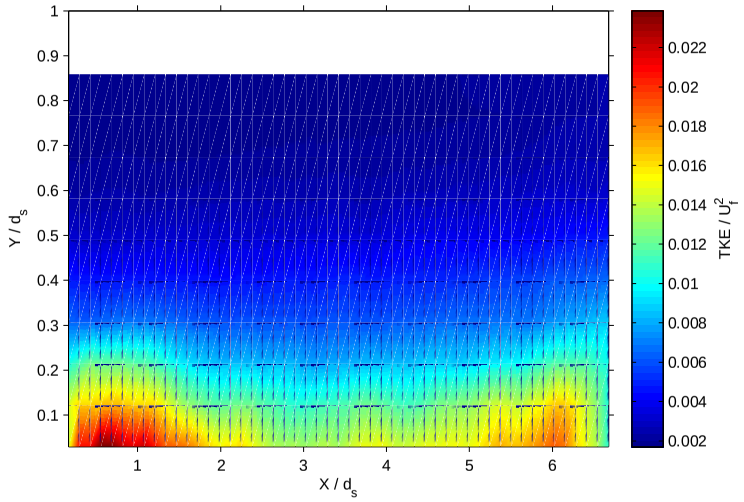

(a) TKE colour plot, position 1

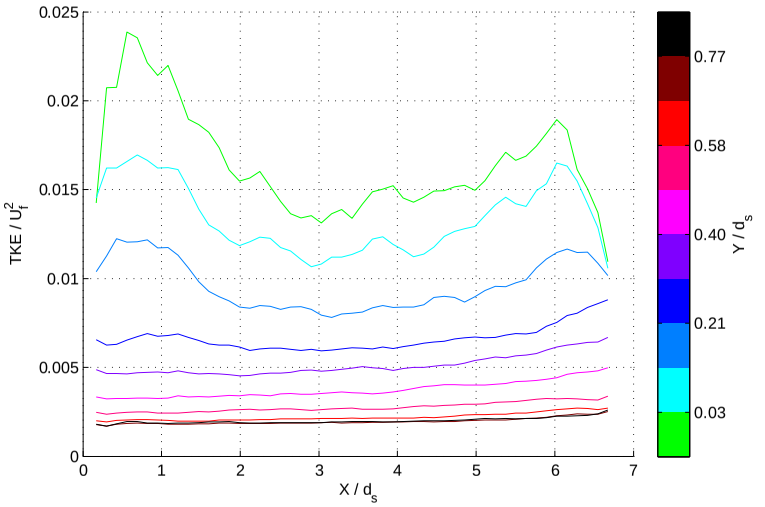

(b) TKE horizontal profiles, position 1

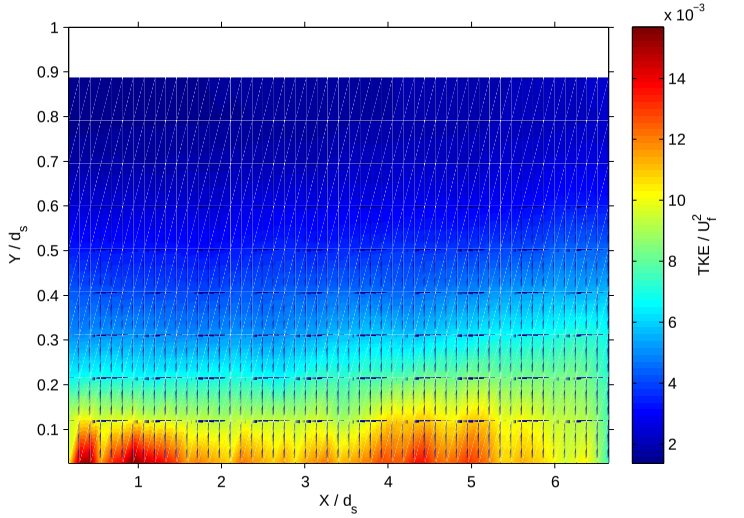

(c) TKE colour plot, position 2

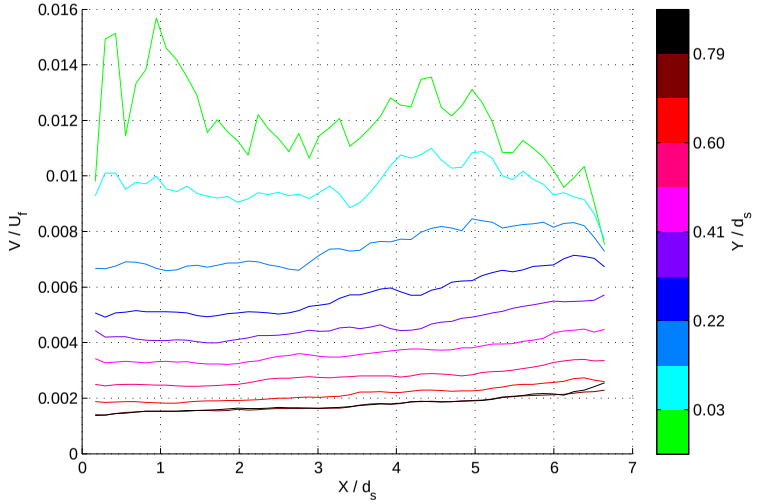

(d) TKE horizontal profiles, position 2

Figure 6.5: TKE for impermeable configuration, positions 1 and 2

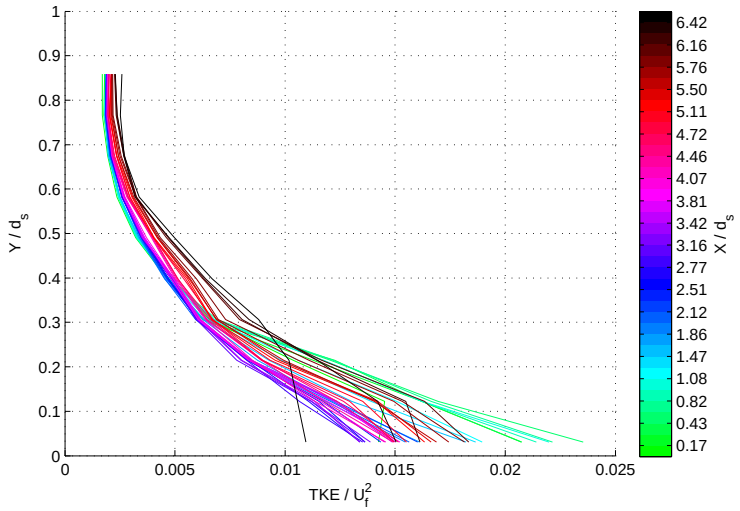

(a) TKE vertical profiles, position 1

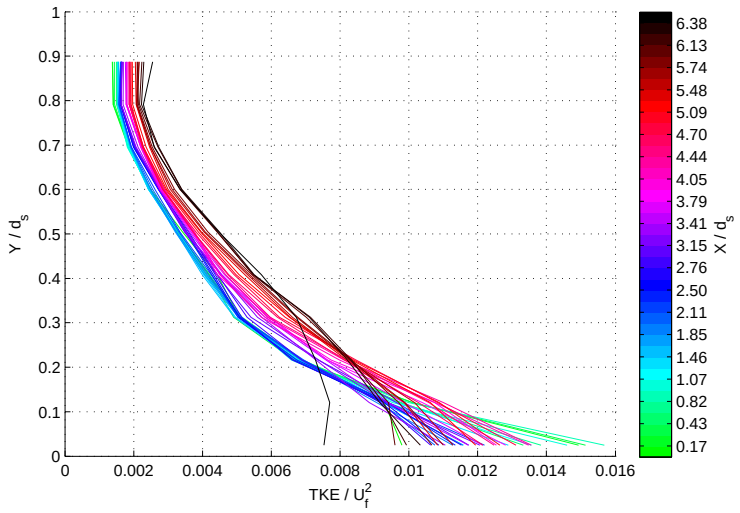

(b) TKE vertical profiles, position 2

Figure 6.6: TKE vertical profiles for impermeable configuration, positions 1 and 2

the stream-bed layer. Minimum TKE values occur at the free-surface. Figure 6.6 shows that the vertical gradient of TKE near the free-surface is close to zero.

The influence of the vertical velocity gradients caused by the lateral bars in the stream-bed layer can be seen Figure 6.5. Peaks in the near-bed TKE correspond to the areas of higher vertical velocity gradient seen in Figure 6.4. These peaks cause the spread in near-bed values seen in the vertical TKE profiles (Figure 6.6). Further up the water column there is much less variability in the TKE profiles with distance downstream.

Figure 6.7 shows colour plots and horizontal profiles of the Reynolds stresses for the impermeable configuration, for positions 1 and 2.

Vertical Reynolds stress profiles for the impermeable configuration are shown in Figure 6.8.

The maximum values of Reynolds stress occur a short distance above the bed. As for the TKE data, the expected zero value at the impermeable bed is not resolved as particles could not be tracked within the stream-bed layer. Figure 6.8 shows that the Reynolds stresses near the free-surface are close to zero. This is expected as there can be no fluctuation in vertical velocity at the free-surface.

Near the bed, peaks in Reynolds stress occur in positions corresponding to the lateral bars in the stream-bed layer. These peaks are less clearly-defined than those in the TKE profiles, however.

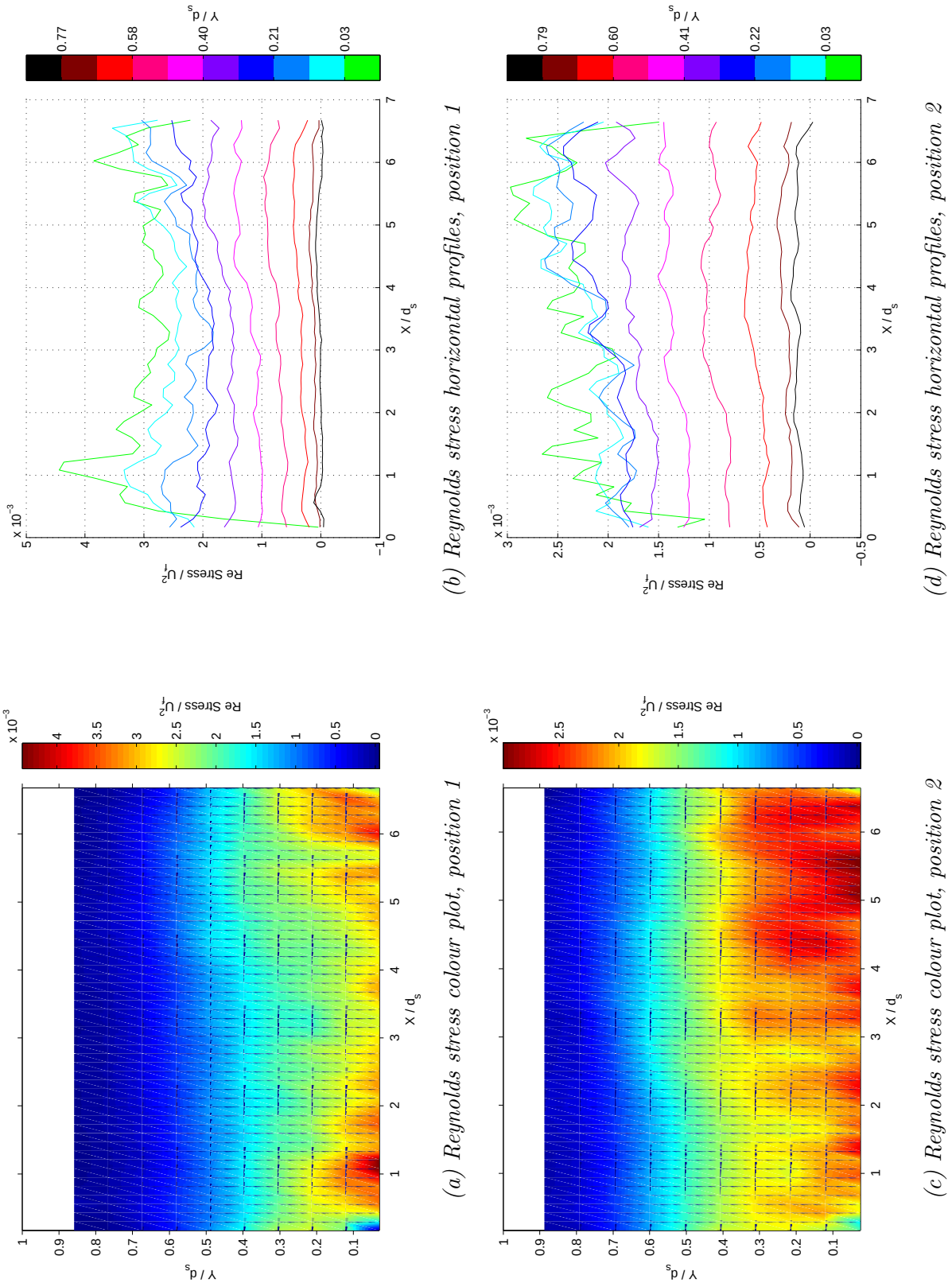

(a) *Reynolds stress colour plot, position 1*

(b) *Reynolds stress horizontal profiles, position 1*

(c) *Reynolds stress colour plot, position 2*

(d) *Reynolds stress horizontal profiles, position 2*

Figure 6.7: Reynolds stress for impermeable configuration, positions 1 and 2

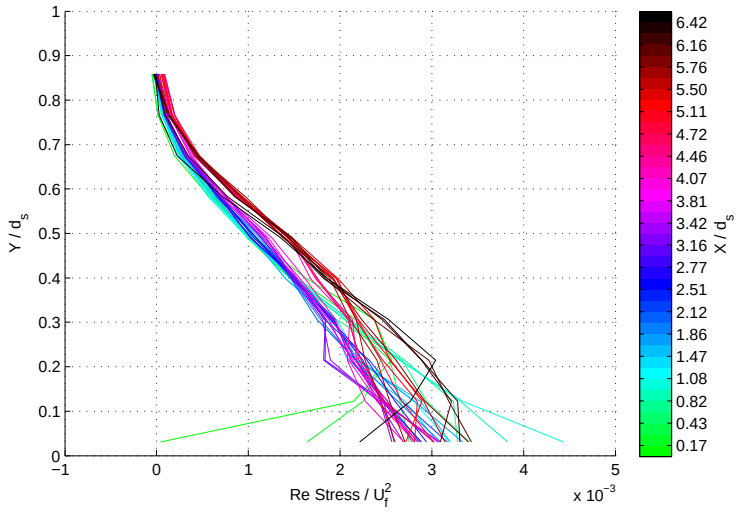

(a) Reynolds stress vertical profiles, position 1

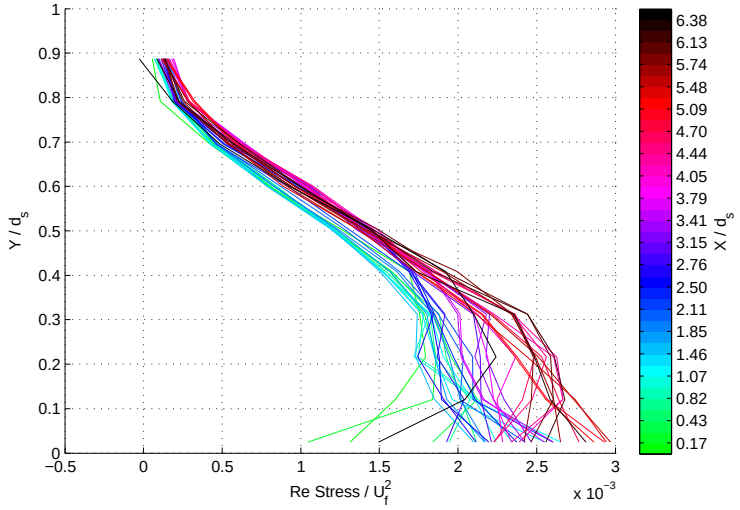

(b) Reynolds stress vertical profiles, position 2

Figure 6.8: Reynolds stress vertical profiles for impermeable configuration, positions 1 and 2

6.3 "Gaining Stream" Runs

6.3.1 Mean flows

Figure 6.9 shows velocity vectors (coloured according to magnitude) and streamlines for the gaining configuration runs in positions 1 and 2 respectively. In position 1 (Figure 6.9a) the influence of vertical flow through the bed on the surface flow is clearly shown by the shape of the streamlines, particularly at the upstream end. In position 2 (Figure 6.9b), although the streamlines in the subsurface layer show that vertical velocities were still present at the stream-bed there is no obvious influence on the shape of the streamlines.

Figure 6.10 shows the u-velocity fields and vertical profiles for the gaining configuration in position 1. U-velocity plots for position 2 are shown in Figure 6.11. Because the u-velocities in the surface layer are substantially higher than those in the subsurface layer, and the subsurface velocities decrease with distance downstream, different colour scales are used for the plots showing only the subsurface fields (Figures 6.10c and 6.11c).

In the surface layer the u-velocity profiles in position 1 were strongly influenced by interactions with the subsurface layer. Throughout the depth of the surface layer the u-velocities increased with distance downstream. At the free-surface this effect was more pronounced: the surface velocities at the upstream end were suppressed to the extent that the vertical gradient was reversed and the shape of the velocity profile was substantially altered. This was believed to be due to a large-scale eddy in the surface flow upstream of the measurement window. Further downstream in position 1 the shape of the velocity profiles was closer to that expected for a free-surface flow.

Near the bed, u-velocities in position 2 increased with distance downstream, similar to those in position 1. There was generally consistency across the two positions (note that in position 2 the profiles were able to be resolved closer to the stream-bed than in position 1). Further above the bed the u-velocity profiles for position 2 converge to the shape expected for a free-surface flow. It is interesting to note that in position 2 there is less variation with distance downstream than in the u-velocity profiles for the impermeable configuration

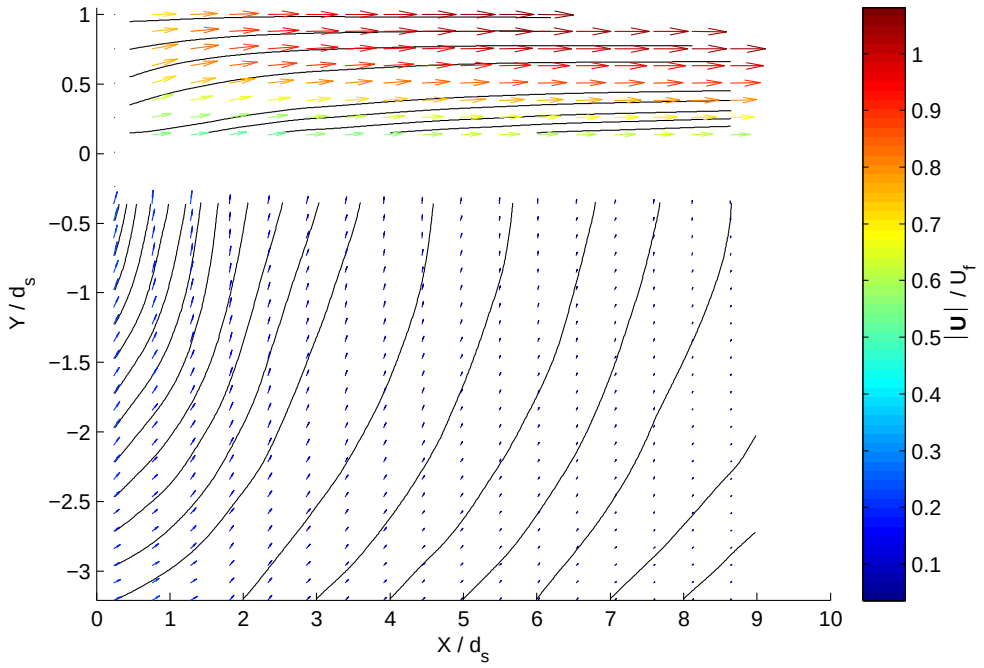

(a) Position 1

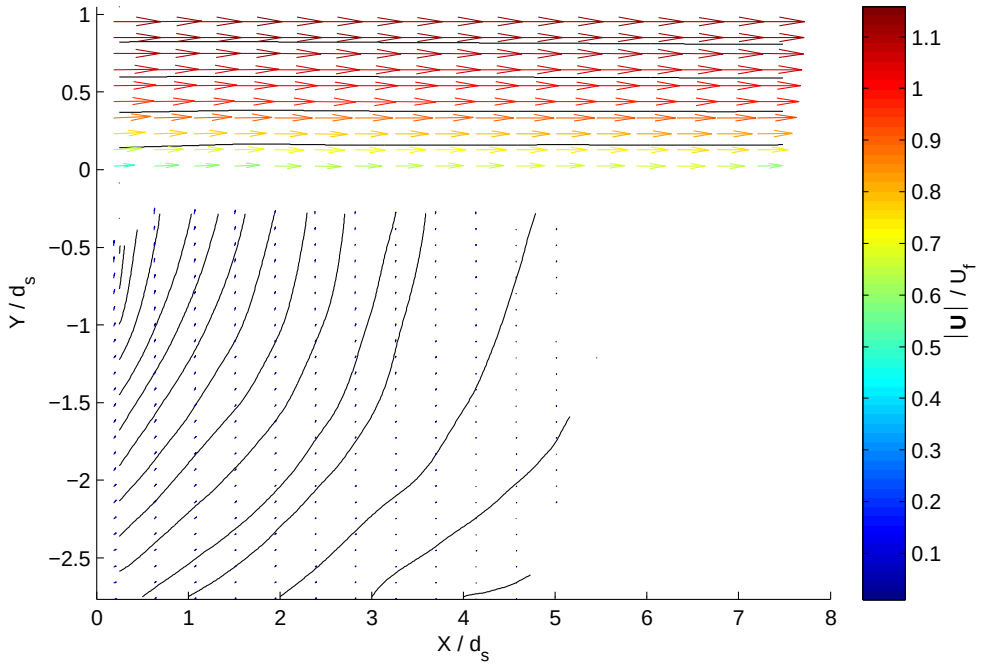

(b) Position 2

Figure 6.9: Vector and streamline plots for gaining configuration

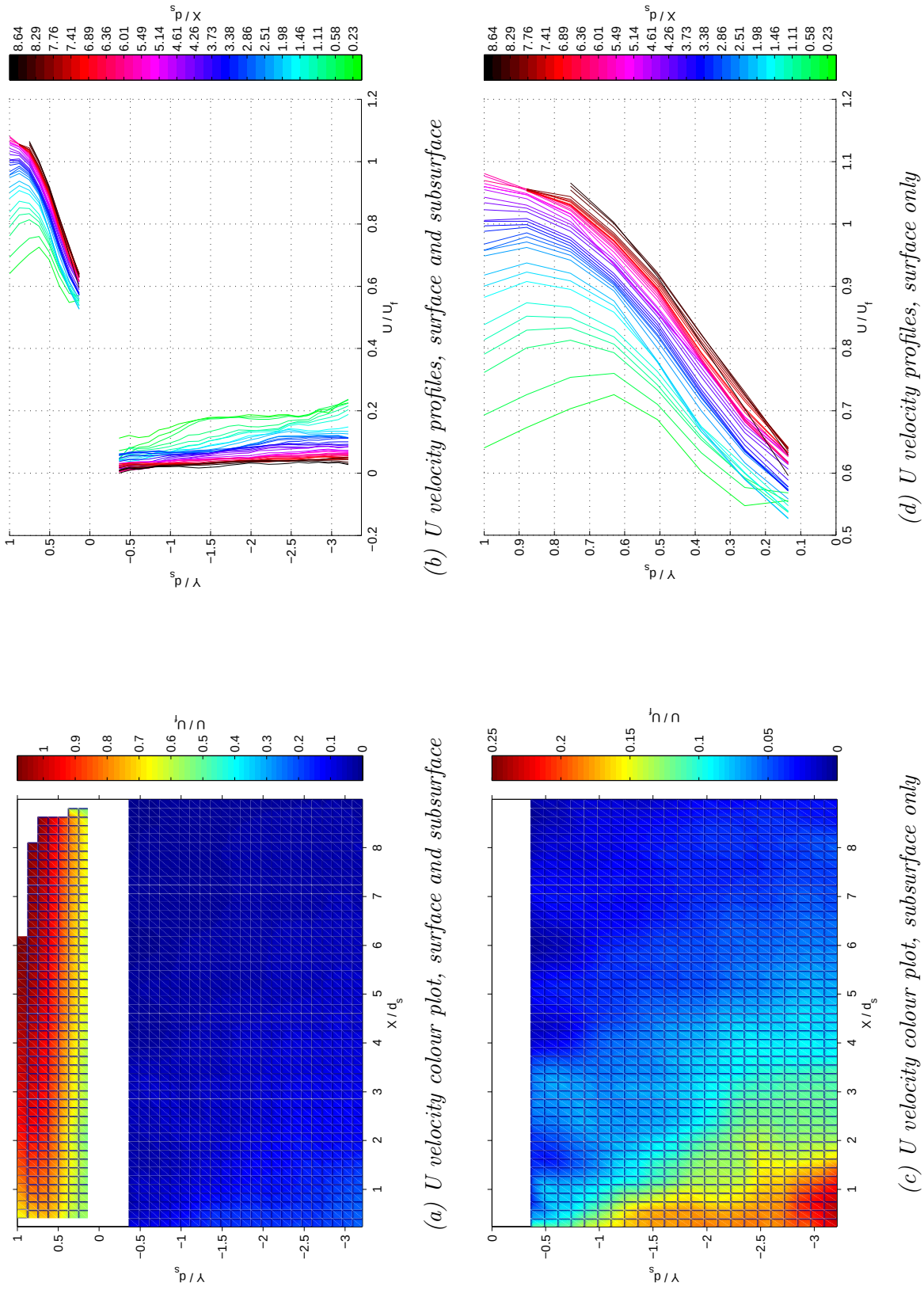

(a) U velocity colour plot, surface and subsurface

(b) U velocity profiles, surface and subsurface

(c) U velocity colour plot, subsurface only

(d) U velocity profiles, surface only

Figure 6.10: U velocities for Gaining configuration, position 1

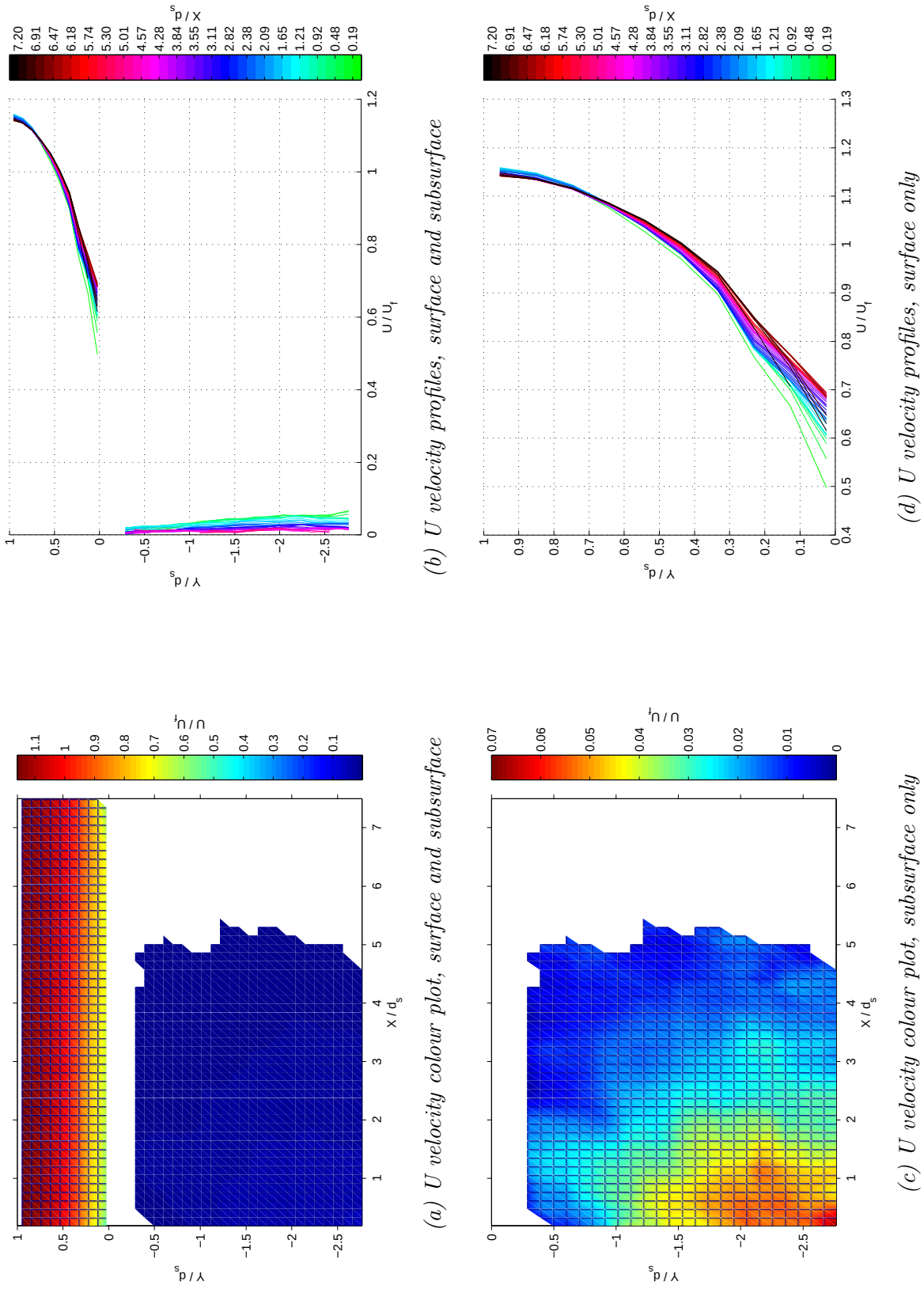

(a) U velocity colour plot, surface and subsurface

(b) U velocity profiles, surface and subsurface

(c) U velocity colour plot, subsurface only

(d) U velocity profiles, surface only

Figure 6.11: U velocities for Gaining configuration, position 2

(Figure 6.3). This supports the assumption that the velocity profiles for the impermeable configuration were influenced by secondary currents.

In the subsurface layer u-velocities decreased with distance downstream. This was the opposite to the trend in velocities immediately above the bed in the surface layer.

Figure 6.12 shows the v-velocity fields and horizontal profiles for the gaining configuration in position 1 and position 2. Note that the colour plots for the two positions use different scales as the vertical velocities are lower in position 2.

The highest vertical velocities were measured at the upstream end of the subsurface layer, immediately beneath the stream-bed. Vertical velocities in the subsurface layer decreased with depth, and with distance downstream. These trends were generally consistent across the two positions; the higher velocities at the upstream end of position 2 (Figure 6.12d) are likely to be attributable to lower data coverage in this region (see Appendix D).

The v-velocity horizontal profile plots (Figures 6.12b and 6.12d) both show the surface and subsurface v-velocities in two reasonably distinct groups. This is due to deceleration that must occur in order for conservation of mass to be maintained when the flow exits from the porous matrix into the clear-fluid flow. The ratio of the v-velocities immediately above and below the stream-bed layer is consistent with the measured porosity of the SAP spheres.

In the surface layer the vertical velocities were strongest near the bed at the upstream end of position 1, and tended towards zero at the surface. In position 1 there was a decreasing trend with distance downstream, similar to the subsurface layer. In position 2 this was not evident, and the influence of a lateral bar in the stream-bed layer at $x/d_s = 1.5$ can be seen in Figure 6.12d.

Figure 6.13 shows the porous Reynolds number (Re_p) calculated from the velocity field results, using the measured hydraulic properties (k_i and ϕ) to estimate the length scale. This definition of the length scale is preferable for numerical modelling, as it uses parameters that are required for the model (see Chapter 4). In the clear fluid layer the length scale was the flow depth, so the values of Re_p are equivalent to a locally-defined Reynolds number, defined in the normal way (i.e. using a representative length and velocity scales for the mean flow).

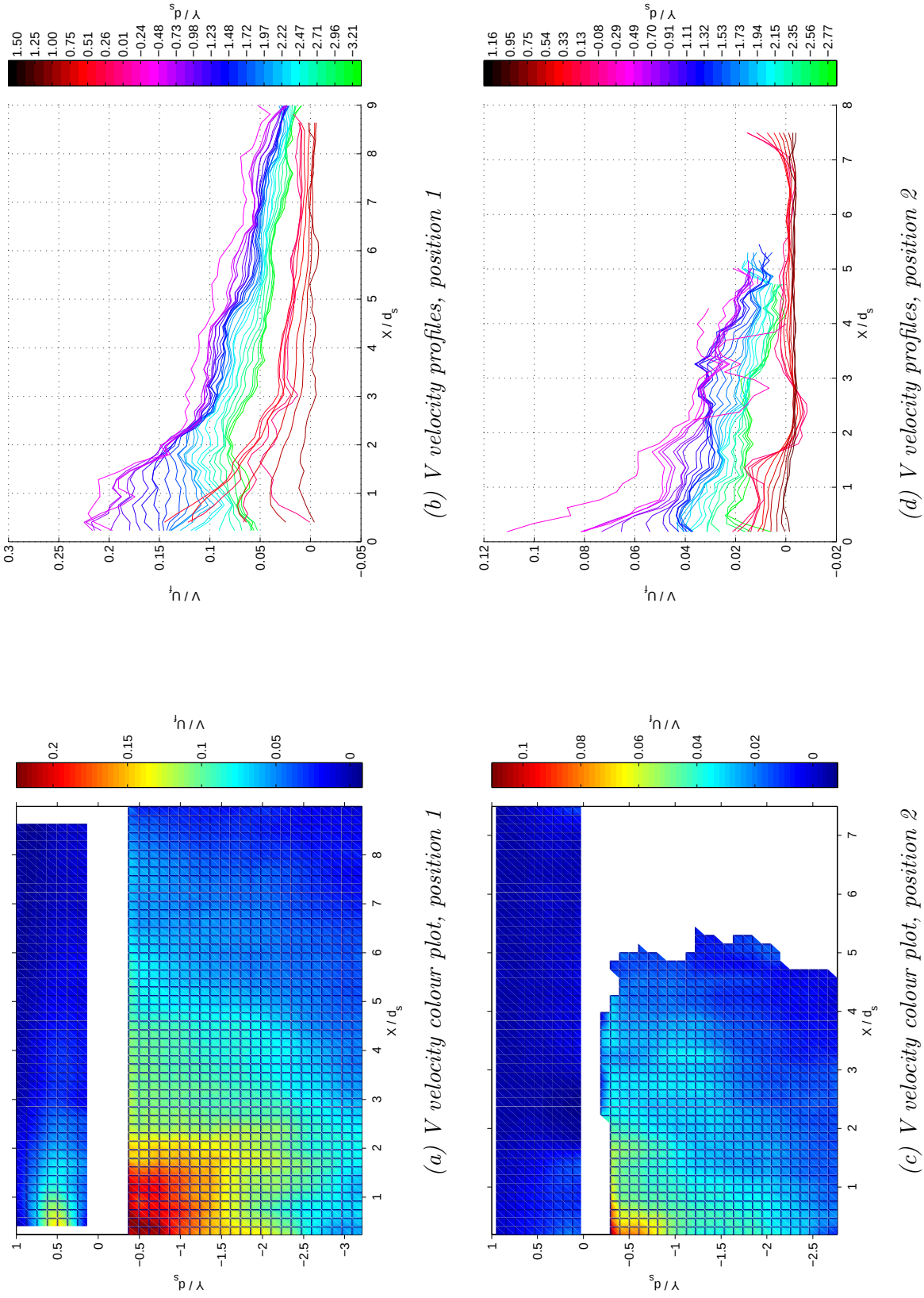

(a) V velocity colour plot, position 1

(b) V velocity profiles, position 1

(c) V velocity colour plot, position 2

(d) V velocity profiles, position 2

Figure 6.12: V velocities for Gaining configuration, positions 1 and 2

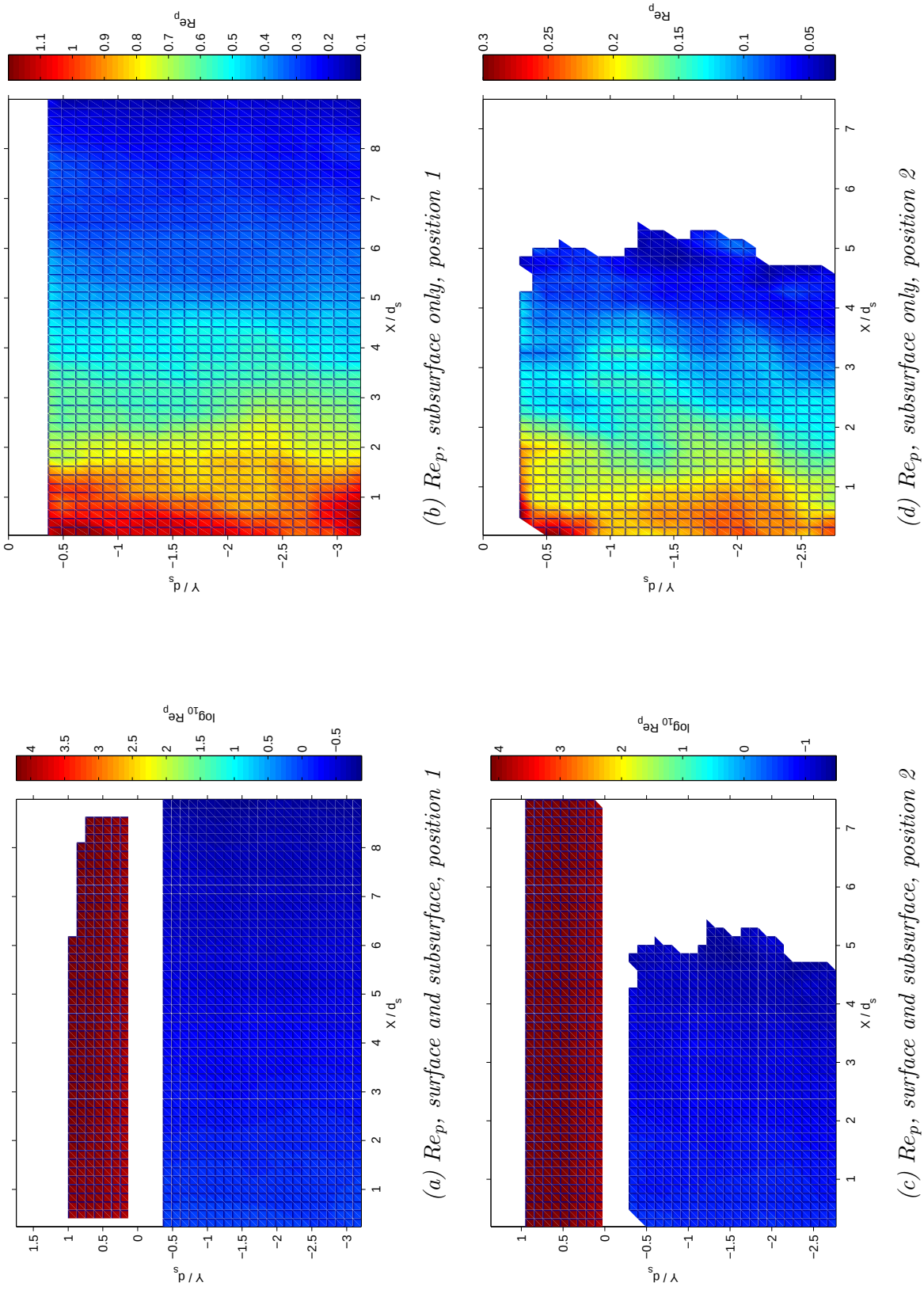

(a) Re_p, surface and subsurface, position 1

(b) Re_p, subsurface only, position 1

(c) Re_p, surface and subsurface, position 2

(d) Re_p, subsurface only, position 2

Figure 6.13: Porous Reynolds numbers (Re_p) based on hydraulic properties for positions 1 and 2, gaining stream configuration

Figure 6.14 shows Re_p for the gaining configuration, using the diameter of the hydrated SAP spheres ($0.01m$) as an estimate of the length scale. The values of Re_p based on the particle diameter are approximately 75 times higher than Re_p based on hydraulic parameters (as shown in Figure 6.13). The threshold values of Re_p given by Bear (1972) for non-linear and turbulent porous media flow are for Re_p in terms the of average particle diameter in the porous medium. As the average particle diameter is not typically specified in a numerical model, this difference between the two methods of defining Re_p has implications for how Re_p is used in the numerical model for handling the transition between laminar and turbulent flow. Based on the threshold values given by Bear (1972), the flow in the subsurface layer was non-Darcian for all of position 1, and up to approximately $x/d_s = 2$ in position 2. Near the inlet in position 1 the flow was transitioning to turbulence, and was close to fully turbulent near the interface.

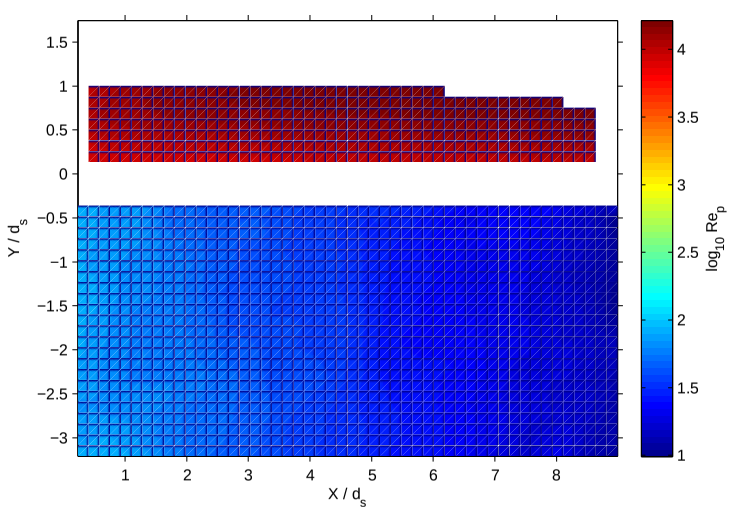

(a) Re_p, surface and subsurface, position 1

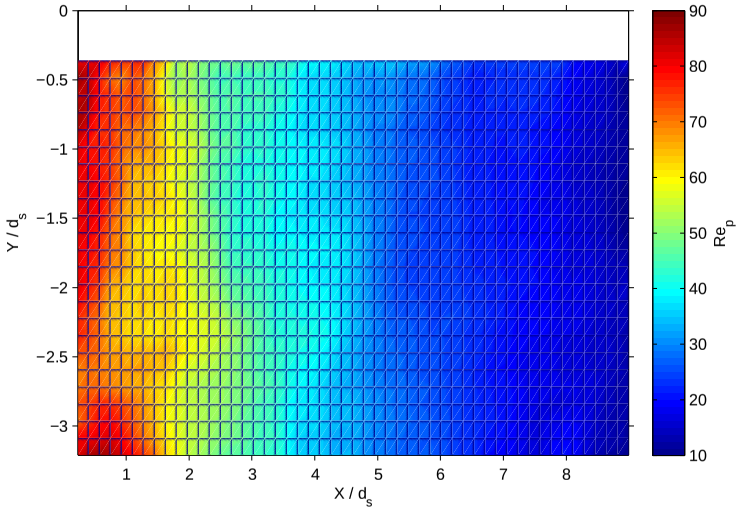

(b) Re_p, subsurface only, position 1

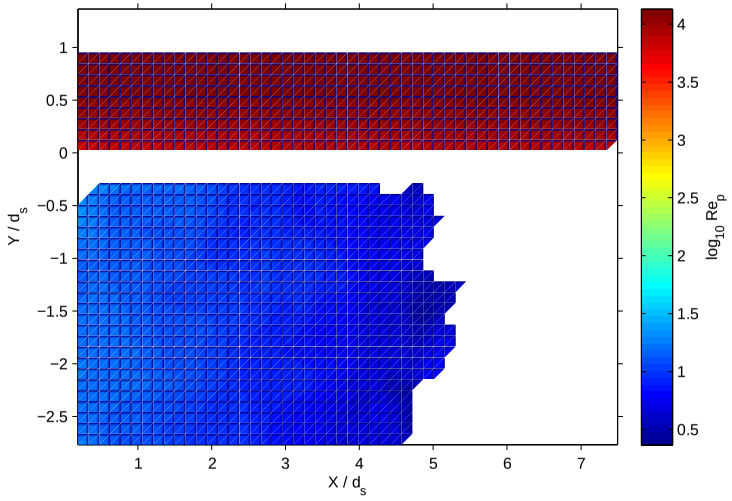

(c) Re_p, surface and subsurface, position 2

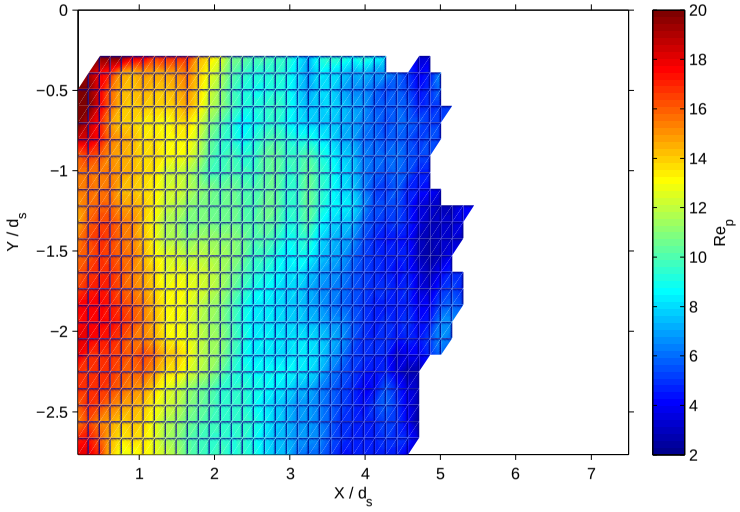

(d) Re_p, subsurface only, position 2

Figure 6.14: Porous Reynolds numbers (Re_p) based on grain diameter for positions 1 and 2, gaining stream configuration

6.3.2 Turbulent statistics

Figure 6.15 shows colour plots and horizontal profiles of turbulent kinetic energy (TKE) for the gaining configuration in positions 1 and 2. It should be noted that the plots (and all other plots of turbulent statistics in this chapter) are for the surface layer only.

Vertical TKE profiles for the gaining configuration in both positions are shown in Figure 6.16.

In position 1 the highest values of TKE were measured at the upstream end, corresponding roughly to the area with the highest vertical velocities. In this region there is a relatively weak relationship between TKE and distance above the bed. With distance downstream there was a reduction in TKE values at all depths and an increasing vertical gradient.

In position 2, where vertical velocities through the surface - subsurface interface were lower and the u-velocity profiles were less distorted, the shape of the vertical profiles was similar to the impermeable case, with maximum values near the stream-bed and the vertical gradient approaching zero towards the surface. There was a generally decreasing trend in TKE with distance downstream. Near the bed the influence of the lateral stream-bed bars can be seen in Figure 6.15d, with regions of elevated TKE from approximately $x/d_s = 0$ to $x/d_s = 2.5$ and $x/d_s = 5$ to $x/d_s = 7.5$.

Figure 6.17 shows colour plots and horizontal profiles of the Reynolds stresses for the gaining configuration in positions 1 and 2.

Vertical profiles of Reynolds stress for the gaining configuration are shown in Figure 6.18.

Similar to the TKE, in areas where there are strong vertical flows upward through the stream-bed the Reynolds stress profiles deviate substantially from the shape expected for an open-channel flow (i.e. the impermeable case). Where the vertical gradient of the u-velocity profile reverses at the upstream end of position 1 (see Figure 6.10d) the Reynolds stresses are negative, as expected.

In areas where the vertical velocities were weaker, the Reynolds stress profiles more closely resemble those for the impermeable case. Rather than a uniform gradient from a maximum value at the bed to zero at the surface there is, however,

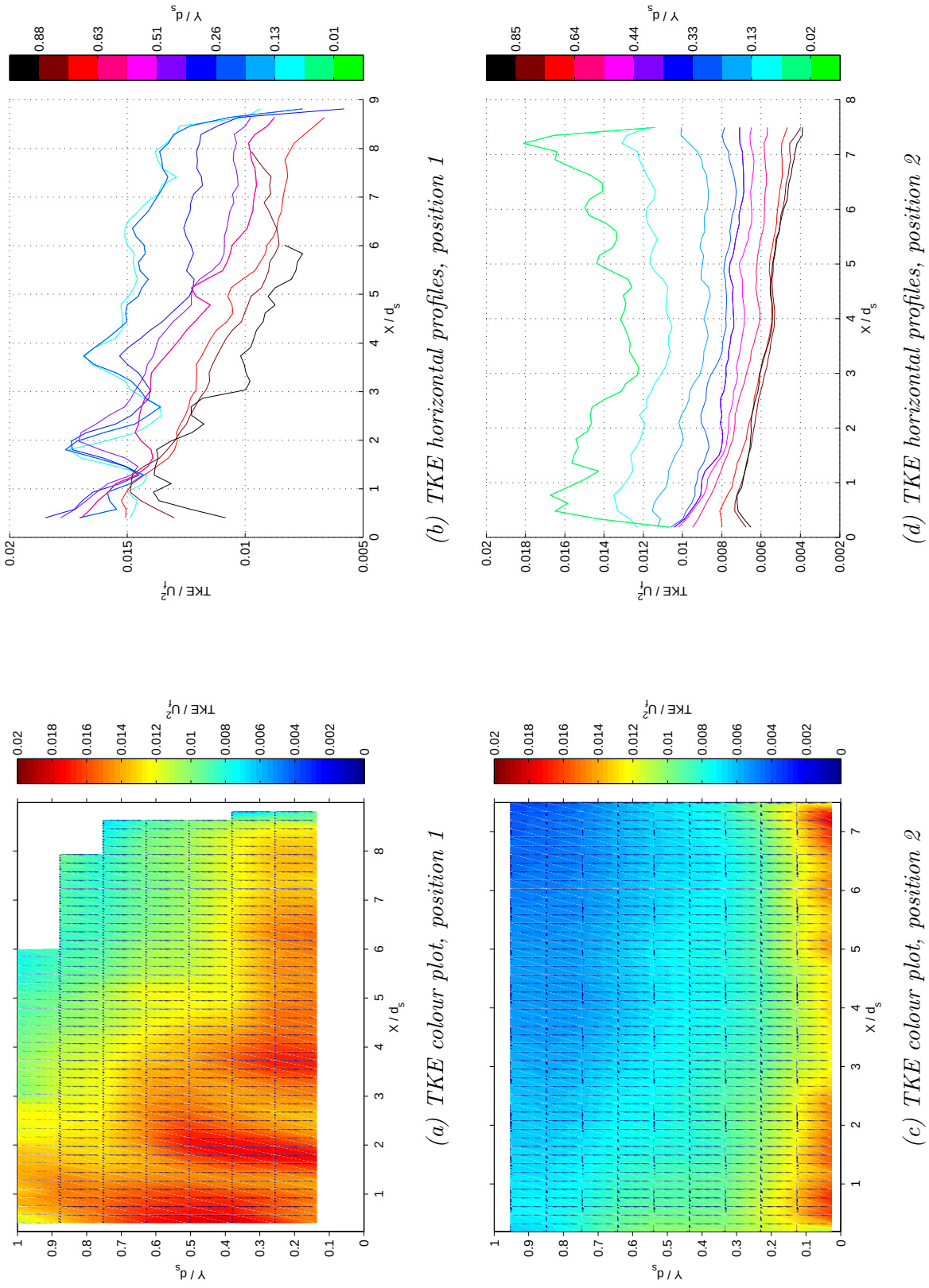

(a) TKE colour plot, position 1

(b) TKE horizontal profiles, position 1

(c) TKE colour plot, position 2

(d) TKE horizontal profiles, position 2

Figure 6.15: TKE for gaining configuration, positions 1 and 2

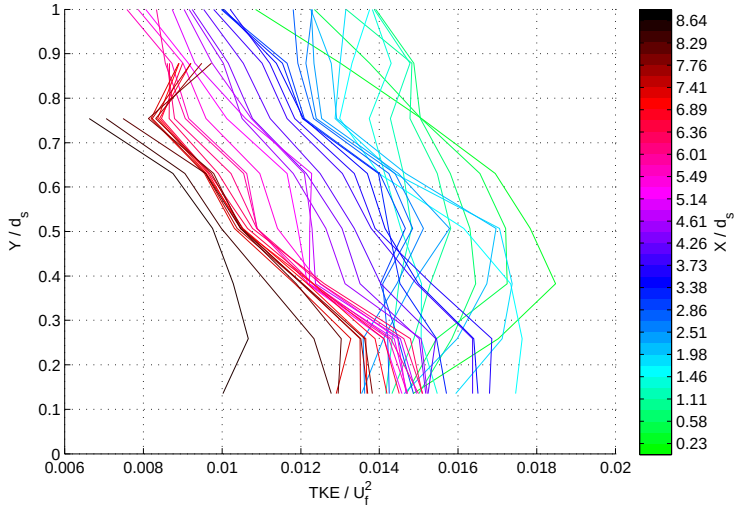

(a) TKE vertical profiles, position 1

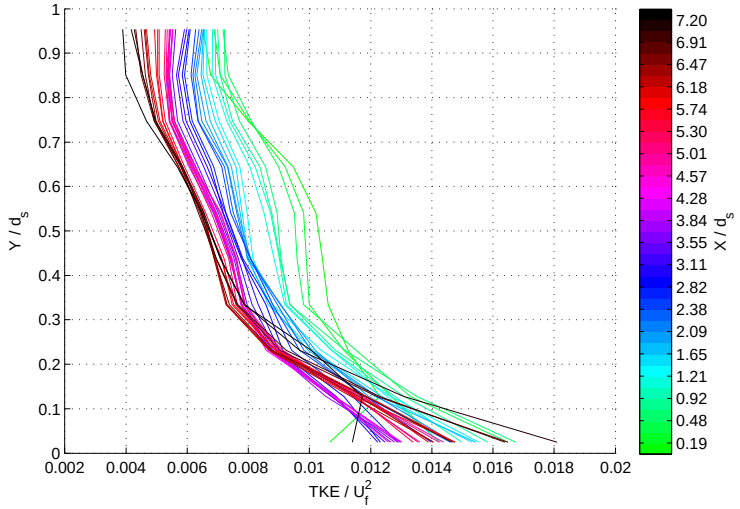

(b) TKE vertical profiles, position 2

Figure 6.16: TKE vertical profiles for gaining configuration, positions 1 and 2

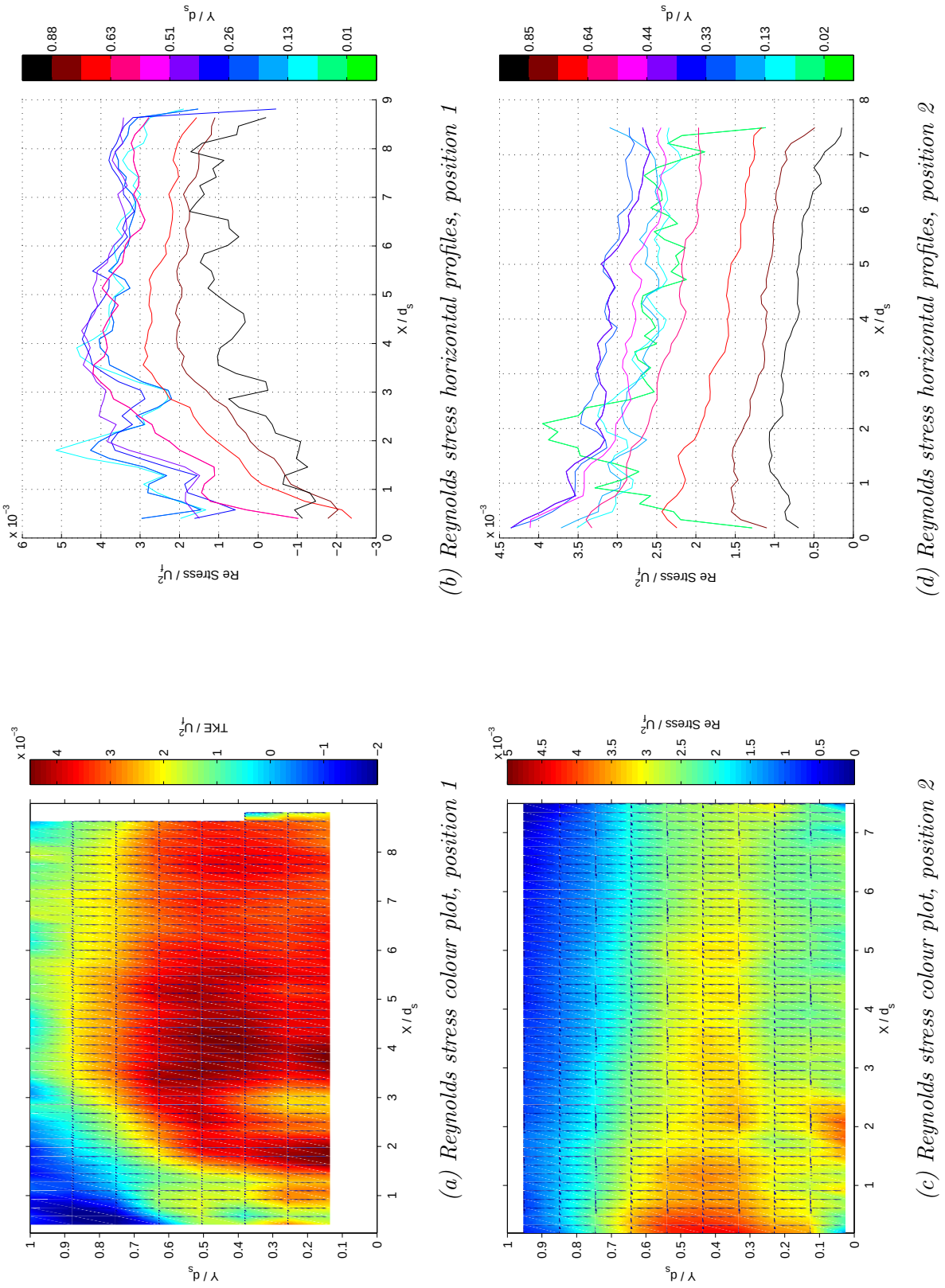

(a) *Reynolds stress colour plot, position 1*

(b) *Reynolds stress horizontal profiles, position 1*

(c) *Reynolds stress colour plot, position 2*

(d) *Reynolds stress horizontal profiles, position 2*

Figure 6.17: Reynolds stress for gaining configuration, positions 1 and 2

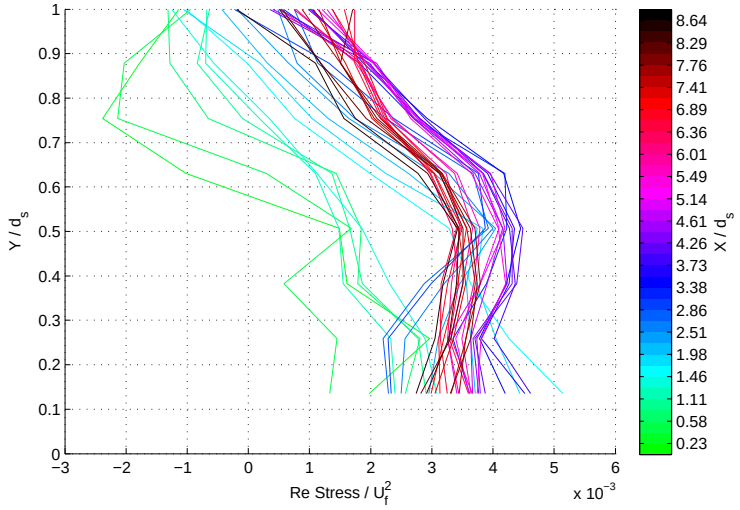

(a) Reynolds stress vertical profiles, position 1

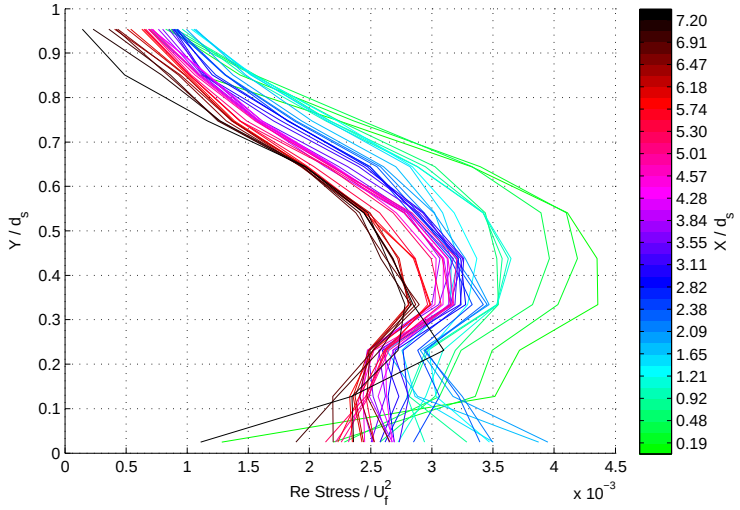

(b) Reynolds stress vertical profiles, position 2

Figure 6.18: Reynolds stress vertical profiles for gaining configuration, positions 1 and 2

a peak in Reynolds stress slightly below mid-depth.

In position 1 there is no clear trend in Reynolds stress with distance downstream. In position 2 the Reynolds stress values at all depths decrease with distance downstream, and the peak at mid-depth becomes less prominent.

Plots of the estimated turbulence mixing length and turbulent viscosity for the gaining configuration are included in Appendix 6. These estimates were used as guidance for determining how the transition from laminar to turbulent flow was dealt with in the development of the numerical model.

6.4 "Losing Stream" Runs

6.4.1 Mean flows

Figure 6.19 shows velocity vectors (coloured according to magnitude) and streamlines for the losing configuration runs in positions 1 and 2 respectively. In position 1 (Figure 6.19a), particularly at the downstream end, there was strong downward flow through the bed, which is clearly shown by the curvature of the streamlines. At the downstream end, near the free surface, there is a region of lower velocities. Although the flow direction did not reverse in this region, the suppressed velocities are a strong indication of a large-scale eddy or re-circulation in the surface layer, downstream of the region in which velocities were measured. In position 2 (Figure 6.19b) some curvature of the streamlines in the surface flow can be seen, although this is less pronounced than for position 1. The limited amount of data in the subsurface layer for position 2 shows that although there were measurable subsurface vertical flows at the downstream end of this position, further upstream the vertical velocities were too weak to advect significant numbers of particles into the subsurface layer. Therefore the coverage was too low for velocities to be calculated.

Figures 6.20 and 6.21 show the u-velocity fields and vertical profiles for the losing configuration in positions 1 and 2 respectively. Note that the colour plots for the full domain and subsurface have different scales, and that in Figure 6.21 the subsurface domain is not shown separately.

At the upstream end of position 2, where the vertical velocities were weakest,

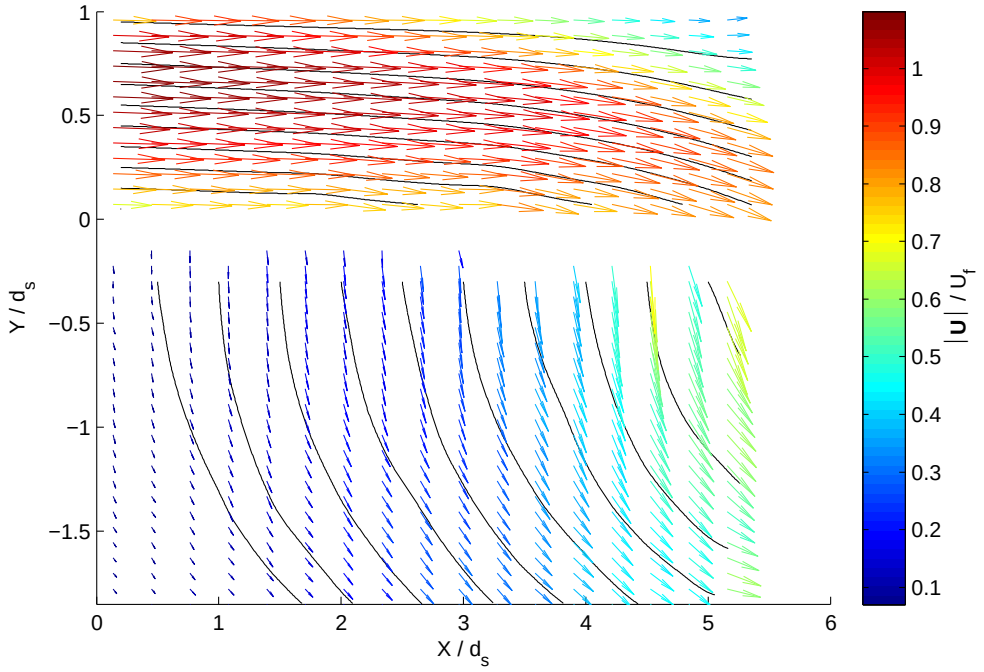

(a) Position 1

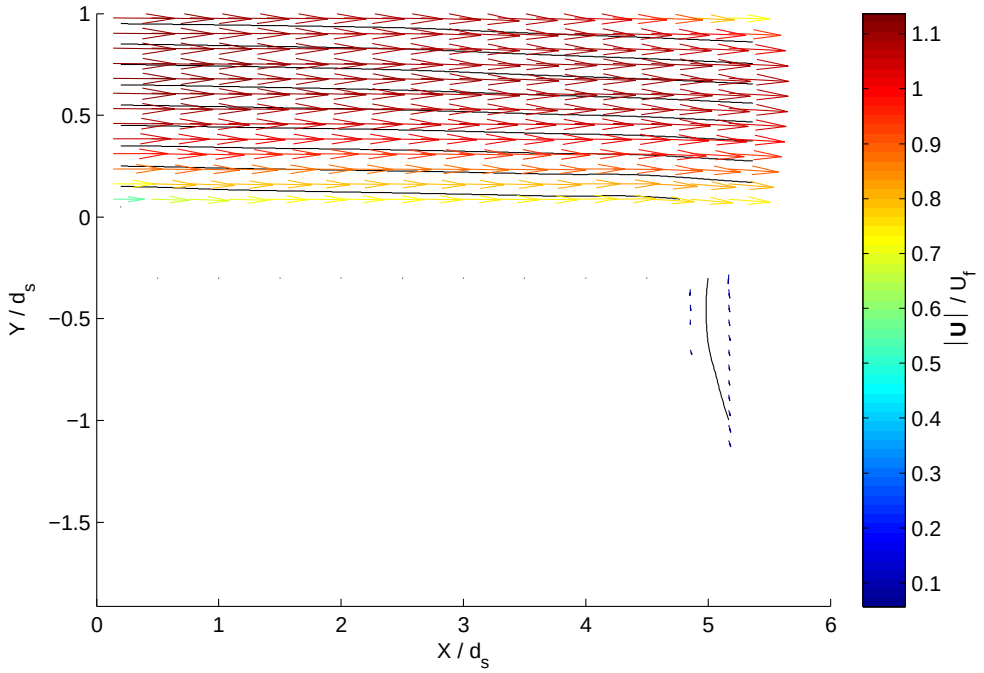

(b) Position 2

Figure 6.19: Vector and streamline plots for losing configuration

the u-velocity profiles appear similar to those expected for a free-surface flow (albeit with higher near-bed velocities due to the "slip" boundary). The u-velocities decrease with distance downstream, and towards the downstream end of position 2 the velocities near the free-surface start to become suppressed. The region of highly suppressed u-velocities at the downstream end of position 2 was anomalous, and is likely to have been influenced by a distortion in the raw PTV images at the free-surface.

Suppressed u-velocities at the free-surface were seen throughout position 1. With distance downstream the velocity profiles in Figure 6.20d become increasingly distorted and the point at which the vertical gradient reversed moves closer to the surface-subsurface interface. In the subsurface layer the u-velocities increased with distance downstream: the highest velocities (approximately 50% of the flux velocity) were closest to the downstream free-discharge boundary. The vertical gradient in the subsurface layer also increased with distance downstream.

Figure 6.22 shows the v-velocity fields and horizontal profiles for the losing configuration in positions 1 and 2. Note that the colour plots for the two positions have different scales, as the vertical velocities in position 2 were lower, and could only be resolved in the surface layer.

The highest vertical velocities in the losing configuration were measured immediately beneath the stream-bed at the downstream end of the subsurface layer, near the discharge boundary. This is consistent with what was measured for the gaining configuration, where the highest vertical velocities were at the upstream end, nearest to the inflow boundary.

Similar to the gaining configuration, the v-velocity horizontal profile plots (Figures 6.22b and 6.22d) show that the v-velocity profiles for the layers fall into two distinct groups. The ratio of vertical velocities for points immediately above and below the stream-bed layer is consistent with the measured porosity of the porous matrix.

In the subsurface layer the v-velocities decreased with depth and with distance upstream from the discharge boundary. Although only a limited amount of data was collected in the subsurface layer for position 2, the magnitudes of the v-velocity data were consistent with the values from the upstream end of position 1.

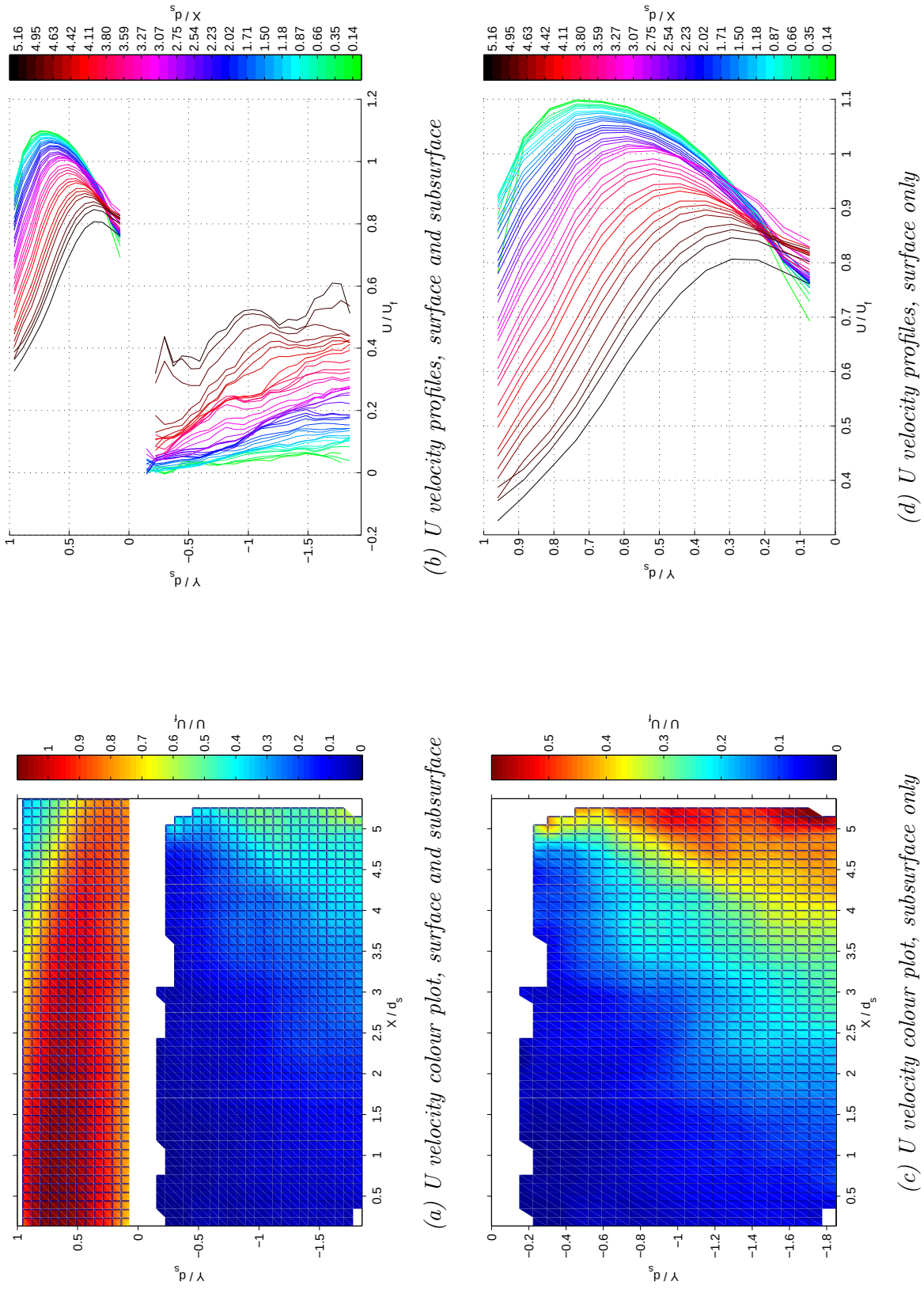

(a) U velocity colour plot, surface and subsurface

(b) U velocity profiles, surface and subsurface

(c) U velocity colour plot, subsurface only

(d) U velocity profiles, surface only

Figure 6.20: U velocities for losing configuration, position 1

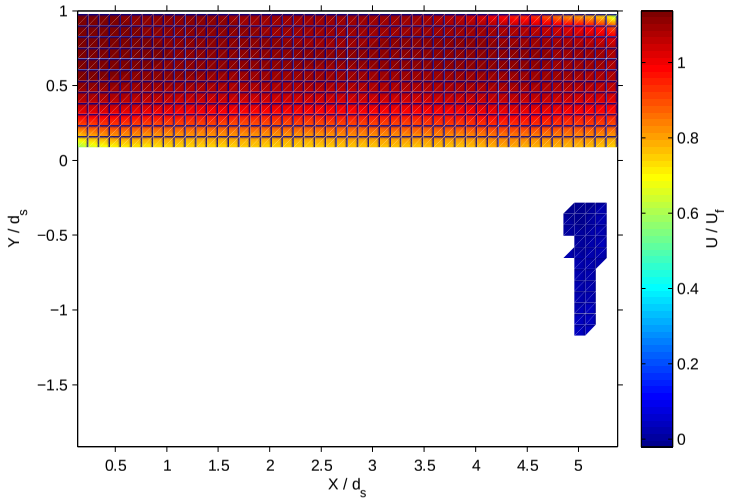

(a) U velocity colour plot, surface and subsurface

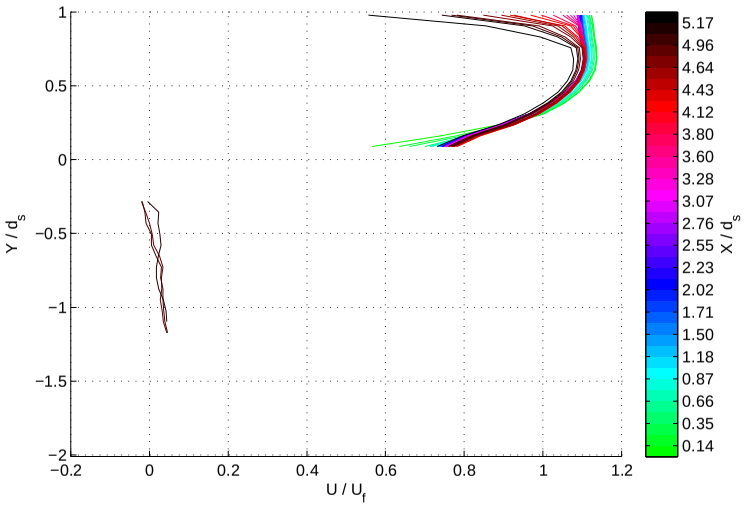

(b) U velocity profiles, surface and subsurface

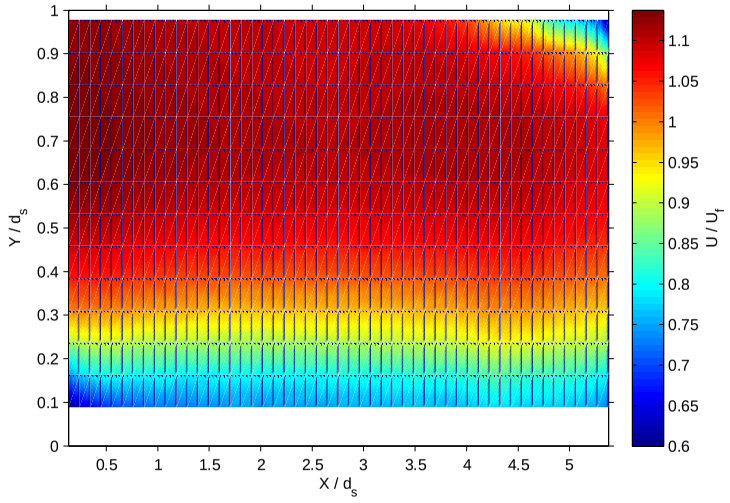

(c) U velocity colour plot, surface only

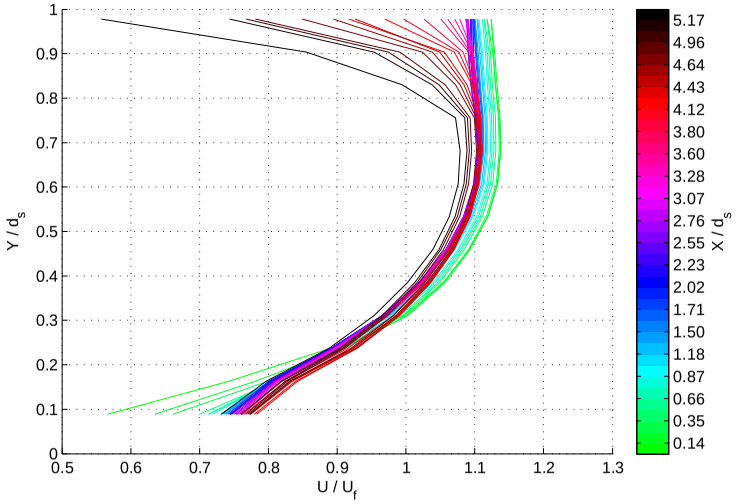

(d) U velocity profiles, surface only

Figure 6.21: U velocities for losing configuration, position 2

For position 1 the v-velocities near the free-surface were close to zero. At the downstream end of the surface layer there was a relatively strong vertical gradient in v-velocities. The v-velocity immediately above the bed was approximately 15% of the flux velocity. The vertical gradient decreased with distance upstream. In position 2, although the measured v-velocities in the surface layer were predominantly negative, the effect of the lateral bars in the stream-bed layer is clear at $x/d_s = 4.5$ in Figure 6.22c.

Figure 6.23 shows Re_p (using k_i and ϕ to estimate the length scale) for the losing stream configuration.

Figure 6.24 shows the values of Re_p, based on the diameter of the hydrated SAP spheres, for the losing configuration. As discussed in Section 6.3.1, this definition of Re_p results in higher values than were obtained using the hydraulic properties to estimate the length scale. At the downstream end of position 1, where interactions with the surface flow are strongest, Re_p is above the threshold given by (Bear, 1972) for turbulent flow in a porous medium. This is consistent with observations of the PTV particle motion during the experimental runs.

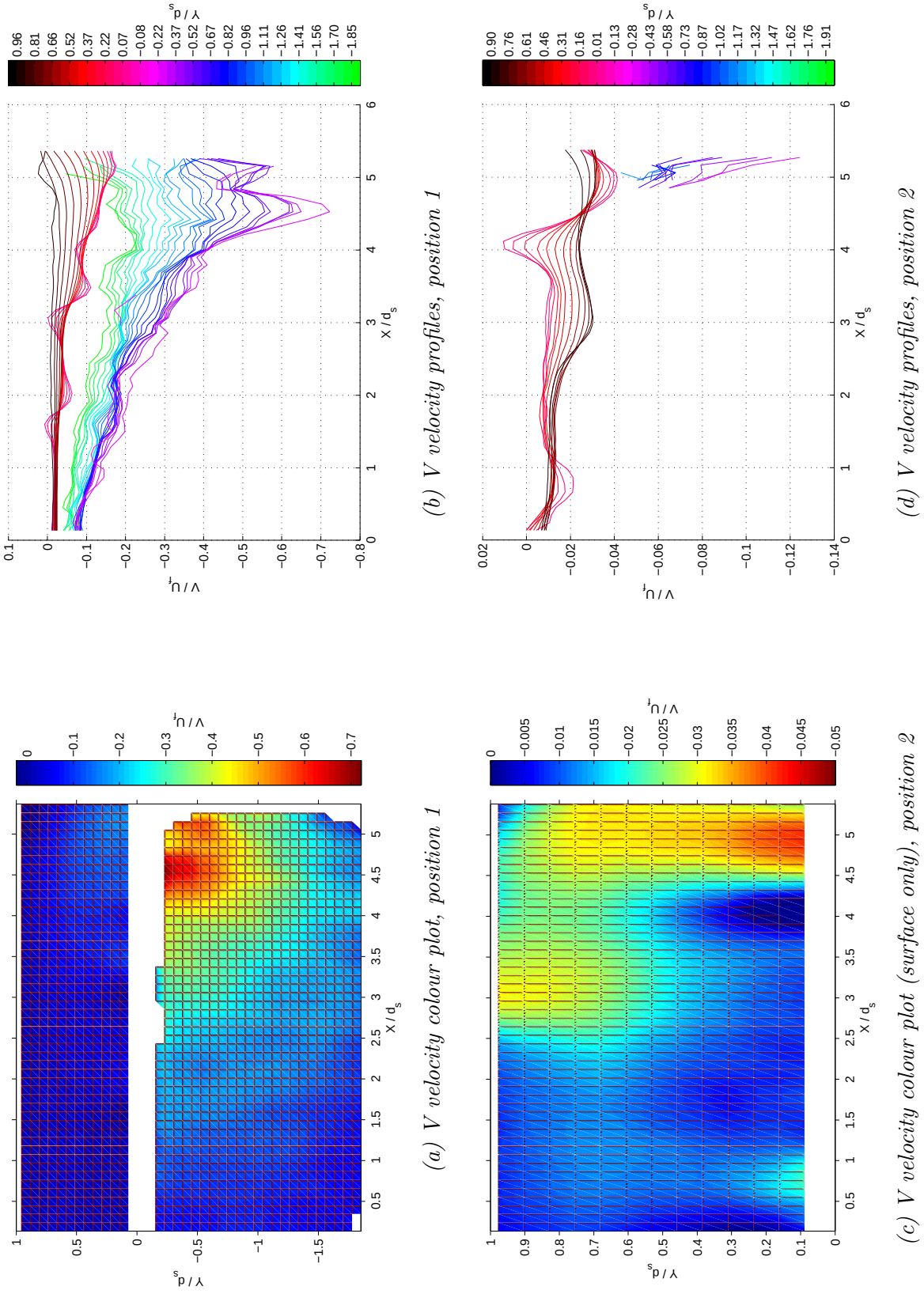

(a) V velocity colour plot, position 1

(b) V velocity profiles, position 1

(c) V velocity colour plot (surface only), position 2

(d) V velocity profiles, position 2

Figure 6.22: V velocities for losing configuration, positions 1 and 2

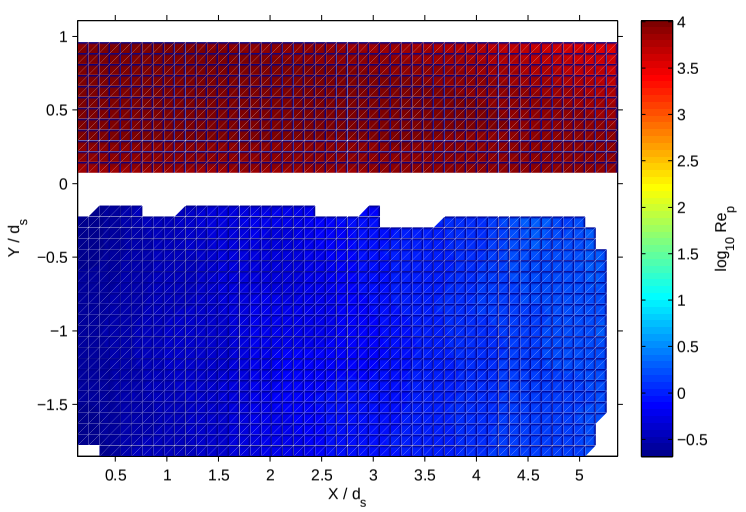

(a) Re_p, surface and subsurface, position 1

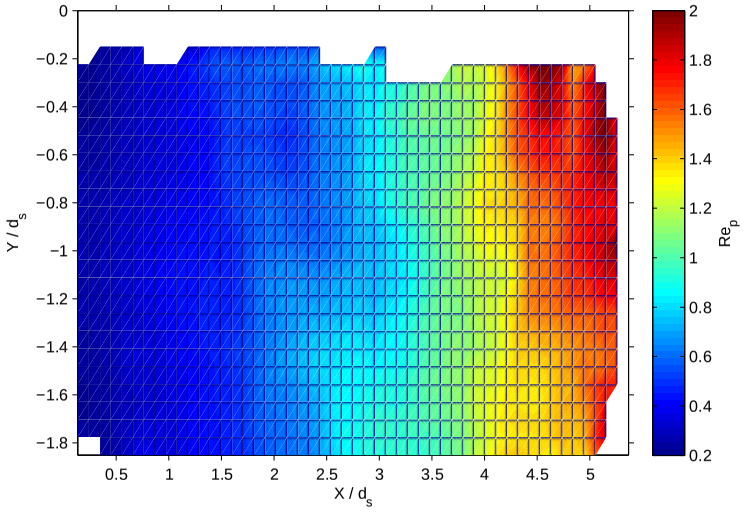

(b) Re_p, subsurface only, position 1

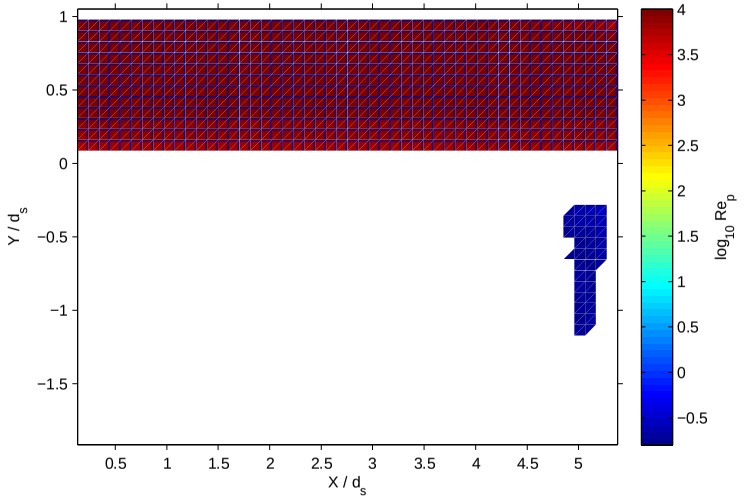

(c) Re_p, surface and subsurface, position 2

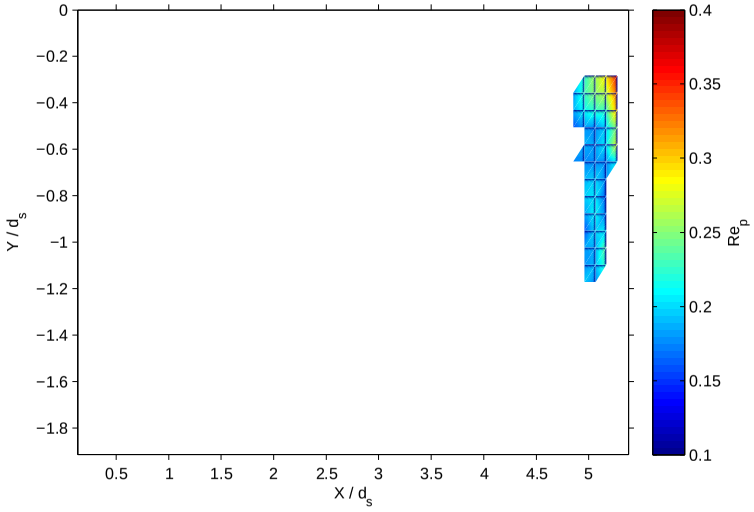

(d) Re_p, subsurface only, position 2

Figure 6.23: Porous Reynolds numbers (Re_p) based on hydraulic properties for positions 1 and 2, losing stream configuration

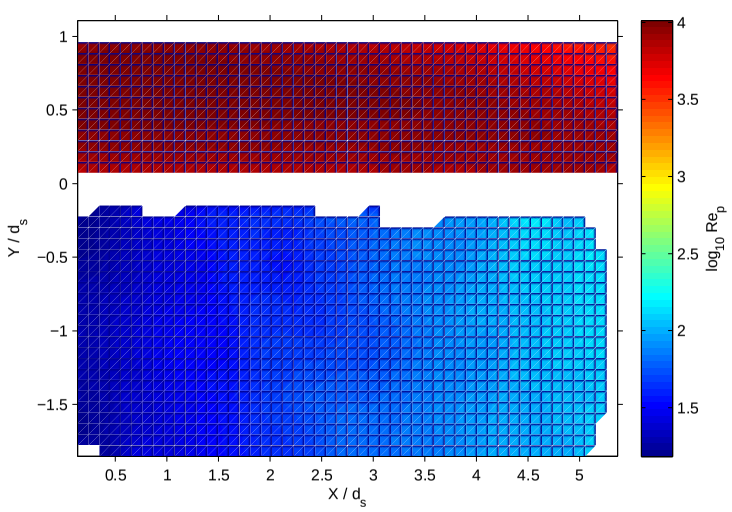

(a) Re_p, surface and subsurface, position 1

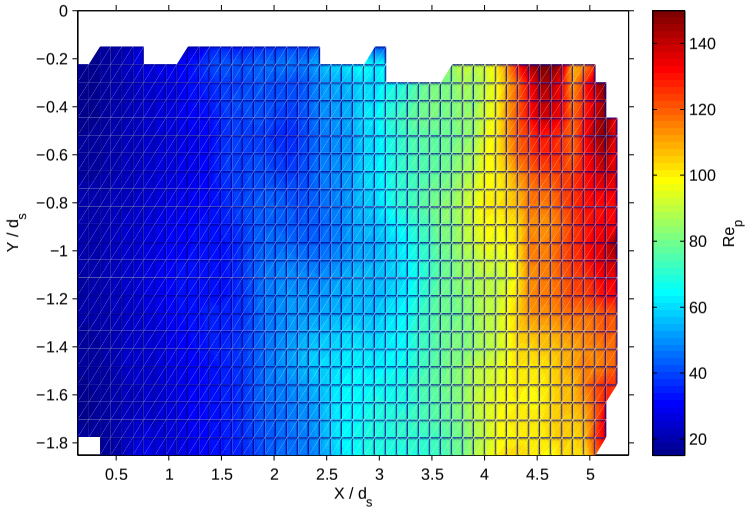

(b) Re_p, subsurface only, position 1

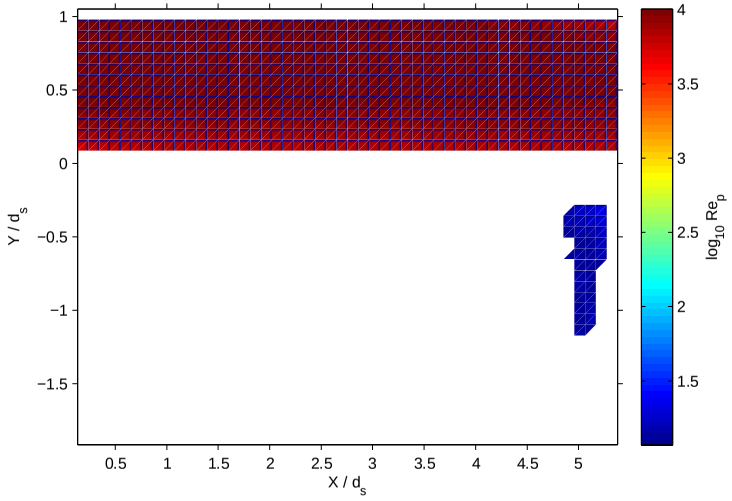

(c) Re_p, surface and subsurface, position 2

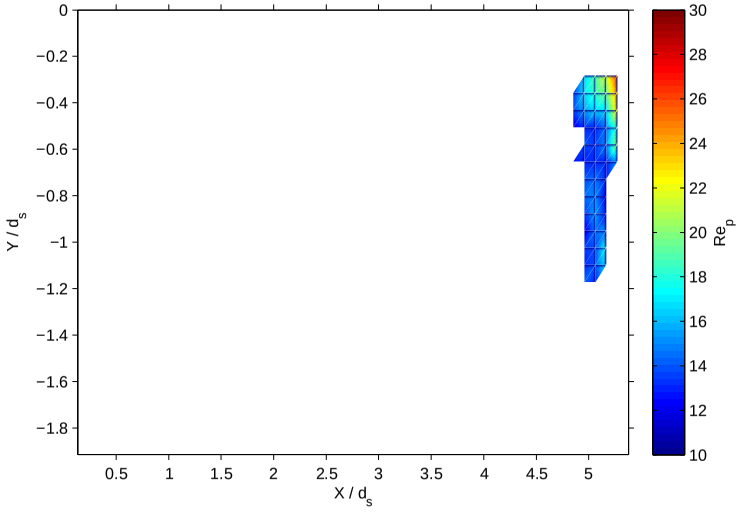

(d) Re_p, subsurface only, position 2

Figure 6.24: Porous Reynolds numbers (Re_p) based on grain diameter for positions 1 and 2, losing stream configuration

6.4.2 Turbulent statistics

Figure 6.25 shows colour plots and horizontal profiles of TKE for the losing configuration in positions 1 and 2.

Vertical profiles of TKE for the losing configuration are shown in Figure 6.26.

At the upstream end of position 2 the vertical TKE profile (Figure 6.26b) is similar to that expected for an open-channel flow, with the maximum values near the bed and a zero gradient at the free-surface. Further downstream in position 2, corresponding to the region in which the u-velocity gradient is reversed, the TKE begins to increase again near the free surface. As with the u-velocities, the highly elevated values of TKE at the downstream end of position 2 are likely to be caused by free-surface distortions in the raw PTV images.

In position 1 (Figure 6.26a) the trend seen in the position 2 vertical TKE profile continues to develop. The depth at which the TKE gradient reverses increases with distance downstream. At the surface-subsurface interface the TKE decreases with distance downstream as the vertical velocity through the bed increases.

Figure 6.27 shows colour plots and horizontal profiles of the Reynolds stresses for the losing configuration in positions 1 and 2.

Vertical Reynolds stress profiles for the losing configuration are shown in Figure 6.28.

In position 2, where the u-velocity profiles were relatively unmodified and v-velocities were negligible, the Reynolds stress profiles were similar to those expected for an open-channel flow, with maximum values near the surface-subsurface interface and tending to zero at the free-surface. Towards the downstream end of position 2, where u-velocities begin to be suppressed near the free-surface (see Figure 6.21) and v-velocities become more significant (see Figure 6.22c) there is an increase in Reynolds stress near the free-surface and a slight reduction near the bed. Similar trends were seen in the TKE in this region (see Figure 6.25c).

Further downstream in position 1, the general shape of the vertical profiles remains similar but the values at a given depth decrease with distance downstream. This is shown both by the relative position of the vertical profiles (Figure 6.28a) changing, and the downwards curve of the horizontal profiles (Figure 6.27b). Negative values of Reynolds stress occur in Figure 6.28a where the vertical gradient

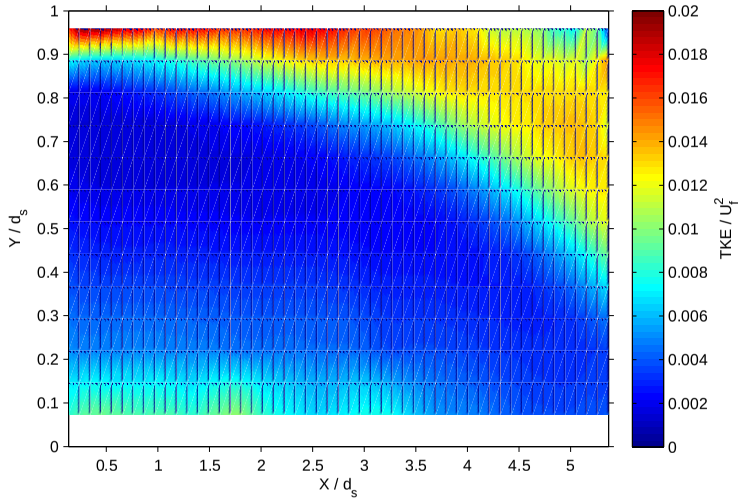

(a) TKE colour plot, position 1

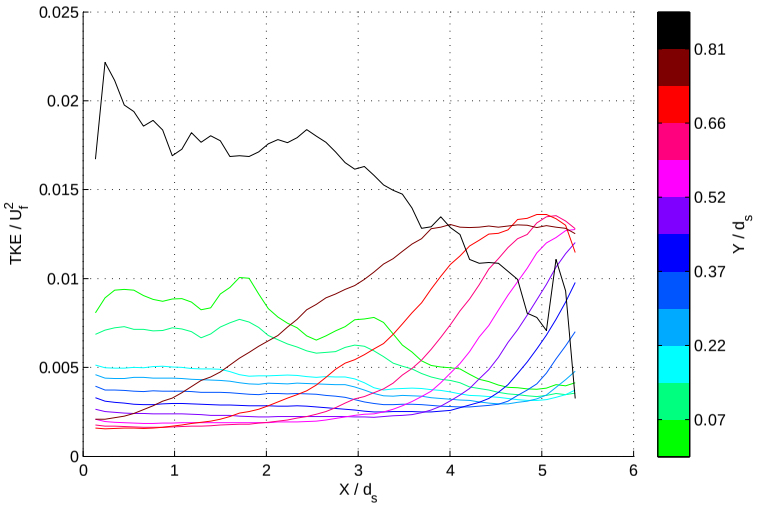

(b) TKE horizontal profiles, position 1

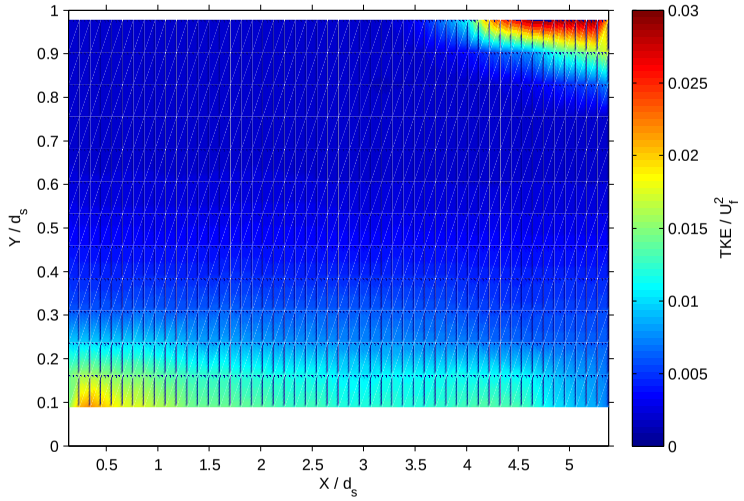

(c) TKE colour plot, position 2

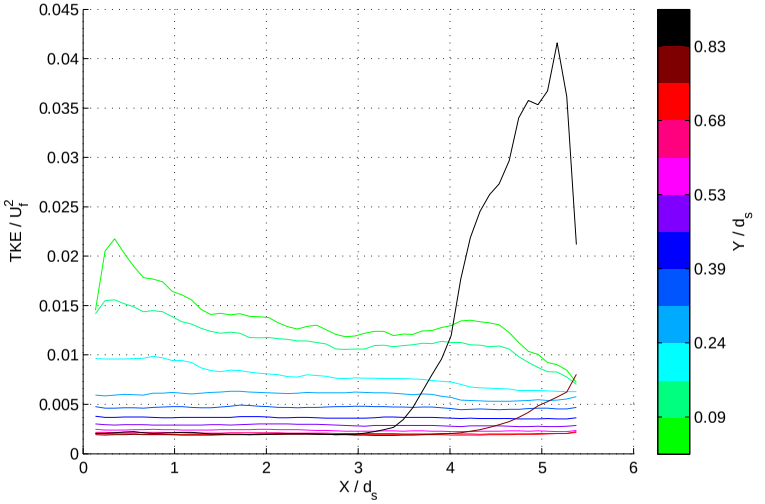

(d) TKE horizontal profiles, position 2

Figure 6.25: TKE for losing configuration, positions 1 and 2

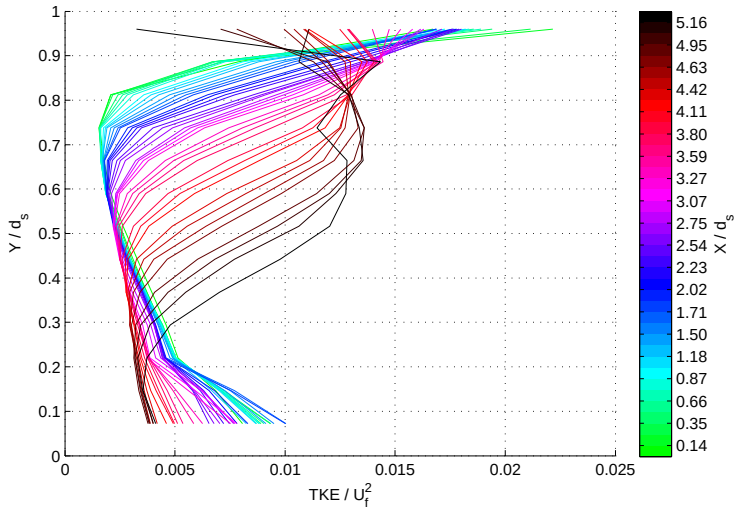

(a) TKE vertical profiles, position 1

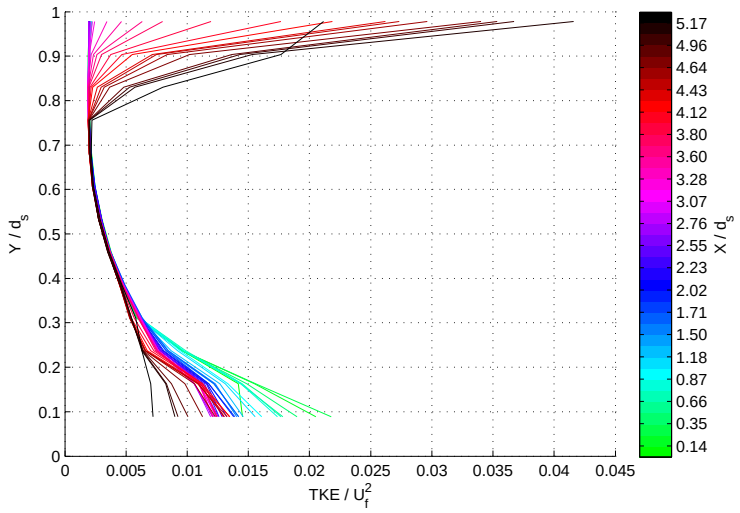

(b) TKE vertical profiles, position 2

Figure 6.26: TKE vertical profiles for losing configuration, positions 1 and 2

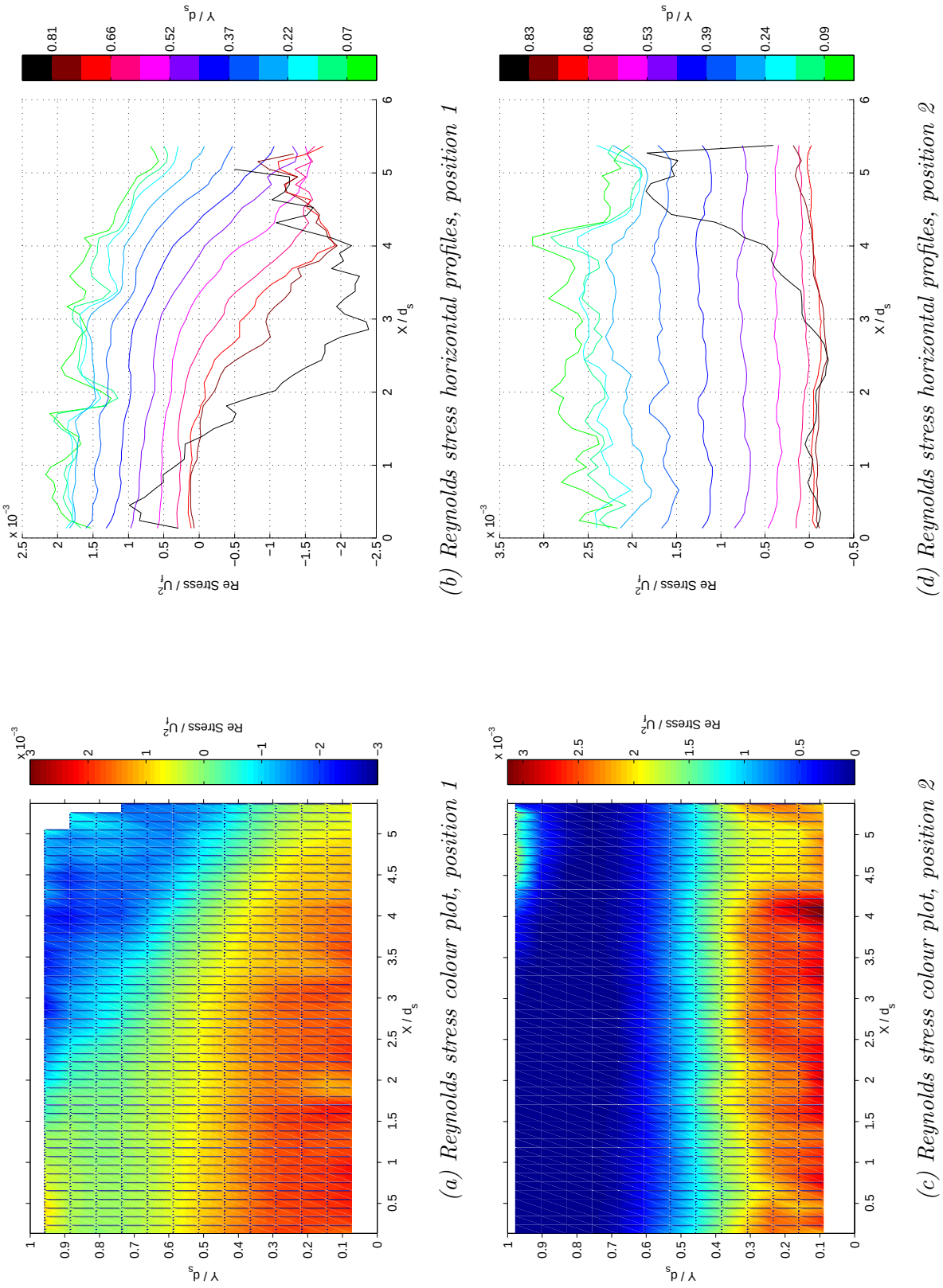

(a) Reynolds stress colour plot, position 1

(b) Reynolds stress horizontal profiles, position 1

(c) Reynolds stress colour plot, position 2

(d) Reynolds stress horizontal profiles, position 2

Figure 6.27: Reynolds stress for losing configuration, positions 1 and 2

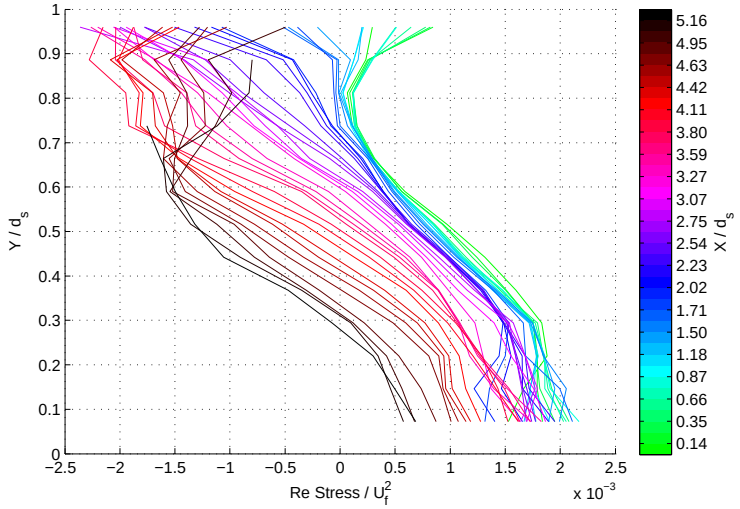

(a) Reynolds stress vertical profiles, position 1

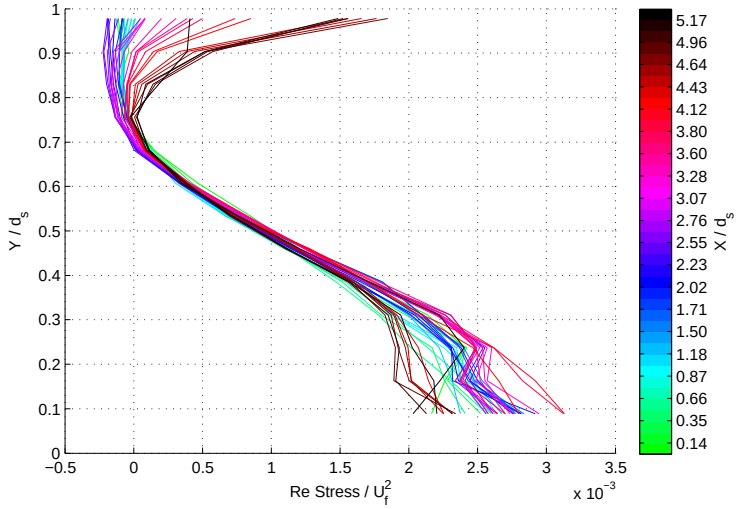

(b) Reynolds stress vertical profiles, position 2

Figure 6.28: Reynolds stress vertical profiles for losing configuration, positions 1 and 2

of the u-velocity profile is negative.

Plots of the estimated turbulence mixing length and turbulent viscosity for the losing configuration are included in Appendix 6.

6.5 Chapter Summary

In this chapter the results of the experimental programme are presented. Results from three experimental configurations were analysed: impermeable bed, "gaining stream" and "losing stream".

Mean flow fields and velocity profiles, and turbulent statistics (TKE and Reynolds stresses) are presented for the three configurations. For each configuration, data from two measurement windows in the flume were presented. Mean flow data was presented for both the subsurface and surface layers. Turbulent statistics were presented for the surface layer only, as the PTV analysis cannot distinguish between temporal fluctuations caused by turbulence and spatial fluctuations caused by the geometry of the porous medium.

The impermeable-bed configuration gave a baseline for comparing the mean flow and turbulent statistic profiles from the other two configurations. It is thought that leakage around the edges of the impermeable layer caused secondary currents that resulted in the u-velocity magnitudes changing with distance downstream. The shape of the velocity profiles was generally unaffected however. The influence of the lateral bars in the "stream-bed" layer could be clearly seen in the v-velocity profiles.

Although the lateral bars were clearly acting as roughness elements, it was not possible to calculate a roughness coefficient (such as Manning's n) from the laboratory results as the free-surface slope could not be measured with sufficient accuracy. It was assumed that the overall roughness of the "stream-bed" layer was not substantially different to what would have occurred without the layer in place (if this had been possible without the porous medium being scoured away).

In both the "gaining stream" and "losing stream" configurations the velocities in the subsurface layer were highest close to the respective boundaries of the porous region (i.e. the upstream end for the gaining case and the downstream end for the losing case). Both the horizontal and vertical velocities in the subsurface

layer decayed towards the middle of the porous region.

In regions where there were strong exchange fluxes across the surface - sub-surface interface, there were substantial modifications to the mean flow profiles and turbulent statistics in the surface layer.

The laboratory results for the gaining and losing configurations provided a set of data to which numerical model results could be compared.

Chapter 7

Numerical Model Verification and Testing

7.1 Overview

The aim of the numerical model verification and testing programme was to show that the DANS numerical model is capable of modelling flows in surface water (clear fluid), groundwater and mixed (interacting groundwater and surface water) domains.

The finite-volume RANS and DANS models are referred to as FV-RANS and FV-DANS respectively.

The results shown in this chapter are double-averaged values; the angle-brackets and overbars on the variable symbols have been dropped for clarity.

The first results presented in this chapter are for two "book-end" scenarios: a fully clear-fluid domain (Section 7.2) and a fully porous domain (Section 7.3). The ability of the FV-DANS model to accurately simulate flows for these scenarios is a necessary, but not sufficient, condition for the model to be able to simulate flows in mixed porous / clear-fluid domains - i.e. running the book-end scenarios successfully does not guarantee that the mixed domain case will be successful, but if the model cannot be verified for the book-end scenarios then it cannot be expected to work successfully for the mixed case.

Following the clear-fluid and porous cases, results are presented in Section 7.4

for a scenario replicating the "gaining stream" laboratory experiments (as discussed in Chapter 6). The FV-DANS model could not replicate the "losing stream" experiments; the results presented for this configuration are for lower flow velocities than those measured in the laboratory.

The two laboratory configurations are rather extreme cases of groundwater - surface water interactions. They involve discontinuities in the hydraulic properties (i.e. large step-changes in k_i and ϕ at the surface - subsurface interface), and flows that transition from laminar to turbulent (or *vice versa*) over a short distance. The relatively short length of the laboratory flume meant that the upstream and downstream boundaries influenced the laboratory results, and these boundary conditions were challenging to incorporate into a numerical model. Therefore it was not expected that results from the FV-DANS model would match the laboratory data well in all parts of the domain. Rather, this section of the model testing was aimed at replicating the key features of the flow, and confirming the model's ability to handle the transition between laminar and turbulent flow.

All scenarios were run on a standard laptop computer. Run-times were not excessive, with a maximum of around 10 minutes to converge to steady-state from assumed initial conditions for the laboratory scenarios, therefore the use of higher-performance computational resources was not explored.

7.2 Clear-Fluid Flow

Outputs from the FV-RANS and FV-DANS models were verified against published experimental data and model results for turbulent clear-fluid flow between parallel plates (i.e. two solid, impermeable boundaries). The initial purpose of running this scenario was to ensure that the RANS model (with the two different turbulence models) was functioning correctly, resulting in the expected velocity profiles, before it was converted to the FV-DANS model.

After the FV-RANS and FV-DANS models had been verified for the parallel-plates configuration, the free-surface boundary condition (as described in Chapter 4) was implemented in the FV-DANS model. Outputs from the FV-DANS model in a free-surface configuration were verified against published model results

and compared with results from HEC-RAS.

7.2.1 Flow between parallel plates

The FV-RANS model was run for a steady turbulent flow between two smooth parallel plates, with both the $k - \epsilon$ and single-equation turbulence models. The upstream boundary condition was a uniform velocity, and the velocity profile developed with distance downstream. At the upstream end of the domain there were non-zero vertical velocities as the shape of the horizontal velocity profile developed. After a short distance downstream the flow was one-dimensional, with negligible vertical velocities. The reported results are the fully-developed profiles from the downstream end of the domain.

The model domain was set up with $dx = 0.5\ m$ and $dy = 0.01\ m$, with refinement in the y-direction at the solid boundaries. The model was run with a time-step of 1 s.

For a clear-fluid flow the additional terms that were added to the FV-RANS model to convert it to the FV-DANS model are expected to become negligible, and the two models should give results that are effectively the same. Results from the FV-RANS and FV-DANS models with identical inputs were compared to check that this was the case. Profiles of velocity and turbulent kinetic energy from both the FV-RANS and FV-DANS models were compared.

For this stage of the verification the default parameter values (as given in Chapter 2) were used for both the $k - \epsilon$ and single-equation turbulence models.

7.2.1.1 Velocity profiles: FV-RANS model

Prior to verifying the FV-RANS outputs against published data, several baseline data sets were compared to give an indication of how closely model data can be expected to fit experimental data, and the level of variability between different model types. Figure 7.1 compares dimensionless velocity profiles from experimental data (Rodi, 1980), a RANS model with a $k - \epsilon$ turbulence model (Rodi, 1980),and a DNS model (Kim et al., 1987) (data published in Pope (2000))

Table 7.1 shows the normalised root-mean-squared (RMS) errors for the baseline data sets plotted in Figure 7.1, firstly comparing the two models to the

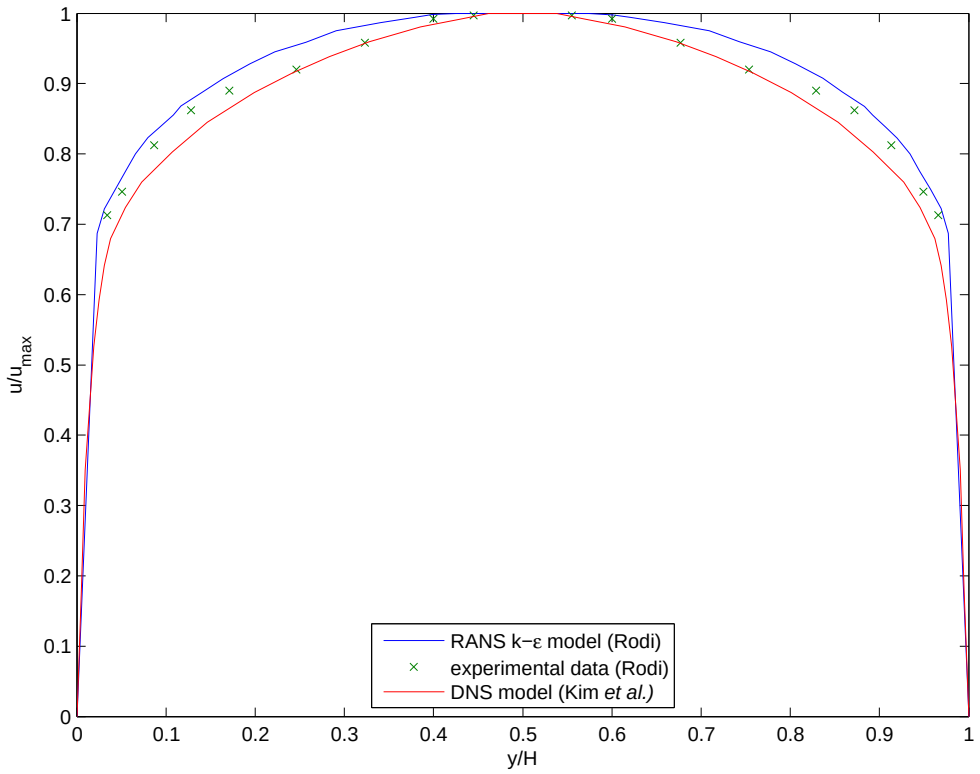

Figure 7.1: Published experimental and modelled velocity profile data

experimental data, and then the models to each other. Both models fit the experimental data well ($< 4\%$ RMS error), and the level of agreement between the two models is reasonably good.

Table 7.1: Normalised RMS errors for dimensionless u-velocity profiles: baseline data

"Observed"	Predicted	Normalised RMS error (%)
Rodi experimental	Rodi RANS model	2.3
Rodi experimental	Kim et al DNS model	3.7
Rodi RANS model	Kim et al DNS model	5.5

Figure 7.2 shows the dimensionless velocity profiles generated by the FV-RANS model, with both the $k - \epsilon$ and single-equation turbulence models, compared to Rodi's RANS model.

Table 7.2 shows the normalised RMS errors for the dimensionless u-velocity

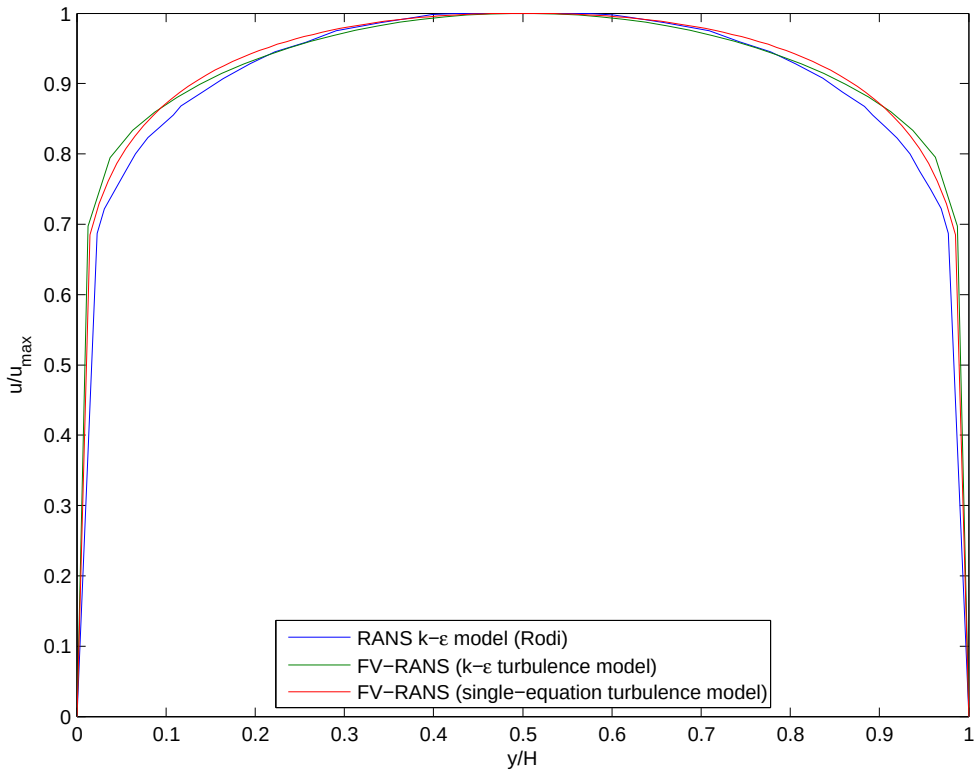

Figure 7.2: Velocity profile verification: Rodi RANS model and FV-RANS

profiles generated by the FV-RANS model, compared to Rodi's model results.

Table 7.2: Normalised RMS errors for dimensionless u-velocity profiles

"Observed"	Predicted	Normalised RMS error (%)
Rodi RANS model	FV-RANS ($k-\epsilon$ turbulence model)	3.4
Rodi RANS model	FV-RANS (single-equation turbulence model)	2.4

The level of error between the velocity profiles generated by the FV-RANS model and Rodi's results is similar to the errors between the published model and experimental results shown in Figure 7.1, and less than the error between the two sets of model results. Although the FV-RANS model produces an acceptably close match to the published results with both turbulence models, it is unclear

why the velocity profile generated using the single-equation turbulence model is a slightly better match to Rodi's RANS results (which used a $k-\epsilon$ model) than the profile generated with the $k-\epsilon$ model.

7.2.1.2 Turbulent kinetic energy: FV-RANS model

Figure 7.3 compares dimensionless TKE profiles from published experimental data and results from a RANS model with a $k-\epsilon$ turbulence model (Rodi, 1980).

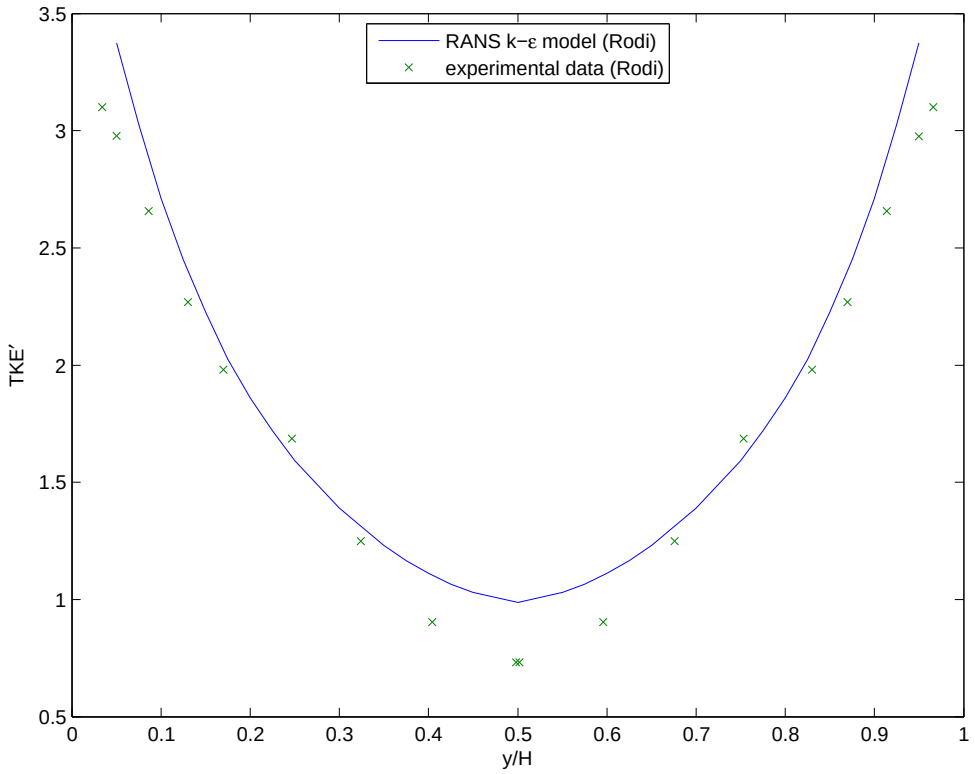

Figure 7.3: Published experimental and modelled TKE profile data

The normalised RMS error between Rodi's experimental and numerical TKE profiles is 16.2%. This provides a benchmark for how well a turbulence model can be expected to fit experimental data.

Figure 7.4 compares dimensionless TKE profiles generated by the FV-RANS model, with both the $k-\epsilon$ and single equation turbulence models, to Rodi's

RANS data. The TKE data was non-dimensionalised by U_τ^2.

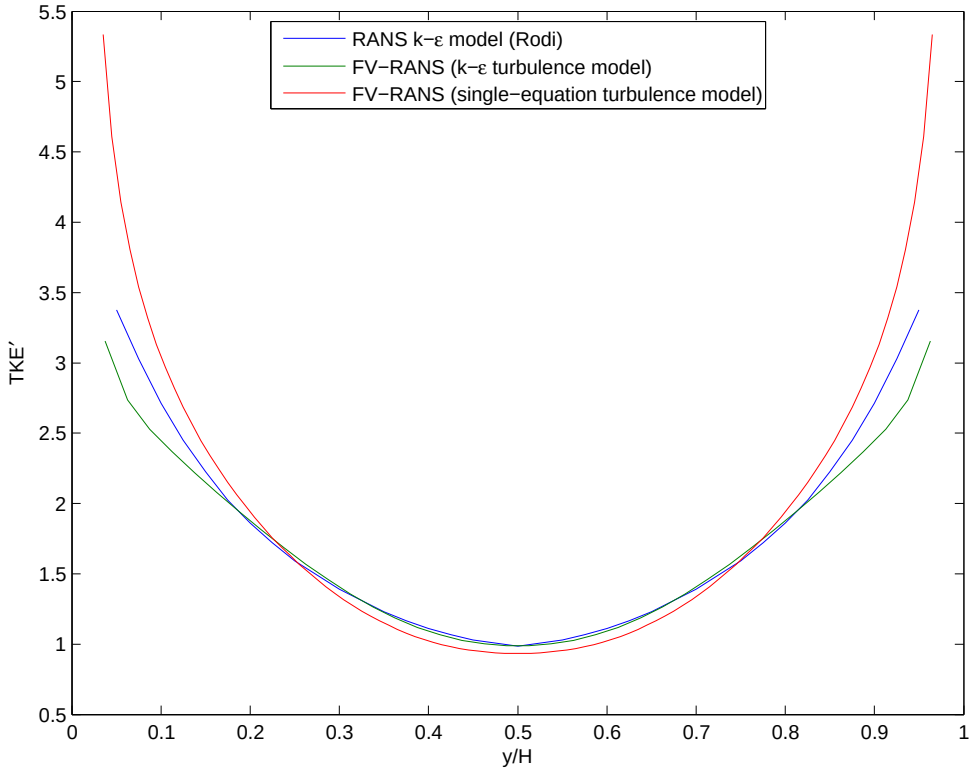

Figure 7.4: TKE profile: Rodi RANS model and FV-RANS

Table 7.3 shows the normalised RMS errors for the dimensionless TKE profiles from the FV-RANS model, compared to Rodi's model data. As expected, the match between the two $k-\epsilon$ models is closer than between the single-equation and $k-\epsilon$ model. Without knowing the exact details of Rodi's numerical model, it is not possible to explain why the match is not even closer, given that they are the same form of model.

7.2.1.3 Velocity: comparing FV-RANS and FV-DANS models

Figure 7.5 shows the dimensionless velocity profiles generated by the FV-RANS and FV-DANS models. The hydraulic properties in the DANS model were set to values representative of a clear-fluid flow (i.e. $\phi = 1$ and $k_i \gg 1$). All other

Table 7.3: Normalised RMS errors for dimensionless TKE profiles

"Observed"	Predicted	Normalised RMS error (%)
Rodi RANS model	FV-RANS (k-eps turbulence model)	6.6
Rodi RANS model	FV-RANS (single-equation turbulence model)	8.0

inputs and parameters that the two models have in common were identical. As expected, the two profiles coincide almost exactly.

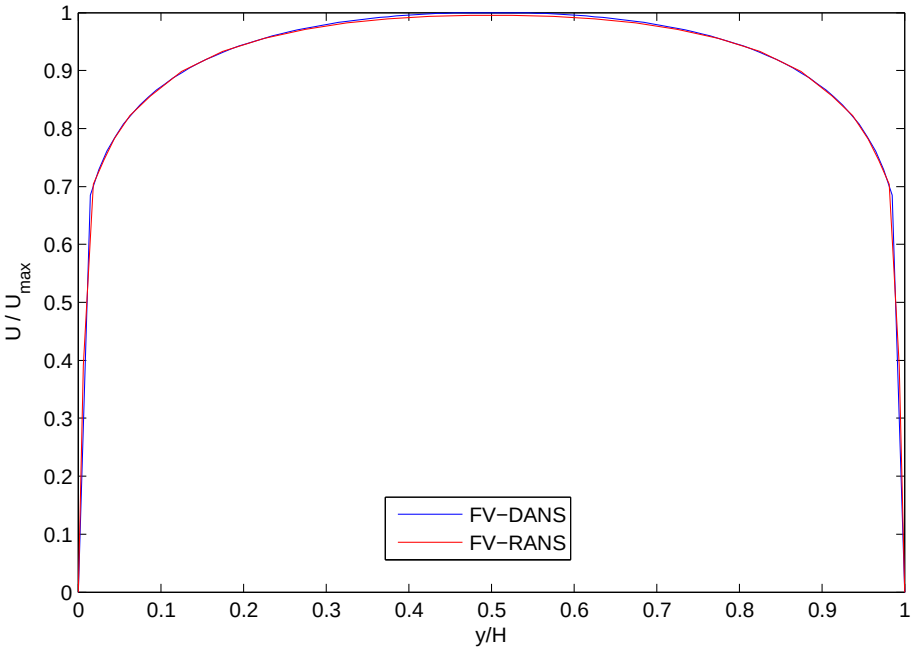

Figure 7.5: Velocity profile verification: FV-RANS and FV-DANS

7.2.1.4 TKE: comparing FV-RANS and FV-DANS models

Figure 7.6 shows the dimensionless TKE profiles generated by the FV-RANS and FV-DANS models. Like the velocity profiles for the two models, the difference between the TKE profiles is negligible, which shows that (at least for the simple case that was modelled) with appropriately-specified hydraulic properties the FV-DANS model reverts to the RANS equations for clear-fluid flow.

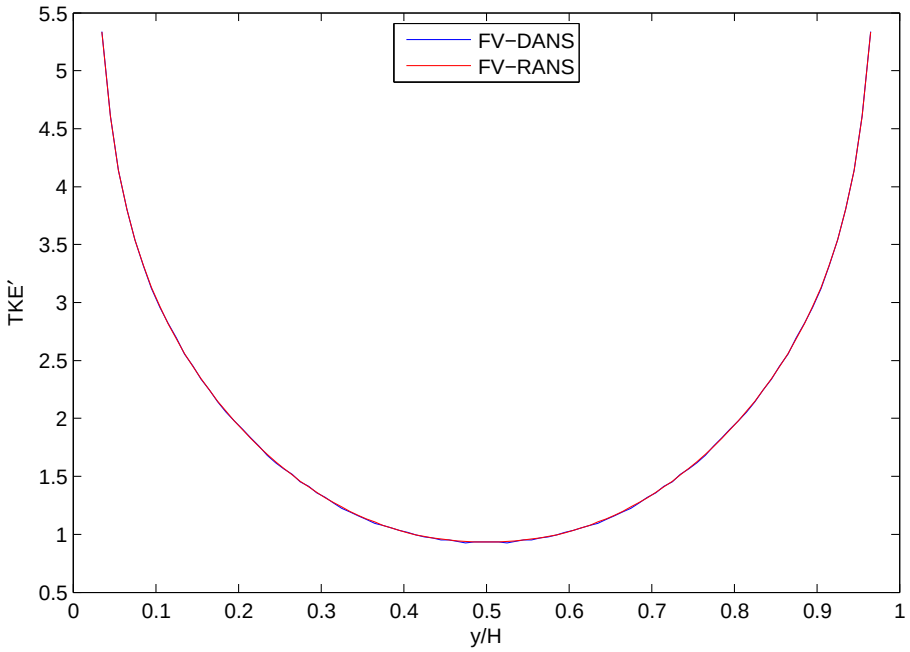

Figure 7.6: TKE profile verification: FV-RANS and FV-DANS

7.2.2 Free-surface flow

Following the parallel-plates verification scenarios, the FV-DANS model was run for a steady, turbulent clear-fluid flow with a free-surface boundary condition (as discussed in Chapter 4). As all components of the FV-DANS model had been added by this stage of the numerical model development, for this scenario the turbulence model parameters were calibrated to improve the match between the results obtained with the single-equation model, and the published RANS (with $k-\epsilon$) model results (Rodi, 1980). The default and calibrated values of the turbulence model parameters are shown in Table 7.4. With the exception of C_d, the constant in the equation used to calculate ϵ, the calibrated parameters were close to or identical to the default values. The need for a higher value of C_d to get a good match with the TKE profile is perhaps a reflection of the method used to calculate the mixing length.

The model was set up with $dx = 1\ m$ and $dy = 0.05\ m$, with refinement in the y-direction at the bed. The model was run with a time-step of $1\ s$.

Table 7.4: Default and calibrated parameter values for single-equation turbulence model

Parameter	Default literature value	Calibrated value
σ_k	1.0	0.8
C_μ	0.09	0.07
C_{y1}	2.4	2.4
C_{y2}	0.003	0.003
A_0	26	26
C_d	0.08	0.15

7.2.2.1 Velocity profiles

Figure 7.7 shows dimensionless velocity profiles from the FV-DANS model (with the calibrated turbulence model) and Rodi's RANS model results. The RMS error between the two profiles is 1.1%.

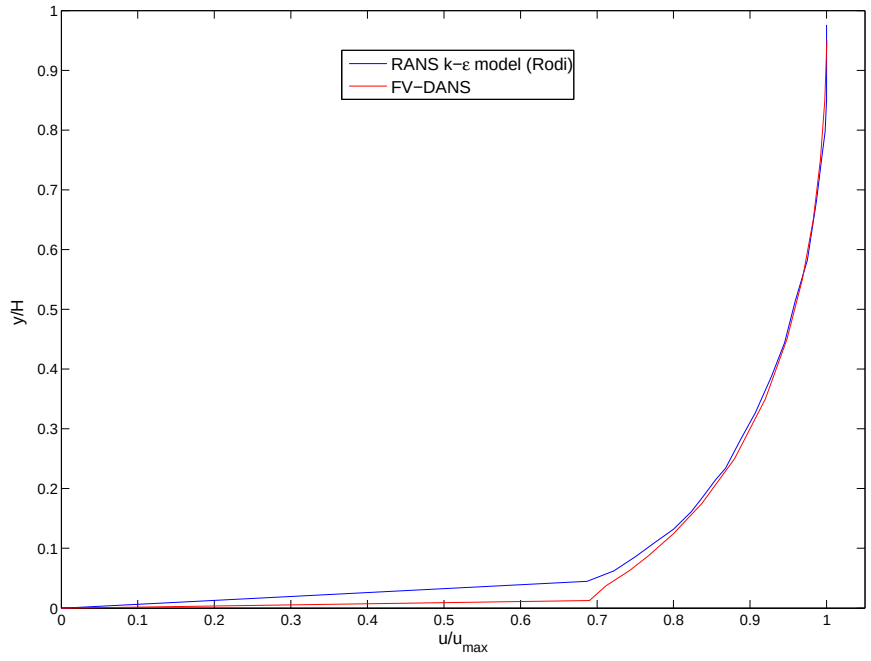

Figure 7.7: Free-surface dimensionless velocity profiles: FV-DANS and RANS (Rodi, 1980)

The majority of the error between the two velocity profiles is near the impermeable boundary. This indicates that the key difference between the two models is in how the wall boundary condition is handled. Overall, the match is very

good.

7.2.2.2 Turbulence

Figure 7.8 shows dimensionless TKE profiles from the FV-DANS model and Rodi's RANS model results. The RMS error between the two TKE profiles is 7.1%.

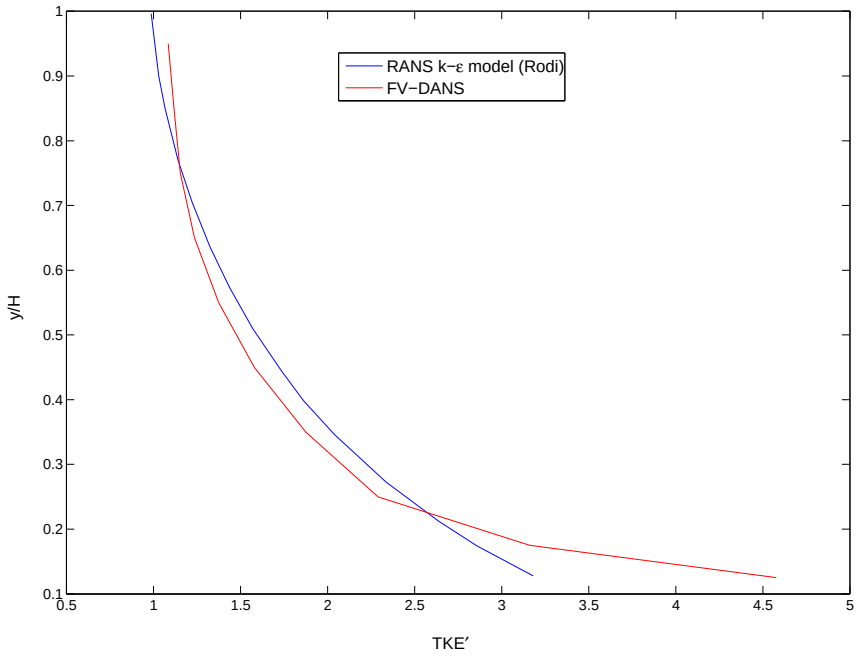

Figure 7.8: Free-surface dimensionless TKE profiles: FV-DANS and RANS (Rodi, 1980)

The RMS error is slightly less than the error between the parallel-plates TKE profiles from FV-RANS model (with the single-equation turbulence model) and Rodi's RANS results. The fact that the calibration of the turbulence model parameters (as shown in Table 7.4) was more effective for the velocity profiles than for the TKE is not a concern, however, as the primary purpose of the model is to generate velocity fields, not turbulence statistics.

7.2.2.3 Longitudinal free-surface profiles

Free-surface elevation profiles from the FV-DANS model were compared with equivalent results from HEC-RAS (Brunner, 2002) for a range of steady flows with varying flow depths and velocities.

As discussed in Chapter 3, HEC-RAS is an industry-standard package for 1D open-channel flow modelling, and is similar to the open-channel component of many existing integrated models. Although the dimensionality of HEC-RAS and the FV-DANS model is different, and they use different governing equations, it is expected that for a comparable flow scenario the results from the two models should be similar.

A straight channel with a uniform wide rectangular cross-section and a smooth horizontal bed was set up in HEC-RAS.

Open-channel bed roughness is not parameterised in the FV-DANS model in the same way as it is in HEC-RAS (i.e. with a Manning's n), rather it is represented by the hydraulic properties (ϕ and k_i) of the bed material. With the hydraulic properties set to $\phi = 1$ and $k_i \gg 1$ throughout the domain, the bottom boundary in the FV-DANS model is treated as a smooth impermeable wall. Therefore in the HEC-RAS model it was necessary to specify a Manning's roughness coefficient that was representative of a smooth surface. A range of $n = 0.009 - 0.011$ is given by Neale and Price (1964) for smooth PE / PVC pipes (for units of metres and seconds). Taking the lower end of this range, Manning's n in the HEC-RAS model was set to $n = 0.009$.

Boundary conditions are specified differently in the two models. For example, in HEC-RAS the discharge (in m^3/s) is set as an upstream boundary condition. The model solves the SWE for the flow depth and reports a depth-averaged velocity. In the FV-DANS model a velocity profile is specified at the upstream boundary. Because of these differences some trial-and-error was required to set up comparable scenarios.

The basis for comparing the two models was the slope of the energy grade-line (EGL), as defined in Figure 2.6. The EGL slope is one of the standard results reported by HEC-RAS. For the FV-DANS model the depth-averaged u-velocity was used to calculate the velocity head.

Results for the two models are shown in Figure 7.9 and Table 7.5. The slope of the EGL from each model is shown for a range of flow depths and three different depth-averaged velocities.

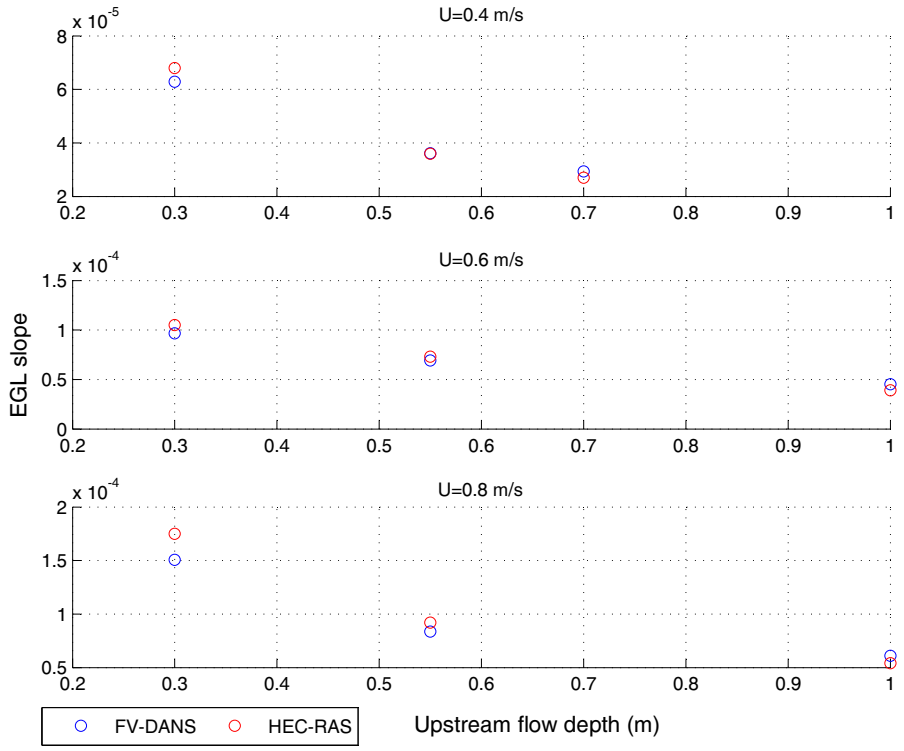

Figure 7.9: Comparison of EGL slopes from FV-DANS and HEC-RAS

The EGL slope from FV-DANS model does not appear to be systematically lower or higher than the results from HEC-RAS. This could be a reflection of the trial-and-error required to set up the comparisons. In absolute terms the difference between the two models is greatest at shallower flow depths, but there is no clear trend in the percentage difference.

The results of the two models are sufficiently close to give confidence in the ability of the FV-DANS model to simulate a simple open-channel flow.

Table 7.5: Comparison of EGL slopes from FV-DANS and HEC-RAS

Depth-averaged velocity (m/s)	Upstream flow depth (m)	EGL slope		
		FV-DANS	HEC-RAS	% difference
0.4	0.55	3.61×10^{-5}	3.60×10^{-5}	0.3%
0.4	0.3	6.29×10^{-5}	6.80×10^{-5}	-7.5%
0.4	0.7	2.94×10^{-5}	2.70×10^{-5}	8.7%
0.6	0.55	6.92×10^{-5}	7.30×10^{-5}	-5.2%
0.6	0.3	9.67×10^{-5}	1.05×10^{-4}	-7.9%
0.6	1	4.51×10^{-5}	3.90×10^{-5}	15.6%
0.8	0.55	8.37×10^{-5}	9.20×10^{-5}	-9.1%
0.8	0.3	1.51×10^{-4}	1.75×10^{-4}	-13.9%
0.8	1	6.10×10^{-5}	5.40×10^{-5}	12.9%

7.3 Porous Media Flow

To confirm that the FV-DANS model reverts to Darcy's Law for porous-media flow with a sufficiently low value of Re_p, a series of runs was done with the FV-DANS model, with $k_i \ll 1$ and $\phi < 1$ throughout the domain.

Initially no spatial variation of hydraulic parameters was considered - i.e. the model domain was a single uniform porous layer. The model was run for various combinations of k_i, ϕ and U_i with a uniform horizontal inflow at the upstream end.

The hydraulic properties were then varied spatially, with step-changes in k_i and ϕ. The purpose of these tests was to check whether the numerical treatment of the double-averaged terms (as described in Section 4.8.2) was functioning as intended.

For all of the porous-media verification scenarios the FV-DANS model was run with a free-surface boundary. The model was therefore simulating flow in an unconfined aquifer, which is the most relevant case for modelling an aquifer that interacts with a surface water body. Storativity and specific yield (as discussed in Section 2.3.1) are not included in the FV-DANS model, but as these terms only occur in the time-derivative term of the groundwater flow equation (Equation 2.27), it is expected that the FV-DANS model will match a Darcian steady flow model for either confined or unconfined flow.

The model was set up with $dx = 0.1\ m$ and $dy = 0.05\ m$. The model was run with a time-step of 60 s.

7.3.1 Darcian flow in a homogeneous domain

For the homogeneous-domain porous media verification scenarios the range of permeability considered was $k_i = 1 \times 10^{-11}\ m^2$ to $k_i = 1 \times 10^{-6}\ m^2$. This covers the range of permeabilities given by Bear (1972) for well-sorted gravel, well-sorted sand, and gravel / sand mixes. The upper end of the range is more permeable than the upper limit given for gravels; this is necessary to represent cobbles / boulders at or near a stream-bed. The measured permeability of SAP spheres that were used in the laboratory experiments (as described in Chapter 5) also falls within this range.

It was not considered necessary to test the performance of the model with lower permeability values. It is not the permeability itself, but the value of Re_p that determines whether a flow is Darcian. Therefore if the model performs well for combinations of velocity and permeability that result in a Re_p value below the upper threshold for Darcian flow, it is reasonable to assume that it would perform similarly well for Darcian flows with lower permeability values.

The values of ϕ considered represent the range from poorly sorted sand / gravel mixes ($\phi = 0.15$) through to topsoil ($\phi = 0.6$) (Bear, 1972).

Figure 7.10 shows plots of the hydraulic gradient $\frac{\partial h}{\partial x}$ vs. Darcy velocity U_D for the range of permeabilities considered. The points on the plots are the results of the FV-DANS model runs, and the reference lines are the relationship between hydraulic gradient and Darcy velocity that is expected from Darcy's Law, defined as follows:

$$\frac{\partial h}{\partial x} = -\frac{1}{K} U_D \tag{7.1}$$

where $\frac{\partial h}{\partial x}$ is the piezometric head gradient in the x direction, K is hydraulic conductivity (NB: not the intrinsic permeability), and U_D is the Darcy velocity (i.e. $U_D = \phi U_i$).

For combinations of velocity and permeability that resulted in $Re_p < 0.1$ (where Re_p is defined based on the hydraulic properties) the data points from the FV-DANS model, plotted in blue in Figure 7.10, lie exactly on the Darcy's Law reference line. Data points from model runs with $Re_p \geq 0.1$, plotted in red, deviate from the line. This threshold for the upper limit of Darcian flow is consistent with the values calculated in the laboratory results (Chapter 6) where the upper threshold of Darcian flow given by Bear (1972) for Re_p based on particle diameter was related to Re_p based on hydraulic properties.

Figure 7.11 shows the hydraulic gradient vs. Darcy velocity for four different values of ϕ, with k_i held constant. The solid line is the relationship between hydraulic gradient and Darcy velocity expected from Darcy's Law (as in Equation 7.1). Changing ϕ while holding k_i constant only changes the relationship between the Darcy velocity and the pore velocity. Therefore all of the results shown in Figure 7.11 plot on the same line. All of the points plotted on Figure 7.11 were

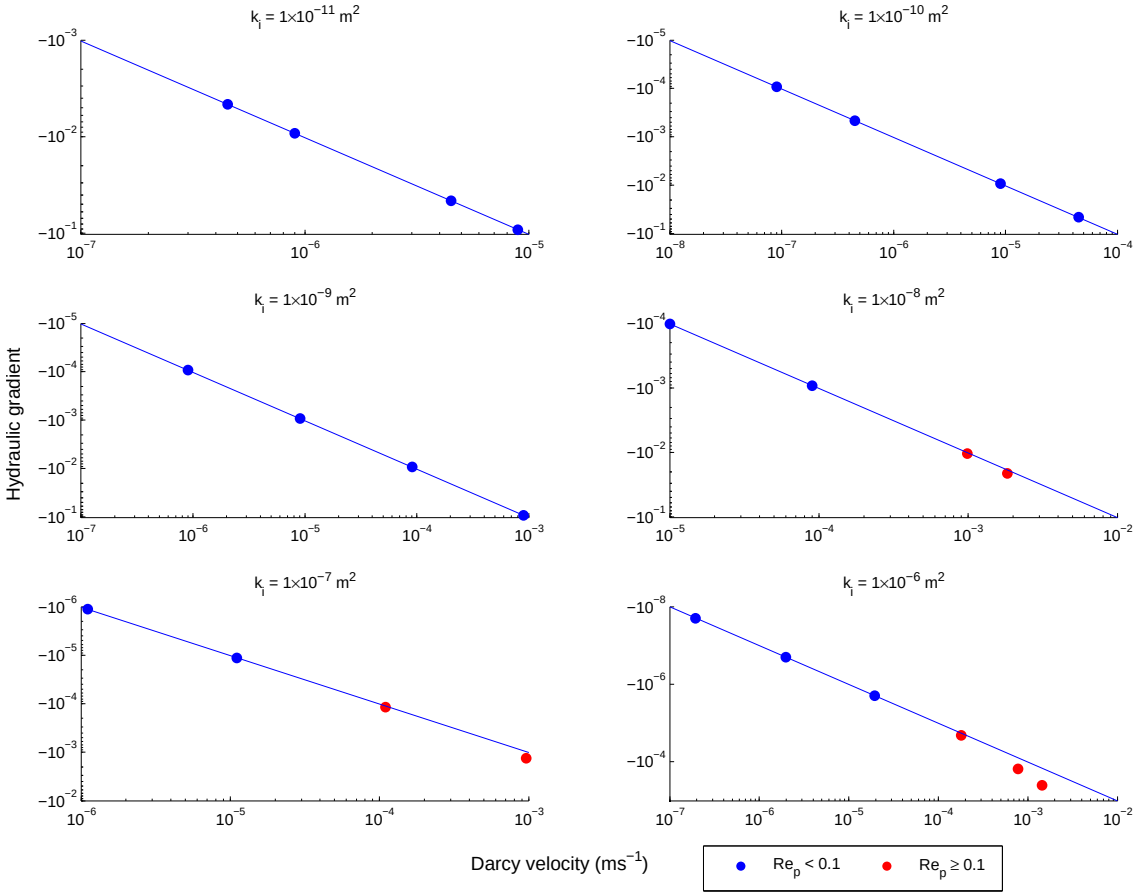

Figure 7.10: Hydraulic gradient vs. Darcy velocity for varying k_i. Solid lines are the values expected from Darcy's Law.

from model runs with $Re_p < 0.1$. Therefore, as expected, all data points fall exactly on the reference line.

7.3.2 Darcian flow in an inhomogeneous domain

To test whether the FV-DANS model handles spatial changes in hydraulic properties correctly, the model was run for scenarios that included step-changes in hydraulic properties. Although in natural porous materials there is typically a relationship between porosity and permeability, holding one property constant in the model while varying the other is a useful way of testing whether the addi-

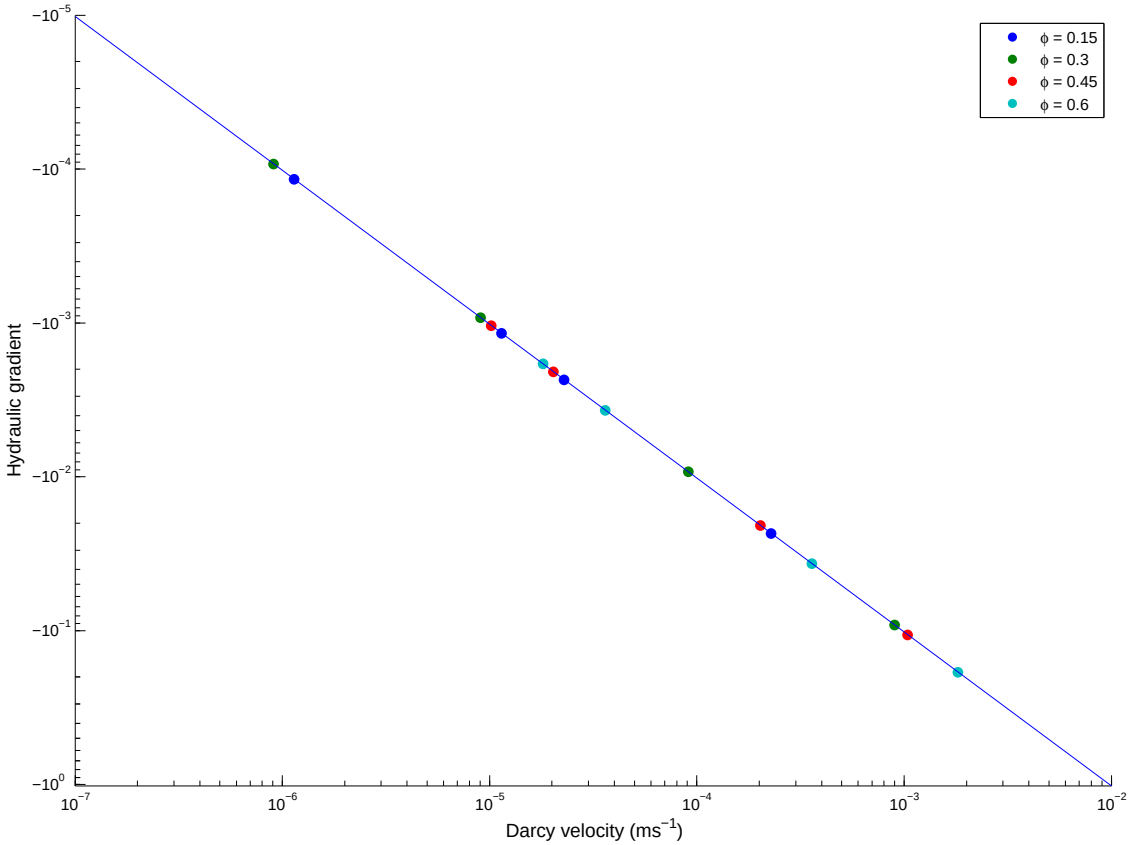

Figure 7.11: Hydraulic gradient vs. Darcy velocity for varying ϕ. Solid line is the value expected from Darcy's Law.

tional terms that arise from the double-averaging process have been implemented correctly.

Two 1D scenarios were run: a step-change in k_i with ϕ held constant, and a step-change in ϕ with k_i held constant. A third scenario considered a 2D change in k_i. For all three scenarios a uniform inflow boundary condition was applied, with the inflow velocity sufficiently low to ensure that the flow was fully in the Darcian regime.

Figure 7.12 shows the effective pressure (deviation from hydrostatic), Darcy velocity (post-processed from the model results) and pore velocity along the x-axis for a domain with a step-change in permeability, where the porosity is held

constant. The Darcy and pore velocities both remain constant along the x-axis, as expected. At the step-change in permeability there is a sudden change in the pressure gradient. The pressure gradient on both sides of the step-change matches the value expected from Darcy's Law for the combination of Darcy velocity and permeability used in the model run.

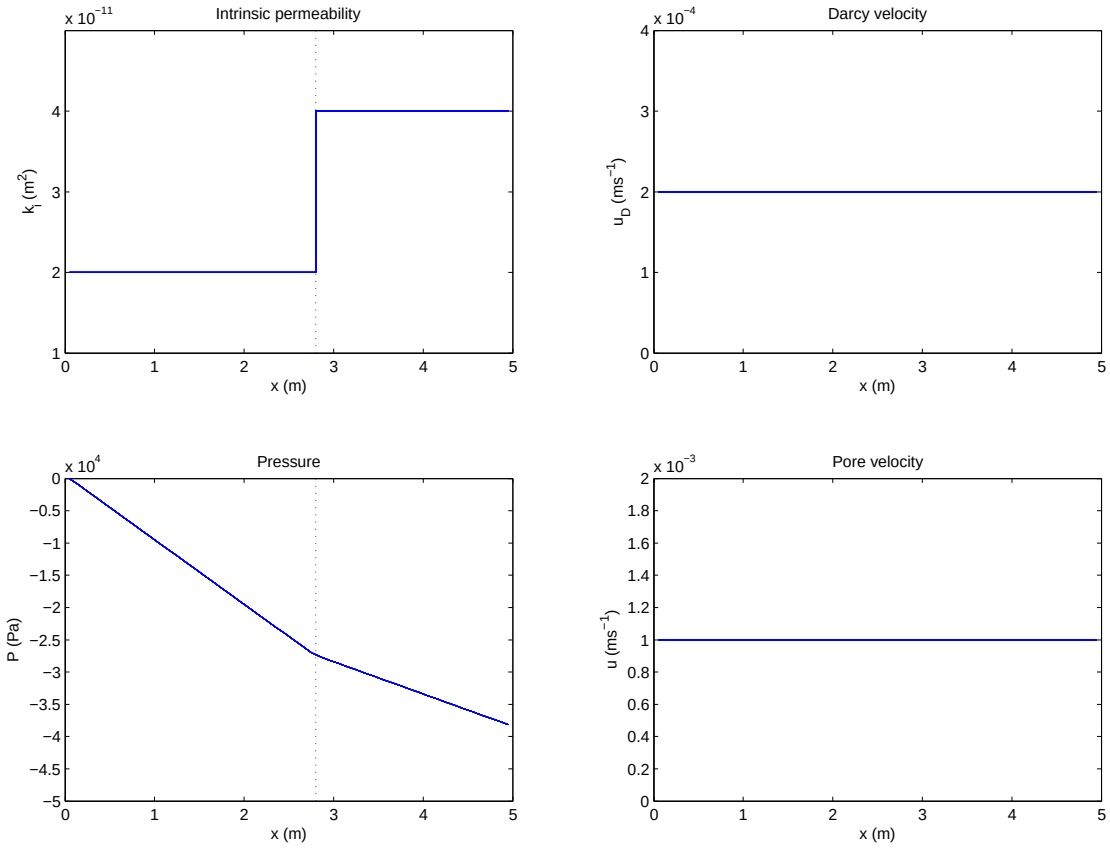

Figure 7.12: Effect of varying k_i in an inhomogeneous domain

Figure 7.13 shows the effective pressure, Darcy velocity and pore velocity along the x-axis for a domain with a step-change in porosity, where the permeability is held constant. The pressure gradient, which is the value expected from Darcy's Law, remains constant throughout the domain, as there is no change in Darcy velocity or permeability. At the upwards step-change in porosity there is a corresponding downwards step-change in pore velocity, which ensures that

mass-flux is conserved across the cell-face where the step-change occurs.

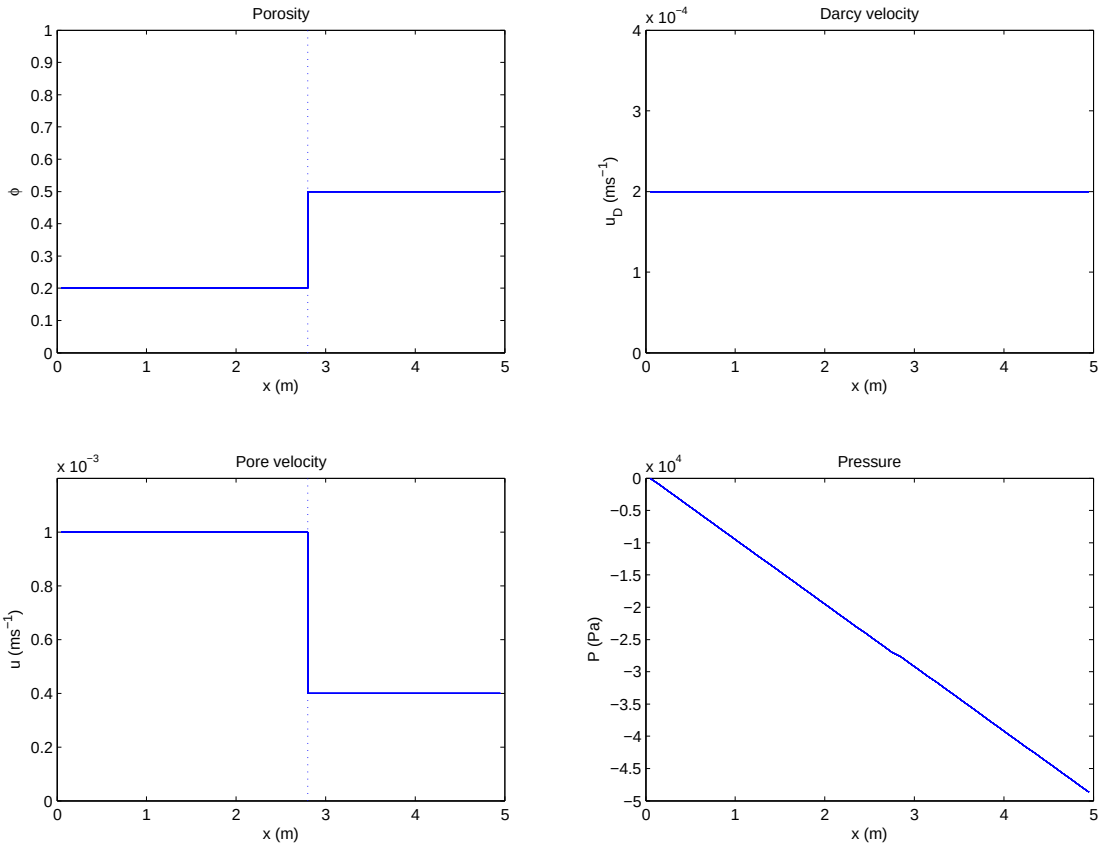

Figure 7.13: Effect of varying ϕ in an inhomogeneous domain

Figure 7.14 shows the effective pressure profile in the x-direction, and vertical and horizontal velocity fields for a Darcian flow scenario with a 2D spatial variation in permeability (as shown in the top sub-plot of Figure 7.14). The porosity, ϕ, was constant throughout the domain. The lower permeability zone in the bottom right quadrant of the domain acts as an obstacle, driving a greater proportion of flow into the upper layer. Vertical upwards flow was generated immediately upstream of the change in permeability. In the upper layer, where the horizontal velocity increased but there was no change in permeability, there was a corresponding increase in the pressure gradient. As expected, in the region where vertical flow was generated there was a slight vertical pressure gradient, as

shown by the difference in the pressure profiles at the top and bottom boundaries in this region. This can be seen more clearly in the zoomed-in pressure profile that shows the area either side of the step-change. Further downstream there was no vertical flow, and the pressure gradients for the two layers match. The overall mass balance error (i.e. comparing inflows to outflows) for the simulation was 0.04%.

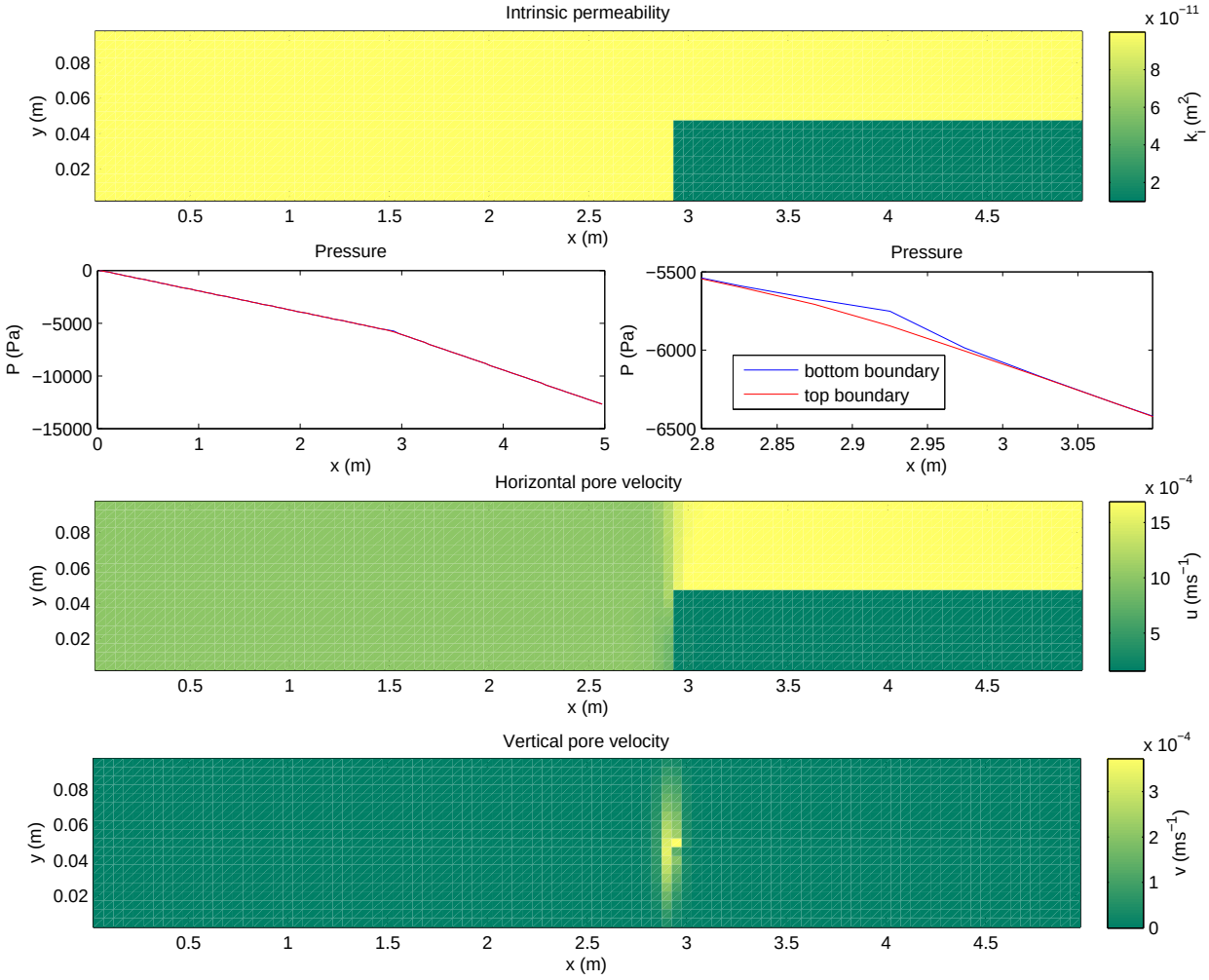

Figure 7.14: Effect of 2D variation of k_i (discontinuities in the $x-$ and y-directions) on pressure gradient and pore velocities.

7.3.3 Non-Darcian flow

As seen in Figure 7.10, if Re_p (based on the hydraulic properties) is greater than 0.1 the hydraulic gradient calculated from the FV-DANS model results does not match the value calculated from Darcy's Law.

Figure 7.15 shows the ratio of the modelled hydraulic gradient to the value calculated from Darcy's Law, for a range of Re_p values, from $Re_p = 1.65 \times 10^{-6}$ to $Re_p = 2.63$. The data points plotted in Figure 7.15 are from the same model runs used to generate Figures 7.10 and 7.11, plus additional runs at higher values of Re_p. For $Re_p < 0.1$ the FV-DANS model gives a hydraulic gradient the same as that expected from Darcy's Law, and the points plot on the dotted reference line at a ratio of 1.0. At higher values of Re_p the flow clearly becomes non-Darcian as the contribution from the form-drag term becomes non-negligible, and the ratio of the modelled hydraulic gradient to the expected Darcy's Law value is greater than 1.0.

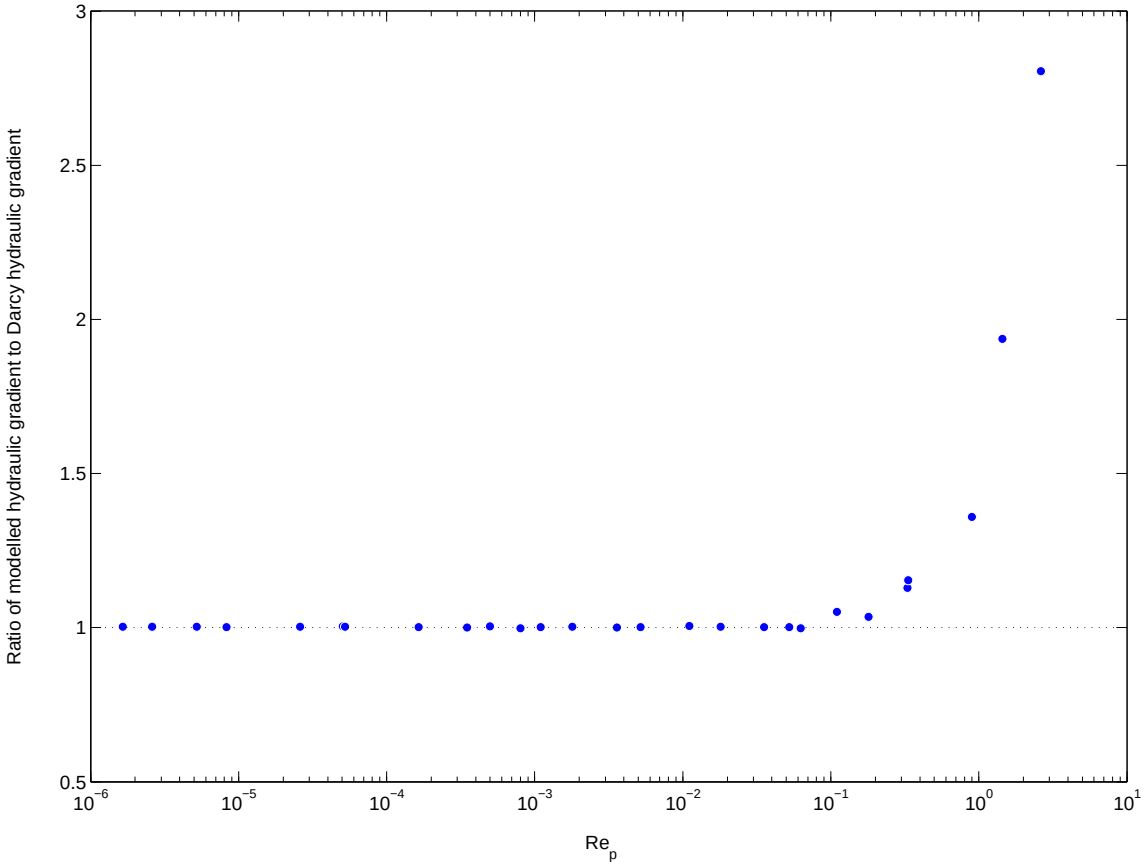

Figure 7.15: Ratio of modelled hydraulic gradient to Darcy's law hydraulic gradient

7.4 Verification Against Laboratory Data

The FV-DANS model was set up to replicate both the "gaining stream" and "losing stream" configurations that were modelled in the laboratory.

For both of the laboratory scenarios the FV-DANS model was configured with two layers, using the dimensions of the laboratory flume and the measured hydraulic properties of the transparent soil material (as discussed in Chapter 5). As the hydraulic properties of the slotted streambed layer (that was used to retain the transparent soil in place) were not known, they were assumed to be similar to the underlying porous layer, and the streambed layer was therefore not explicitly included in the numerical model.

As described in Chapter 6, the measured velocities for the "losing 1" laboratory results (i.e. the data set closest to the outlet for the losing configuration) showed highly suppressed horizontal velocities near the free-surface, which are thought to be due to a large-scale eddy or recirculation downstream of the field of measurement, and beyond the downstream extent of the porous layer. Attempts to replicate this exact scenario with the FV-DANS model, using the measured data as a boundary condition in the surface layer, were unsuccessful as the exact cause of the suppressed velocity profiles is unclear. Therefore a scenario replicating the general features of the "losing stream" configuration run in the FV-DANS model, without the suppressed free-surface velocities in the surface layer, and with a lower outflow in the subsurface layer.

The horizontal impermeable plate that was added at the surface-subsurface interface in the laboratory to prevent the flow "short-circuiting" at the downstream end of the losing configuration was represented in the numerical model as a thin layer with very low conductivity and porosity. This layer was effectively a no-flow boundary. The impermeable layer was not included in the numerical model for the gaining configuration, as the velocities in both the surface and subsurface layers that were used as an upstream boundary condition for this configuration were measured downstream of the impermeable plate. Initially this approach was attempted for the losing configuration, but was unsuccessful due to model instability. Incorporating the impermeable plate layer into the model domain allowed the vertical flow across the interface to occur away from the outflow boundary,

which improved stability.

For both the gaining and losing scenarios the model was set up with $dx = 0.1\ m$ and $dy = 0.005\ m$. The mesh was refined in the x-direction at the inlet for the gaining scenario, and at the outlet for the losing scenario. For both scenarios the mesh was refined in the y-direction at the interface. The model was run with a time-step of $0.5\ s$.

Table 7.6 summarises the parameters used in the FV-DANS model for both the gaining and losing stream runs. These are default or baseline values. The sensitivity of model results to certain parameters is discussed in Section 7.5.

The values of a and b in the turbulence damping function were set based on the threshold values of the porous Reynolds number, Re_p, given by Bear (1972) for the transition to turbulence in a porous medium (where Re_p is based on the average particle diameter in the porous medium). As the Re_p used in the numerical model was based on hydraulic properties rather than particle diameter, the relationship established in Chapter 6 between the two definitions of Re_p was used to convert Bear's threshold values.

In this section, unless specified otherwise, the reported velocities are pore velocities, rather than Darcy fluxes. This is consistent with how the laboratory results have been presented in Chapter 6.

Table 7.6: Default model parameters for gaining and losing stream scenarios

Parameter	Description and units	Value
Hydraulic properties (porous layer)		
k_i	Intrinsic permeability (m^2)	4.28×10^{-9}
ϕ	Porosity	0.233
Fluid properties		
ρ	density (kg/m^3)	1000
μ	dynamic viscosity (kgm^1s^1)	0.001
"Standard" turbulence model parameters		
c_μ	constant in μ_t equation	0.07
σ_k	constant in TKE equation	0.8
c_k	constant in porous TKE production term	0.28
κ	von Kármán constant	0.41
C_d	constant in ϵ equation	0.15
Turbulence damping parameters		
A_0	constant from van Driest (1956)	26
a	mid-point for porous damping function	0.65
b	steepness of porous damping function	0.4
C_{y1}	constant from Wallin and Johansson (2000)	2.4
C_{y2}	constant from Wallin and Johansson (2000)	0.003
C_v	vertical flow adjustment	0.22

7.4.1 Non-dimensionalisation

The numerical model velocity and turbulence results were non-dimensionalised in the same way as the laboratory results.

The x and y co-ordinates were non-dimensionalised by the surface flow depth, d_s, from the relevant laboratory scenario, which was also used to set the depth of the surface flow at the inflow boundary. In the vertical direction the top of the porous layer was set to $y/d_s = 0$, so that the porous layer has negative values of y/d_s.

The velocities were non-dimensionalised by the flux velocity, U_f. The value of U_f was taken from the laboratory results for the relevant scenario.

Turbulent statistics were non-dimensionalised by U_f^2. As discussed in Section 6.1.1, this allows for comparison of the laboratory and numerical results presented in this thesis, but does not allow for direct comparison with other studies where a different non-dimensionalisation has been used.

7.4.2 Gaining stream configuration

For the gaining stream configuration the FV-DANS model was set up so that the inflow boundary of the model corresponded to the upstream end of the measurement window for Position 1 in the laboratory flume (see Figure 6.1). The mesh was configured to match the measured surface flow depth from the "gaining 1" laboratory results.

7.4.2.1 Boundary conditions

To reproduce the gaining stream configuration in the FV-DANS model, it was necessary to specify inlet boundary conditions for both pressure and velocity. Normally in groundwater models either a flux or a head is specified on a boundary; "mixed" boundary conditions are less common as conditions requiring them rarely occur in nature (Yeh et al., 2005). The configuration that was used in the laboratory is rather unusual in terms of "real-world" flows: the closest equivalent would be an open-ended pressurised pipe buried beneath a river, discharging into the river gravels.

The measured upstream velocities from the Position 1 laboratory data were used as the inflow boundary condition in the FV-DANS model. Because the laboratory measurements did not cover the full domain, interpolation and extrapolation was required to generate full velocity profiles. Figure 7.16 shows the full horizontal and vertical velocity profiles that were specified as boundary conditions. These profiles were interpolated onto the model mesh.

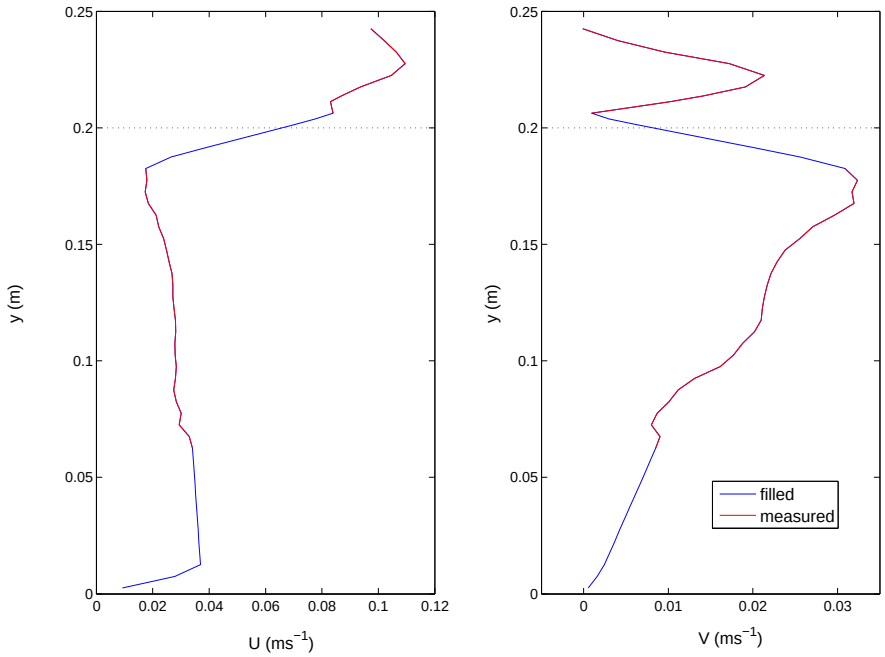

Figure 7.16: Horizontal and vertical velocity boundary conditions for gaining stream configuration. Dotted line shows position of surface - subsurface interface.

In the laboratory the vertical pressure gradient that drove the upward flow across the surface-subsurface interface was created by a head difference across the flume's upstream sluice-gate (see Figure 5.4). This head difference was measured, but there was no measurement of head-losses between the head-tank and the porous layer, or of the pressure distribution at the upstream end of the measurement window. Some trial-and-error was therefore required to specify a physically-reasonable pressure distribution on the boundary. The upper limit for the maximum value of this distribution was constrained by the measured head difference across the laboratory flume's upstream sluice gate. Assuming the pres-

sure distribution in the surface layer upstream of the measurement window (i.e. where the bed was impermeable) was close to hydrostatic, the effective pressure was set to zero at the interface. Figure 7.17 shows the effective pressure (i.e. the deviation from hydrostatic pressure) boundary condition that was specified in the subsurface layer.

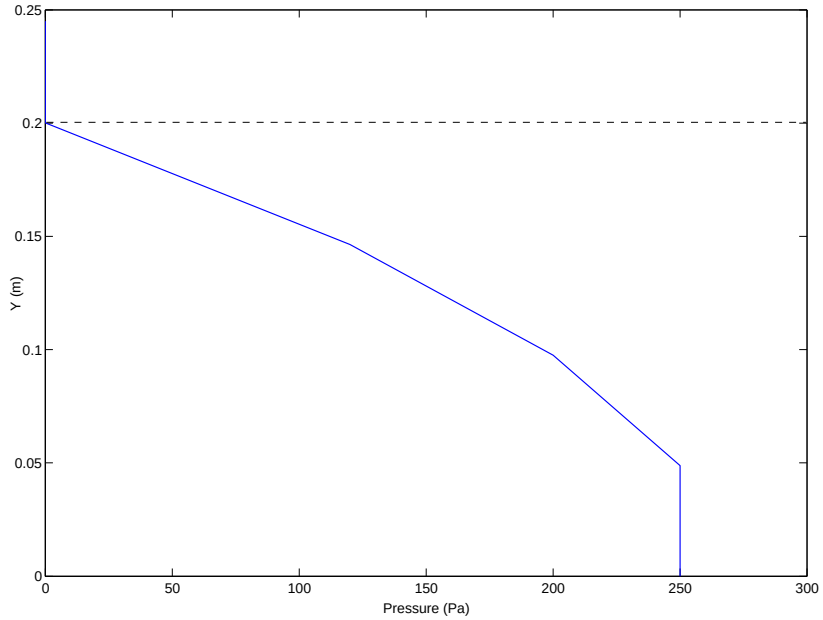

Figure 7.17: Effective pressure boundary condition for gaining stream configuration. Dotted line shows position of surface - subsurface interface.

For a given value of permeability, a certain driving pressure was required to give the expected velocity field. Incorrect specification of the pressure resulted in mass-balance error at the inlet boundary, as the model attempted to resolve the conflict between the specified pressure distribution (which sets up the vertical pressure gradient), the specified inflow velocities, and the calculated pressure gradients further downstream. The overall effect of the mass-balance error was that the model failed to converge to the expected velocities. It was found that with the measured value of permeability ($4.28 \times 10^{-9}\ m^2$) the boundary pressure required to reproduce velocity fields similar to the laboratory data was approximately twice the maximum possible value, based on the measured head difference at the upstream end of the laboratory flume. This indicated that the measured value of

permeability was not correct. Increasing the permeability to 7×10^{-9} m^2 allowed the model to reproduce the key features of the measured flows with reasonable accuracy, with the pressure boundary condition as shown in Figure 7.17.

The change in permeability indicates either that there were errors in the permeability testing, or that the porous medium behaved differently in the flume to how it behaved in the test-cell. The SAP spheres that were used as the transparent soil in the laboratory (see Chapter 5) were not a rigid material. It is therefore possible that the porous matrix was able to compress slightly in the x-direction in the flume, creating a zone of higher permeability at the upstream end of the subsurface layer. Alternatively, the material may have compressed slightly in the permeability test cell.

7.4.2.2 Hydraulic properties

Figure 7.18 shows vertical profiles of the permeability and porosity that were specified in the FV-DANS model for the gaining configuration. There was no variation of hydraulic properties in the x-direction in the model.

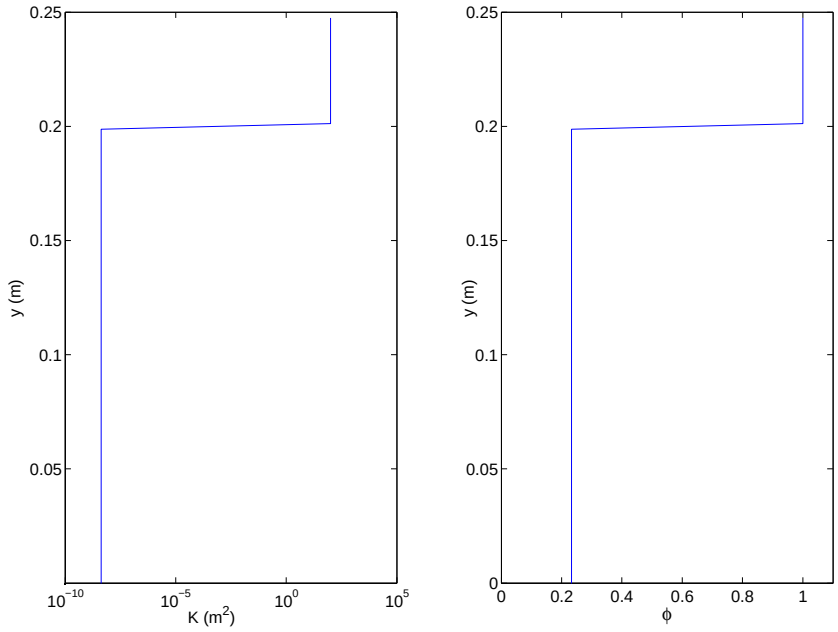

Figure 7.18: Vertical profiles of hydraulic properties (permeability and porosity) for gaining configuration.

7.4.2.3 Mean flow results

Figure 7.19 shows modelled dimensionless velocity vectors (scaled by the flux velocity for the "gaining1" laboratory run, $U_f = 0.151\ ms^{-1}$) for the full model domain. As seen in the laboratory data (Figure 6.9), motion in the subsurface layer was concentrated towards the upstream end of the domain. Downstream of approximately $x/d_s = 10$ the subsurface velocities were negligible; the decay of subsurface motion with distance downstream was slightly more rapid than in the laboratory data.

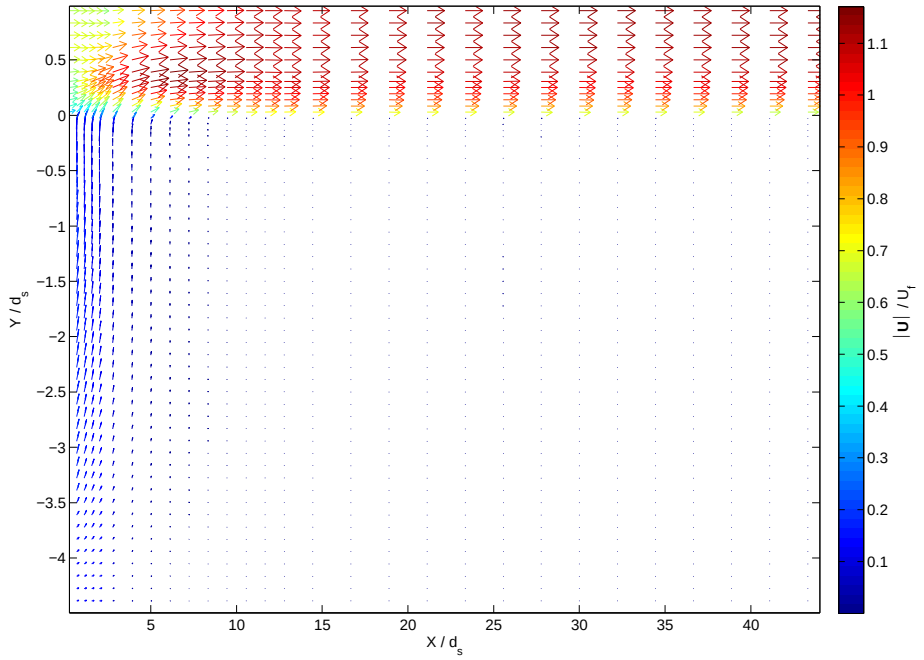

Figure 7.19: Vector plot for gaining configuration; full model domain

Dimensionless velocity vectors and streamlines for the portion of the computational domain that corresponds to the Position 1 laboratory results are shown in Figure 7.20. This is the upstream region of the domain where the strongest interactions between the porous-media and clear fluid regions occurred. Compared to the laboratory results (Figure 6.9a), the general structure of the modelled flow was very similar. Near the inlet, the flows immediately below the interface were predominantly vertical, which generated sufficient vertical flow in the surface layer to substantially modify the shape of the streamlines. The streamlines

reverted to horizontal further downstream. Deeper in the subsurface layer, the flow near the inlet had a stronger horizontal component.

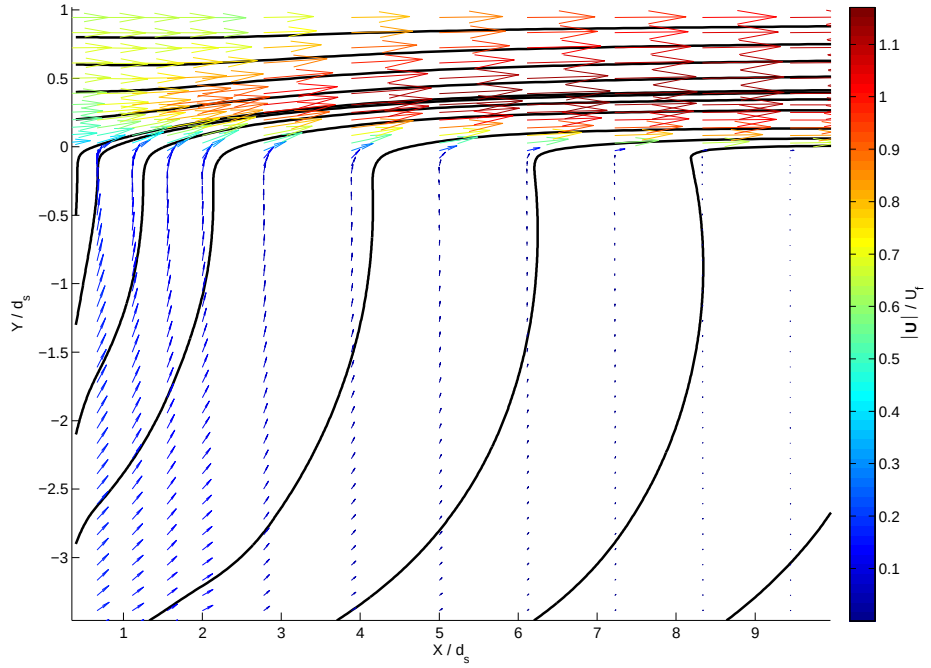

Figure 7.20: Vector and stream plot for gaining configuration; area covered by Position 1 laboratory data

The modelled effective pressure for the full computational domain is shown in Figure 7.21. There were no laboratory results with which to compare the modelled pressures, but the model results make physical sense. As expected, the pressure gradient was concentrated at the upstream end of the domain, where the velocities in the porous layer were highest, and interaction between the two layers was greatest. Further downstream, where the velocities in the porous layer and flow across the interface were negligible, the pressure gradient was also negligible. The lack of any substantial pressure gradient in the surface layer (i.e. above $Y/d_s = 0$) is consistent with the free-surface elevation measurements from the laboratory, which showed no measurable slope on the free-surface.

A colour plot of modelled U-velocities (i.e. the horizontal velocity component) for the full computational domain is shown in Figure 7.22. The modelled U-velocities for the upstream area of the domain, which is covered by the Position

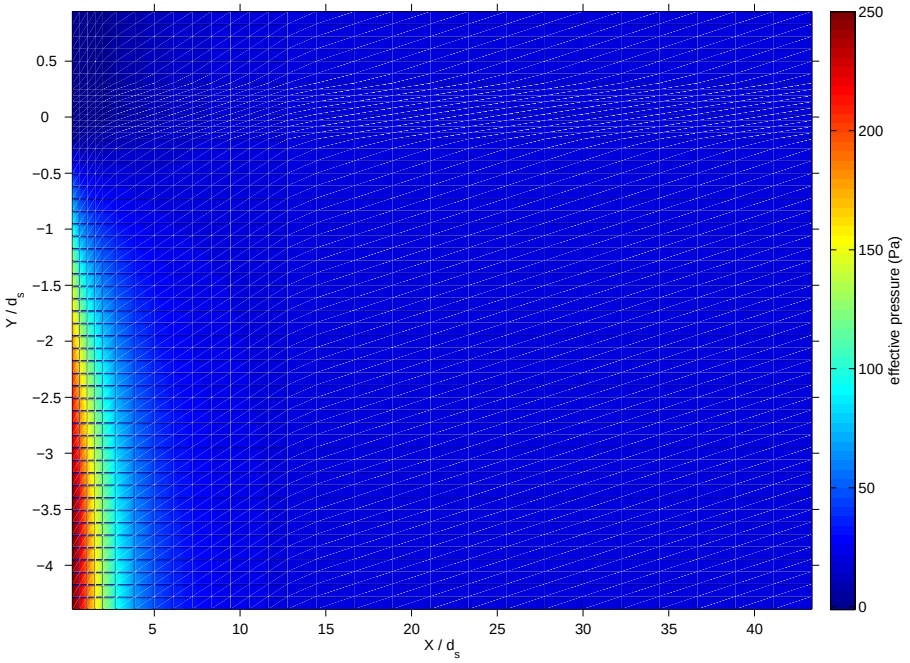

Figure 7.21: Effective pressure colour plot; full model domain

1 laboratory results, are shown in Figure 7.23. Figure 7.24 shows modelled U-velocities for the subsurface layer in this region, with the colour scale adjusted to highlight the subsurface velocities. Vertical profiles of modelled U-velocity for the area covered by the Position 1 laboratory data are shown in Figure 7.25. Figure 7.26 shows vertical profiles of U-velocity for the remainder of the domain, downstream of Position 1.

In both the surface and subsurface layers, the trends in the modelled U-velocities were consistent with the laboratory data. The surface velocity profile at the inlet (as shown in Figure 7.16) was slightly suppressed at the free-surface. With distance downstream the surface U-velocities increased, both at the free-surface and nearer the interface, as mass was introduced from the subsurface layer, until a velocity profile of the shape expected for a turbulent free-surface flow was eventually reached. The peak modelled U-velocity of $U/U_f = 1.15$ at the downstream end of the domain was consistent with the laboratory results.

The model results show horizontal velocities from the surface flow penetrating slightly below the interface at the upstream end of the domain, as seen in

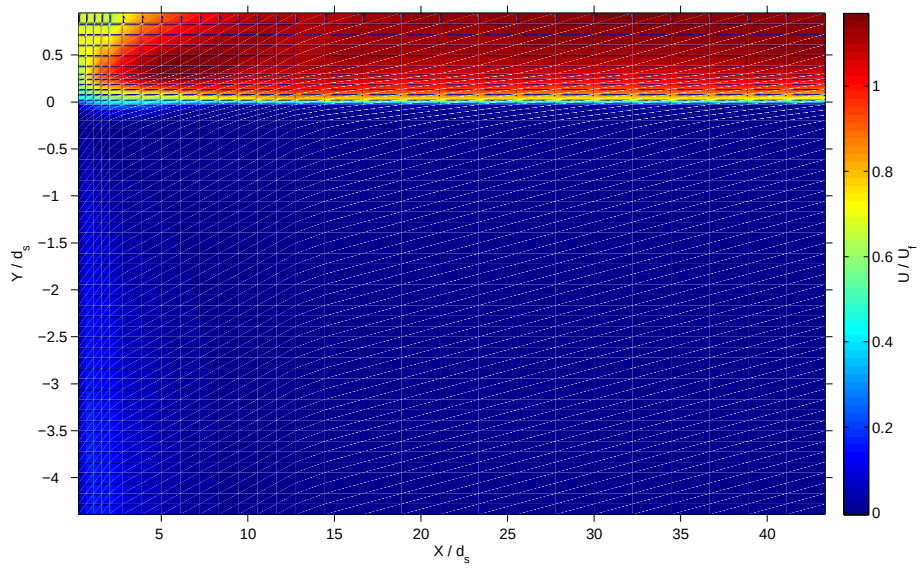

Figure 7.22: U velocity colour plot for gaining configuration; full model domain

Figures 7.24 and 7.25. Further downstream, beyond $x/d_s \approx 4.5$, although the interface was not acting as a no-slip boundary (i.e. $U/U_f > 0$ at $y/d_s = 0$), penetration of the velocity profile below the interface was not substantial. The model's behaviour at the interface could not be compared with laboratory results, as there was a gap in the laboratory data on either side of the interface.

In the subsurface layer, the general trends in the velocity profiles and the downstream extent of motion were consistent with what was measured in the laboratory.

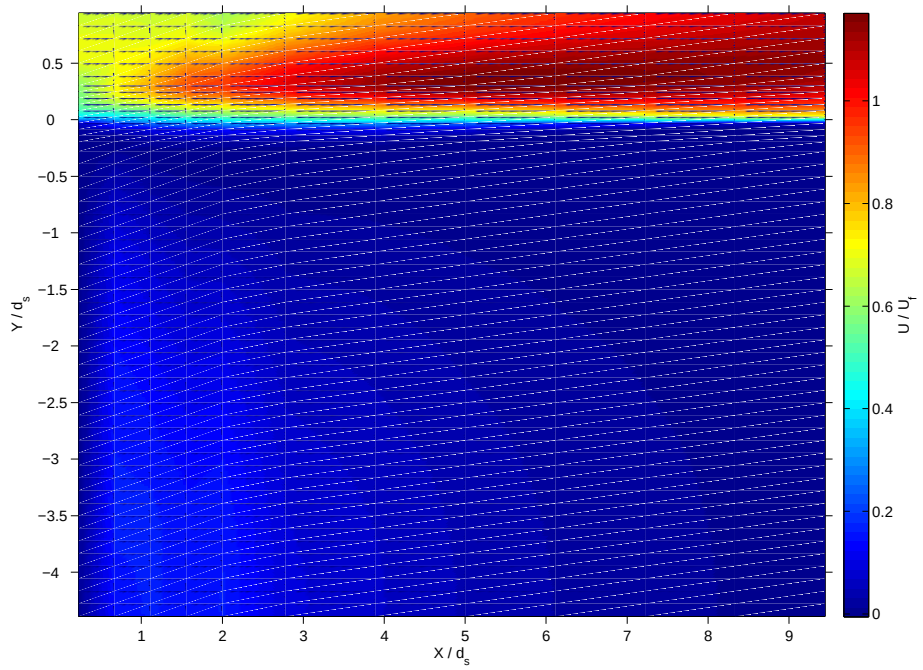

Figure 7.23: U velocity colour plot for gaining configuration; area covered by Position 1 laboratory data

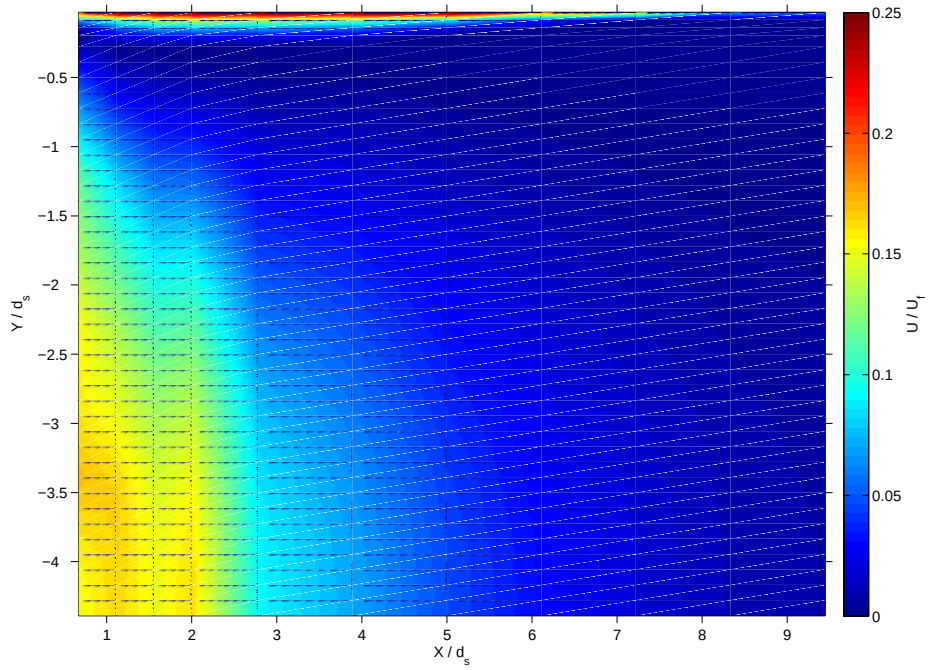

Figure 7.24: U velocity colour plot for gaining configuration; subsurface area covered by Position 1 laboratory data

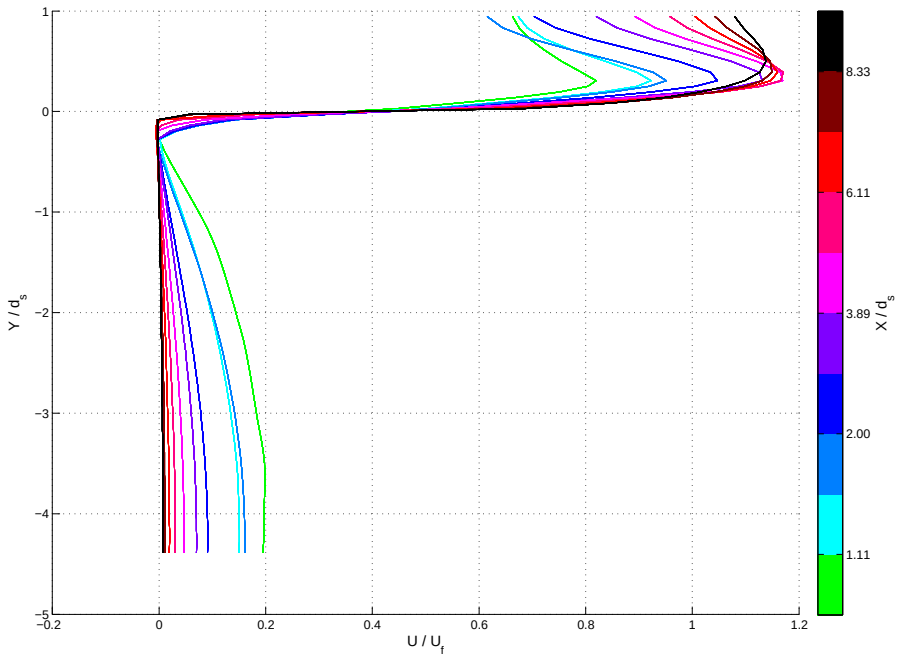

Figure 7.25: U velocity profiles for gaining configuration; area covered by Position 1 laboratory data

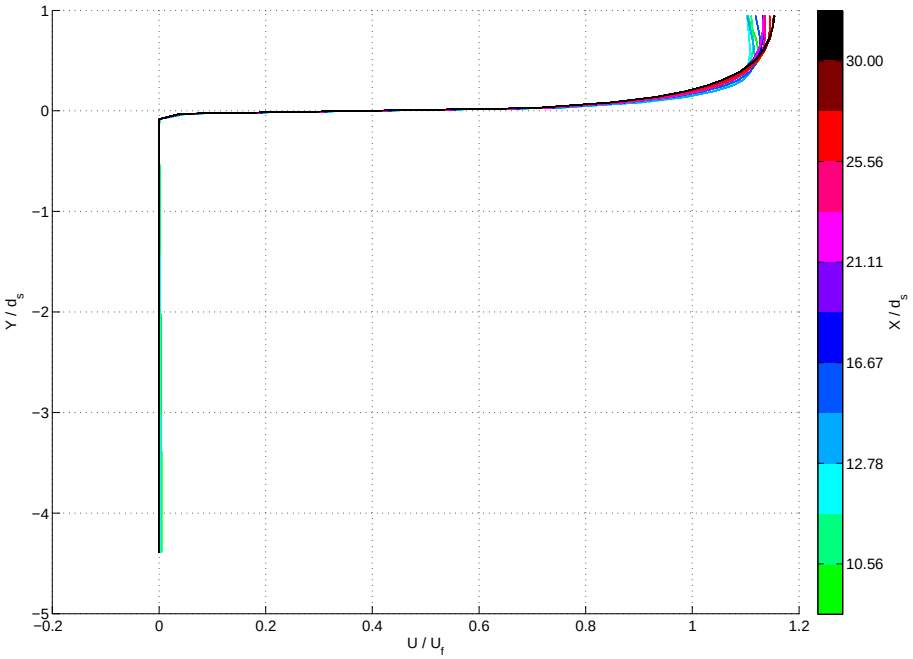

Figure 7.26: U velocity profiles for gaining configuration; downstream portion of domain

A colour plot of modelled dimensionless V-velocities (i.e. the vertical velocity component) for the full model domain is shown in Figure 7.27. V-velocities for the area covered by the Position 1 laboratory data are shown in Figure 7.28. Vertical and longitudinal profiles of V-velocity are shown in Figure 7.29.

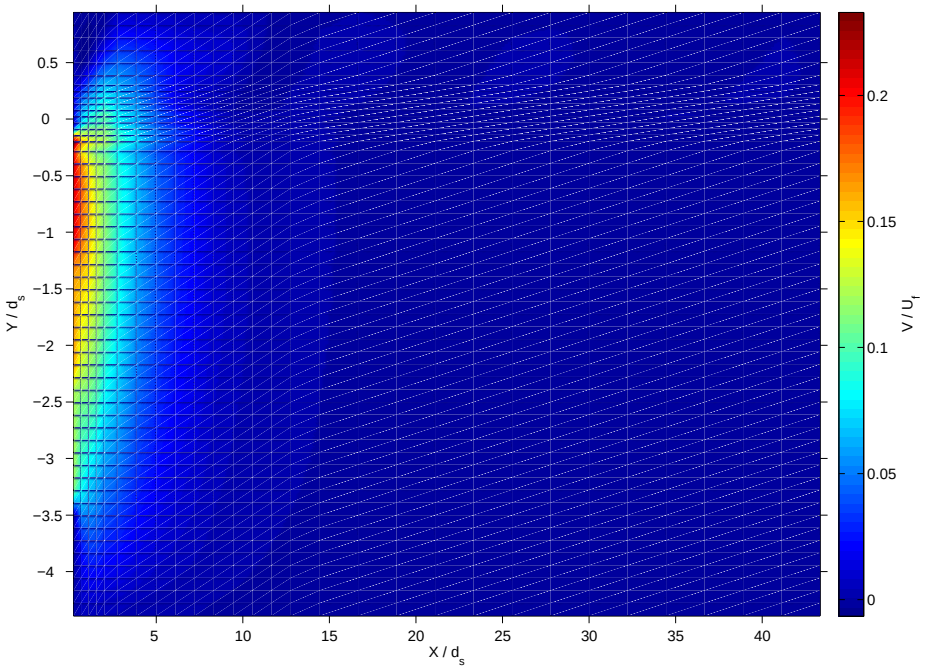

Figure 7.27: V velocity colour plot for gaining configuration; full model domain

As with the U-velocities, the modelled V-velocities exhibit the same general trends as the laboratory results. The peak modelled vertical velocity of $U/U_f = 0.22$, and the location at which the peak occurred, were consistent with the laboratory results. The highest V-velocities were modelled at the upstream end of the domain immediately below the interface, with a zone of high vertical velocity extending down to approximately $y/d_s = -2.5$, which was consistent with the laboratory measurements. In the downstream portion of the domain, beyond $U/U_f \approx 10$, the V-velocities in both layers became negligible.

There was a rapid reduction in V-velocity above the interface. This is consistent with the step-change in porosity. Although the laboratory data showed a decrease in V-velocity across the interface (either side of the gap in the measured data), there was a zone of increased V-velocity, with a peak at approximately

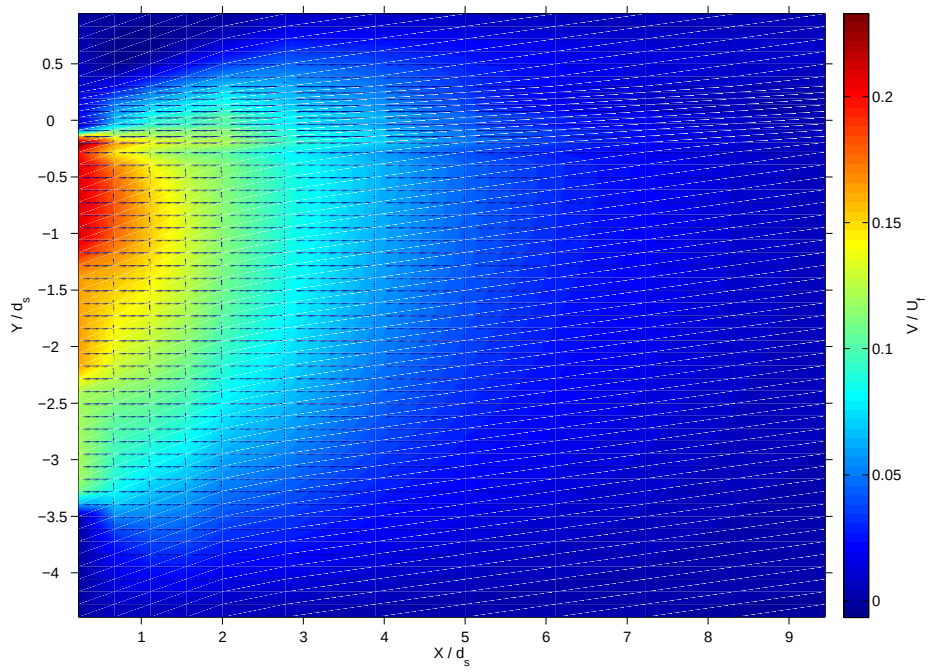

Figure 7.28: V velocity colour plot for gaining configuration; area covered by Position 1 laboratory data

$y/d_s = 0.5$ at the upstream end of the measurement window. The cause of this was unclear; the modelled results make more physical sense.

The steps in the vertical profile of V-velocity at the upstream end on the domain (Figure 7.29a) are due to the boundary pressure being defined as a piecewise linear distribution (Figure 7.17). Each step in the V-velocity profile corresponds to a change in the slope of the pressure distribution.

The cause of the oscillations near the interface (i.e. around $Y/d_s = 0$) in Figures 7.29a and 7.29b is unclear; it is likely that they are due to the large step-change (10 orders of magnitude) in hydraulic properties that occurs across a single cell boundary at the interface. In a natural system a more gradual transition would be expected, and the hydraulic properties could be transitioned over a number of model cells.

Colour plots of the porous Reynolds number, Re_p, are shown in Figure 7.30. Figure 7.30a shows the subsurface layer for the portion of the domain covered by the Position 1 laboratory data. Compared to the laboratory results (Figure 6.13d), the modelled values of Re_p are slightly higher. This is expected,

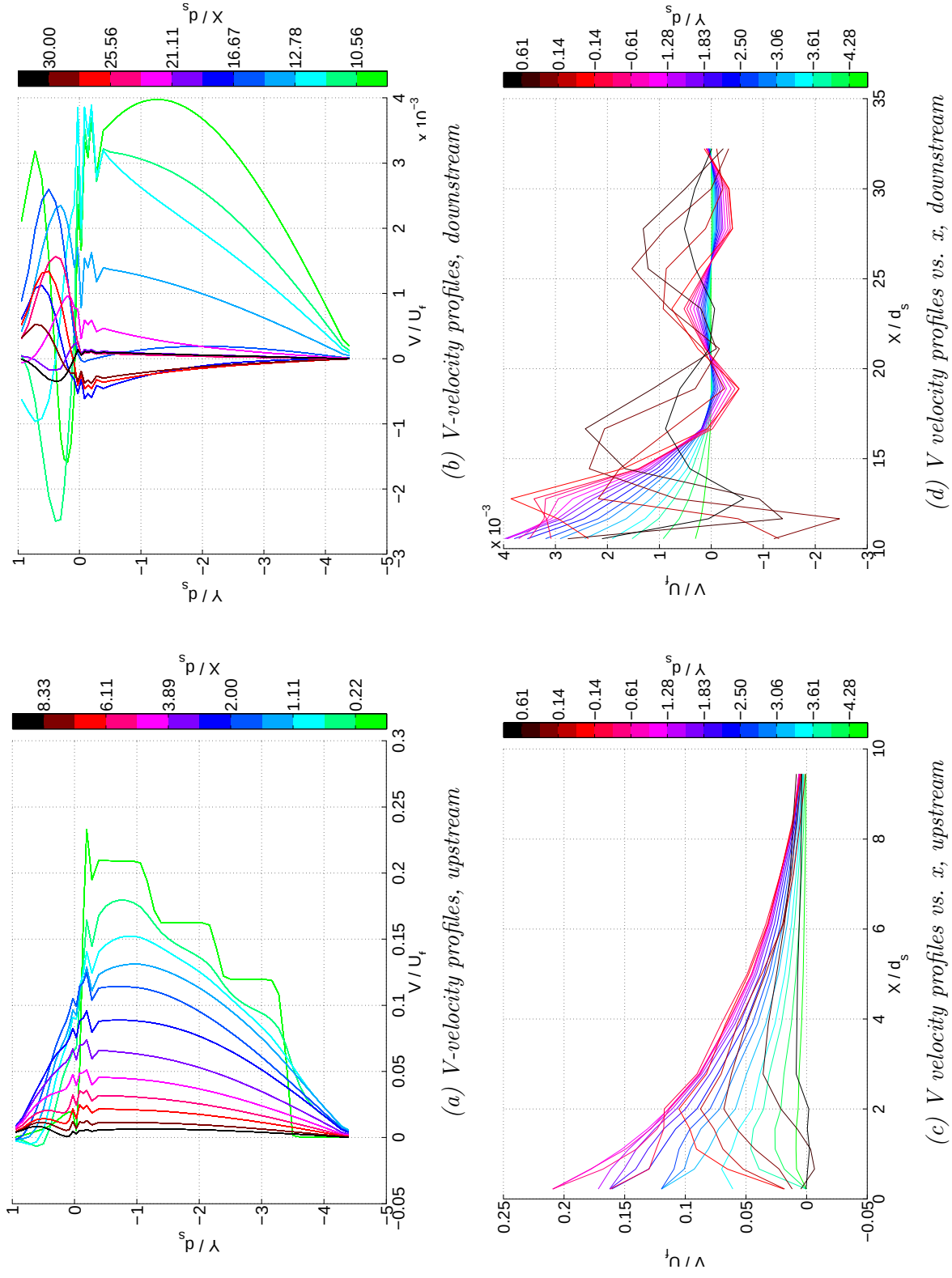

(a) V-velocity profiles, upstream *(b) V-velocity profiles, downstream*

(c) V velocity profiles vs. x, upstream *(d) V velocity profiles vs. x, downstream*

Figure 7.29: V velocities for gaining configuration

however, as the modelled velocities were also slightly lower. Near the inlet, where the U-velocities were highest, Re_p was approximately 1.2. The laboratory results near the inlet had $Re_p \approx 1.0$, although these values were calculated using the measured value of k_i, rather than the permeability that was used in the model. As the length-scale in Re_p is calculated using $\sqrt{k_i}$, increasing k_i give an increased value of Re_p for the same velocity.

As the mid-point value for the turbulence damping function was set to 0.65 in the FV-DANS model[1], this indicates that the flow near the inlet was non-Darcian, and transitioning towards turbulence. This is not a guarantee that the model will predict significant values of TKE in this region, however.

Immediately below the interface there was a zone of higher Re_p, which is shown in more detail in Figure 7.30b. The values of Re_p in this region reached a maximum value of 2.1, which indicates that modelled flow was turbulent in a small area of the porous layer below the interface. The modelled turbulent statistics presented below support this. As there was a gap in the laboratory data around the interface, the near-bed values of Re_p cannot be compared with laboratory results.

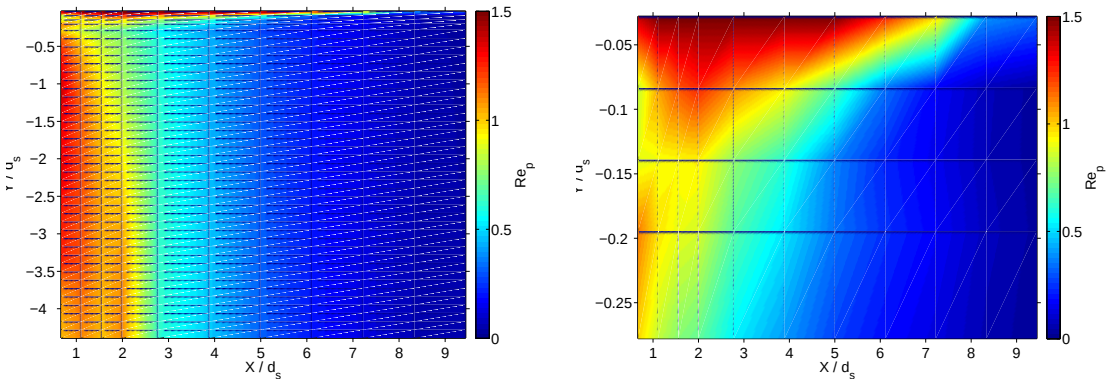

(a) "Gaining1" region; subsurface

(b) "Gaining1" region; subsurface near interface

Figure 7.30: Porous Reynolds numbers, Re_p, for gaining configuration.

[1]Based on the threshold values of Re_p given by Bear (1972), and the relationship that was established in Chapter 6 between Re_p based on grain diameter and Re_p based on hydraulic properties

7.4.2.4 Turbulent statistics

A colour plot of modelled dimensionless turbulent kinetic energy (TKE) for the entire computational domain is shown in Figure 7.31. Vertical profiles of modelled TKE are shown in Figure 7.32. Figure 7.32a shows the upstream region, covered by the Position 1 laboratory data, and Figure 7.32b shows the remainder of the domain. In the profiles the majority of the subsurface layer, where TKE was effectively zero, has been truncated.

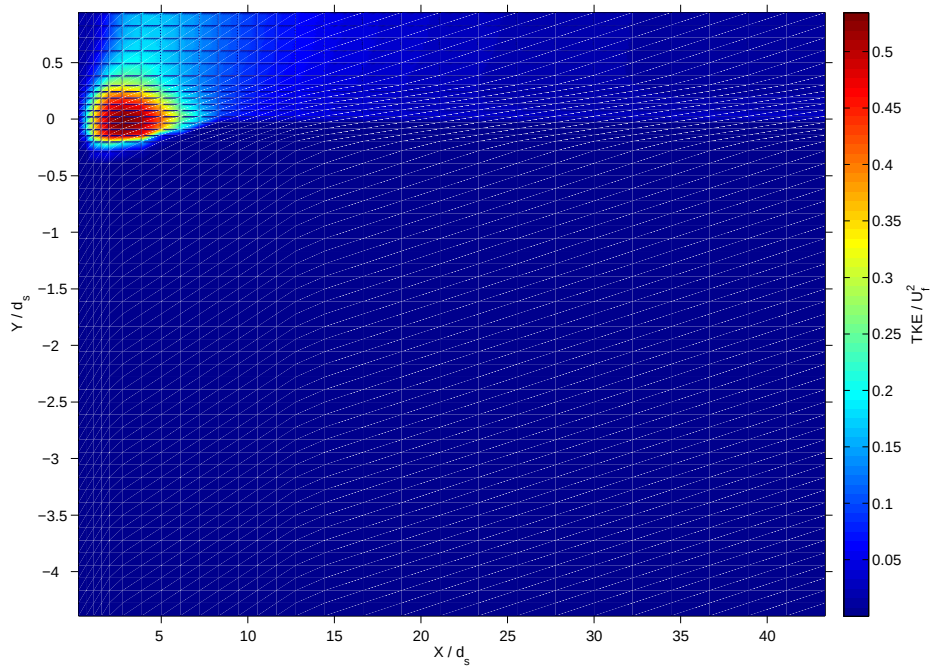

Figure 7.31: TKE colour plot for gaining configuration; full model domain

Although the laboratory results showed elevated TKE in the region where vertical flows across the interface are strongest (Figures 6.15 and 6.16), the values predicted by the numerical model were substantially higher. At the lower extent of the laboratory data for Position 1 ($y/d_s = 0.15$, see Figure 6.16a) the modelled TKE values were approximately 25 times greater than the laboratory values. The laboratory data for Position 2 (Figure 6.16b), which extended down further towards the interface, showed a more pronounced peak in the TKE profiles near the interface than the Position 1 laboratory profiles. It is possible that if the Position 1 data had extended closer to the interface, the Position 1 TKE profiles

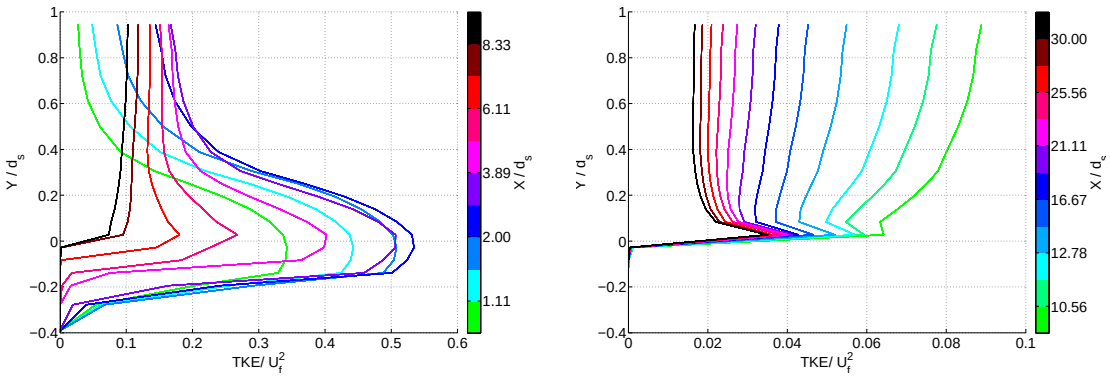

(a) "Gaining1" region *(b) downstream*

Figure 7.32: TKE profiles for gaining configuration; subsurface layer truncated

would have also had a higher peak, closer to what the model predicted. Further downstream (Figure 7.32b) the modelled TKE was a reasonably close match to the laboratory data (Figure 6.16b).

Figure 7.33 illustrates the TKE budget for the gaining configuration in the region where the model predicts high values of TKE (NB: these plots show dimensional values). The higher TKE was clearly caused by the region of high production around the interface, where the vertical velocity was high. The TKE was being advected upwards and downstream, consistent with the flow direction. Although there was also a region of high dissipation, this was predominantly below the high production region.

Figure 7.34 shows the TKE budget in the near-bed region in greater detail, with production and dissipation plotted using the same colour scale. Above a dimensionless depth of approximately $y/d_s = 0.15$ dissipation was greater than production. The cause of the zone of high TKE production around the interface is related to elevated values of the turbulent mixing length where the vertical velocity was high. Higher values of the mixing length, which were required for the model to run stably (and which were supported by the estimates of mixing length from the laboratory data, as shown in Appendix E), resulted in higher values of turbulent viscosity, μ_t, which in turn resulted in higher production. Plots of modelled mixing length and μ_t are shown in Appendix F.

Figure 7.35 shows dimensionless Reynolds stress for the entire domain. Fig-

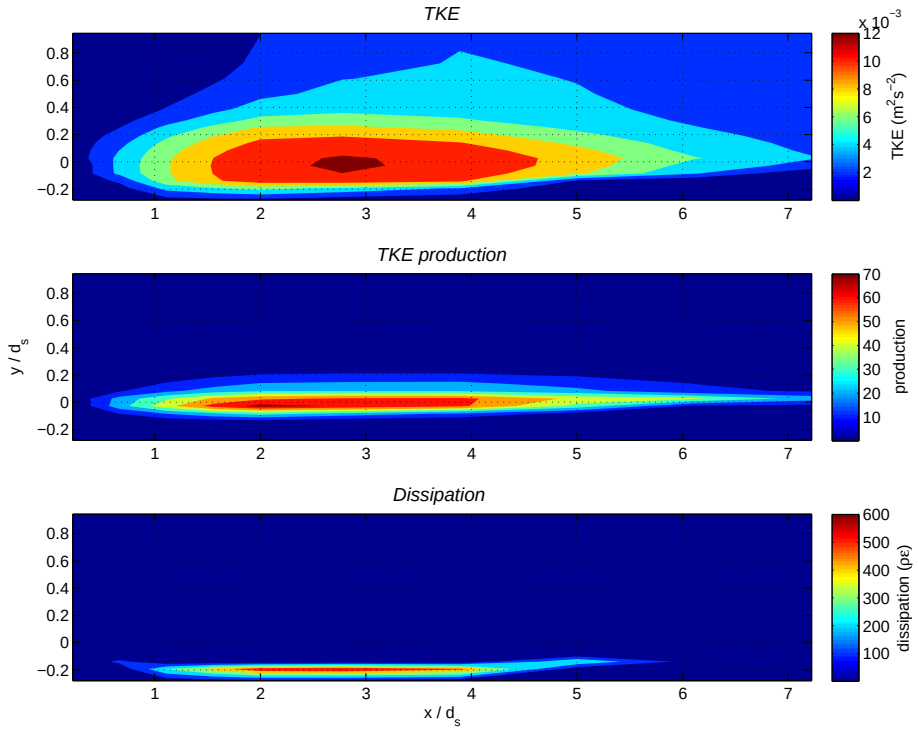

Figure 7.33: TKE budget for gaining configuration: TKE, production and dissipation

ure 7.36 shows vertical profiles of Reynolds stress, with the subsurface layer truncated.

The modelled Reynolds stresses were highest in the region with strong vertical flow. This is consistent with the laboratory results (Figures 6.17a and 6.18a). However, like the modelled TKE, the peak values of modelled Reynolds stress near the interface in the upstream part of the domain were substantially higher than the values calculated from the laboratory data: approximately 25 times larger at the lower extent of the laboratory data for Position 1. As with the TKE data, the laboratory values of Reynolds stress end at $y/d_s = 0.15$, and it is possible that a peak occurred below this.

In the surface layer, where the vertical gradient of the U-velocity profile was reversed (i.e. where the free-surface velocities were less than the mid-depth velocities), the modelled Reynolds stresses were negative. This is consistent with the laboratory data. Although the peak negative value occurred at a similar location to the peak negative value in the laboratory profile (Figure 6.18a), the magni-

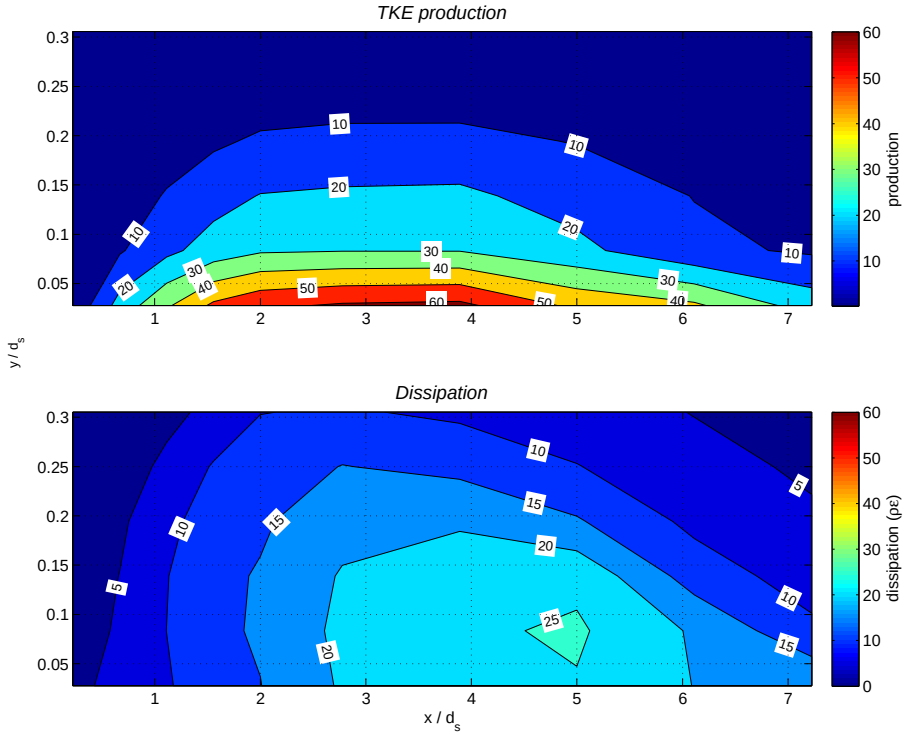

Figure 7.34: TKE budget for gaining configuration: TKE production and dissipation in near-bed region

tude was approximately 16 times greater. Further downstream, as the surface velocity profiles evolved, the Reynolds stresses eventually became positive over the full depth of the surface-flow layer. The shapes of the downstream Reynolds stress profiles were similar to the laboratory data: tending towards zero near the free-surface, and a peak value slightly above the interface. The modelled peak values downstream were generally slightly higher than the laboratory values, but overall a much closer match to the laboratory data.

In the laboratory data the presence of the slotted "stream-bed" layer in the flume caused some anomalies in the turbulent statistics near the bed. As this layer was not included in the numerical model, this behaviour was not replicated.

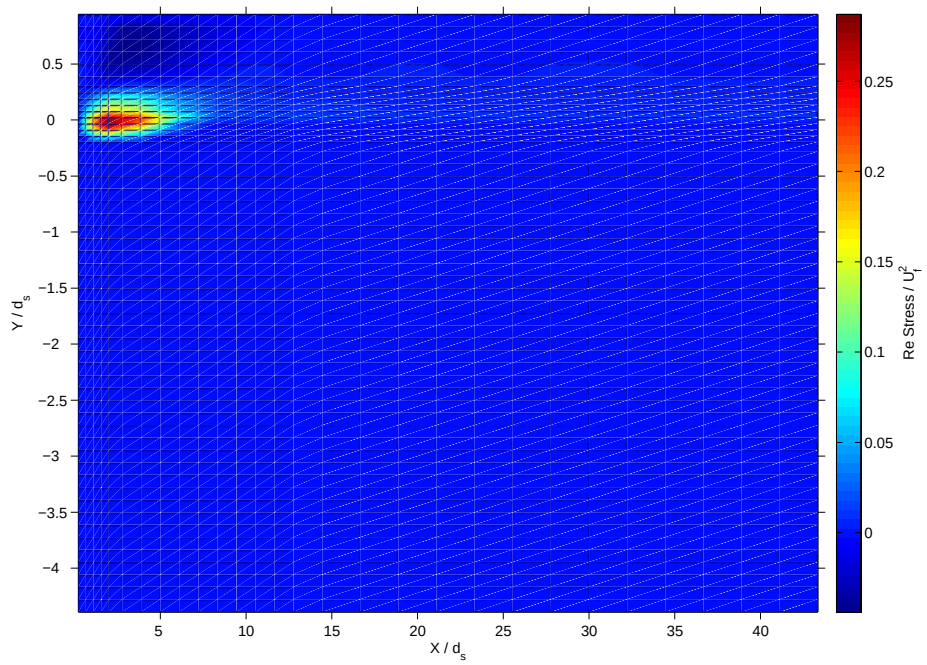

Figure 7.35: Reynolds stress colour plot for gaining configuration; full model domain

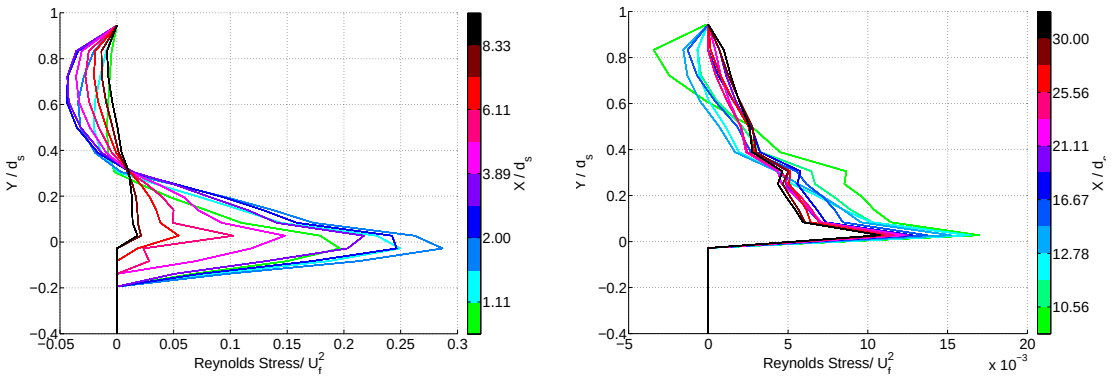

(a) "Gaining1" region *(b) downstream*

Figure 7.36: Reynolds stress profiles for gaining configuration; subsurface layer truncated

7.4.3 Losing stream configuration

In the laboratory results for the "losing stream" configuration, the surface-layer velocity profiles at the downstream end of the measurement window, near the downstream end of the porous layer, were heavily suppressed at the free-surface. As discussed in Chapter 6, it is likely that this was caused by a large-scale eddy or recirculation in the flume, downstream of where the velocity fields were measured. Initial attempts to replicate this with the FV-DANS model by specifying the measured downstream velocity profiles from both the surface and subsurface layers as boundary conditions were unsuccessful. It is likely that this was because the measured surface velocity profiles were largely caused by conditions that were not measured in the laboratory, and therefore were unable to be included in the model domain.

The model was configured with a thin horizontal low-permeability layer at the interface, representing the impermeable plate that was used in the laboratory, immediately downstream of the "losing 1" measurement window, to prevent the flow "short-circuiting" between the surface layer and the downstream boundary of the porous layer. The horizontal extent of this layer was approximately one surface flow depth, starting from the downstream boundary of the model. The vertical profile of permeability at the downstream end of the domain is shown in Figure 7.37. Upstream of the impermeable plate layer the hydraulic properties were the same as for the gaining configuration (see Figure 7.18).

The measured velocity profile from the Position 1 losing stream laboratory results was specified as an outflow boundary condition in the subsurface layer, and a uniform flow boundary condition (i.e. zero gradient in the $x-$direction, as was used in the gaining configuration) was specified in the surface layer. With the measured subsurface velocity profiles, which had horizontal velocities of up to 60% of the flux velocity, the model did not converge to steady-state. The velocity profiles in the surface layer started to exhibit similar behaviour to the laboratory results, with suppressed free-surface velocities. However, the model became unstable before reaching steady-state. This may be because the numerical methods employed in the FV-DANS model are not sophisticated enough to adequately handle a recirculation in the free-surface flow and / or the very high velocities in

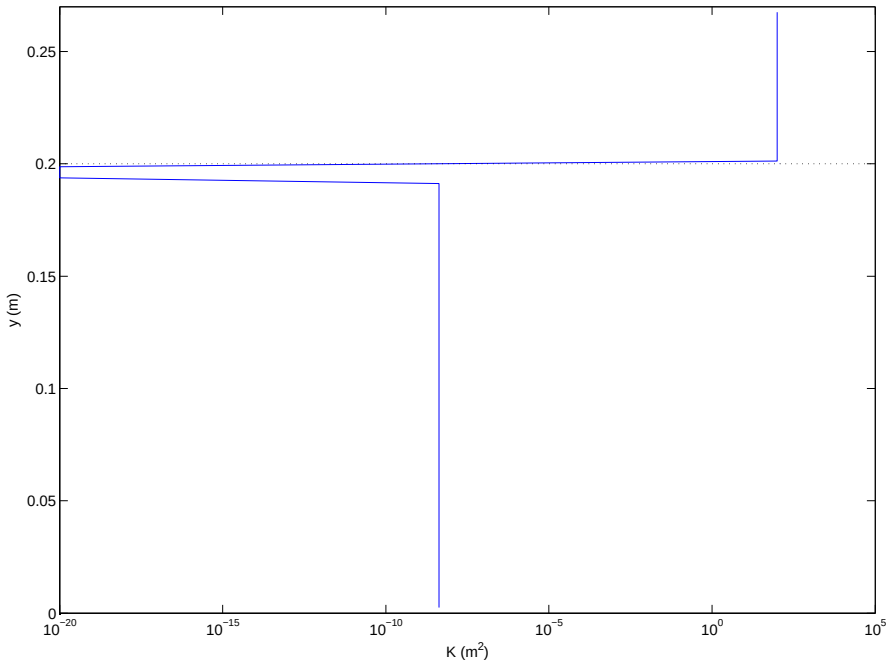

Figure 7.37: Permeability profile with impermeable plate layer. Dotted line shows position of the surface - subsurface interface.

the porous layer, which were higher than anything likely to be encountered in a natural flow.

Due to the issues discussed above, the FV-DANS model was unable to replicate the laboratory results for the losing configuration. However, it was still considered worthwhile to explore the losing flow scenario. Therefore, the results presented in Sections 7.4.3.2 and 7.4.3.3 for the losing stream configuration are for a scenario with the subsurface outflow set to 30% of the flux velocity. Although this was lower than the outflow measured in the laboratory, it was still a substantial subsurface flow in the context of natural groundwater - surface water interactions. The horizontal impermeable layer near the outlet was retained, and a uniform flow boundary condition was specified in the surface layer. The model results, while exhibiting similar trends to the laboratory data, are not expected to be a close match; comparisons to the laboratory results are qualitative.

7.4.3.1 Boundary conditions

At the upstream boundary in the surface layer the measured U-velocity profile from upstream end of the "losing 2" laboratory data-set was specified as the inflow boundary condition. This profile is shown in Figure 7.38. There was no inflow in the subsurface layer.

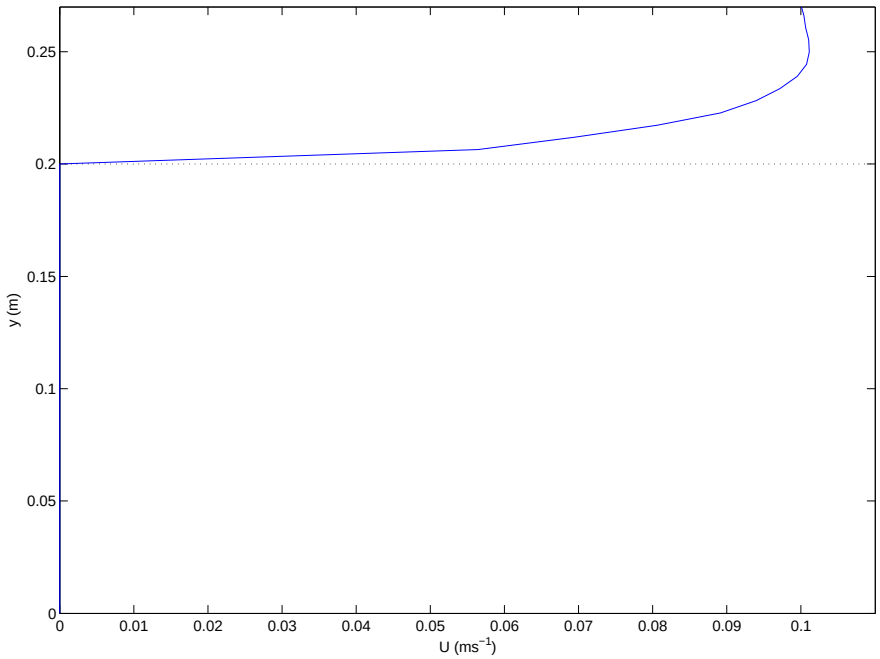

Figure 7.38: Inlet velocity boundary condition for losing stream configuration

As discussed above, the outflow velocity in the subsurface layer was set to 30% of the flux velocity. This value was constant over the depth of the layer. The outlet boundary condition in the surface layer was uniform flow (i.e. zero gradient), the same as in the gaining configuration.

7.4.3.2 Mean flows

Modelled velocity vectors for the full numerical domain are shown in Figure 7.39. The vector magnitudes were scaled by the flux velocity for the "losing 2" laboratory data, $U_f = 0.089\ ms^{-1}$. The flow was generally consistent with the laboratory data (Figure 6.19), with the horizontal extent of subsurface motion concentrated over approximately 4 flow depths at the downstream end of the domain. In the laboratory there was subsurface motion for approximately 6 flow depths upstream. However, as the modelled outflow velocity was lower than the measured values it is expected that the flow in the porous layer would be over a smaller area.

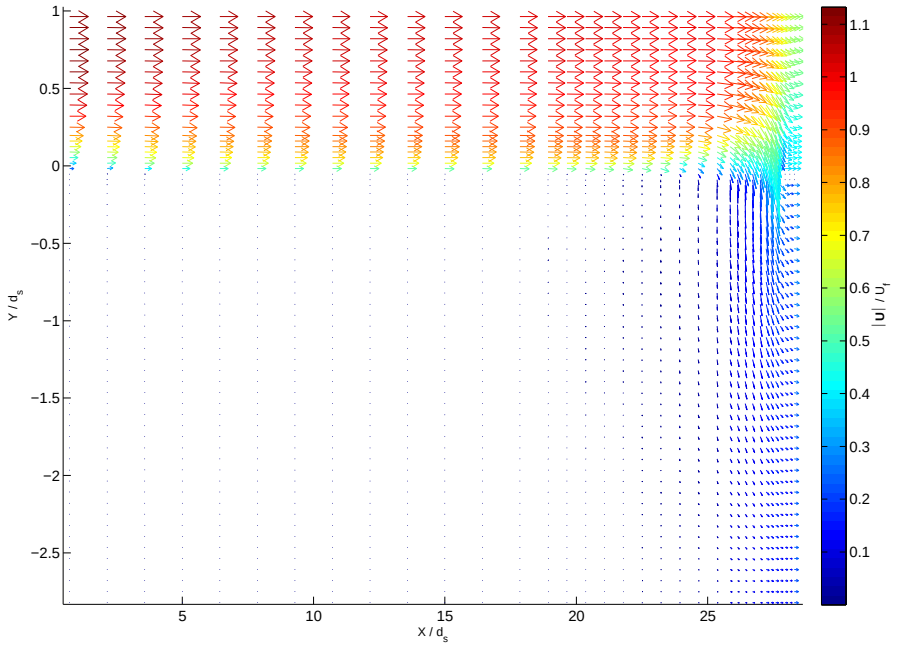

Figure 7.39: Velocity vector plot for losing configuration; full model domain

Modelled dimensionless velocity vectors and streamlines are shown in Figure 7.40 for the area covered by the Position 1 laboratory data (i.e. the downstream end of the domain). The general structure of the modelled flow field was consistent with the laboratory data (Figure 6.19a). Immediately upstream of the impermeable plate layer the flow at the interface was predominantly vertical. The vertical motion at the interface was sufficient to cause noticeable curvature in the

surface layer streamlines. This curvature persisted over the impermeable plate (i.e. beyond $x/d_s = 27.5$) as the velocity profile re-adjusted.

In the subsurface layer the flow became more horizontal with depth. The flow straightened in the area beneath the impermeable plate (which was not included in the laboratory data), becoming predominantly horizontal over the full depth of the subsurface layer.

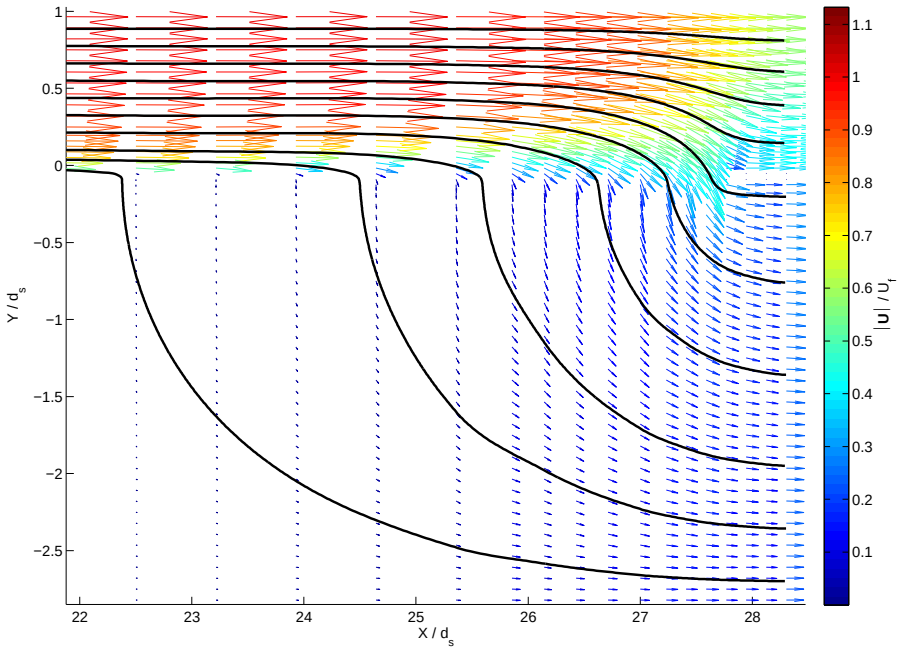

Figure 7.40: Velocity vector and streamline plot for losing configuration; area covered by Position 1 laboratory data.

The modelled effective pressures for the losing configuration are shown in Figure 7.41. As expected (and consistent with the gaining configuration) the pressure gradient was concentrated at the downstream end of the domain, where the subsurface velocities were strong. In the surface layer, as for the gaining configuration, the pressure gradient was negligible. This is qualitatively consistent with the laboratory results, which showed no measurable slope on the free-surface.

A colour plot of modelled U-velocities for the full computational domain is shown in Figure 7.42. Figure 7.43 shows the U-velocities for the area at the downstream end of the domain covered by the Position 1 "losing stream" labora-

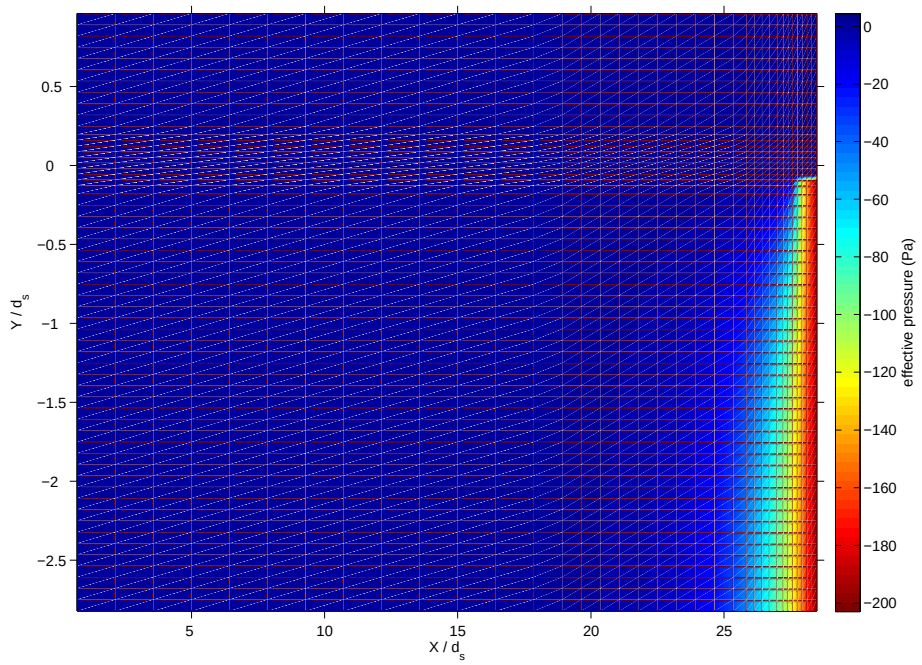

Figure 7.41: Modified pressure colour plot for losing configuration; full model domain

tory data. Subsurface U-velocities for the downstream portion of the domain are shown in Figure 7.44. The colour-scale in this figure has been adjusted to highlight the subsurface U-velocities. Vertical profiles of the dimensionless U-velocity in the area covered by the Position 1 laboratory data are shown in Figure 7.45. Figure 7.46 shows U-velocity profiles for the upstream portion of the domain, where interactions between the two layers are negligible.

Despite the modelled velocities being lower, the trends in the modelled U-velocities were generally consistent with the laboratory data (Figure 6.20). In the surface layer the U-velocities reduced with distance downstream in the region where there was strong vertical flow across the interface. Unlike the laboratory results, however, the shape of the profiles remained relatively uniform, as the influence of the laboratory flume's downstream boundary was not represented in the numerical model. Upstream of the strongly-losing region the U-velocity profiles were relatively uniform; there was some slight adjustment to the specified boundary velocity profile in the surface layer, and subsurface velocities were negligible. Figure 7.44 shows a region of high U-velocities immediately below

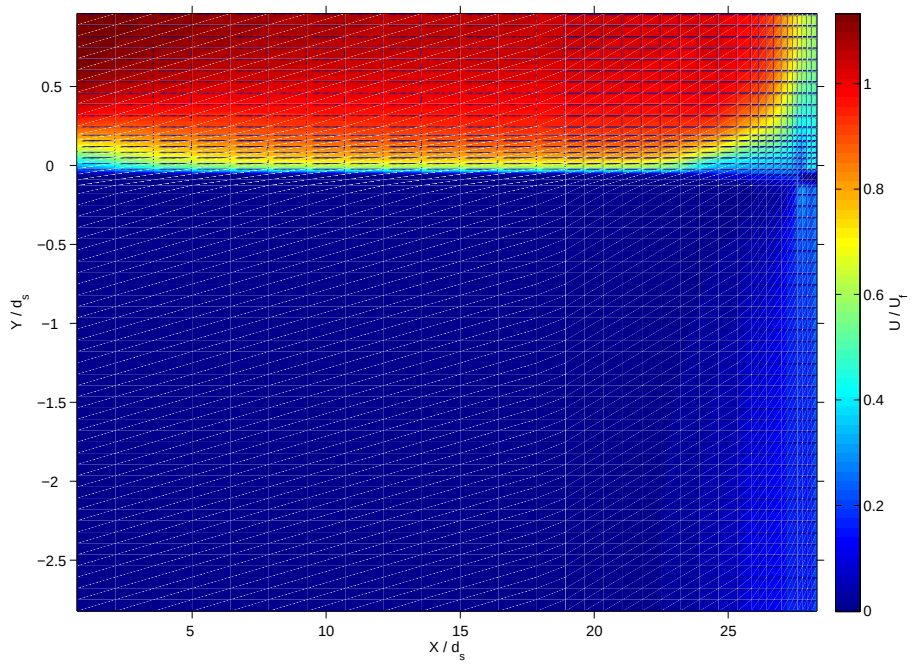

Figure 7.42: U-velocity colour plot for losing configuration; full model domain.

the interface towards the downstream end of the domain. As seen in the gaining configuration model results, the surface - subsurface interface did not act as a no-slip boundary, but the surface flow's penetration into the subsurface layer was relatively small in the upstream portion of the domain where vertical flows across the interface were negligible.

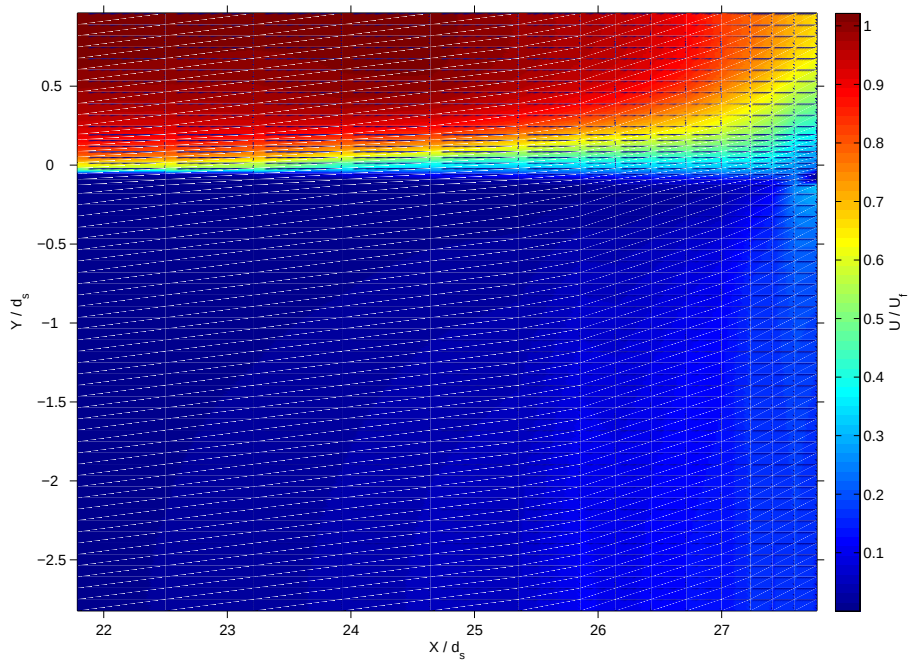

Figure 7.43: U-velocity colour plot for losing configuration; area covered by Position 1 laboratory data.

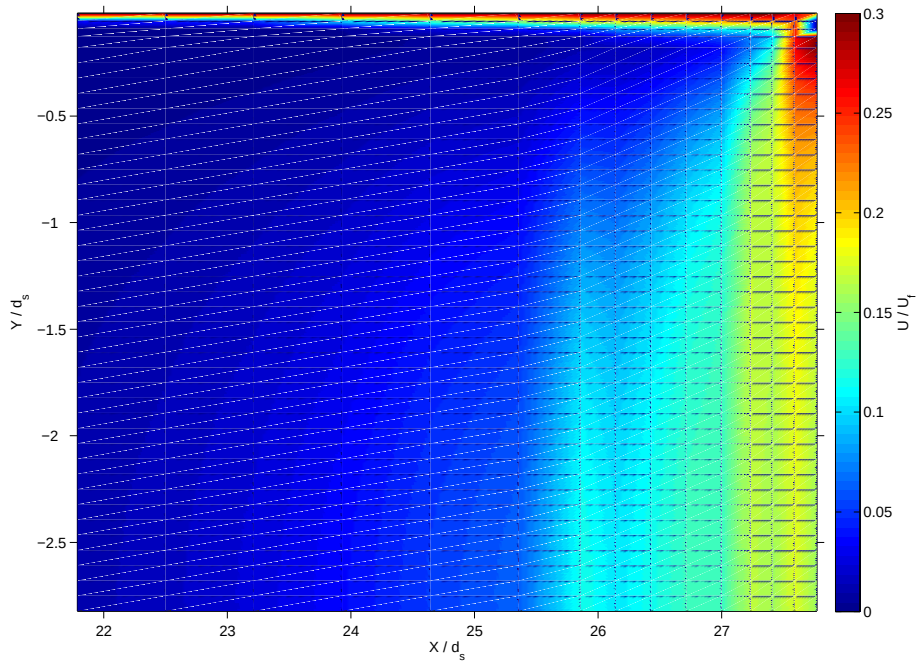

Figure 7.44: U-velocity colour plot for losing configuration; subsurface only.

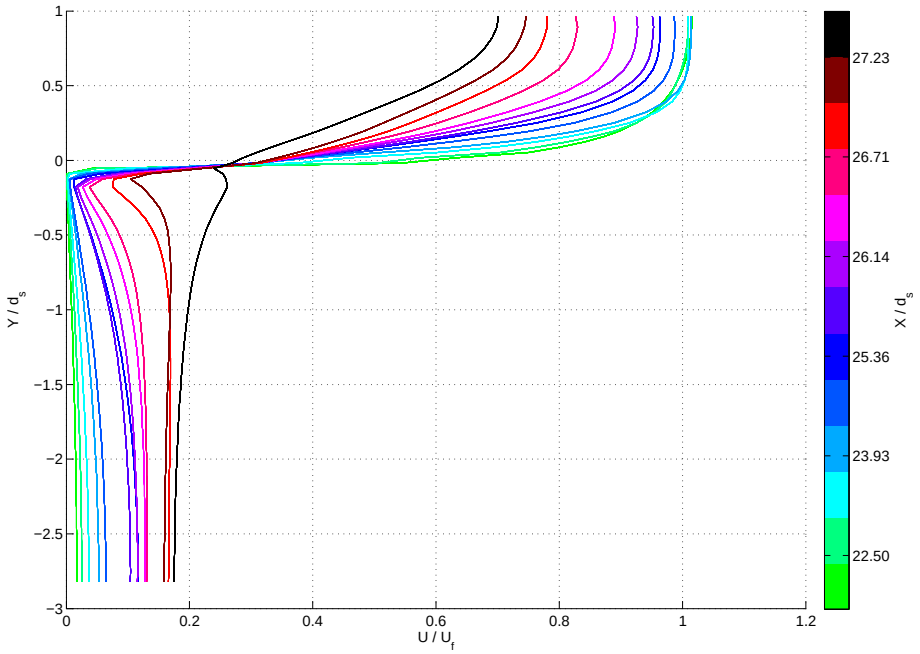

Figure 7.45: U-velocity profiles for losing configuration; area covered by Position 1 laboratory data.

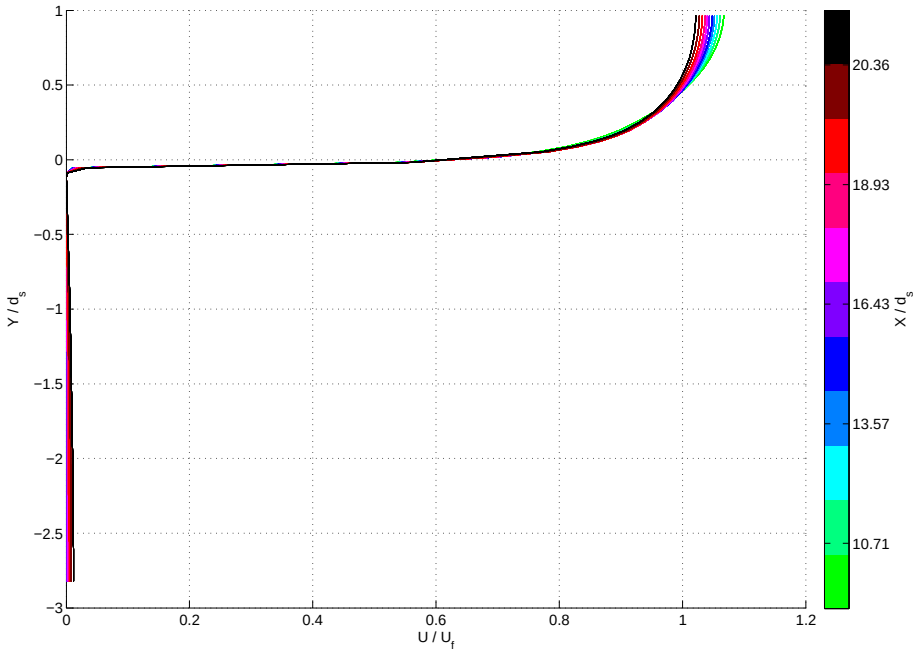

Figure 7.46: U-velocity profiles for losing configuration; upstream area.

A colour plot of the dimensionless V-velocity for the losing configuration is shown in Figure 7.47. The figure shows the full model domain. Figure 7.48 shows the V-velocities for the area covered by the Position 1 laboratory data. Figure 7.49 shows vertical and longitudinal profiles of dimensionless V-velocity for the losing configuration. As with the gaining configuration results, the oscillations in the profiles near the interface are likely to be related to the discontinuities in the hydraulic properties. As discussed in Section 7.4.2.3, this is less likely to be an issue in models of natural systems.

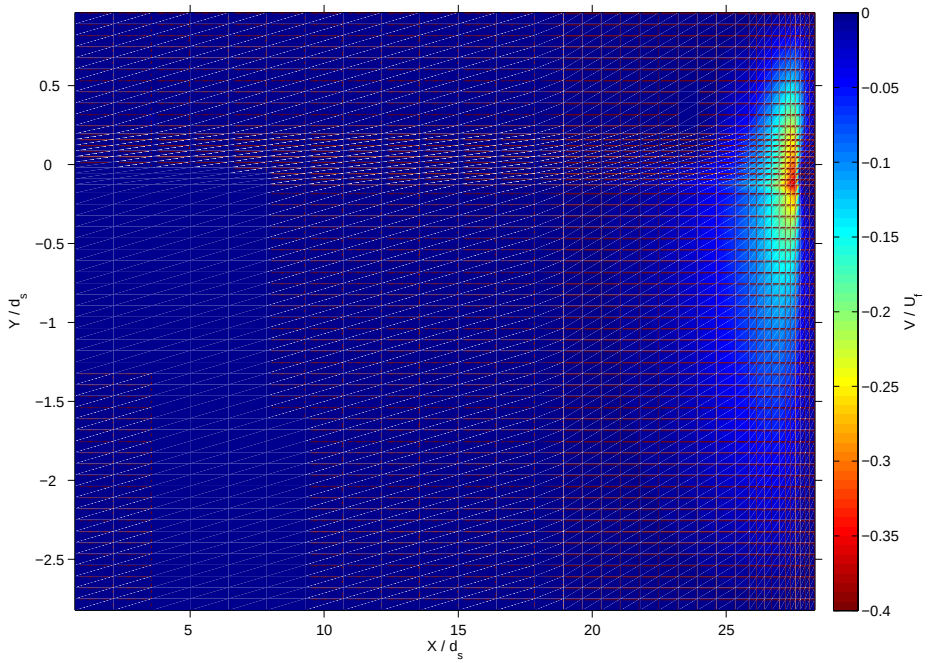

Figure 7.47: V-velocity colour plot for losing configuration; full domain.

The maximum modelled V-velocities were around the interface at the downstream end of the domain, immediately upstream of the impermeable plate layer($x/d_s = 27.75$). As in the gaining configuration, the peak vertical velocities were immediately below the interface, corresponding to the step-change in porosity. The zone of high vertical velocities extended approximately three surface flow depths upstream of the outlet.

Plots of the modelled porous Reynolds number, Re_p, for the losing configuration are shown in Figure 7.50. Figure 7.50 shows Re_p for the subsurface layer

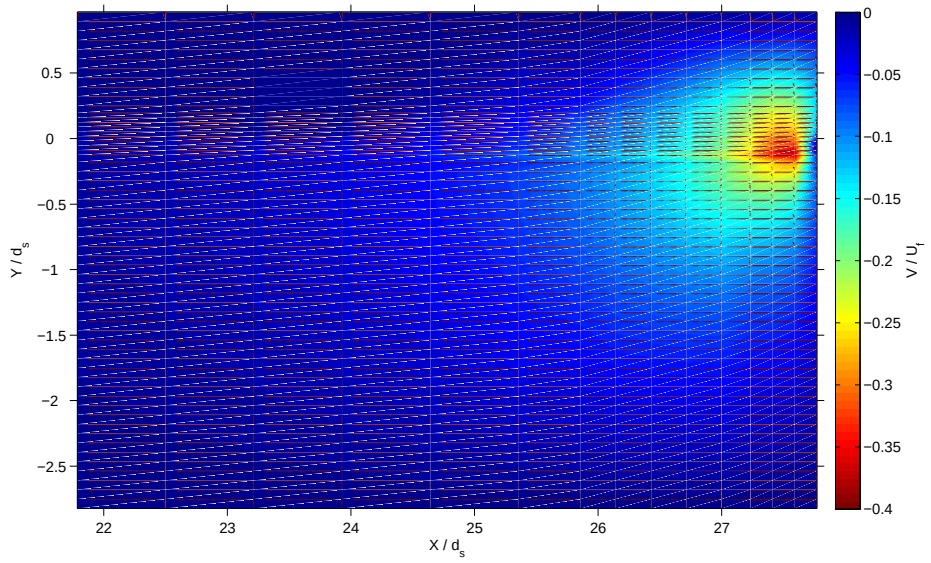

Figure 7.48: V-velocity colour plot for losing configuration; area covered by Position 1 laboratory data.

in the portion of the domain covered by the Position 1 laboratory data. As with the results for the gaining configuration, the modelled Re_p values are broadly consistent with the laboratory data (Figure 6.23), with the highest values near the outlet, at interface level. Over the majority of the depth of the subsurface layer, near the outlet, Re_p was in the $0.5 - 1.0$ range. This indicates that the modelled flow was non-Darcian, and starting to transition to turbulence.

Beneath the interface, immediately upstream of the impermeable layer, there was a zone of higher Re_p, which is shown in more detail in Figure 7.50b. The peak value of $Re_p = 1.6$ in this region was lower to the modelled peak for the gaining configuration. However, compared to the gaining configuration the zone of high Re_p extended deeper into the subsurface layer. A likely cause for this is that the losing configuration was transporting high-momentum fluid from the surface layer into the subsurface layer. This deeper penetration of turbulence into the subsurface layer is supported by the turbulent statistics presented below.

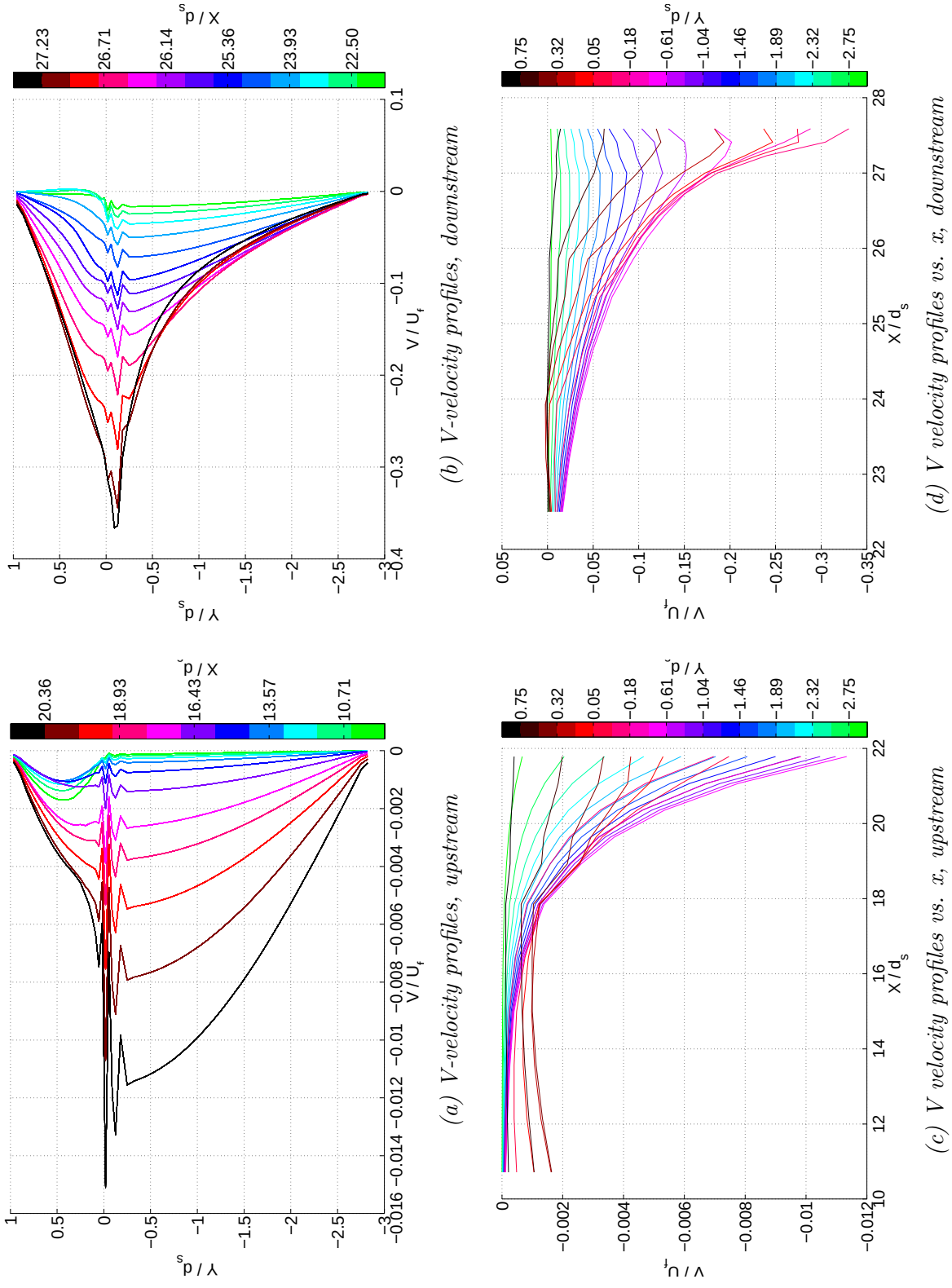

(a) V-velocity profiles, upstream *(b) V-velocity profiles, downstream*

(c) V velocity profiles vs. x, upstream *(d) V velocity profiles vs. x, downstream*

Figure 7.49: V velocities for losing configuration

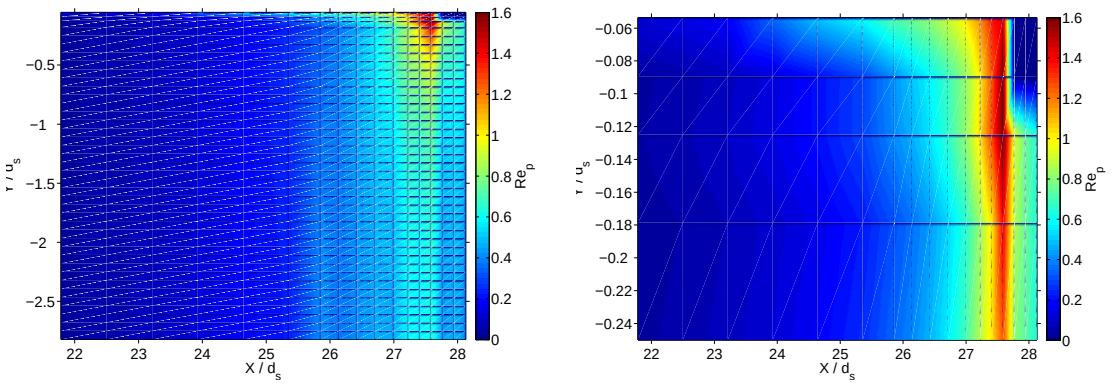

(a) "Losing1" region; subsurface

(b) "Losing1" region; subsurface near interface

Figure 7.50: Porous Reynolds numbers, Re_p, for losing configuration.

7.4.3.3 Turbulent statistics

Figure 7.51 shows dimensionless TKE over the full model domain for the losing configuration. Figure 7.52 shows vertical profiles of dimensionless TKE. Figure 7.52b contains the profiles for the area of the domain covered by the Position 1 laboratory data, and Figure 7.52a covers the remainder of the domain, upstream.

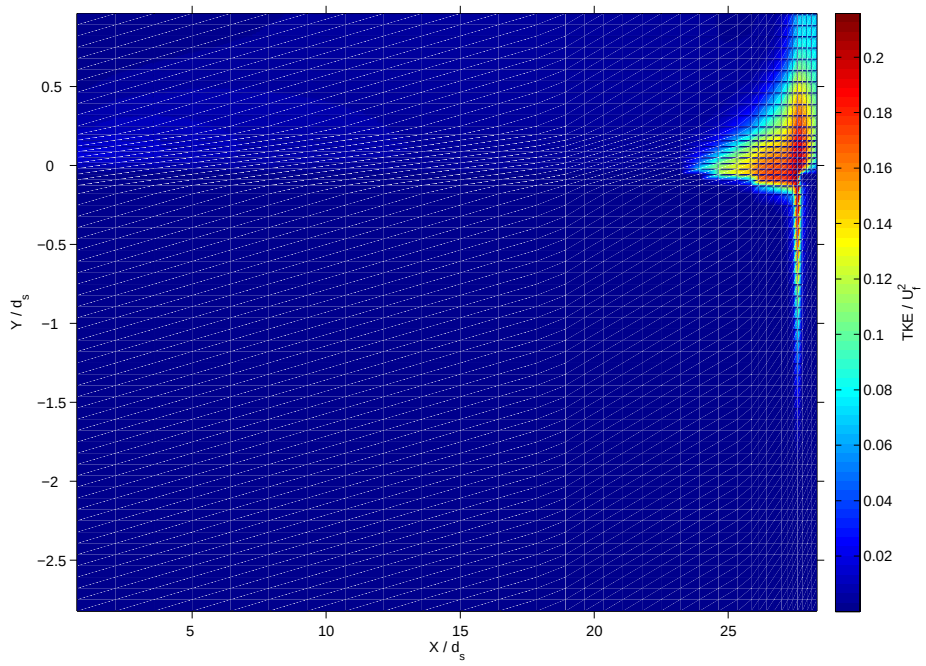

Figure 7.51: TKE colour plot for losing configuration; full model domain.

For the losing configuration, the TKE profiles from the laboratory results were dominated by the effect of the suppressed free-surface velocities, which distorted the shape of the velocity profiles in the surface layer (Figures 6.25 and 6.26). As this distortion was near the free-surface not present in the model results, the modelled TKE was dominated by the vertical flow across the interface, and the general adjustment of the surface velocity profiles to account for the mass lost from the surface flow. In the downstream region of the domain the peak values near the interface were substantially higher than any of the laboratory values. Further upstream in the domain both the shape of the modelled profiles and their peak values above the interface were consistent with the laboratory results.

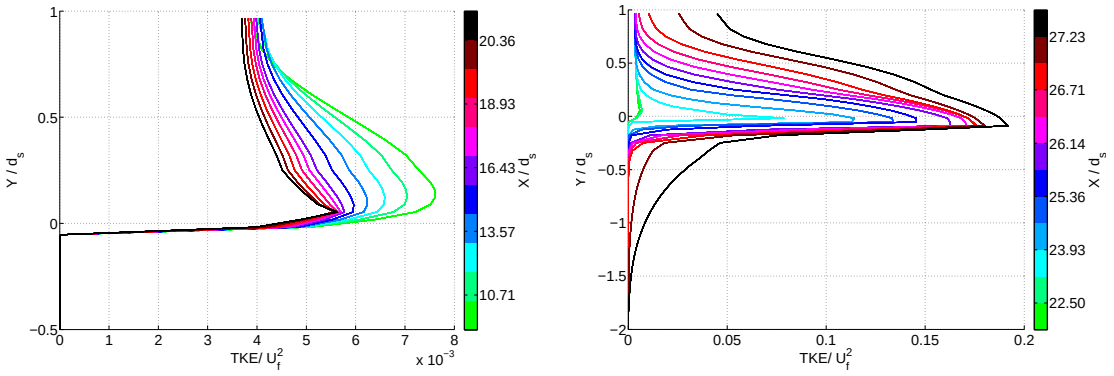

(a) upstream *(b) "Losing1" region*

Figure 7.52: TKE profiles for losing configuration; subsurface layer truncated

Figure 7.53 shows the TKE budget at the downstream end of the domain for the losing stream configuration. The region of high TKE was caused by a region of high production around the interface, where the vertical velocities were highest. There was moderately high production in the strongly-losing region surface layer, up to $y/d_s = 0.5$. The TKE was transported downstream over the impermeable layer. Although there was also a region of high dissipation, this was predominantly below the high-production region.

As discussed in Section 7.4.2.4 for the gaining configuration, the elevated mixing lengths near the interface where the vertical velocities were strong contributed to higher values of μ_t, which in turn increased the TKE production. Plots of the modelled values of mixing length and μ_t are shown in Appendix F.

A detailed view of the TKE production and dissipation in the near-bed region is shown in Figure 7.54. Apart from a small region immediately upstream of the impermeable plate, the peak values of dissipation were substantially higher than the production, which prevented the TKE from being transported deeper into the porous layer, apart from the narrow zone of high TKE seen in Figure 7.51.

A colour plot of dimensionless Reynolds stress for the full model domain is shown in Figure 7.55. Profiles of dimensionless Reynolds stress for the losing configuration are shown in Figure 7.56. Figure 7.56b shows the downstream area covered by the Position 1 laboratory data, and Figure 7.56a shows the remainder of the domain, upstream.

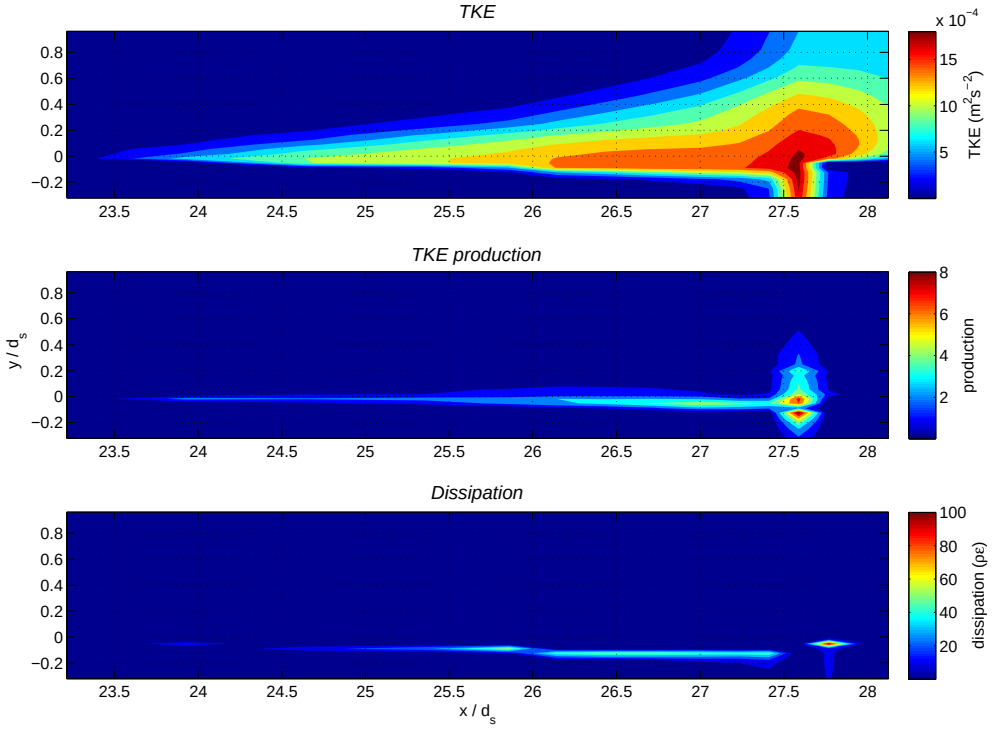

Figure 7.53: TKE budget for losing configuration. From top to bottom: TKE, production and dissipation

As with the TKE results discussed above, the modelled Reynolds stress profiles at the downstream end of the domain were substantially different to the laboratory values (Figures 6.27 and 6.28). This was due to the modelled surface velocity profiles not being distorted like those measured in the laboratory. The modelled Reynolds stresses remained positive everywhere for the losing configuration. Near the outlet the peak values were slightly below the interface. Figure 7.55 shows a zone of higher Reynolds stress extending approximately one surface flow depth below the interface.

Further upstream, as shown in Figure 7.56a, the Reynolds stress profiles were more consistent with the laboratory results. The peak values above the interface were a good match to the Position 2 laboratory values. Although the modelled subsurface outflows for the losing configuration were less than the values measured in the laboratory, the inflow boundary condition in the surface layer was from measured data. Therefore at the upstream end of the domain, where the effect

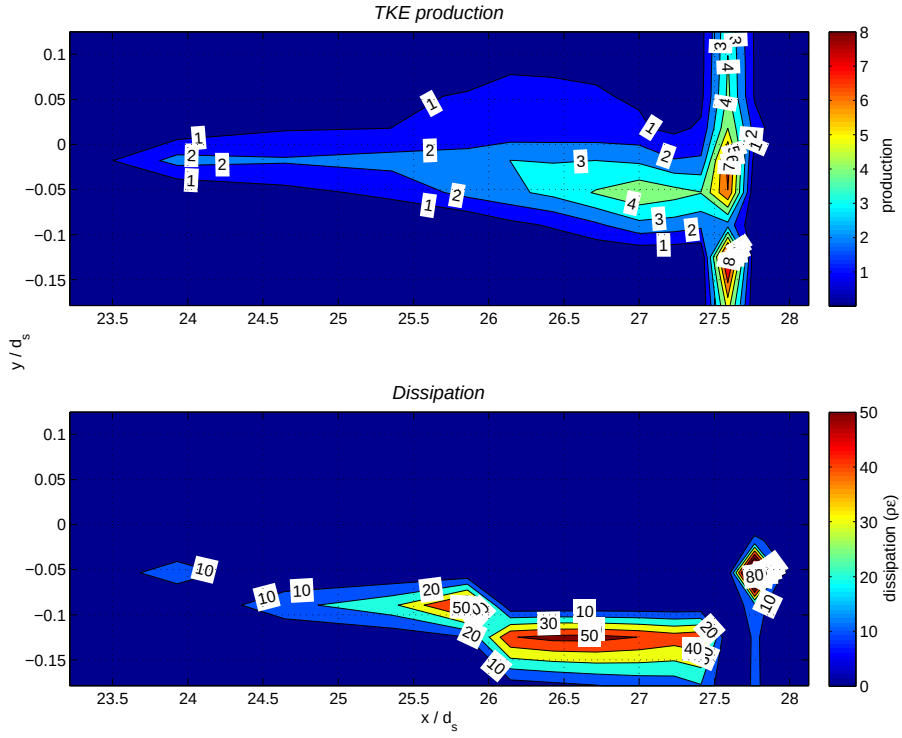

Figure 7.54: TKE budget for losing configuration: TKE production (top) and dissipation (bottom) in near-bed region

of fluxes across the interface was negligible, the modelled turbulent statistics are able to be compared directly with the laboratory results. The cause of the oscillations in the profiles is unclear; this behaviour was not seen in the Reynolds stress profiles for the gaining configuration.

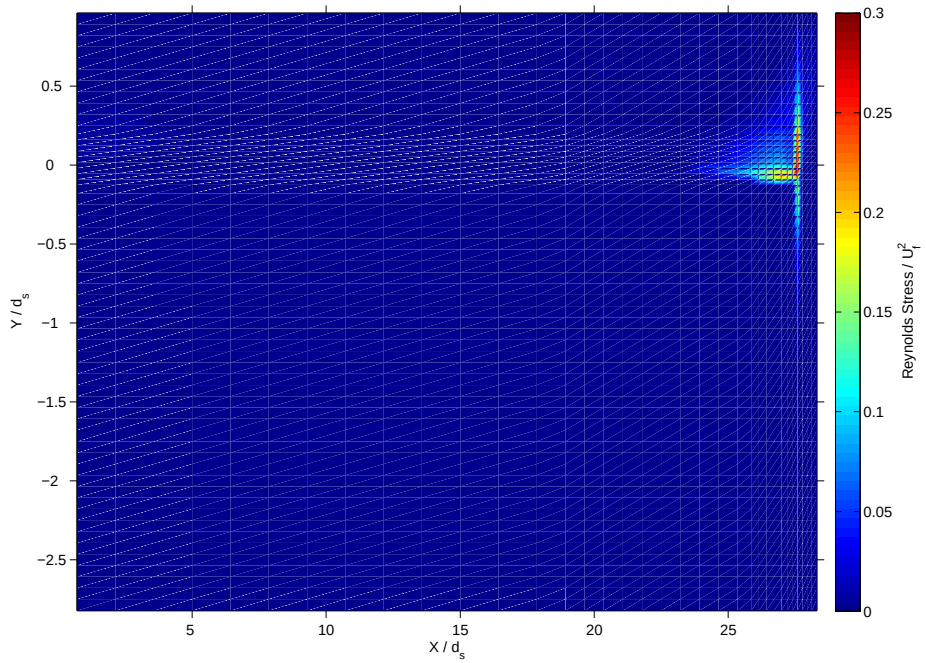

Figure 7.55: Reynolds stress colour plot for losing configuration; full model domain.

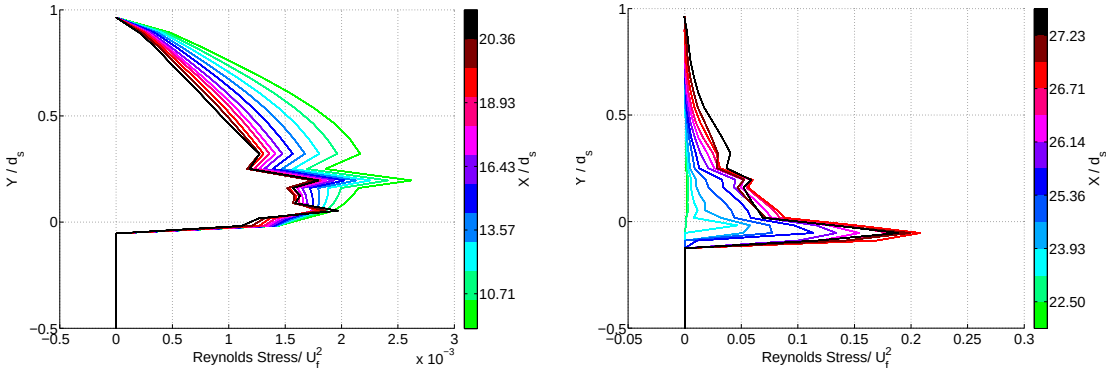

(a) upstream *(b) "Losing1" region*

Figure 7.56: Reynolds stress profiles for losing; subsurface layer truncated

7.5 Sensitivity Testing

For the gaining configuration, the sensitivity of the numerical model results to the parameters in the turbulence model was tested. The focus of this testing was the parameters that have been introduced in the FV-DANS model to handle the transition between turbulent and laminar flow: a, the midpoint value for the turbulence damping function; b, the steepness parameter in the damping function; and c_v, the vertical flow adjustment in the mixing length calculation.

In this section the baseline results are from the model run for which full results were presented in Section 7.4.2.

7.5.1 Sensitivity to damping function midpoint parameter, a

The value of the a parameter in the turbulence damping function (which sets the value of Re_p at which the damping function is equal to 0.5) was halved, doubled, and multiplied by 10. Attempts to run the model with a lower value of a were unsuccessful, as the model was unstable. The values of b (the steepness parameter in the turbulence damping function) were changed by corresponding amounts, so that the shape of the damping function was retained.

Figure 7.57 shows the damping function plotted against Re_p for the four different values a.

Figure 7.58 shows the sensitivity of the U-velocity profiles to a, the midpoint value for the turbulence damping function. Over the majority of the profile, varying a had very little effect.

Figure 7.59 shows the detail of the upstream profile in the region immediately below the interface. Reducing a resulted in the U-velocity profile penetrating slightly further into the subsurface layer, relative to the baseline case. Increasing a had the opposite effect.

Figure 7.60 shows the effect on the V-velocity profile of varying a. Reducing a had only no effect on peak value of the V-velocity profile, and only a minor effect further downstream. Increasing a resulted in a slight decrease in the peak V-velocity. The net effect of the change in vertical velocity on the downstream

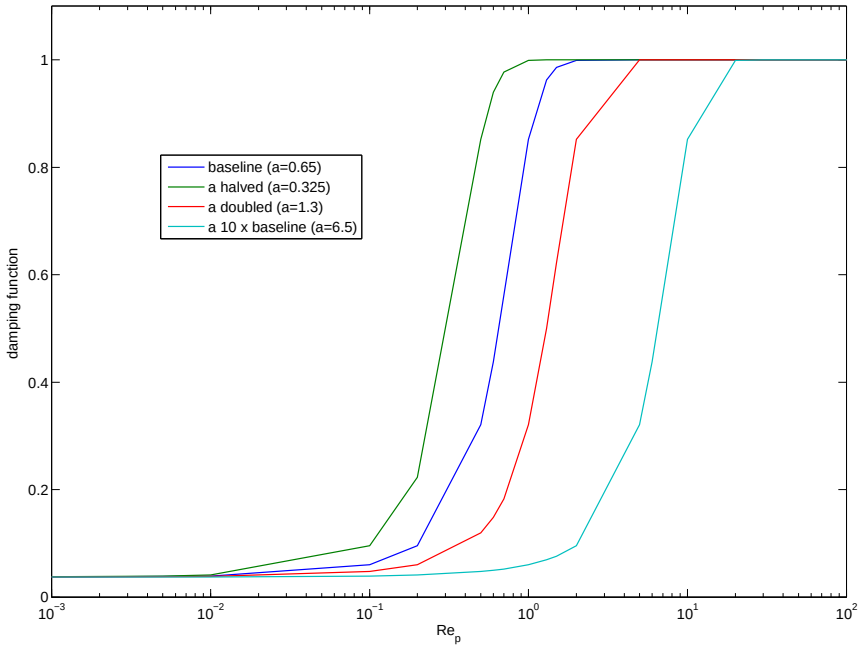

Figure 7.57: Turbulence damping function vs. Re_p with varying 'a' parameter.

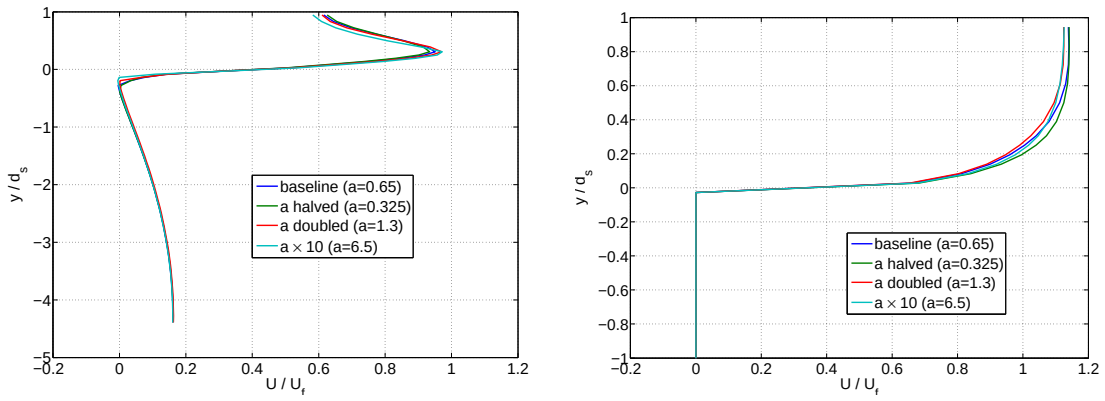

(a) $x/d_s = 2$ *(b) $x/d_s = 40$, subsurface layer truncated*

Figure 7.58: Sensitivity of U-velocity profiles to varying 'a' in turbulence damping function

U-velocity profiles (Figure 7.58b) was negligible.

The effect of varying a on the TKE profiles is shown in Figure 7.61.

Decreasing a resulted in higher values of the turbulence damping function at lower values of Re_p. This allowed the TKE profile to penetrate further into

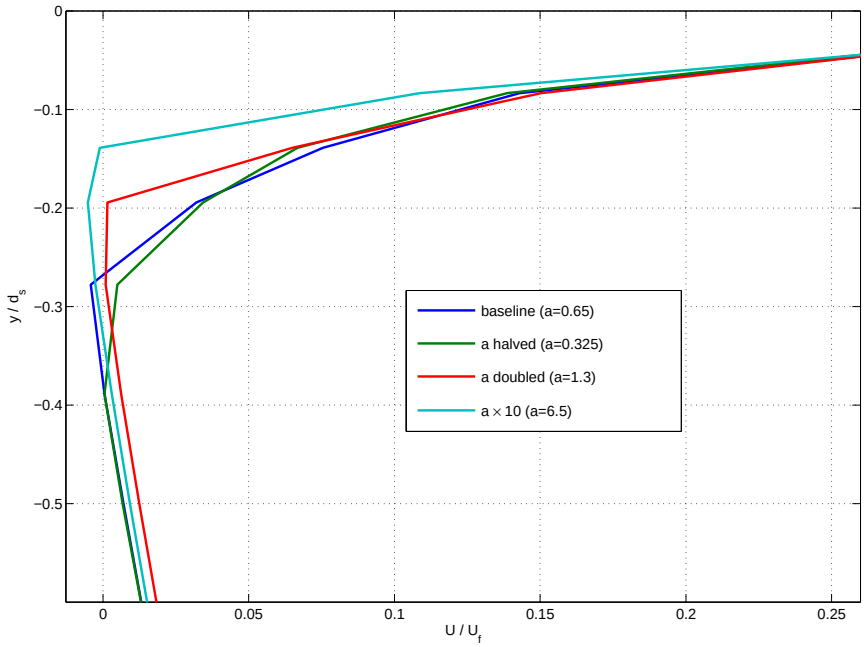

Figure 7.59: Sensitivity of U-velocity profiles to varying 'a' in turbulence damping function: near-bed region

the subsurface layer. Increasing the values of the damping function resulted in a lower peak value in the TKE profile, relative to the baseline case. Closer to the free-surface the profile was similar to the baseline. Increasing a resulted in lower peak values of TKE and less penetration into the subsurface layer. The effect of varying a on the downstream TKE profiles (Figure 7.61b) was also negligible.

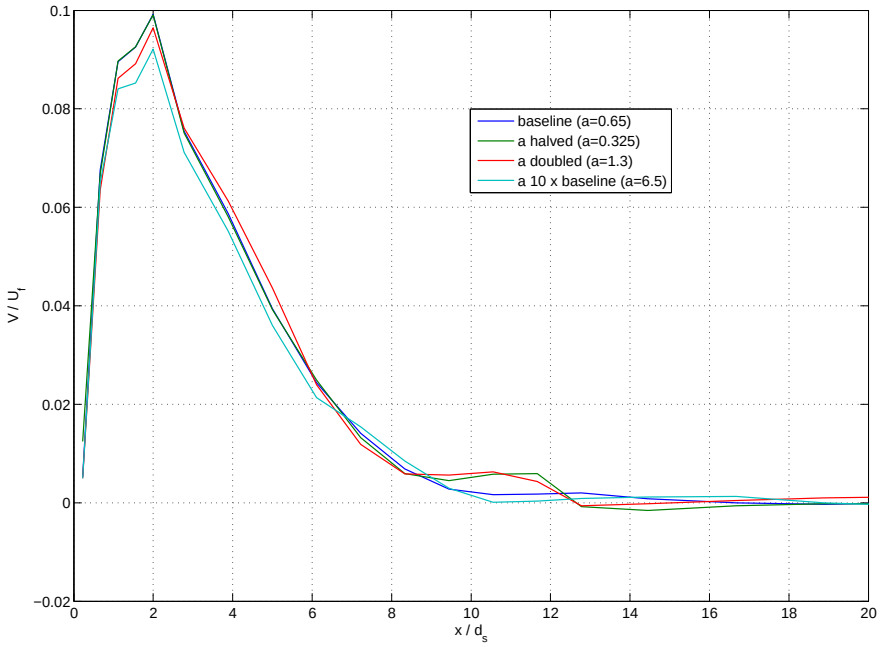

Figure 7.60: Sensitivity of interface V-velocity profiles to varying 'a' in turbulence damping function

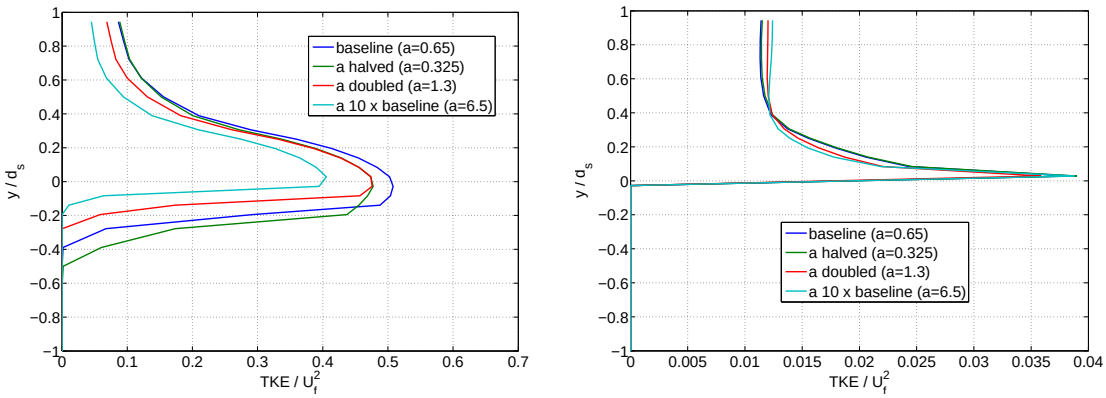

(a) $x/d_s = 2$ (b) $x/d_s = 40$

Figure 7.61: Sensitivity of TKE profiles to varying 'a' in turbulence damping function ; subsurface layer truncated.

7.5.2 Sensitivity to damping function steepness parameter, b

The value of the b parameter in the turbulence damping function (which sets the steepness of the transition between 0 and 1) as halved to 0.2 and doubled to 0.8; a was held constant at $a = 0.65$. The damping function, plotted against Re_p, is shown in Figure 7.62 for the three values of b.

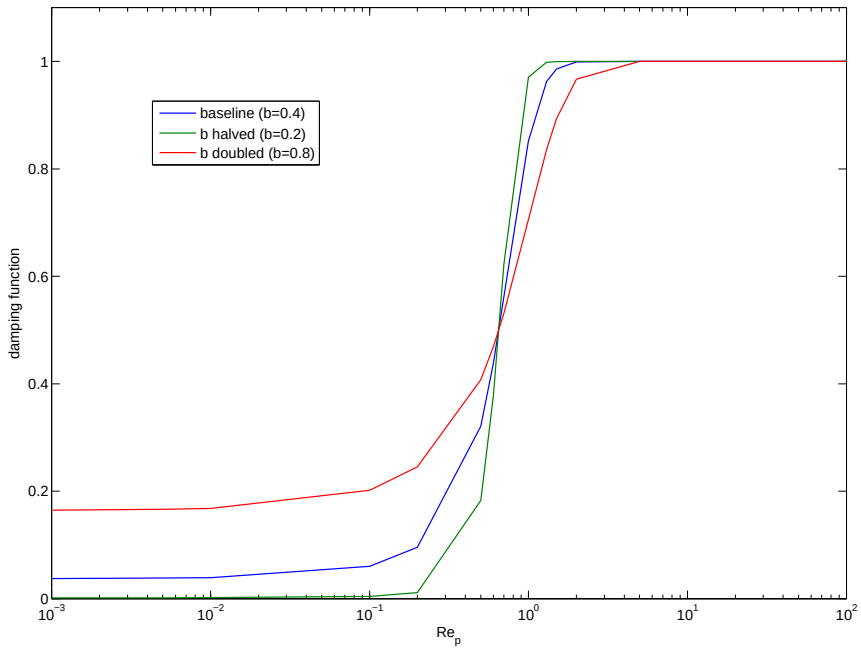

Figure 7.62: Turbulence damping function vs. Re_p with varying 'b' parameter.

The horizontal and vertical velocity profiles for the three values of b were indistinguishable.

Figure 7.63 shows the effect of varying b on the TKE profiles at the upstream and downstream ends of the domain, respectively. At the upstream end (Figure 7.63a), where there was a strong vertical flow, increasing b had a very small effect on the peak TKE value and on the shape of the TKE profile beneath the bed. Decreasing b had a negligible effect. At the downstream end of the domain (Figure 7.63b) the profiles for the three values of b were indistinguishable.

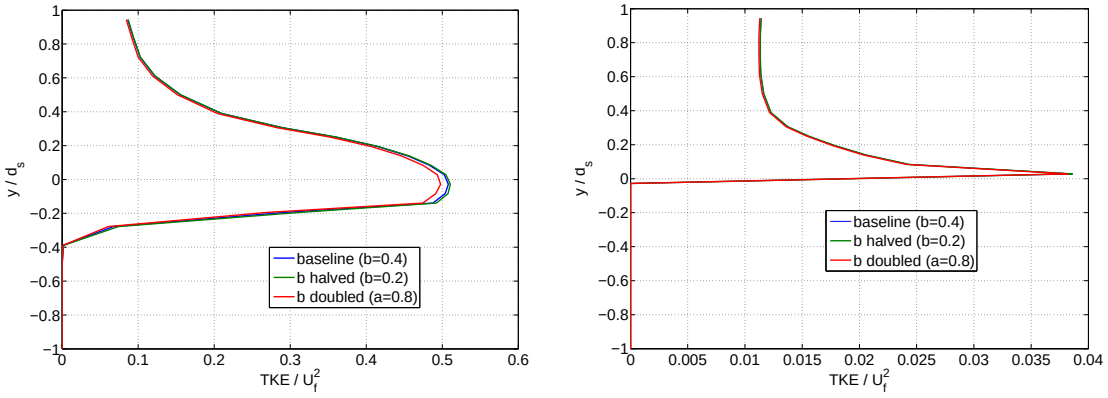

(a) $x/d_s = 2$ *(b)* $x/d_s = 40$

Figure 7.63: Sensitivity of TKE profiles to varying 'b' in turbulence damping function; subsurface layer truncated.

7.5.3 Sensitivity to mixing length vertical flow adjustment parameter, c_v

The value of c_v, the vertical flow adjustment in the mixing length calculation, was halved to $c_v = 1.1$ and doubled to $c_v = 4.4$. For the baseline model runs (as described in Sections 7.4.2 and 7.4.3), $c_v = 2.2$ had been chosen as a value that most closely reproduced the elevated mixing lengths that were seen in the laboratory data (see Appendix E), without compromising the model's stability. Very low values of c_v (or not adjusting the mixing length at all where vertical flows across the bed were strong) resulted in the model being unstable for both the gaining and losing configurations. With $c_v = 1.1$ the maximum number of iterations had to be increased and the under-relaxation parameter α_u reduced in order to get the model to run.

Figure 7.64 shows the effect of varying c_v on the U-velocity profiles. In the subsurface layer there was very little effect on the U-velocity. The main effect was seen in the surface layer at the upstream end of the domain (Figure 7.64a). Reducing c_v increased the U-velocity near the interface and reduced the free-surface velocity, relative to the baseline. Increasing c_v resulted in decreased velocities both near the interface and at the free surface.

Figure 7.65 shows the effect of varying c_v on the V-velocity profile at the inter-

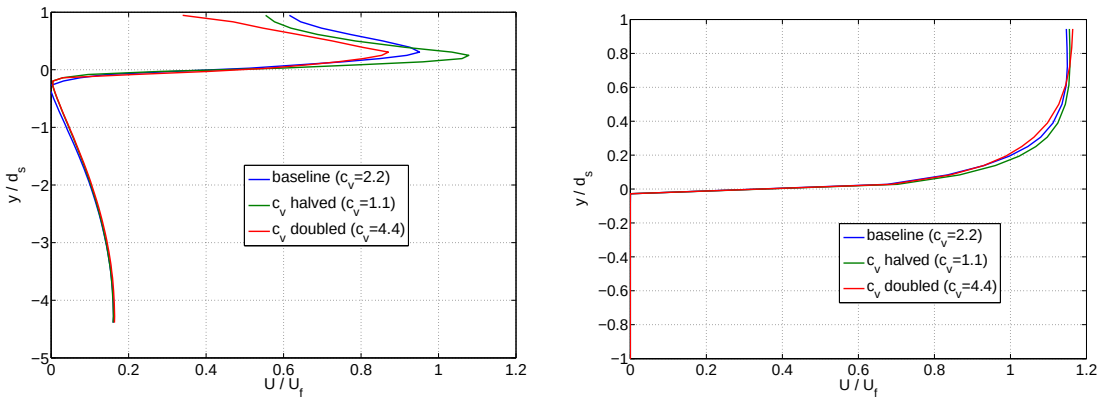

(a) $x/d_s = 2$ *(b)* $x/d_s = 40$, *subsurface layer truncated*

Figure 7.64: Sensitivity of U-velocity profiles to varying c_v *in mixing length calculation.*

face. Changing c_v slightly altered the shape of the V-velocity profile, but did not affect the peak value. Further downstream there was little change to the vertical velocities. The net effect on the downstream U-velocity profiles (Figure 7.64b) was negligible, showing that varying c_v affected the rate at which the velocity profiles evolved in response to the flux across the interface.

Figure 7.66 shows the effect of varying c_v on the TKE profiles. With c_v reduced, the peak value of TKE near the interface was also reduced; near the free-surface the difference from the baseline case was less pronounced. This is consistent with the mixing length being reduced in the interface region, where the vertical velocities were strongest, leading to reduced TKE production. Increasing c_v had very little effect on the TKE at the interface, but altered the shape of the TKE profile in the surface layer, and the extent to which the profile penetrated into the subsurface layer. At the downstream end of the domain (Figure 7.66b) the difference between the three TKE profiles was minimal.

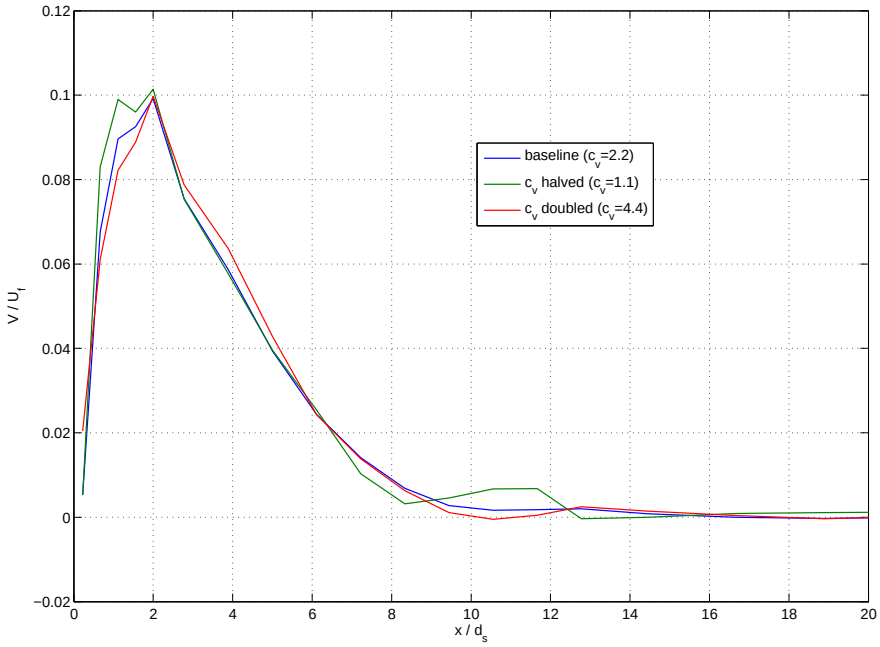

Figure 7.65: Sensitivity of interface V-velocity profiles to varying c_v in mixing length calculation

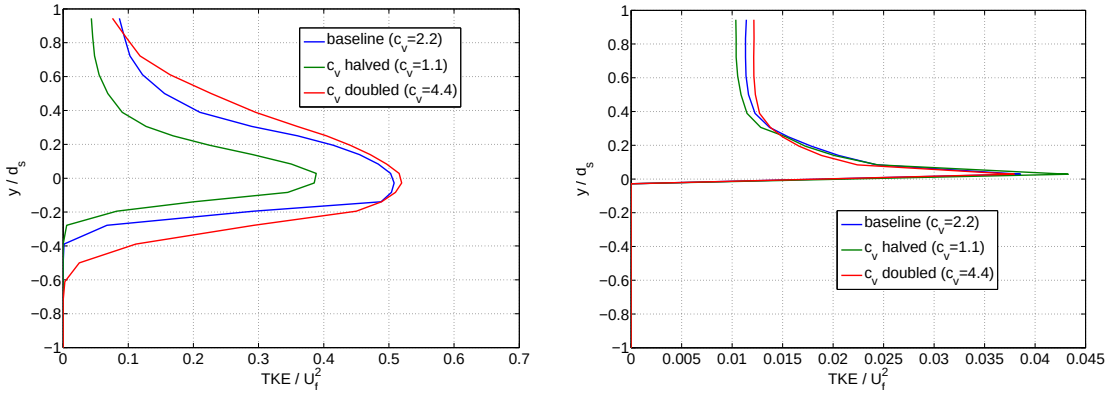

(a) $x/d_s = 2$ (b) $x/d_s = 40$

Figure 7.66: Sensitivity of TKE profiles to varying c_v in mixing length calculation; subsurface layer truncated.

7.6 Chapter Summary

In this chapter it has been shown that the FV-DANS model (the finite-volume implementation of the double-averaged Navier-Stokes equations) is capable of modelling surface water (clear fluid), groundwater, and mixed-domain flows.

As an intermediate step in the development of the FV-DANS model, a finite-volume implementation of the Reynolds-averaged Navier-Stokes Equations (FV-RANS) was developed. Mean flow and turbulence results from the FV-RANS model for a turbulent clear-fluid flow between two parallel plates were verified against published data. Two turbulence models were tested in the FV-RANS model: the commonly-used $k - \epsilon$ model, and the Kolmogorov-Prandtl single-equation model. A good match to published RANS model data was achieved for the time-averaged velocities with both turbulence models. The match to published turbulent kinetic energy (TKE) data was also reasonable with both turbulence models.

When the FV-RANS and FV-DANS models were compared for the parallel-plates case in a clear-fluid domain (with the single-equation turbulence model used in both models), the results were close to identical. This showed that the additional terms in the FV-DANS model were negligible for a clear-fluid flow, and at least for this simple case the FV-DANS model reverted to the RANS equations.

With a free-surface boundary added to the FV-DANS model, longitudinal free-surface profile results were compared with equivalent outputs from HEC-RAS. There was a reasonably good level of agreement between the two models. An exact match was not expected, as HEC-RAS uses different governing equations (the St Venant equations) and handles stresses at the bed differently (using a roughness parameterisation).

The FV-DANS model was tested for laminar porous media flows in a homogeneous domain. The hydraulic properties (intrinsic permeability, k_i and porosity, ϕ) were varied over the ranges typically expected for alluvial aquifers and streambeds.

For flows with $Re_p < 0.1$ (where Re_p was the porous Reynolds number, defined from the hydraulic properties) the modelled hydraulic gradients for flows with a range of permeabilities and velocities were an exact match to the values expected

from Darcy's Law. With higher values of Re_p the modelled hydraulic gradient deviated from the Darcy's Law value. This upper limit for Darcian flow was consistent with published values.

Varying the porosity of the porous medium changed the pore velocity, but had no effect on the Darcy velocity (i.e. the mass flux), as expected.

With a step-change in permeability there was a corresponding change in the pressure gradient. With a step-change in porosity there was a corresponding change in the pore velocity, and the pressure gradient remained the same.

Having established that the FV-DANS model was capable of simulating both clear-fluid and porous media flows, the model was set up to replicate the "gaining stream" and "losing stream" configurations that were physically modelled in the laboratory.

For the gaining configuration it was necessary to specify both pressure and velocity boundary conditions at the inlet boundary. In order to set a physically-reasonably pressure boundary condition that was compatible with the measured boundary velocities it was necessary to adjust the permeability of the subsurface layer upwards from the measured value. This indicated that either the permeability testing of the transparent soil was inaccurate, or that the behaviour of the transparent soil in the laboratory flume was not consistent with it's behaviour in the test-cell.

The key features of the mean flow were predicted well by model: strong vertical flow through the interface at the upstream end of the domain; horizontal motion in the subsurface layer that dissipated with distance downstream; and surface velocity profiles that evolved with distance downstream in response to the mass and momentum fluxes through the interface.

The FV-DANS model failed to replicate the measured flows for the losing configuration, as it was unable to reproduce the unusual behaviour of the surface flow at the downstream end of the domain, where the flow in the laboratory flume appeared to be recirculating. The numerical model became unstable before reaching steady-state. With a lower outflow velocity, however, the model was able to reproduce some of the key flow features of the losing configuration.

Although the trends in the turbulence statistics were correctly simulated by the model for both the gaining and losing configurations, the magnitudes of TKE

and Reynolds Stress were substantially higher than those calculated from the laboratory data in regions with strong vertical flow across the interface. Away from these regions, the magnitudes of the turbulent statistics were a much closer match to the laboratory values.

A sensitivity analysis showed that varying the mid-point parameter, a, for the turbulence damping function, and the vertical flow adjustment, c_v, in the mixing length calculation had a relatively large effect on the TKE values where there was strong vertical flow. This effect diminished with distance downstream, however, and the overall effect on the mean flows was minor. From the sensitivity analysis it can be inferred that the main effect of the mismatch between laboratory and numerical TKE values was on the shape of the surface velocity profiles as they evolved.

The fact that the FV-DANS model was able to replicate the key flow features for the gaining configuration (and at least in part for the losing configuration), and was able to simulate the transition between laminar and turbulent flow, gives a good degree of confidence that the model will be applicable to naturally-occurring groundwater - surface water interactions. In a real-world setting the spatial gradients of hydraulic properties are typically less severe, and the subsurface flow velocities are generally lower.

Chapter 8

Conclusions and Recommendations

8.1 Conclusions

The overall objective of this thesis was to determine whether it is feasible to model interacting groundwater and surface water flows in a single domain with a single system of governing equations.

The ability to model groundwater and surface water as two components of a single resource is vital for robust catchment management. This is widely acknowledged, however the range of modelling tools available reflects the fact that groundwater and surface water were traditionally managed separately, and that the methods for modelling each evolved in parallel. Fully saturated groundwater flows are typically modelled using a governing equation derived from Darcy's Law. Surface water flows are typically modelled using the Shallow Water Equations, or an approximation thereof.

More recently, coupled models that attempt to simulate interactions between groundwater and surface water flows have been developed. These models use the traditional governing equations, and attempt to couple two sub-domains. Research in this area has been dominated by attempts to improve the coupling methods. However, this approach neglects certain aspects of the physics at the interface between the surface and subsurface flow. Coupled models typically ignore momentum conservation at the interface, and can perform poorly in terms

of mass-conservation at the interface.

It can be shown that the traditional governing equations for both surface and subsurface flow can be derived from the Navier-Stokes Equations. In both cases this involves a spatial average; if the flow is turbulent a time-average is also required. To derive the Shallow Water Equations the averaging is done in time and over the depth of the flow. For the groundwater flow equation, averaging over a representative volume of the porous medium allows the medium to be treated as a continuum, and removes the need to know the internal geometry of the pore space (as would be the case if the flow was being modelled with the Navier-Stokes Equations).

The concept of double-averaging allows the same averaging process, both temporally and spatially, to be applied to both clear-fluid and porous media flows. When the Navier-Stokes Equations are double-averaged (which is equivalent to spatially-averaging the Reynolds-averaged Navier-Stokes Equations), additional surface integral terms arise from the spatial averaging process. These can be parameterised to represent viscous drag and form drag in the porous medium and at the interface. In a clear-fluid flow the drag terms are negligible if appropriate value of the hydraulic properties are specified.

8.1.1 Numerical model development

A finite-volume implementation of the Double-Averaged Navier-Stokes (DANS) Equations was developed. This model is referred to in the thesis as the FV-DANS model. The key novel feature of the FV-DANS model is its ability to handle laminar porous media flow and turbulent clear-fluid flow in the same simulation, using the same governing equations.

The finite-volume method was chosen for the model as it the conventional choice for computational fluid dynamic (CFD) models; the FV-DANS model has more in common with CFD models than traditional hydraulic models. In addition, an analogy can be drawn between the finite volume method, which treats a cell-centre value of a variable as being representative of the variable over the entire cell, and the double-averaging methodology, which averages the governing equations over a representative volume (or a representative area for the

2D case). There is a trend towards using the finite-volume method in groundwater modelling, as it offers greater mesh flexibility and has better mass-conservation performance than the finite difference and finite elements that have been used traditionally.

Like the Reynolds-averaged Navier-Stokes (RANS) Equations, the DANS equations contain turbulent stress terms that arise from the time-averaging process. The presence of these terms creates a closure problem, which necessitates the use of a turbulence model. In the FV-DANS model the Kolmogorov-Prandtl single-equation model was used. This model has a transport equation for the turbulent kinetic energy (TKE), and an estimate of the turbulence mixing length is used to calculate the turbulent viscosity.

The additional surface integral terms that arise out of volume-averaging the RANS equations represent viscous drag and form drag forces in a porous medium. These terms were parameterised using Darcy's Law and the Forchheimer equation respectively. With appropriately-specified hydraulic properties these terms are negligible in a clear-fluid flow.

In order to show that the FV-DANS model was capable of simulating flows in mixed domains, containing both porous and clear-fluid flows, it was first necessary to show that the model performed well for clear-fluid and porous-media flows individually. The FV-DANS model was run for a range of clear-fluid and porous flow scenarios that could be verified against published data, analytical solutions or existing equivalent models.

For a turbulent clear-fluid flow between two parallel plates the FV-DANS model produced mean flow and turbulence results that were identical to a finite-volume RANS model, showing that (at least for this relatively simple case) the DANS equations revert back to the RANS equations for clear-fluid flows. The RANS model had been developed as an intermediate step towards development of the FV-DANS model, and had been verified against published data. Using the RANS model the single-equation turbulence model had been compared to the commonly-used $k - \epsilon$ model and was found to give similar results.

To handle the free-surface boundary a rigid-lid approach with a mass-flux correction term was used in the FV-DANS model. This method does not allow for detailed computation of the free-surface geometry, but was considered

appropriate for showing the feasibility of the single-domain approach. Energy grade-line slopes for a range of free-surface flows were compared to results from equivalent scenarios run in the 1D hydraulic model HEC-RAS. The results from the two models matched to within ±15%, which was considered reasonable given that the dimensionality and governing equations of HEC-RAS are different to the FV-DANS model.

Testing the FV-DANS model with a homogeneous porous domain showed that for values of $Re_p < 1$ (where Re_p is a porous Reynolds Number based on the hydraulic properties) the hydraulic gradients predicted by the model were an exact match to the values expected from Darcy's Law. Above this threshold value of Re_p the non-linear form-drag term caused the modelled gradient to deviate from Darcy's Law. The upper threshold for Darcian flow was consistent with published values.

When discontinuities in hydraulic properties (i.e. step-changes in permeability or porosity) were introduced into the domain the model behaved as expected, with corresponding changes to the pressure gradient or pore velocity, as appropriate.

Interacting groundwater and surface water flows typically involve a transition between laminar and turbulent flows. In computational fluid dynamics modelling, however, it is more usual to specify *a priori* whether the flow being modelled is laminar or turbulent throughout the domain. Methods for handling the boundary conditions for turbulence transport equations are typically based on impermeable, no-slip boundaries. One of the key novel contributions of this thesis was the development of a "turbulence damping function" approach that allowed the model to determine an effective bed level, i.e. the point at which the porous medium had a wall-like effect on the free-surface flow. Below this point the turbulence model was still solved, but the damping function was used to ensure that TKE production and the turbulent viscosity were suppressed.

8.1.2 Physical modelling

Although the primary focus of this thesis was on numerical modelling, an experimental programme was conducted in order to collect a set of detailed velocity-field and turbulence data that could be compared to the numerical model results.

An experimental technique was developed that allowed two-dimensional velocity fields to be measured in interacting surface and subsurface flows, using a novel combination or a refractive-index-matched transparent soil material and particle tracking velocimetry (PTV).

Experiments representing a river flow over a shallow aquifer were set up in a glass-walled laboratory flume, with a free-surface flow over a layer of the transparent soil. Boundary conditions in the flume were adjusted to simulate both gaining and losing streamflows. The gaining configuration produced a zone of strong upwards vertical flow at the upstream end of the porous layer, and the losing configuration produced a zone of strong downwards flow at the downstream end of the layer.

By illuminating a vertical cross-section of the flow using a light-sheet, the motion through the pore-spaces in the subsurface layer could be observed and measured in a plane approximately one surface flow depth in from the flume wall.

Analysis of the PTV data also allowed turbulent statistics to be calculated for the surface component of the flows. Although the subsurface flow appeared turbulent in some areas, it was not considered feasible to calculate turbulent statistics for the subsurface layer, as the analysis was unable to distinguish between temporal velocity fluctuations caused by turbulence and spatial fluctuations caused by the internal geometry of the porous medium.

The experimental flows were shown to be stable and repeatable. Flux balances were calculated for the measured velocity fields to ensure that the PTV analysis produced meaningful results for both the surface and subsurface components of the flow.

Averaging individual image frames from a long steady-state experimental run was approximately equivalent to a Reynolds-averaging process. Various options for spatial interpolation of the velocity fields were investigated in order to strike a balance between capturing the key features of the velocity field, and ensuring

that there was sufficient data in the interpolation region to provide meaningful time-averages. In the surface layer, which was more densely seeded with tracking particles, the default spatial interpolation method, triangulation, was used. In the subsurface layer a "binning" method was used, where a rectangular region was defined around each grid point. This was successful with a bin size of 40 mm. This was considered large enough relative to the grain diameter of the transparent soil (approximately 10 mm) for the subsurface velocity fields to be interpreted as double-averaged values.

The mean flow results for the gaining configuration showed that horizontal motion in the subsurface layer was mainly confined to a region extending approximately four surface flow depths downstream of the inflow boundary. The majority of the vertical exchange across the surface - subsurface interface occurred within the first two surface flow depths.

For the losing configuration the highest velocities in the subsurface layer were concentrated in a region extending approximately three surface flow depths upstream from the outflow boundary. High vertical velocities occurred over a similar region. The subsurface flow velocities were substantially higher than for the gaining configuration: up to 60% of the flux velocity. The surface flows in the losing configuration were strongly influenced by the downstream boundary in the flume: towards the downstream end of the porous layer the velocities at the free-surface appeared to be modified by a large-scale eddy or recirculation downstream of the measurement window.

For both the gaining and losing configurations the mean flow profiles and turbulent statistics in the surface layer were heavily modified in the regions where there were strong exchange flows across the surface - subsurface interface.

8.1.3 Comparison of laboratory and numerical results

Having shown that the FV-DANS model performed well for clear-fluid and porous-media flows individually, the model was then set up to simulate the gaining stream and losing stream configurations that were run in the laboratory flume. As some of the conditions in the laboratory flume were highly challenging to replicate in the numerical model, the focus of this phase of the investigation was to replicate

the key features of the flow, rather than to achieve an exact match at any given point of the domain.

For the FV-DANS model to successfully replicate the key features of the gaining configuration it was necessary to adjust the permeability, k_i upwards from the value measured in the laboratory for the transparent soil material. With this adjustment, the model results were a good match in terms of peak vertical flows, the overall effect on the surface flow downstream, and the regions of the subsurface layer in which the flow was concentrated.

In the region with strong vertical flow across the surface - subsurface interface, the TKE predicted by the model was substantially higher than the values calculated from the laboratory data. Away from this region, however, the modelled TKE values were consistent with the laboratory values. The modelled TKE was shown to be relatively sensitive to the turbulence-transition parameters in the region with strong vertical flow. The effect of this on the mean flows was minimal, however.

The exact causes of the model stability issues that resulted in the FV-DANS model being unable to replicate the "losing stream" laboratory results are unclear. The need for complicated boundary conditions (due to the influences of boundaries in the laboratory flume) is likely to be a factor, as are the rapid transition from turbulent to laminar flow and the discontinuities in the hydraulic properties.

Although the model failed to replicate the "losing stream" laboratory configuration with the measured outflow velocities, it was able to reproduce the key features of the flow with lower velocities, and was also able to simulate the "gaining stream" configuration well. This gives confidence that the FV-DANS model will be applicable to naturally-occurring stream-aquifer interactions, which typically have less extreme gradients in hydraulic properties and lower vertical velocities across the interface.

8.2 Recommendations for Further Work

While the results presented in this thesis show the feasibility of the single-domain approach using the DANS equations for modelling interacting groundwater and surface-water flows, a number of further developments are required to make the model capable of modelling natural flows.

The FV-DANS model is currently able to simulate flow in a two-dimensional vertical slice through a free-surface flow and the underlying porous material. This dimensionality does not allow the model to account for the shape of the river cross-section. At a catchment or reach scale, a gaining or losing stream will typically result in horizontal flow in the shallow aquifer, perpendicular to the channel centre-line in the $x - y$ plane. The model cannot currently handle this. Extending the model to three spatial dimensions would resolve these issues.

The method currently used to handle the free-surface boundary condition constrains the free-surface to the top row of mesh cells. Using a more sophisticated approach such as volume-of-fluid (VOF) would allow the model to handle scenarios with more variable free-surface geometry, such as wetting and drying of a river channel.

The FV-DANS model can currently handle the fully-connected case of groundwater - surface water interactions, where the porous material underlying the surface flow remains fully saturated. Incorporating variably-saturated flow into the model would make it more able to handle natural coupled flow systems.

As the FV-DANS model does not use a traditional bed-roughness treatment at the surface-subsurface interface, further work is required to understand the relationship between the parameterisations that were used for drag forces (including how the conductivity and porosity are transitioned at the interface), and traditional approaches to specifying bed roughness. Understanding this relationship would help to give users of existing modelling approaches greater confidence in transitioning to the DANS approach.

There is significant scope for further experimental and numerical investigation on the transition between turbulent and laminar flows. More detailed laboratory measurements with data collected closer to the surface - subsurface interface may shed light on how the mixing length should be handled where there is strong

vertical flow. Alternatively, incorporating a more sophisticated turbulence model may remove the reliance on a mixing length estimate.

As the focus of this thesis has been on demonstrating the feasibility of a single-domain approach for modelling groundwater - surface water interactions, the numerical method and solver algorithm have not been optimised. There is scope for improvements in these to be investigated. For modelling larger-scale natural systems in three spatial dimensions, more advanced computational resources (either a multi-processor desktop computer or a high-performance computing facility) should also be considered. This may require changes to the model to allow for parallel processing.

Water quality is highly interconnected with water quantity. In addition to modelling water flows to set limits on abstractive use, it is becoming increasingly important to model transport of nutrients and other contaminants in order to set limits on their use in catchments. Existing tools for modelling contaminant transport are less integrated than water flow modelling tools: currently separate contaminant transport models are used for groundwater and surface water. Because the FV-DANS model contains a double-averaged transport equation for turbulent kinetic energy, which is based on a general scalar advection - diffusion equation, the numerical foundations for being able to model contaminant transport are already present in the model.

Appendices

Appendix A

Reynolds averaging of the Navier-Stokes Equations

For an arbitrary variable, a, applying a Reynolds decomposition results in:

$$a = A + a' \tag{A.1}$$

where A is the mean part of a, and a' is the temporal fluctuation around the mean.

The mean component A in Equation A.1 is strictly defined as an ensemble average (i.e. sampling many repeated experiments at the same time and position), which is defined as:

$$\overline{a}(x,t) = A(x,t) = \frac{1}{N}\sum_{n=1}^{N} a_n(x,t) \tag{A.2}$$

where the overline ($\overline{a}$) represents the Reynolds averaging operator. In practice it is seldom possible to obtain a meaningful ensemble average, and therefore A is

normally defined as a time-average:

$$\overline{a}(x,t) = A(x,t) = \frac{1}{T}\int_{t_0}^{t_0+T} a(x,t)dt \tag{A.3}$$

The time-average in Equation A.3 is an acceptable substitute for the ensemble average in Equation A.2 so long as it is possible to choose the time-scale T so that it is long compared to the time-scale of the fluctuations (a'), but short compared to the time-scale of any changes to the mean.

The following rules apply to Reynolds-averaged variables:

$$\begin{aligned}
\overline{A} &= A && \text{(A.4)}\\
\overline{\overline{a}b} &= \overline{a}\overline{b} && \text{(A.5)}\\
\overline{a'} &= \overline{a - A} = \overline{a} - A = A - A = 0 && \text{(A.6)}\\
\overline{\frac{\partial a}{\partial x_i}} &= \frac{\partial \overline{a}}{\partial x_i} = \frac{\partial A}{\partial x_i} && \text{(A.7)}\\
\overline{Ca} &= C\overline{a} = CA && \text{(A.8)}\\
\overline{ab} &= \overline{(A+a')(B+b')} = \overline{AB + a'B + b'A + a'b'} && \text{(A.9)}\\
&= AB + \overline{a'B} + \overline{b'A} + \overline{a'b'} = AB + \overline{a'b'}
\end{aligned}$$

where a and b are variables and C is a constant.

Applying Equation A.7 to the continuity equation gives:

$$\overline{\frac{\partial u_i}{\partial x_i}} = \frac{\partial}{\partial x_i}\overline{u_i} = \frac{\partial U_i}{\partial x_i} = 0 \tag{A.10}$$

Thus the divergence of the Reynolds-averaged continuity equation is also zero, i.e. it is incompressible.

Using Equations A.7 and A.6, it can also be shown that the divergence of the fluctuating component of the continuity equation is zero:

$$\overline{\frac{\partial u_i'}{\partial x_i}} = \frac{\partial}{\partial x_i}\overline{u_i - U_i} = 0 \tag{A.11}$$

This result can be used later in the averaging of the momentum equations.

Applying a Reynolds average to each term in the momentum equations, and then applying the averaging rules gives:

$$\overline{\frac{\partial u_i}{\partial t}} + \overline{u_j \frac{\partial u_i}{\partial x_j}} = -\frac{1}{\rho}\overline{\frac{\partial p}{\partial x_i}} + \nu\overline{\frac{\partial^2 u_i}{\partial x_j \partial x_j}} \tag{A.12}$$

$$\frac{\partial U_i}{\partial t} + U_j \frac{\partial U_i}{\partial x_j} + \overline{u'_j \frac{\partial u'_i}{\partial x_j}} = -\frac{1}{\rho}\frac{\partial P}{\partial x_i} + \nu\frac{\partial^2 U_i}{\partial x_j \partial x_j} \tag{A.13}$$

The additional term containing velocity fluctuations arises in Equation A.13 as a result of applying the averaging rules rule for products of variables (Equation A.10). This term can be re-written as follows using the product rule and the fact that the divergence of the fluctuating component of the continuity equation is zero:

$$\begin{aligned} \overline{u'_j \frac{\partial u'_i}{\partial x_j}} &= \frac{\partial}{\partial x_j}\overline{u'_i u'_j} - \overline{u'_i \frac{\partial u'_j}{\partial x_j}} \\ &= \frac{\partial}{\partial x_j}\overline{u'_i u'_j} \end{aligned} \tag{A.14}$$

Therefore Equation A.13 can be re-written as follows:

$$\frac{\partial U_i}{\partial t} + U_j \frac{\partial U_i}{\partial x_j} = -\frac{1}{\rho}\frac{\partial P}{\partial x_i} + \frac{\partial}{\partial x_j}\left(\nu\frac{\partial U_i}{\partial x_j} - \overline{u'_i u'_i}\right) \tag{A.15}$$

Multiplying Equation A.15 by the density ρ (which is assumed to be constant in time and space) gives the momentum equation in the format that has been used in the numerical model:

$$\rho\frac{\partial U_i}{\partial t} + \rho U_j \frac{\partial U_i}{\partial x_j} = \frac{\partial P}{\partial x_i} + \frac{\partial}{\partial x_j}\left(\mu\frac{\partial U_i}{\partial x_j} - \rho\overline{u'_i u'_i}\right) \tag{A.16}$$

Equations A.10 and A.16 are known as the Reynolds-averaged Navier-Stokes (or RANS) equations. They are the governing equations for the time-averaged

velocity and pressure fields in a turbulent flow.

The term $\rho\overline{u_i' u_i'}$ in Equation A.16 is known as the turbulent stress, or Reynolds Stress. It is dominant over the viscous stresses in turbulent flows. The additional variables that appear in the RANS equations create a closure problem (i.e. there are more unknowns than equations). This necessitates a model for the turbulent stresses. Turbulence models are also referred to as closure schemes.

Appendix B

Derivation of the DANS equations

The Double-averaged Navier-Stokes (DANS) Equations can be derived using the RANS equations as a starting point. Nikora et al. (2007a) discuss the differences between time-space and space-time averaging, and conclude that time-space averaging is more appropriate for modelling rough-bed flows. It is assumed that this also applies to coupled surface - subsurface flows, and that the volume averaging can be done as an extension to the traditional Reynolds averaging process.

The DANS equations are derived from the RANS equations by decomposing Reynolds-averaged variables into spatially-averaged and spatially-fluctuating components. Two averaging theorems, the volume-averaging theorem and the general transport equation (Whitaker, 1967) are then applied to each term in the continuity and momentum equations as appropriate. The Reynolds averaging rules (see Appendix A) also apply to the spatial averaging process.

The spatial decomposition is as follows:

$$A = \langle A \rangle + \tilde{U} \tag{B.1}$$

where $\langle A \rangle$ is the spatially-averaged component and $\tilde{U}$ is the spatially-fluctuating component.

The volume-averaging theorem for an arbitrary variable θ is as follows:

$$\langle \frac{\partial \theta}{\partial x_i} \rangle = \frac{1}{\phi} \frac{\partial \phi \langle \theta \rangle}{\partial x_i} - \frac{1}{V_f} \iint\limits_{S_{int}} \theta n_i dS \tag{B.2}$$

and the transport theorem is:

$$\langle \frac{\partial \theta}{\partial t} \rangle = \frac{1}{\phi} \frac{\partial \phi \langle \theta \rangle}{\partial t} - \frac{1}{V_f} \iint\limits_{S_{int}} \theta v_i n_i dS \tag{B.3}$$

where ϕ is the porosity, V_f is the volume of fluid in the averaging volume, $S_i nt$ is the surface of the fluid-solid interface contained within the averaging volume, and v_i is the velocity of the fluid-solid interface.

B.1 The continuity equation

The Reynolds-averaged form of the continuity equation for an incompressible fluid of constant density is:

$$\frac{\partial U_i}{\partial x_i} = 0 \tag{B.4}$$

Applying the volume-averaging theorem gives:

$$\langle \frac{\partial U_i}{\partial x_i} \rangle = \frac{1}{\phi} \frac{\partial \phi \langle U_i \rangle}{\partial x_i} - \frac{1}{V_f} \iint\limits_{S_{int}} U_i n_i dS = 0 \tag{B.5}$$

If the solid phase of the porous matrix is impermeable the surface integral vanishes (Whitaker, 1996), leaving:

$$\frac{1}{\phi} \frac{\partial \phi \langle U_i \rangle}{\partial x_i} = 0 \tag{B.6}$$

For either porous media or clear fluid flow the porosity is expected to be in the range $0 < \phi \leq 1$, therefore in Equation B.6 $\frac{1}{\phi} \neq 0$, and the double-averaged

form of the continuity equation is:

$$\frac{\partial \phi \langle\, U_i \rangle}{\partial x_i} = 0 \tag{B.7}$$

B.2 The momentum equation

The double-averaged form of the momentum equation is derived by initially applying the averaging theorems to the RANS momentum equation term by term.

B.2.1 Local acceleration

Applying the transport theorem gives:

$$\langle \frac{\partial U_i}{\partial t} \rangle = \frac{1}{\phi} \frac{\partial \phi \langle U_i \rangle}{\partial t} - \frac{1}{V_f} \iint\limits_{S_{int}} U_i v_i n_i dS \tag{B.8}$$

Applying the product rule of differentiation to the first term on the right-hand side of Equation B.8 gives:

$$\langle \frac{\partial U_i}{\partial t} \rangle = \frac{\partial \langle U_i \rangle}{\partial t} + \frac{\langle U_i \rangle}{\phi} \frac{\partial \phi}{\partial t} - \frac{1}{V_f} \iint\limits_{S_{int}} U_i v_i n_i dS \tag{B.9}$$

B.2.2 Convective acceleration

It is assumed that the convective acceleration term can be written as follows:

$$U_j \frac{\partial U_i}{\partial x_j} = \frac{\partial U_i U_j}{\partial x_j} \tag{B.10}$$

Applying the volume averaging theorem to the right-hand side of Equation B.10 gives:

$$\langle \frac{\partial U_i U_j}{\partial x_j} \rangle = \frac{1}{\phi} \frac{\partial \phi \langle U_i U_j \rangle}{\partial x_j} - \frac{1}{V_f} \iint\limits_{S_{int}} U_i U_j n_i dS \tag{B.11}$$

The velocity terms can be decomposed into double-averaged and spatially-fluctuating components:

$$\langle U_i U_j \rangle = \langle (\langle U_i \rangle + \tilde{u_i})(\langle U_j \rangle + \tilde{u_j}) \rangle \tag{B.12}$$

Expanding out the decomposed velocity terms in Equation B.12 and substituting back into Equation B.11 gives:

$$\langle \frac{\partial U_i U_j}{\partial x_j} \rangle = \frac{1}{\phi} \frac{\partial \phi \langle U_i \rangle \langle\ U_j \rangle}{\partial x_i} + \frac{1}{\phi} \frac{\partial \phi \langle \tilde{u_i} \tilde{u_j} \rangle}{\partial x_j} + \frac{1}{\phi} \frac{\partial \phi \langle \langle U_i \rangle \tilde{u_j} \rangle}{\partial x_j} + \frac{1}{\phi} \frac{\partial \phi \langle \tilde{u_i} \langle\ U_j \rangle \rangle}{\partial x_j} - \frac{1}{V_f} \iint\limits_{S_{int}} U_i U_j n_i dS \tag{B.13}$$

Applying one of the Reynolds averaging rules ($\langle \langle a \rangle b \rangle = \langle a \rangle \langle b \rangle$), the terms in Equation B.13 containing products of double-averaged and spatially-fluctuating components can be re-written as:

$$\langle \langle U_i \rangle \tilde{u_j} \rangle = \langle U_i \rangle \langle \tilde{u_j} \rangle \tag{B.14}$$

As the mean of the fluctuating component is zero by definition (i.e. $\langle \tilde{u_j} \rangle = 0$) the terms containing products of double-averaged and spatially-fluctuating components vanish, simplifying Equation B.13 to:

$$\langle \frac{\partial U_i U_j}{\partial x_j} \rangle = \frac{1}{\phi} \frac{\partial \phi \langle U_i \rangle \langle U_j \rangle}{\partial x_i} + \frac{1}{\phi} \frac{\partial \phi \langle \tilde{u_i} \tilde{u_j} \rangle}{\partial x_j} - \frac{1}{V_f} \iint\limits_{S_{int}} U_i U_j n_i dS \tag{B.15}$$

The product rule can be applied to first term on the right-hand side of Equation B.15, with two of its factors bracketed (i.e. so that the product rule is applied as if a product of two factors, rather than three, is being differentiated):

$$\frac{1}{\phi} \frac{\partial \langle U_i \rangle (\phi \langle\ U_j \rangle)}{\partial x_i} = \frac{1}{\phi} \left(\phi \langle U_j \rangle \frac{\partial \langle U_i \rangle}{\partial x_i} + \langle U_i \rangle \frac{\partial \phi \langle U_j \rangle}{\partial x_i} \right) \tag{B.16}$$

A result from the derivation of the double-averaged continuity equation (Equation B.5) allows the second term on the right-hand side of Equation B.16 to be

replaced by a surface integral:

$$\frac{1}{\phi}\frac{\partial\langle U_i\rangle(\phi\langle U_j\rangle)}{\partial x_i} = \phi\langle U_j\rangle\frac{\partial\langle U_i\rangle}{\partial x_i} + \frac{\langle U_i\rangle}{V_f}\iint\limits_{S_{int}} U_j n_i dS \tag{B.17}$$

Putting the modified terms back into the expression for the double-averaged convective acceleration (Equation B.15) gives:

$$\langle\frac{\partial U_i U_j}{\partial x_j}\rangle = \phi\langle U_j\rangle\frac{\partial\langle U_i\rangle}{\partial x_i} + \frac{\langle U_i\rangle}{V_f}\iint\limits_{S_{int}} U_j n_i dS + \frac{1}{\phi}\frac{\partial\phi\langle\tilde{u}_i\tilde{u}_j\rangle}{\partial x_j} - \frac{1}{V_f}\iint\limits_{S_{int}} U_i U_j n_i dS \tag{B.18}$$

B.2.3 Gravity term

The gravity term in the momentum equation is not altered by double-averaging:

$$\langle g_i\rangle = g_i \tag{B.19}$$

B.2.4 Pressure term

Applying the volume-averaging theorem to the pressure-gradient term in the RANS momentum equation gives:

$$\frac{1}{\rho}\langle\frac{\partial P}{\partial x_i}\rangle = \frac{1}{\rho}\left(\frac{1}{\phi}\frac{\partial\phi\langle P\rangle}{\partial x_i} - \frac{1}{V_f}\iint\limits_{S_{int}} P n_i dS\right) \tag{B.20}$$

B.2.5 Viscous stress term

Applying the volume-averaging theorem to the viscous-stress term in the RANS equations gives:

$$\langle \frac{\partial}{\partial x_j}\left(\nu \frac{\partial U_i}{\partial x_j}\right)\rangle = \frac{1}{\phi}\frac{\partial}{\partial x_j}\left(\phi\langle \nu \frac{\partial U_i}{\partial x_i}\rangle\right) - \frac{1}{V_f}\iint\limits_{S_{int}}\left(\nu \frac{\partial U_i}{\partial x_j}\right) n_i dS \tag{B.21}$$

B.2.6 Reynolds stress term

Applying the volume-averaging theorem to the Reynolds stress term in the RANS equations gives:

$$\langle \frac{\partial \overline{u_i' u_j'}}{\partial x_j}\rangle = \frac{1}{\phi}\frac{\partial \phi \langle \overline{u_i' u_j'}\rangle}{\partial x_j}\rangle - \frac{1}{V_f}\iint\limits_{S_{int}} \overline{u_i' u_j'} n_i dS \tag{B.22}$$

B.2.7 Combined double-averaged momentum equation terms

The double-averaged forms of all the terms in the RANS momentum equation can now be combined to give:

$$\underbrace{\frac{\partial\langle U_i\rangle}{\partial t} + \langle U_i\rangle\frac{\partial\phi}{\partial t} - \frac{1}{V_f}\iint\limits_{S_{int}} U_i v_i n_i dS}_{\text{local acceleration}}$$

$$+ \underbrace{\langle U_j\rangle\frac{\partial\langle U_i\rangle}{\partial x_j} + \frac{\langle U_i\rangle}{V_f}\iint\limits_{S_{int}} U_j n_i dS + \frac{1}{\phi}\frac{\partial\phi\langle\tilde{u}_i\tilde{u}_j\rangle}{\partial x_j} - \frac{1}{V_f}\iint\limits_{S_{int}} U_i U_j n_i dS}_{\text{convective acceleration}}$$

$$= g_i + \underbrace{\frac{1}{\rho}\left(\frac{1}{\phi}\frac{\partial\phi\langle P\rangle}{\partial x_i} - \frac{1}{V_f}\iint\limits_{S_{int}} P n_i dS\right)}_{\text{pressure gradient}} + \underbrace{\frac{1}{\phi}\frac{\partial}{\partial x_j}\phi\langle\nu\frac{\partial U_i}{\partial x_j}\rangle - \frac{1}{V_f}\iint\limits_{S_{int}}\left(\nu\frac{\partial U_i}{\partial x_j}\right) n_i dS}_{\text{viscous stress}}$$

$$\underbrace{- \frac{1}{\phi}\frac{\partial\phi\langle\overline{u_i' u_j'}\rangle}{\partial x_j}\rangle - \frac{1}{V_f}\iint\limits_{S_{int}}\overline{u_i' u_j'} n_i dS}_{\text{Reynolds stress}} \quad \text{(B.23)}$$

Re-arranging Equation B.23 to group all the integral terms together gives:

$$\begin{aligned}
&\frac{\partial\langle U_i\rangle}{\partial t} + \langle U_i\rangle\frac{\partial\phi}{\partial t} + \phi\langle U_j\rangle\frac{\partial\langle U_i\rangle}{\partial x_i} \\
&\qquad = g_i + \frac{1}{\rho\phi}\frac{\partial\phi\langle P\rangle}{\partial x_i} + \frac{1}{\phi}\frac{\partial}{\partial x_j}\phi\langle\nu\frac{\partial U_i}{\partial x_i}\rangle - \frac{1}{\phi}\frac{\partial\phi\langle\overline{u_i' u_j'}\rangle}{\partial x_j}\rangle - \frac{1}{\phi}\frac{\partial\phi\langle\tilde{u}_i\tilde{u}_j\rangle}{\partial x_j} \\
&\qquad\qquad - \frac{1}{\rho V_f}\iint\limits_{S_{int}} P n_i dS + \frac{1}{V_f}\iint\limits_{S_{int}}\left(\nu\frac{\partial U_i}{\partial x_j}\right) n_i dS \\
&+ \frac{1}{V_f}\iint\limits_{S_{int}} U_i v_i n_i dS - \frac{\langle U_i\rangle}{V_f}\iint\limits_{S_{int}} U_j n_i dS + \frac{1}{V_f}\iint\limits_{S_{int}} U_i U_j n_i dS + \frac{1}{V_f}\iint\limits_{S_{int}}\overline{u_i' u_j'} n_i dS
\end{aligned} \quad \text{(B.24)}$$

If the solid fraction of the porous medium is impermeable then all of the integral terms on the bottom line of B.24 are zero, and if the porous medium is assumed to be immobile then porosity does not change over time (i.e. $\frac{\partial\phi}{\partial t} = 0$).

This allows Equation B.24 to be simplified to:

$$\frac{\partial\langle U_i\rangle}{\partial t} + \phi\langle U_j\rangle\frac{\partial\langle U_i\rangle}{\partial x_i} = g_i + \frac{1}{\rho\phi}\frac{\partial\phi\langle P\rangle}{\partial x_i} + \frac{1}{\phi}\frac{\partial}{\partial x_j}\phi\langle\nu\frac{\partial U_i}{\partial x_i}\rangle - \frac{1}{\phi}\frac{\partial\phi\langle\overline{u_i'u_j'}\rangle}{\partial x_j}\rangle - \frac{1}{\phi}\frac{\partial\phi\langle\tilde{u}_i\tilde{u}_j\rangle}{\partial x_j} - \frac{1}{\rho V_f}\iint\limits_{S_{int}} Pn_i dS + \frac{1}{V_f}\iint\limits_{S_{int}}\left(\nu\frac{\partial U_i}{\partial x_j}\right)n_i dS \quad \text{(B.25)}$$

Parameterisations are used for the remaining integral terms in Equation B.25

Appendix C

Laboratory run details

Run name	flow meter (l/s)	flux velocity (mm/s)	depths			Head gradient	Position in flume		Surface profile				
			u/s of sluice-gate	d/s of sluice-gate	in flume	dH (mm)	x upstream (mm)	x downstream (mm)	x=0 (u/s end)	x=100	x=200	x=300	x=400 (d/s end)
Gaining1 Slot 1	1.9	151.3	73	40.4	43	32.6	220	620	44.5	44.3	42.8	43.8	43
Gaining1 Slot 2	1.9	151.3	73	40.4	43	32.6	220	620	44.5	44.3	42.8	43.8	43
Gaining1 Slot 3	1.9	151.3	73	40.4	43	32.6	220	620	44.5	44.3	42.8	43.8	43
Gaining1 Bar 1	1.9	151.3	73	40.4	43	32.6	220	620	44.5	44.3	42.8	43.8	43
Gaining1 Bar 2	1.9	151.3	73	40.4	43	32.6	220	620	44.5	44.3	42.8	43.8	43
Gaining1 Bar 3	1.9	151.3	73	40.4	43	32.6	220	620	44.5	44.3	42.8	43.8	43
Gaining 2 Slot	1.8	116.7	84.2	46.7	52.8	37.5	600	1000	53.8	53.2	52.7	52.9	54.1
Gaining 2 Bar	1.8	116.7	84.2	46.7	52.8	37.5	600	1000	53.8	53.2	52.7	52.9	54.1
Losing 1 Slot	2	93.6		69.6	73.2		1410	1810	73	73.3	73.2	74.2	73.8
Losing 1 Bar	2	93.6		69.6	73.2		1410	1810	73	73.3	73.2	74.2	73.8
Losing 2 Slot	1.9	88.9		69.6	73.2		1040	1440	73	73.3	73.2	74.2	73.8
Losing 2 Bar	1.9	88.9		69.6	73.2		1040	1440	73	73.3	73.2	74.2	73.8
Impermeable 1 Slot	2.1	121.7			59.1		1000	1400					
Impermeable 1 Bar	2.1	121.7			59.1		1000	1400					
Impermeable 2 Slot	2.1	120.9			59.5		1380	1780					
Impermeable 2 Bar	2.1	120.9			59.5		1380	1780					

Appendix D

Coverage plots for PTV runs

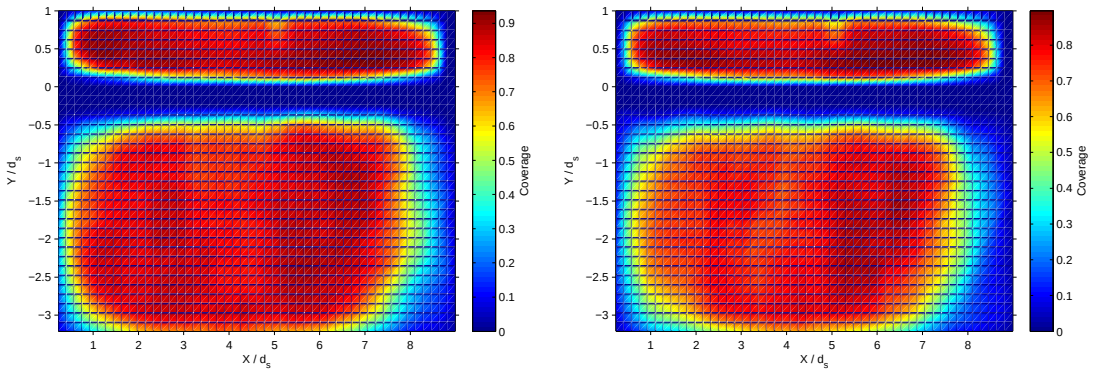

(a) Gaining 1 Slot *(b) Gaining 1 Bar*

Figure D.1: Time-averaged coverage for Gaining 1 run

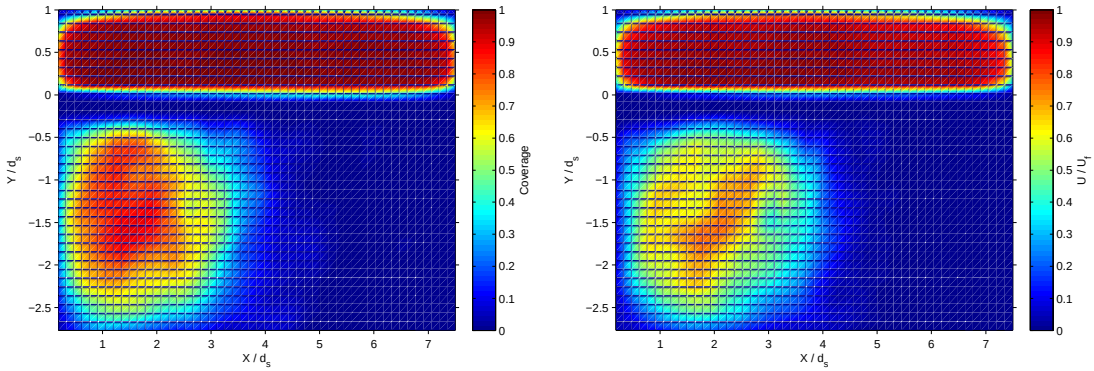

(a) Gaining 2 Slot *(b) Gaining 2 Bar*

Figure D.2: Time-averaged coverage for Gaining 2 run

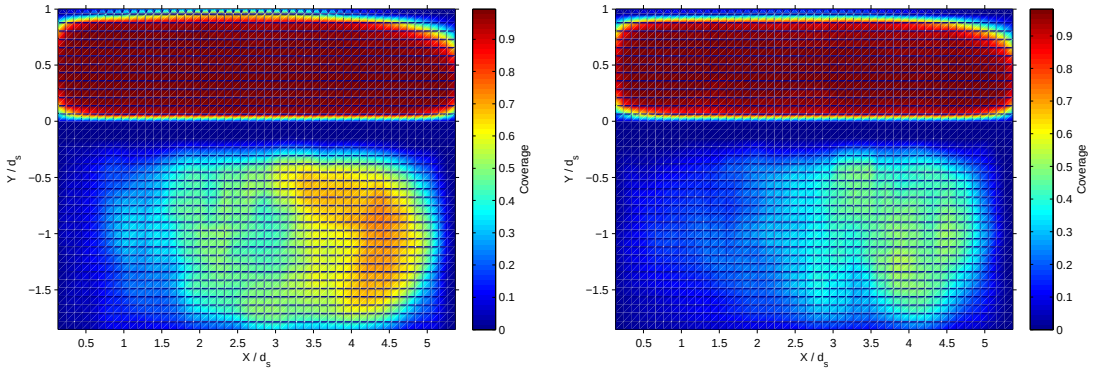

(a) Losing 1 Slot *(b) Losing 1 Bar*

Figure D.3: Time-averaged coverage for Losing 1 run

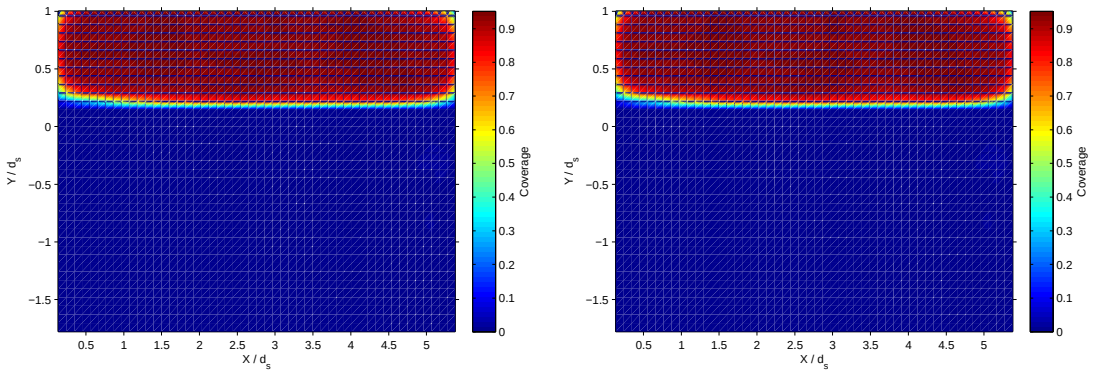

(a) Losing 2 Slot *(b) Losing 2 Bar*

Figure D.4: Time-averaged coverage for Losing 2 run

Appendix E

Turbulent viscosity and mixing length estimates from laboratory data

E.1 Mixing length

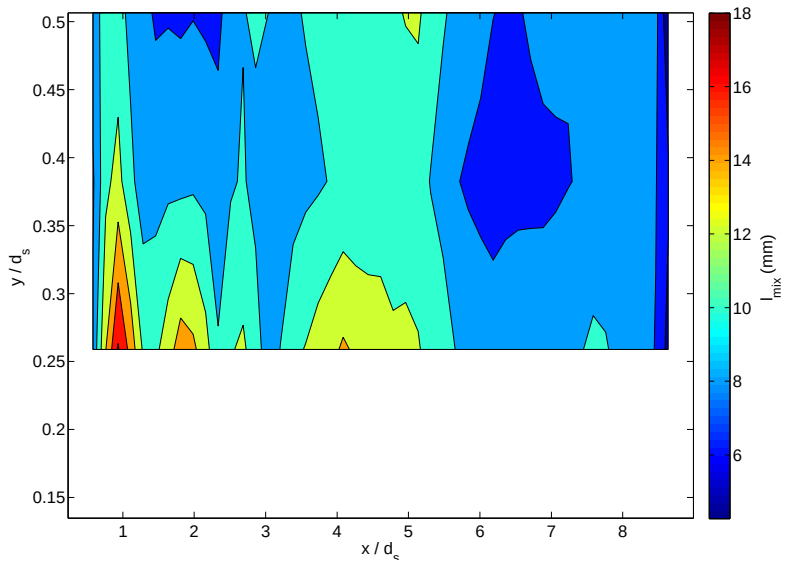

Figure E.1: Mixing length estimate from laboratory data; gaining configuration, position 1

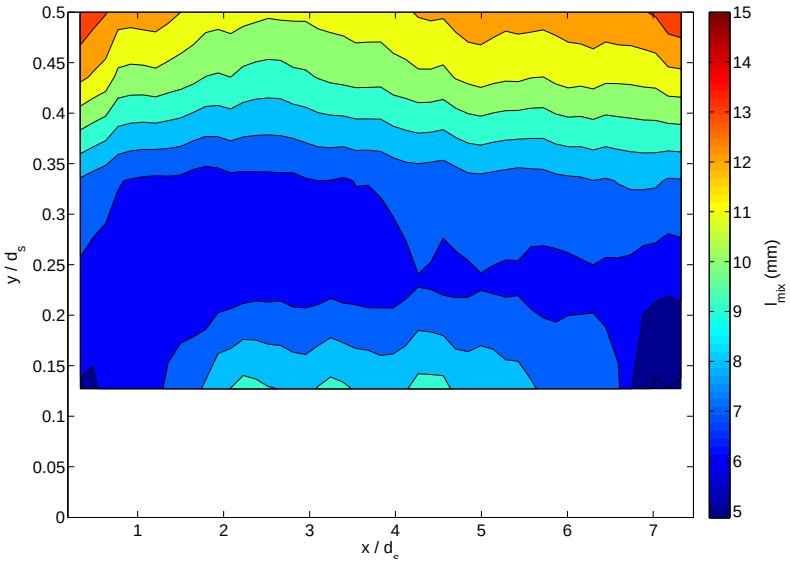

Figure E.2: Mixing length estimate from laboratory data; gaining configuration, position 2

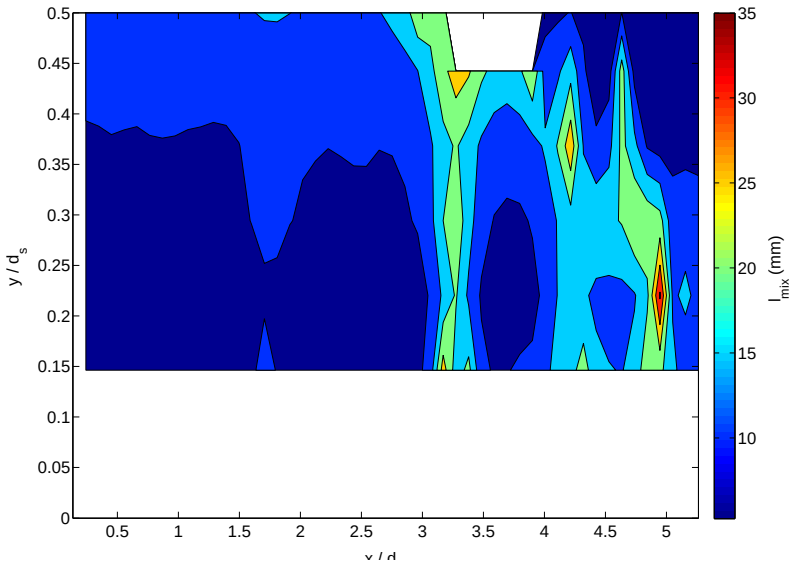

Figure E.3: Mixing length estimate from laboratory data; losing configuration, position 1

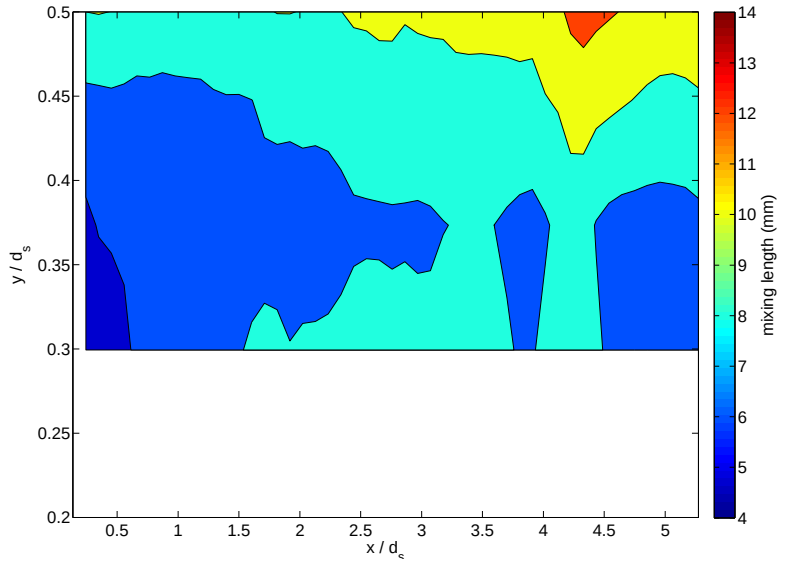

Figure E.4: Mixing length estimate from laboratory data; losing configuration, position 2

E.2 Turbulent viscosity

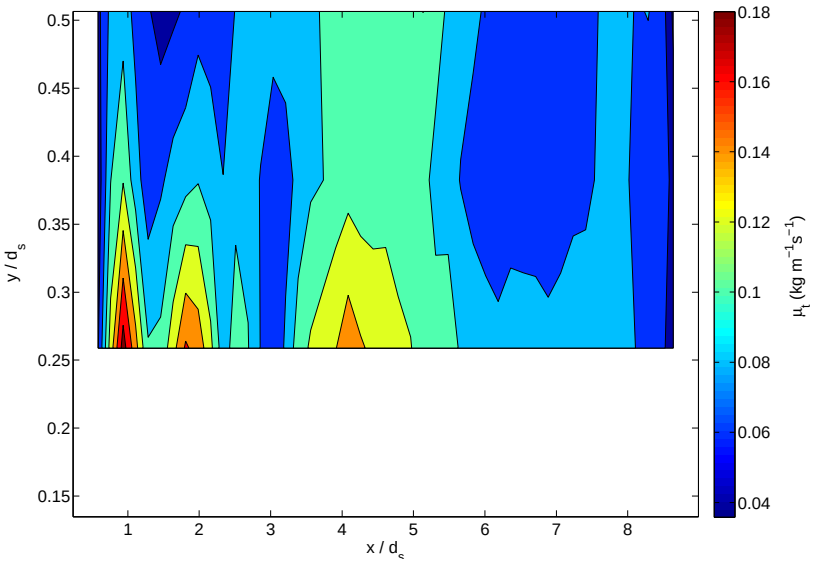

Figure E.5: Turbulent viscosity estimate from laboratory data; gaining configuration, position 1

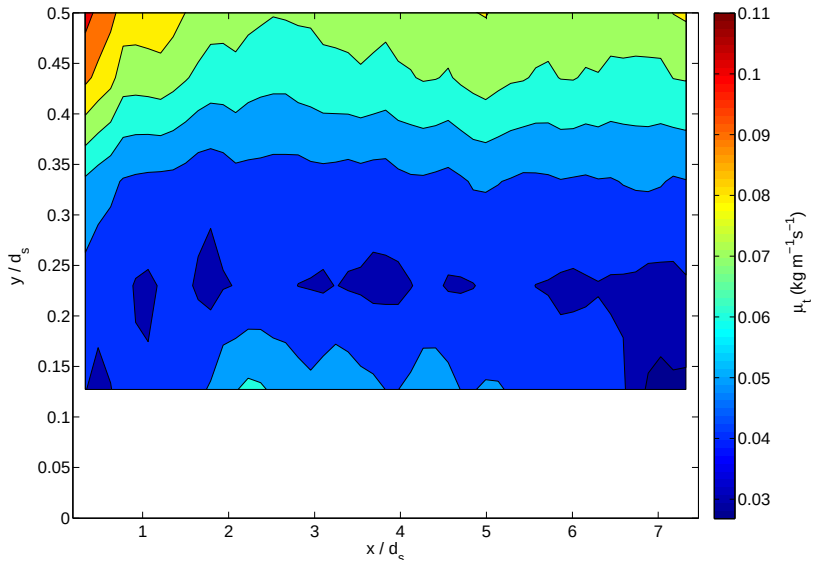

Figure E.6: Turbulent viscosity estimate from laboratory data; gaining configuration, position 2

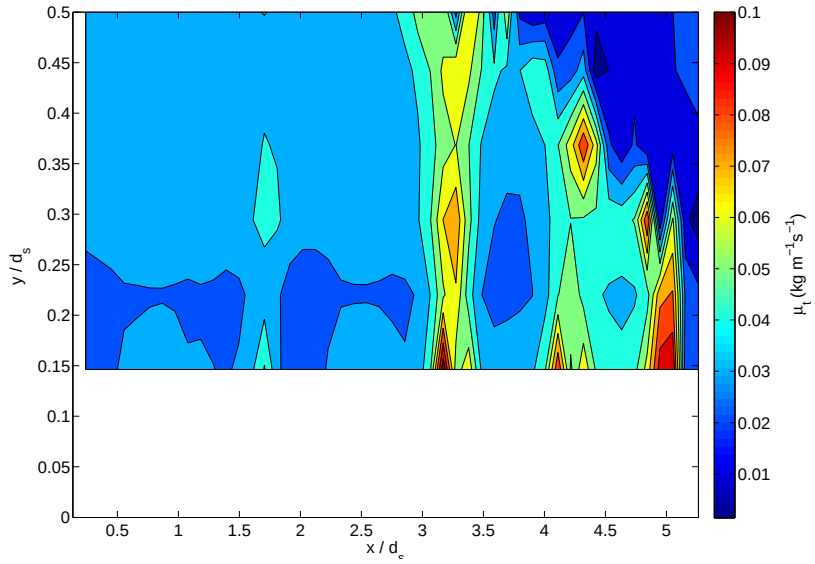

Figure E.7: Turbulent viscosity estimate from laboratory data; losing configuration, position 1

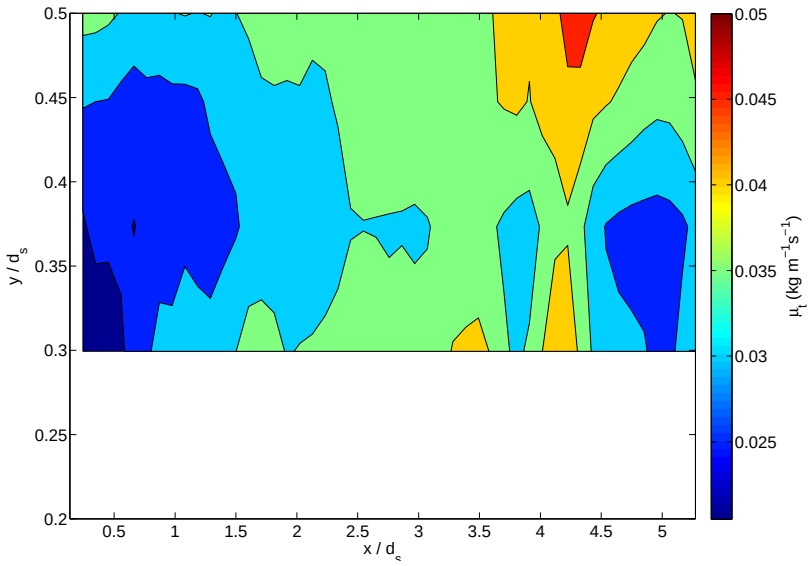

Figure E.8: Turbulent viscosity estimate from laboratory data; losing configuration, position 2

Appendix F

Modelled turbulent viscosity and mixing length

F.1 Mixing length

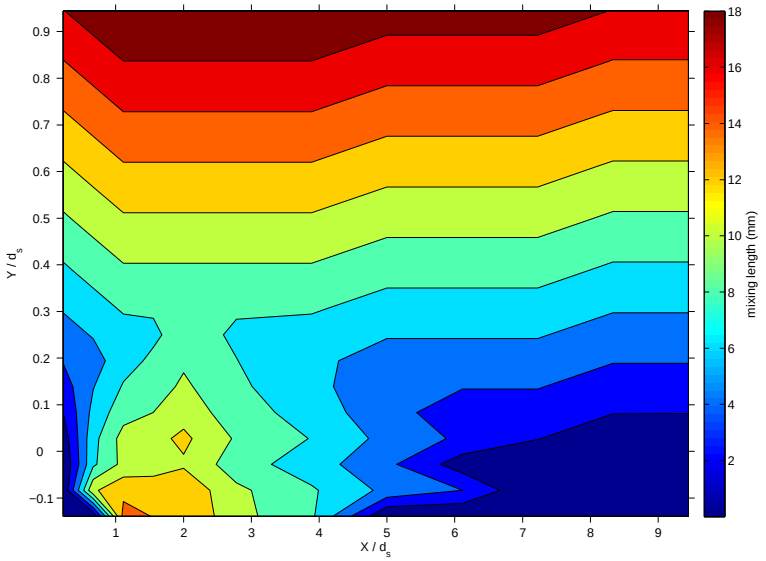

Figure F.1: Modelled mixing length; gaining configuration, upstream

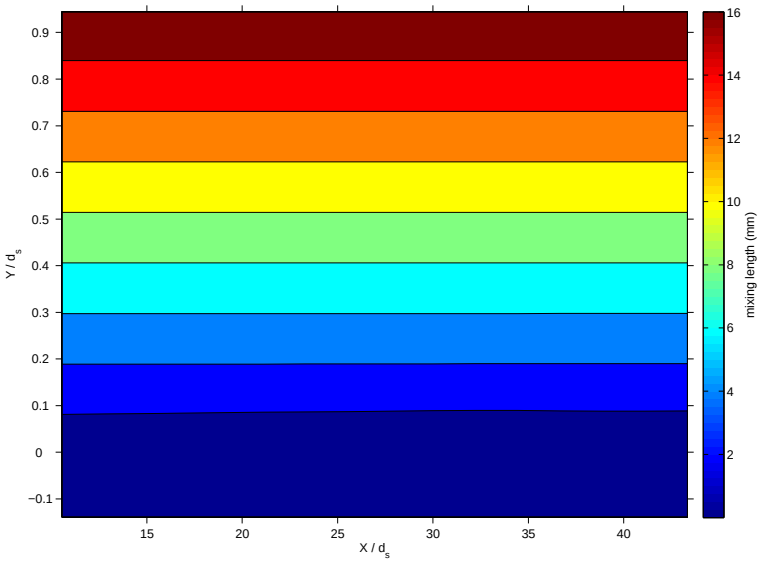

Figure F.2: Modelled mixing length; gaining configuration, downstream

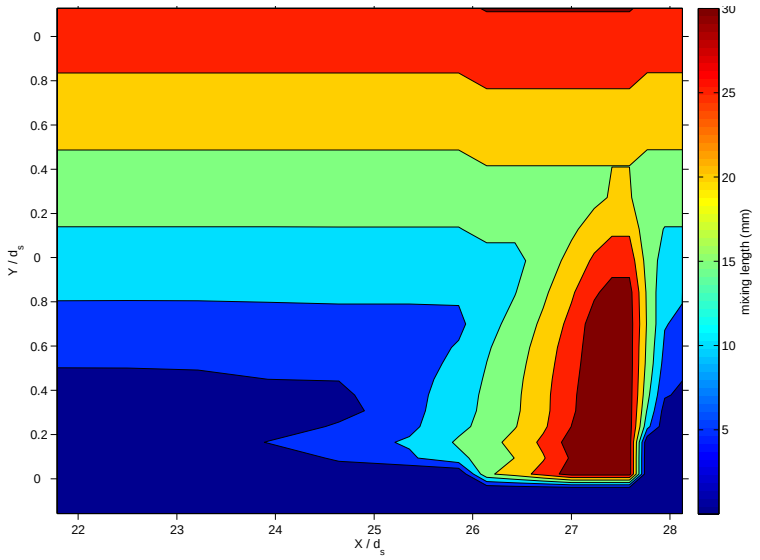

Figure F.3: Modelled mixing length; losing configuration

F.2 Turbulent viscosity

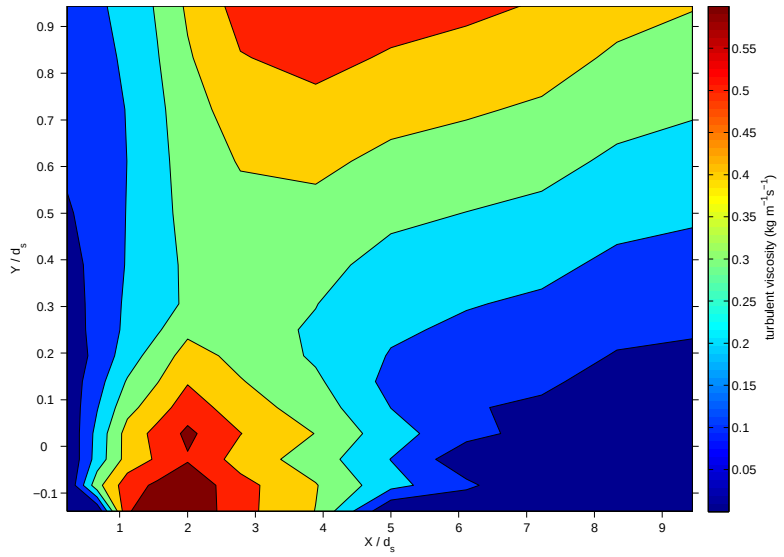

Figure F.4: Modelled turbulent viscosity; gaining configuration, upstream

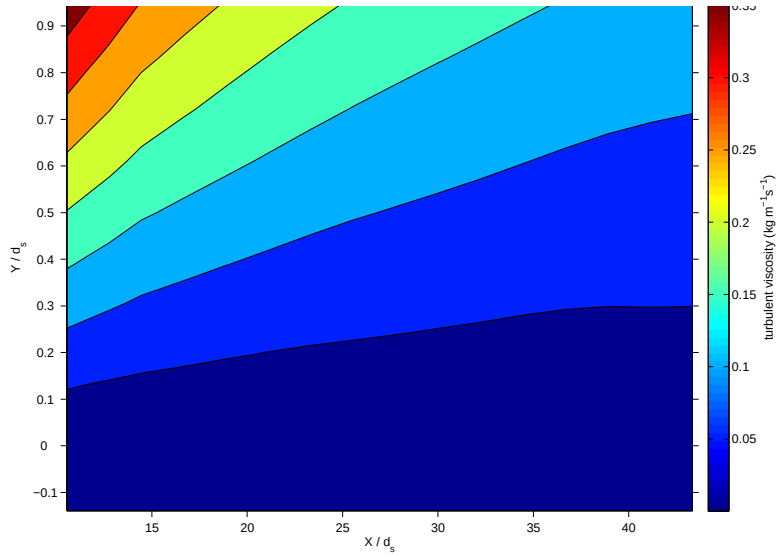

Figure F.5: Modelled turbulent viscosity; gaining configuration, downstream

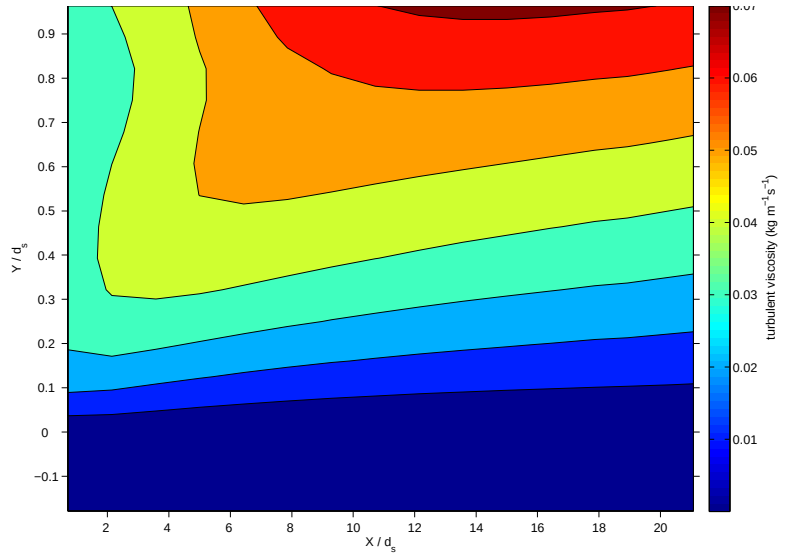

Figure F.6: Modelled turbulent viscosity; losing configuration, upstream

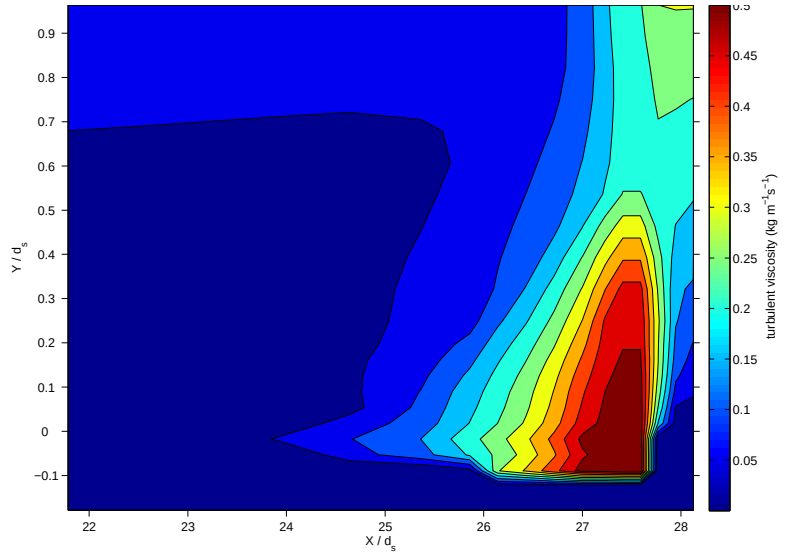

Figure F.7: Modelled turbulent viscosity; losing configuration, downstream

References

Andersen, P., Kays, W. and Moffat, R. (1975), 'Experimental results for transpired turbulent boundary-layer in an adverse pressure-gradient', *Journal of Fluid Mechanics* **69**, 353–375.

Anderson, M. P. and Woessner, W. W. (1992), *Applied Groundwater Modelling: Simulation of Flow and Advective Transport*, Academic Press, Inc., San Diego.

Aqualinc (2007), Canterbury groundwater model 2, Technical report, Aqualinc Research Ltd.

Aqualinc (2010), Update of water allocation data and estimate of actual water use of consented takes - 2009-10, Technical report, Aqualinc Research Ltd, report H10002 for Ministry for the Environment.

Babkin, V. and Vuglinsky, V. (2003), The Earth and its physical features, *in* I. Shiklomanov and J. Rodda, eds, 'World Water Resources at the Beginning of the Twenty-First Century', International Hydrology Series, Cambridge University Press, pp. 1–18.

Bakker, A. (2006), 'Applied computational fluid dynamics lecture notes.'.
URL: *http://www.bakker.org/dartmouth06/engs150/*

Bear, J. (1972), *Dynamics of Fluids in Porous Media*, Environmental Science Series, Elsevier, New York.

Bear, J. and Bachmat, Y. (1990), *Introduction to Modelling of Transport Phenomena in Porous Media*, Vol. 4 of *Theory and Applications of Transport in Porous Media*, Kluwer Academic Publishers.

Beavers, G. S. and Joseph, D. D. (1967), 'Boundary conditions at a naturally permeable wall', *Journal of Fluid Mechanics* **30**(1), 197–207.

Breugem, W., Boersma, B. and Uittenbogaard, R. (2006), 'The influence of wall permeability on turbulent channel flow.', *Journal of Fluid Mechanics* **562**, 35–72.

Brown, G. (2002), 'Henry darcy and the making of a law', *Water Resources Research* **38**(7), 11–1 – 11–12.

Brownbill, R., Lamontagne, S., Williams, R., Cook, P., Simmons, C. and Merrick, N. (2011), Interconnection of surface and groundwater systems river losses from losing-disconnected streams., Technical report, NSW Office of Water.

Brunner, G. W. (2002), *HEC-RAS River Analysis System. Hydraulic Reference Manual Version 3.1*, US Army Corp of Engineers.

Brunner, P., Cook, P. G. and Simmons, C. T. (2009), 'Hydrogeologic controls on disconnection between surface water and groundwater', *Water Resources Research* **45**(1), W01422.

Brunner, P. and Simmons, C. T. (2012), 'Hydrogeosphere: A fully integrated, physically based hydrological model', *Ground Water* **50**(2), 170–176.

Brunner, P., Simmons, C. T., Cook, P. G. and Therrien, R. (2010), 'Modeling Surface Water-Groundwater Interaction with MODFLOW: Some Considerations', *Ground Water* **48**(2), 174–180.

Camporese, M., Paniconi, C., Putti, M. and Orlandini, S. (2010), 'Surface-subsurface flow modeling with path-based runoff routing, boundary condition-based coupling, and assimilation of multisource observation data', *Water Resources Research* **46**(2), W02512.

Canterbury Mayoral Forum (2009), 'Canterbury water management strategy: Strategic framework'.

Cardenas, M. B. and Wilson, J. (2006), 'The influence of ambient groundwater discharge on exchange zones induced by currentbedform interactions', *Journal of Hydrology* **331**(12), 103 – 109.

Cardenas, M. B. and Wilson, J. L. (2007), 'Dunes, turbulent eddies, and interfacial exchange with permeable sediments', *Water Resources Research* **43**(8), W08412.

Causon, D., Mingham, C. and Qian, L. (2011), *Introductory Finite Volume Methods for PDEs*, Ventus.

Celia, M. A., Bouloutas, E. and Zarba, R. (1990), 'A general mass-conservative numerical solution for the unsaturated flow eq', *Water Resources Research* **26**(7), 1483–1496.

Chan, H. C., Huang, W. C., Leu, J. M. and Lai, C. J. (2007), 'Macroscopic modeling of turbulent flow over a porous medium', *International Journal of Heat and Fluid Flow* **28**(5), 1157–1166.

Choi, C. Y. and Waller, P. M. (1997), 'Momentum transport mechanism for water flow over porous media', *Journal of Environmental Engineering-ASCE* **123**(8), 792–799.

Chow, V., Maidment, D. and Mays, L. (1988), *Applied Hydrology*, McGraw Hill series in water resources and environmental engineering, McGraw Hill.

COMSOL Multiphysics (2011), 'Forchheimer flow - documentation - model gallery', Webpage. accessed 13/06/2014.
URL: *https://www.comsol.com/model/forchheimer-flow-4413*

Craig, R. F. (1997), *Soil Mechanics (6th Edition)*, E & FN Spon.

Darcy, H. (1856), *Les Fontaines Publiques de la Ville de Dijon*, Dalmont, Paris.

Dark, A., Bright, J. and Weir, J. (2009), Canterbury strategic water study - stage iv, Technical report, Aqualinc Research Ltd. Report L07120/1 prepared for Environment Canterbury.

de Lemos, M. J. S. (2005), Mathematical modeling and applications of turbulent heat and mass transfer in porous media., *in* K. Vafai, ed., 'Handbook of Porous Media', Taylor and Francis, pp. 409 – 454.

de Lemos, M. J. S. and Silva, R. A. (2006), 'Turbulent flow over a layer of a highly permeable medium simulated with a diffusion-jump model for the interface', *International Journal of Heat and Mass Transfer* **49**(3-4), 546–556.

Devlin, J., Schillig, P., Bowen, I., Critchley, C., Rudolph, D., Thomson, N., Tsoflias, G. and Roberts, J. (2012), 'Applications and implications of direct groundwater velocity measurement at the centimetre scale', *Journal of Contaminant Hydrology* **127**, 3 – 14.

Dey, S., Sarkar, S. and Ballio, F. (2011), 'Double-averaging turbulence characteristics in seeping rough-bed streams', *Journal of Geophysical Research* **116**(3), F03020.

Domenico, P. and Schwartz, F. (1990), *Physical and Chemical Hydrogeology*, Wiley.

Environment Agency (UK) (2009), The Hyporheic Handbook, Technical Report SC050070.

Environment Canterbury (2013), 'Groundwater allocation summary', webpage. accessed 11/04/2016.
URL: *http://ecan.govt.nz/services/online-services/monitoring/groundwater-allocation/Pages/groundwater-allocation-summary.aspx*

European Commission (2000), 'Directive 2000/60/EC of the European Parliament and of the Council, establishing a framework for Community action in the field of water policy.'.

Fenemor, A. and Robb, C. (2001), Groundwater management in new zealand, *in* M. Rosen and P. White, eds, 'Groundwaters of New Zealand', New Zealand Hydrological Society Inc., pp. 273 – 289.

Forchheimer, P. (1901), 'Water movement through the ground', *Zeitschrift Des Vereines Deutscher Ingenieure* **45**, 1781–1788.

Freeze, R. A. and Harlan, R. L. (1969), 'Blueprint for a physically-based, digitally-simulated hydrologic response model', *Journal of Hydrology* **9**(3), 237–258.

Freeze, R. and Cherry, J. (1979), *Groundwater*, Prentice-Hall.

Furman, A. (2008), 'Modeling coupled surface-subsurface flow processes: A review', *Vadose Zone Journal* **7**(2), 741–756.

Graham, D. and Butts, M. (2005), Flexible, integrated watershed modelling with MIKE-SHE, *in* V. Singh and D. Frevert, eds, 'Watershed Models', CRC Press, pp. 245 – 272.

Graton, L. C. and Fraser, H. J. (1935), 'Systematic packing of spheres: With particular relation to porosity and permeability', *The Journal of Geology* **43**(8), pp. 785–909.

Gray, W. G. (1975), 'Derivation of equations for multi-phase transport', *Chemical Engineering Science* **30**(2), 229–233.

Gray, W. G. and Oneill, K. (1976), 'General equations for flow in porous-media and their reduction to darcy's law', *Water Resources Research* **12**(2), 148–154.

Hannah, D., Krause, S., Fleckenstein, J., Heppell, K., Pickup, R., Pinay, G., Robertson, A. and Wood, P. (2009), Biogeochemistry and the hydroecology of the hyporheic zone, *in* 'The Hyporheic Handbook', The Environment Agency (UK).

Harbaugh, A., Banta, E., Hill, M. and McDonald, M. (2000), MODFLOW-2000, the U.S. Geological Survey modular ground-water model - user guide to modularization concepts and the ground-water flow process, Technical report, USGS.

Henderson, F. (1966), *Open Channel Flow*, Macmillan Series in Civil Engineering, Macmillan, New York.

Hicks, D. and Mason, P. (1991), *Roughness Characteristics of New Zealand Rivers.*, Water Resources Survey, DSIR Marine and Freshwater.

Hinze (1959), *Turbulence : an introduction to its mechanism and theory.*, McGraw Hill.

Huang, G. and Yeh, G.-T. (2009), 'Comparative study of coupling approaches for surface water and subsurface interactions', *Journal of Hydrologic Engineering* **14**(5), 453 – 462.

Huebner, K. H., Thornton, E. A. and Byron, T. D. (1995), *The Finite Element Method for Engineers*, 3rd edn, Wiley Interscience.

Hunt, B. (1990), 'An approximation for the bank storage effect', *Water Resources Research* **26**(11), 2769 – 2775.

Hunt, B. (2003), 'Unsteady stream depletion when pumping from semi-confined aquifer.', *Journal of Hydrologic Engineering* **8**(1), 12–19.

Hunt, B. (2014), 'Review of strem depletion ssolution, behaviour and calculations', *Journal of Hydrologic Engineering* **19**(1), 167–178.

IGRAC (2013), 'Ten years of assessing the world's groundwater', booklet, International Groundwater Resources Assessment Centre.

IGRAC (2014), 'The hidden resource', webpage. accessed 29/04/2015.
URL: *http://www.thehiddenresource.com*

Ingham, D. and Ma, L. (2005), *Computaional Fluid Dynamics: Applications in Environmental Hydraulics.*, Wiley, chapter Fundamental Equations for CFD in River Flow Simulations., pp. 19–50.

Iskander, M. and Tabe, K. (2010), Geotechnical properties of aquabeads, *in* M. Iskander, ed., 'Modeling with Transparent Soils', Springer-Verlag, pp. 117 – 135.

Kampf, S. K. and Burges, S. J. (2007), 'A framework for classifying and comparing distributed hillslope and catchment hydrological models', *Water Resources Research* **43**(5), W05423.

Kim, J., Moin, P. and Moser, R. (1987), 'Turbulence statistics in fully developed channel flow at low reynolds number.', *Journal of Fluid Mechanics* **177**, 133–166.

Kollet, S. J. and Maxwell, R. M. (2006), 'Integrated surface-groundwater flow modeling: A free-surface overland flow boundary condition in a parallel groundwater flow model', *Advances in Water Resources* **29**(7), 945–958.

Kosugi, K., Hopmans, J. and Dane, J. (2002), *Methods of Soil Analysis. Part 4: Physical Methods*, Soil Science Society of America, Inc., chapter Parametric Models.

Kuznetsov, A. (2004), 'Numerical modelling of tubulent flow in a composite porous / fluid duct utilizing a two-layer $k - \epsilon$ model to account for interface roughness.', *International Journal of Thermal Science* **43**(11), 1047–1056.

Kuznetsov, A. and Becker, S. (2004), 'Effect of the interface roughness on turbulent convective heat transfer in a composite porous / fluid duct.', *International Communications in Heat and Mass Transfer.* **31**(1).

Land and Water Forum (2010), Report of the Land and Water Forum: A fresh start for fresh water, Technical report.

Landcare Research NZ Ltd (2010), 'NZ Land Resource Inventory - Slope', GIS data.
URL: *https://lris.scinfo.org.nz/layer/64-nzlri-slope/*

Lane, S. and Hardy, R. (2002), Porous rivers: a new way of conceptualising and modelling river and floodplain flows, *in* D. Ingham and I. Pop, eds, 'Transport Phenomena in Porous Media 2', Pergamon / Elsevier, pp. 425–449.

Larned, S., Hicks, D., Schmidt, J., Davey, A., Dey, K., Scarsbrook, M., Arscott, D. and Woods, R. (2008), 'The Selwyn River of New Zealand: a benchmark system for alluvial plain rivers', *River Research and Applications* **24**.

Larned, S., Unwin, M. and Boustead, N. (2015), 'Ecological dynamics in the riverine aquifer of a gaining and losing river.', *Freshwater Science* **31**(1), 245–262.

Launder, B. and Sharma, B. (1974), 'Application of the energy-dissipation model of turbulence to the calculation of flow near a spinning disc.', *Letters in Heat and Mass Transfer.* **1**.

Launder, B. and Spalding, D. (1974), 'The numerical computation of turbulent flows', *Computer Methods in Applied Mechanics and Engineering* **3(2)**, 269 – 289.

Leschziner, M. and Rodi, W. (1979), 'Calculation of strongly curved open channel flow', *Journal of the Hydraulics Division, ASCE* **105**.

Manes, C., Pokrajac, D., McEwan, I. and Nikora, V. (2009), 'Turbulence structure of open channel flows over permeable and impermeable beds: A comparative study', *Physics of Fluids* **21**(12).

MathWorks (2016), 'mldivide, - Solve systems of linear equations Ax = B for x', MATLAB documentation webpage. accessed 08/04/2016.
URL: *http://au.mathworks.com/help/matlab/ref/mldivide.html*

Maxwell, R. M. (2009), 'Coupled surface-subsurface modeling across a range of temporal and spatial scales', *Vadose Zone Journal* **8**(4), 823–824.

Maxwell, R. M., Putti, M., Meyerhoff, S., Delfs, J.-O., Ferguson, I. M., Ivanov, V., Kim, J., Kolditz, O., Kollet, S. J., Kumar, M., Lopez, S., Niu, J., Paniconi, C., Park, Y.-J., Phanikumar, M. S., Shen, C., Sudicky, E. A. and Sulis, M. (2014), 'Surface-subsurface model intercomparison: A first set of benchmark results to diagnose integrated hydrology and feedbacks', *Water Resources Research* **50**(2), 1531–1549.

Monnikhoff, B. (2011), *IfmMIKE11 2.0 Coupling the groundwater model FEFLOW® and the surface water model MIKE11®. User Manual.* DHI-WASY GmbH.

Moreau, M. and Bekele, M. (2015), Groundwater component of the Water Physical Stock Account (WPSA), Technical report, GNS Science Consultancy Report 2014/290 for Ministry for the Environment.

Neale, L. and Price, R. (1964), 'Flow characteristics of PVC sewer pipe.', *Journal of the Sanitary Engineering Division ASCE* **90**(SA3), 109 – 129.

Neuman, S. P. (1972), 'Field determination of the hydraulic properties of leaky multiple-aquifer systems.', *Water Resources Research* **8**, 1284–1298.

Neuman, S. P. (1977), 'Theoretical derivation of Darcy's Law', *Acta Mechanica* **25**, 153 – 170.

Nield, D. A. (1991), 'The limitations of the Brinkman-Forchheimer equation in modelling flow in a saturated porous medium and at an interface.', *International Journal of Heat and Fluid Flow* **12**(3).

Nield, D. A. and Bejan, A. (2013), *Covection in Porous Media: 4th Edition*, Springer.

Nikora, V., Goring, D., McEwan, I. and Griffiths, G. (2001), 'Spatially averaged open-channel flow over rough bed', *Journal of Hydraulic Engineering-ASCE* **127**(2), 123–133.

Nikora, V., McEwan, I., McLean, S., Coleman, S., Pokrajac, D. and Walters, R. (2007a), 'Double-averaging concept for rough-bed open-channel and overland flows: Theoretical background', *Journal of Hydraulic Engineering-ASCE* **133**(8), 873–883.

Nikora, V., McLean, S., Coleman, S., Pokrajac, D., McEwan, I., Campbell, L., Aberle, J., Clunie, D. and Kol, K. (2007b), 'Double-averaging concept for rough-bed open-channel and overland flows: Applications', *Journal of Hydraulic Engineering-ASCE* **133**(8), 884–895.

Niswonger, R. G. and Prudic, D. E. (2010), Documentation of the streamflow-routing (SFR2) package to include unsaturated flow beneath streamsa modification to SFR1, Technical report, US Geological Survey.

Niswonger, R. G., Prudic, D. and Regan, R. (2006), Documentation of the unsaturate-zone flow (UZF1) package for modeling unsaturated flow between the land surface and the water table with MODFLOW-2005., Technical report, US Geological Survey.

Nokes, R. (2013), *Streams Version 2.01: System Theory and Design*, Department of Civil and Natural Resources Engineering, University of Canterbury.

Omnova Solutions (2012), 'Portfolio sheet: Solvent-based resins for coatings', webpage. accessed 26/05/2015.
URL: *http://www.hubronspeciality.com/wp-content/uploads/2013/09/Portfolio-Sheet-SB-Resins-for-coatings-EMEA-Oct-2012.pdf*

Panday, S. and Huyakorn, P. S. (2004), 'A fully coupled physically-based spatially-distributed model for evaluating surface/subsurface flow', *Advances in Water Resources* **27**(4), 361–382.

Panday, S., Langevin, C., Niswonger, R. G., Ibaraki, M. and Hughes, J. (2013), MODFLOW-USG version 1: An unstructured grid version of MODFLOW for simulating groundwater flow and tightly coupled processes using a control volume finite-difference formulation, *in* 'U.S. Geological Survey Techniques and Methods', book 6, chap. A45, 66p.

Patankar, S. (1980), *Numerical Heat Transfer and Fluid Flow*, Series in computational methods in mechanics and thermal sciences, Taylor and Francis.

Patankar, S. and Spalding, D. (1972), 'A calculation procedure for heat, mass and momentum transfer in three-dimensional parabolic flows.', *International Journal of Heat and Mass Transfer* **15, 10**, 1787 – 1806.

Pokrajac, D. and Manes, C. (2008), 'Interface between turbulent flows above and within rough porous walls', *Acta Geophysica* **56**(3), 824–844.

Poole, G., O'Daniel, S., Jones, K., Woessner, W. W., Bernhardt, E., Helton, A., Stanford, J., Boer, B. and Beechie, T. (2008), 'Hydrologic spiralling: the role of multiple interactive flow paths in stream ecosystems.', *River Research and Applications* **24**(7), 1018–1031.

Pope, S. (2000), *Turbulent Flows*, Cambridge University Press.

Prudic, D., Konikow, L. and Banta, E. (2004), A new streamflow-routing (SFR1) package to simulate stream-aquifer interaction with MODFLOW-2000, Technical Report U.S. Geological Survey Open-file report 2004-1042, USGS.

Rameshwaran, P., Naden, P. S. and Lawless, M. (2011), 'Flow modelling in gravel-bed rivers: rethinking the bottom boundary condition', *Earth Surface Processes and Landforms* **36**(10), 1350–1366.

Rhie, C. and Chow, W. (1983), 'Numerical study of the turbulent flow past and airfoil with trailing edge separation', *American Institute of Aeronautics and Astronautics Journal* **21**(11), 1525–1532.

Ritzema, H. (1994), *Drainage Principles and Applications*, International Institute for Land Reclamation and Improvement.

Rodi, W. (1980), *Turbulence models and their applications in hydraulics - a state of the art review*, IAHR.

Sawyer, A. H., Bayani Cardenas, M. and Buttles, J. (2011), 'Hyporheic exchange due to channel-spanning logs', *Water Resources Research* **47**(8).

Sawyer, A. H. and Cardenas, M. B. (2009), 'Hyporheic flow and residence time distributions in heterogeneous cross-bedded sediment', *Water Resources Research* **45**.

Schäfer, M. (2006), *Computational Engineering - Introduction to Numerical Methods*, Springer.

Shahraiyni, H. T. and Ataie-Ashtiani, B. (2012), 'Mathematical Forms and Numerical Schemes for the Solution of Unsaturated Flow Equations', *Journal of Irrigation and Drainage - ASCE* **138**(1), 63–72.

Shavit, U., Bar-Yosef, G. and Rosenzweig, R. (2002), 'Modified Brinkman equation for a free flow problem at the interface of porous surfaces: The Cantor-Taylor brush configuration case', *Water Resources Research* **38**(12).

Smith, J. W. (2005), Groundwater - surface water interactions in the hyporheic zone, Technical Report SC030155/SR1, Environment Agency (UK).

Spalding, D. (1985), The computation of flow around ships with allowance for free-surface and density-gradient effects, *in* M. R. Heller, ed., 'Maritime Simulation.

Proceedings of the 1st Intercontinental Symposium, Munich.', Springer-Verlag, pp. 101–113.

Sriboonlue, V. (1985), Steady-State Underflow in Gravel Bed Rivers, PhD thesis.

Stevenson, T. (1963), A law of the wall for turbulent boundary layers with suction or injection, Technical Report 166, The College of Aeronautics Cranfield.

Tan, H. and Pillai, K. M. (2009), 'Finite element implementation of stress-jump and stress-continuity conditions at porous-medium, clear-fluid interface', *Computers & Fluids* **38**(6), 1118–1131.

Tennekes, H. and Lumley, J. (1972), *A First Course in Turbulence*, MIT Press.

Theis (1935), 'The relation between the lowering of the piezometric surface and the rate and duration of discharge of a well using groundwater storage.', *American Geophysical Union Transactions* **2**, 519–524.

Theis, C. (1941), 'The effect of a well on the flow of a nearby stream', *American Geophysical Union Transactions* **22**(3).

Vafai, K. (1984), 'Convective flow and heat transfer in variable-porosity media.', *Journal of Fluid Mechanics* **147**, 233–259.

Vafai, K. and Kim, S. J. (1990), 'Fluid mechanics of the interface region between a porous-medium and a fluid layer - an exact solution', *International Journal of Heat and Fluid Flow* **11**(3), 254–256.

Vafai, K. and Kim, S. J. (1995), 'On the limitations of the Brinkman-Forchheimer extended Darcy equation', *International Journal of Heat and Fluid Flow* **16**(1), 11–15.

van Driest, E. (1956), 'On turbulent flow near a wall', *Journal of the Aeronautical Sciences* **23**(11), 1007–1011.

van Dyke, M. (1982), *An Album of Fluid Motion*, Parabolic Press.

van Genuchten, M. T. (1980), 'A closed-form equation for predicting the hydraulic conductivity of unsaturated soils', *Soil Science Society of America Journal* **44**, 892 – 898.

Vrba, J. and van der Gun, J. (2004), The world's groundwater resources, Technical Report IP2004-1, International Groundwater Resources Assessment Centre.

Vreugdenhil, C. (1994), *Numerical Methods for Shallow-Water Flow*, Kluwer Academic Publishers.

Wallin, S. and Johansson, A. (2000), 'An explicit algebraic Reynolds stress model for incompressible and compressible turbulent flows.', *Journal of Fluid Mechanics* **403**, 89–132.

Walters, R. A. and Plew, D. R. (2008), 'Numerical modeling of environmental flows using DAM: Some preliminary results', *Acta Geophysica* **56**(3), 918–934.

Wang, C. and Papell, S. (1983), Three-dimensional turbulent-mixing-length modeling for discrete-hole coolant injection into a crossflow, NASA Technical Paper 2200, NASA.

Wang, H. F. and Anderson, M. P. (1982), *Introduction to Groundwater Modeling: Finite Difference and Finite Element Methods*, Freeman.

Ward, J. (1964), 'Turbulent flow in porous media', *Proceedings of the American Society of Civil Engineers Hydraulics Division* **90**(HY5), 1–12.

Wen, Z., Huang, G. and Zhan, H. (2011), 'Non-Darcian flow to a well in a leaky aquifer using the Forchheimer equation', *Hydrogeology Journal* **19**.

Whitaker, S. (1967), 'Diffusion and dispersion in porous media', *AIChE Journal* **13**(3).

Whitaker, S. (1973), 'Transport equations for multi-phase systems', *Chemical Engineering Science* **28**(1), 139–147.

Whitaker, S. (1986), 'Flow in porous-media. 1. a theoretical derivation of Darcy's Law', *Transport in Porous Media* **1**(1), 3–25.

Whitaker, S. (1996), 'The Forchheimer equation: A theoretical development', *Transport in Porous Media* **25**(1), 27–61.

Whitaker, S. (1998), *The Method of Volume Averaging*, Kluwer Academic Publishers.

Wilcox, D. (1993), *Turbulence Modelling for CFD*, DCW Industries Inc.

Winter, T. C., Harvey, J. W., Franke, O. L. and Alley, W. M. (1998), Ground water and surface water: A single resource, Technical report, US Geological Survey.

Yeh, G.-T. G. and Huang, G. (2007), Coupling approaches for surface water and groundwater interactions in watershed modelling, *in* 'World Environmental and Water Resources Congress 2007: Restoring Our Natural Habitat', ASCE.

Yeh, G.-T., Huang, G., Zhang, F., Cheng, H.-P. and Lin, H.-C. (2005), WASH123D: A numerical model of flow, thermal transport, and salinity, sediment, and water quality transport in watershed systems of 1-d stream-river network, 2-d overland regime, and 3-d subsurface media, Technical report, Prepared for the Office of Research and Development, US Environmental Protection Agency.